Modeling of Multi-Axial Fatigue Damage Under Non-Proportional Variable-Amplitude Loading Conditions

By

Jifa Mei

A dissertation submitted in partial fulfillment
of the requirements for the degree of
Doctor of Philosophy
(Naval Architecture and Marine Engineering)
in The University of Michigan
2017

Doctoral Committee:

Professor Pingsha Dong, Chair
Professor John Allison
Assistant Professor Matthew Collette
Associate Professor David J. Singer
Dr. Zhigang Wei, Tenneco Co.

Jifa Mei

meijifa@umich.edu

ORCID iD: 0000-0002-8859-3933

Acknowledgments

I would like to sincerely thank my advisor, Prof. Pingsha Dong, for not only providing me this opportunity to research into multi-axial fatigue starting from four years ago but also for his detail-oriented and meticulous academic guidance during my Ph.D research. This dissertation could not be done without a substantial amount of meetings and discussions with Prof. Dong. The efforts made by Prof. Dong during this long journey are gratefully appreciated.

My thanks also go to my advisory committee members: Prof. John Allison from the Department of Material Science; Prof. Matthew Collette and Prof. David J. Singer from Naval Architecture and Marine Engineering (NAME) department and Dr. Zhigang Wei from Tenneco. Inc. for providing valuable suggestions and feedbacks. Especially, I am thankful for Dr. Wei's encouragement for me to take on this research topic.

I would also like to thank my colleges for beneficial discussions and help during the enjoyable journey. They are Dr. Shaopin Song, Dr. Shizhu Xing, Xianjun Pei and Hanqing Lu. It's a great pleasure to be able to work with your guys.

Last but not the least, I would like to thank my parent and sisters for their endless support throughout my whole education till today.

Table of Contents

List of Figures

List of Tables

Nomenclature

Chapter 1

A_T measure of non-proportionality in Jiang and Kurah's increment of yield surface model

F_0 rotation factor of non-proportional path

$K_I^{(2)}$ mode I stress intensity factor for a kinked crack

K_I stress intensity factor of mode I crack

$K_{II}^{(2)}$ mode II stress intensity factor for a kinked crack

K_{II} stress intensity factor of mode II crack

K_{III} stress intensity factor of mode III crack

K'_{NP} cyclic coefficient for non-proportional loading

K_f fatigue notch factor

K^p plastic modulus

K_t stress concentration factor

Y_I compliance function for mode I stress intensity factor

Y_{II} compliance function for mode II stress intensity factor

b_0 shear fatigue strength exponent

b_0 material constant in Jiang and Kurah's increment of yield surface model

c_0 material constant used in Armstrong-Frederick model

$f_{y'}$ line force distribution along y' direction in local coordinate system $x' - y' - z'$)

f_{NP} non-proportionality factor used in Itoh et al.'s model

f_b bending frequency

f_t torsion frequency

$m_{x'}$ line moment distribution along x' direction in local coordinate system $x' - y' - z'$)

n' cyclic hardening exponent

q_N hardening parameter for non-proportional loading in Jiang and Kurah's increment of yield surface model

q_P proportional hardening parameter in Jiang and Kurah's increment of yield surface model

$\boldsymbol{a}^i$ backstress component tensor

α_I material dependent additional hardening coefficient

γ_0 material constant used in Armstrong-Frederick model

ε^e pseudo strain

ε_e^p effective plastic strain

θ_c angle of maximum tangential stress

ρ' characteristic length of materials used in Peterson's equation

σ_{0° equivalent stress amplitudes for 90° in phase loading

σ_{90° equivalent stress amplitudes for 90° out of phase loading

σ_{hs} hot spot stress

$\sigma_{hyd,max}$ maximum value of hydrostatic stress that occurs in a cycle

σ_{hyd} hydrostatic stress

σ_a normal stress amplitude

σ_b normal bending structural stress

σ^e pseudo stress

σ_f fatigue limit under tension

σ_i *i*th principal stress

σ_{ij} stress tensor component

σ_k notch stress

σ_m normal membrane structural stress

$\sigma_{n,max}$ maximum normal stress within a cycle

σ_n nominal stress

σ_s normal structural stress

σ_u ultimate tensile strength

σ_y yield strength

$\sigma_y(\varepsilon_e^p)$ yield surface as a function of effective plastic strain

τ_a shear stress amplitude

τ_f fatigue limit under torsion

τ_f' shear fatigue strength coefficient

τ_s in-plane shear structural stress

τ_z transverse shear structural stress

ΔK_e effective stress intensity factor range

ΔK_{th} stress intensity factor threshold value for fatigue crack growth

$\Delta\gamma_{max}$ maximum shear strain range

$\Delta\varepsilon_{von}$ von Mises strain range

$\Delta\sigma_e$ effective stress range

$\Delta\sigma_{eq}^{I}$ principal stress based equivalent stress range

$\Delta\sigma_{von}$ von Mises effective stress range

$\Delta\tau_{oct}$ octahedral shear stress range

ΔK stress intensity factor range

$\Delta\sigma$ normal stress range

$\Delta\tau$ shear stress range

L reference length

$\Delta\tau_{max}$ maximum shear stress range within a cycle

K' cyclic strength coefficient

$d\boldsymbol{\varepsilon}^p$ plastic strain increment tensor

da/dN crack growth rate

$d\boldsymbol{\sigma}$ stress increment tensor

k a material dependent parameter reflecting the effect of normal stress on fatigue damage

$\boldsymbol{S}$ deviatoric stress tensor

$\boldsymbol{a}$ backstress tensor

$\boldsymbol{n}$ normal direction of yield surface

δ phase angle

ρ material dependent characteristic length in Neuber's equation

Chapter 2

AB semi-circular load path

$\Delta\varepsilon_{NP}$ MLP-based equivalent strain range

$\Delta\varepsilon_e$ effective strain range along a proportional path or the distance between two extreme positions within one half cycle defined on $\varepsilon - \sqrt{\beta^{\varepsilon}}\gamma$ strain plane

$\Delta\sigma_{NP}$ MLP-based equivalent stress range

$\Delta\sigma_e$ effective stress range along a proportional path or the distance between two extreme positions within one half cycle defined on $\sigma - \sqrt{\beta}\tau$ stress plane

$\widetilde{AB}$ non-proportional load path

$\overline{AB}$ proportional load path

D_{Max} maximum possible non-proportional damage within one half cycle

D_{NP} fatigue damage caused by non-proportionality of load path

D_P fatigue damage caused by reference proportional load path

dD_{NP} non-proportional fatigue damage caused by load path increment, ds

f_b loading frequency of bending stresses

f_t loading frequency of torsional stresses

g_{NP} non-proportionality damage factor defined on $\sigma - \sqrt{\beta}\tau$ stress plane

g_{NP}^{ε} non-proportionality damage factor defined on $\varepsilon - \sqrt{\beta^{\varepsilon}}\gamma$ strain plane

α^{ε} material sensitivity parameter load-path non-proportionality defined on $\varepsilon - \sqrt{\beta^{\varepsilon}}\gamma$ strain plane

β^{ε} fatigue life equivalency factor between tensile strain and torsional strain ($\beta^{\varepsilon} = 1/3$ taken from literature)

σ_n nominal axial stress

σ_s bending structural stress

τ_n nominal shear stress

τ_s shear structural stress

D total multi-axial fatigue damage of one half cycle

E Young's modulus

G shear modulus

$p(\sigma, \tau)$ weight function against tensile strain energy density increment ($\sigma d\varepsilon$)

$q(\sigma, \tau)$ weight function against shear strain energy density increment ($\tau d\gamma$)

α material sensitivity parameter to load-path non-proportionality defined on $\sigma - \sqrt{\beta}\tau$ stress plane

β fatigue life equivalency factor between tensile stress and torsional stress ($\beta = 3$ taken from literature)

γ shear strain

ε axial strain

η length ratio of minor axis length over major axis of an elliptical load path.

σ axial stress

τ shear stress

υ Poisson's ratio

Chapter 3

σ axial stress

τ shear stress

σ_0 axial stress amplitude in sinusoidal wave loading

τ_0 shear stress amplitude in sinusoidal wave loading

ε axial strain

γ shear strain

β fatigue life equivalency factor calculated using difference between S-N curves obtained under simple cyclic tensile and shear stresses, respectively ($\beta = 3$ taken from literature)

β^{ε} fatigue life equivalency factor calculated using difference between factor between E-N curves obtained under simple cyclic tensile and shear tensile strains, respectively ($\beta^{\varepsilon} = 1/3$ taken from literature)

$\overline{AB}$ proportional load path

$\widetilde{AB}$ non-proportional load path

AB semi-circular load path

D total multi-axial fatigue damage of one half cycle

D_P fatigue damage caused by reference proportional load path

D_{NP} fatigue damage caused by non-proportionality of load path

D_{Max} maximum possible non-proportional damage within one half cycle

g_{NP} non-proportionality damage factor defined on $\sigma - \sqrt{\beta}\tau$ stress plane

$g_{NP}^{(A)}$ non-proportionality damage factor of proportional path A (superscript)

$g_{NP}^{(B)}$ non-proportionality damage factor of non-proportional path B (superscript)

g_{NP}^{ε} non-proportionality damage factor defined on $\varepsilon - \sqrt{\beta^{\varepsilon}}\gamma$ strain plane

α material sensitivity parameter to load-path non-proportionality defined on $\sigma - \sqrt{\beta}\tau$ stress plane

α^{ε} material sensitivity parameter load-path non-proportionality defined on $\varepsilon - \sqrt{\beta^{\varepsilon}}\gamma$ strain plane

$\Delta\sigma_e$ effective stress range along a proportional path or the distance between two extreme positions within one half cycle defined on $\sigma - \sqrt{\beta}\tau$ stress plane

$\Delta\sigma_e^{(A)}$ effective stress range corresponding to proportional path A (superscript)

$\Delta\sigma_e^{(B)}$ effective stress range corresponding to non-proportional path B (superscript)

$\Delta\varepsilon_e$ effective strain range along a proportional path or the distance between two extreme positions within one half cycle defined on $\varepsilon - \sqrt{\beta^{\varepsilon}}\gamma$ strain plane

$\Delta\varepsilon_e^{(A)}$ effective strain range corresponding to proportional path A (superscript)

$\Delta\varepsilon_e^{(B)}$ effective strain range corresponding to non-proportional path B (superscript)

$\Delta\sigma_{NP}$ MLP-based equivalent stress range

$\Delta\sigma_{NP}^{(A)}$ MLP-based equivalent stress range corresponding to proportional path A (superscript)

$\Delta\sigma_{NP}^{(B)}$ MLP-based equivalent stress range corresponding to non-proportional path B (superscript)

$\Delta\varepsilon_{NP}$ MLP-based equivalent strain range

δ phase shift angle between sinusoidal axial loading and shear loading

A semi-major axis length of an elliptical load path

B semi-minor axis length of an elliptical load path

η length ratio of semi-minor axis length over semi-major axis length of an elliptical load path.

f_b loading frequency of bending stresses

f_t loading frequency of torsional stresses

Chapter 4

$\Delta\sigma_0$ applied nominal normal stress range

$\Delta\sigma_{m,e}$ effective membrane structural stress range

D_P fatigue damage caused by the reference loading

$\widetilde{AB}$ non-proportional load path cycle counted by PDMR

$\overline{AB}$ reference path of non-proportional path $\widetilde{AB}$

D_{EC} total fatigue damage defined in Eurocode 3

D_{IIW} total fatigue damage defined in IIW

D_{Max} non-proportional fatigue damage caused by circular load path

D_{NP} load path non-proportionality caused fatigue damage

K_{σ_s} stress concentration factor of normal structural stress

K_{τ_s} stress concentration factor of shear structural stress

M_y remote cyclic bending in y direction of global coordinate system ($x-y-z$)

M_z remote cyclic torsion in z direction of global coordinate system ($x-y-z$)

$f_{i'}$ line force along i' ($i'=x',y',z'$) direction in local coordinate system $x'-y'-z'$

g_{NP} load path non-proportionality factor

$m_{i'}$ line moment along i' ($i'=x',y'$) direction in local coordinate system $x'-y'-z'$

r_e effective bending ratio

r_σ normal structural stress bending ratio

σ_h normal hot spot stress

σ_b bending component of normal structural stress

σ_m membrane component of normal structural stress

σ_n nominal normal stress

$\sigma_s(t)$ normal structural stress

τ_h shear hot spot stress

τ_b bending component of in plane shear structural stress

τ_m membrane component of in plane shear structural stress

τ_n nominal shear stress

$\tau_s(t)$ in plane structural stress

$\tau_z(t)$ Transverse structural stress

$\Delta\sigma_{\mathrm{e}}$ effective structural stress range

$\Delta\sigma_{\mathrm{n,e}}$ nominal effective stress range

ΔS_{NP} moment of load path (MLP) based equivalent structural stress range

ΔS_{NP}^{R} equivalent structural stress with R ratio considered

ΔS_e equivalent structural stress parameter combing both normal and shear structural stress effect

ΔS_σ equivalent normal structural stress range

$\Delta\sigma_{EC}$ Eurocode 3 based effective stress range

$\Delta\sigma_{IIW}$ IIW based effective stress range

$\Delta\sigma_{b,e}$ effective bending structural stress range

$\Delta\sigma_f$ fatigue strength under pure axial loading

$\Delta\tau_0$ applied nominal shear stress range

$\Delta\tau_f$ fatigue strength under pure shear loading

D total fatigue damage

$I(r_\sigma)$ a dimensionless function of bending ratio r_σ

α material sensitivity defined in $\sigma_s - \sqrt{\beta}\tau_s$ plane

δ phase angle difference

Chapter 5

$\widetilde{AB}$ non-proportional load path in in $K_I - \sqrt{\beta^K}\, K_{III}$ plane

$\sqrt{\beta^K}$ fatigue equivalence parameter between K_I and K_{III}

$\overline{AB}$ reference proportional load path of $\widetilde{AB}$

D_{NP}^K load path non-proportionality caused fatigue damage

D_P^K fatigue damage caused by reference load path

$F_I\left(\frac{a}{W}\right)$ compliance function for mode I stress intensity factor as a function of $\frac{a}{W}$

$F_{III}\left(\frac{a}{W}\right)$ compliance function for mode II stress intensity factor as a function of $\frac{a}{W}$

K^* equivalent stress intensity factor

K_I stress intensity factor of mode I crack

K_{II} stress intensity factor of mode II crack

K_{III} stress intensity factor of mode III crack

K_{Max} maximum stress intensity factor range defined in $K_I - \sqrt{\beta^K}\, K_{III}$ plane

a^K material sensitivity parameter to non-proportional loading defined in $K_I - \sqrt{\beta^K} K_{III}$ plane

$\frac{da}{dN}$ fatigue crack growth rate

g_{NP}^{K} load path non-proportionality factor defined in $K_I - \sqrt{\beta^K} K_{III}$ plane

u_1, u_2 nodal displacements

ΔK_{NP} moment of load path (MLP) based equivalent stress intensity factor range

ΔK_{NP} moment of load path (MLP) MLP based equivalent stress intensity factor range

ΔK_e effective stress intensity factor range

B thickness of a plate

D total fatigue damage

F_1, F_2 nodal forces

$P(t)$ applied tensile load

$Q(t)$ applied out of plane shear force

a crack size

w width of a plate

γ fatigue exponent parameter in two-parameter crack growth model

η material-related parameter measuring interaction effects between Mode I and Mode III crack growths

Abstract

This dissertation presents a new path-dependent non-proportional multi-axial fatigue model which is formulated in an incremental form of moment of load path (MLP) on $\sigma - \sqrt{\beta}\tau$ plane, $\varepsilon - \sqrt{\beta^{\varepsilon}}\gamma$ plane or K plane (i.e $K_I - \sqrt{\beta^K}K_{III}$ plane), depending upon if fatigue evaluation is performed in terms of stress-life, strain-life or crack growth life for a given application of interest. The total fatigue damage of an arbitrary non-proportional load path is partitioned into two parts: one is due to proportional part (defined with respect to a reference path) of the load path and the other is due to non-proportional part. The proportional part can be related to an effective stress range measured, e.g., the distance in $\sigma - \sqrt{\beta}\tau$ plane. The non-proportional part can be shown to be related to an integral form of strain energy densities contributed by normal and shear deformation with each being weighted by a path-dependent function. Furthermore, a dimensionless representation of non-proportional damage, termed as load path non-proportionality factor, is used for construction of a MLP based equivalent stress or strain or stress intensity factor range. A material sensitivity parameter to load-path non-proportionality is also considered in the MLP based fatigue damage model for modeling different materials and their different sensitivities to non-proportional loading. A general procedure for determining material sensitivity to load-path non-proportionality is also proposed and demonstrated.

The MLP based fatigue damage model is implemented as an integral part of a recently developed "path-dependent maximum range" or PDMR cycle counting

procedure for performing both cycle counting for arbitrary non-proportional multiaxial loading histories and computing MLP based fatigue damage as each half cycle is being counted. With this new capability, comprehensive validations of the newly developed model are performed by analyzing multi-axial fatigue test data of various forms (from simple to rather complex load paths) of non-proportional loading in four major areas: (a) structural steels; (b) different series of aluminum alloys; (c) various types of welded structural components; and (d) mixed mode fatigue crack growth in carbon steel and stainless steel. In addition to achieving a good correlation of test data in all four areas above, it is also found that structural steels are more sensitive to non-proportional loading than aluminum alloys. Different grades of aluminum alloys exhibit different levels of sensitivity to non-proportional loading, showing an approximately linear relationship between material ductility and material sensitivity to load-path non-proportionality.

MLP based fatigue damage model is further extended for applications in structural life evaluation of welded structures by formulating an equivalent structural stress parameter that takes into consideration of plate thickness effects, bending ratio effects, and residual stress effects. The effectiveness of the equivalent stress parameter in correlating different components from various sources is proven by its ability to collapse all test data into a much narrower band than those with existing methods given in major international codes and standards (e.g., IIW and Eurocode 3). Finally, non-proportional mixed mode fatigue crack growth problem is examined by extending the MLP model to stress intensity plane or *K* plane. A two-parameter mixed-mode crack growth model is then proposed, which takes into account of both load-path non-proportionality induced damage and mean stress effects computed in *K* plane. Analysis of available existing crack

growth data subjected to non-proportional loading shows that the proposed model provides the most effective data correlation than any other available models.

Chaper 1.

Introduction

1.1 Background

Among many of various mechanical failure modes, fatigue failure of materials and structures have drawn much attention owing to the fact that it is one of the most common and dangerous failure modes in engineering structures. It is estimated that about 50-90 percent of mechanical failures are caused by fatigue [1]. Based on ASTM definition [2], fatigue is a process of progressive localized permanent structural change occurring in a material subjected to conditions that produce fluctuating stresses and strains at some point or points and that may culminate in cracks or complete fracture after a sufficient number of fluctuations. One key characteristic of fatigue failure is that fatigue damage process is a localized process, rendering it difficult to be monitored or detected until almost reaching to the end of total fatigue life. As a result, once a fatigue failure occurs, it often leads to sudden or possibly catastrophic damage. To name a few, the downfall of first jet-propelled passenger airplane, the Comet, was caused by fatigue failure of pressurized cabin [3]; the capsize of Alexander L. Kielland oil platform [4], leading to the worst disaster in Norway ever since World War II in Norwegian waters was caused by fatigue failure in one of its fillet welded tubular components. Since fatigue is a localized damage process involving several stages such as crack initiation, micro-crack growth, small crack growth and marco-crack growth with a length scale ranging

from micro-meter to meter scale, design against fatigue failure and fatigue life prediction are thus becoming challenging topics till today.

Ever since Wöhler introduced the concept of S-N curve and fatigue limit in 1850s, mechanical design against fatigue failure has involved significantly in its philosophy. It starts from the initial infinite-life design concept in which structures or components are designed in an extremely conservative manner so that they are only expected to experience cyclic stress that is below fatigue limit to safe-life design in which durability of product is pre-determined by engineers. Later on, fail-safe design, a concept that fatigue failure of one part is accepted (will be replaced once found) as long as the part will not lead to failure of the whole structure. Recently, damage-tolerant design in which fatigue cracks are tolerated as long as they will not lead to failure within the period of inspection interval are developed for expensive and large scale structures.

Major fatigue life prediction models used today such as nominal stress-life (S-N) model, local strain-life ($\varepsilon - N$) model and fatigue crack growth ($da/dN - \Delta K$) model were initially proposed and applied for uniaxial loading or at least for cases when only one dominant stress/strain/crack mode needs to be considered. However, in practice, most engineering components are subjected to multi-axial cyclic stress in service for two main reasons: (a) multi-sources of loading are operative and (b) the complexity of engineering components imposes geometric constraints and as a result multi-axial stress state is introduced. Two most common examples are presented here as illustrations. For the first case, consider a rotating camshaft as shown in Fig. 1.1. The camshaft is under both cyclic torsion and cyclic bending owing to the periodic ignitions inside engine cylinders. Therefore, it can be easily imagined that the surface of the camshaft is in a bi-axial stress

state. As an another example for geometric constraint-induced multi-axial stress state, consider a plate with a hole under uniaxial tensile loading [5], it can be seen from Fig. 1.2 (b) and Fig. 1.2 (c) that, with the increase of plate thickness, materials in the middle surface near the notch root is subjected to a multi-axial (tri-axial) stress state with a gradual increase of tensile stress in transverse direction. Therefore, it can be seen that multi-axial stress state is so common in real engineering structural components that each stress/strain component has to be dealt with properly for fatigue design and life prediction which fall into the regime of multi-axial fatigue.

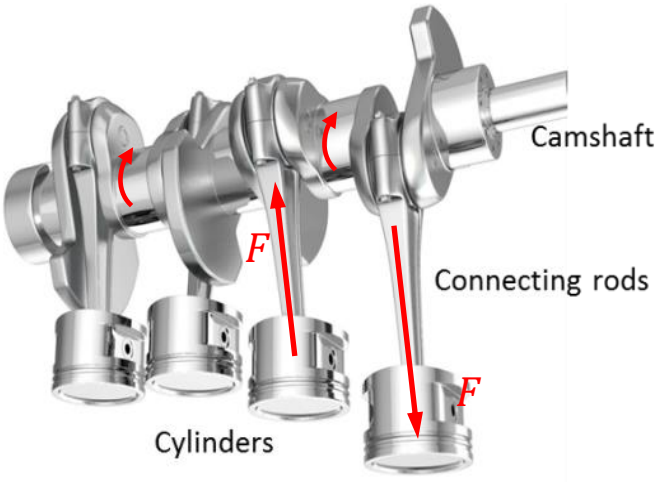

Fig. 1.1 Illustration of multi-loading sources subjected by a camshaft of engine

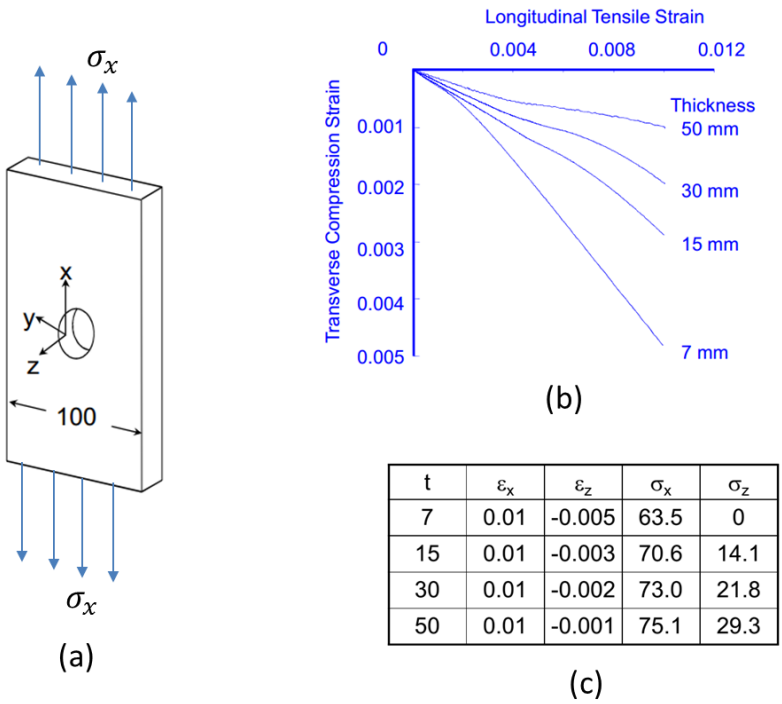

t	ε_x	ε_z	σ_x	σ_z
7	0.01	-0.005	63.5	0
15	0.01	-0.003	70.6	14.1
30	0.01	-0.002	73.0	21.8
50	0.01	-0.001	75.1	29.3

(c)

Fig. 1.2 Illustration of tri-axial stress state at notch root for a plate with hole under uniaxial tension [5]: (a) a plate with a hole under uniaxial tension; (b) plot of tensile strain along loading direction against transverse compressive strain as a function of plate thickness; (c) a list of strain and stress values at notch root for the same axial strain but with different plate thickness

One should be cautious that it is not always the case that multi-axial loading will always leads to multi-axial stress state, as demonstrated in [5, 6]. However, throughout this whole thesis, whenever multi-axial loading or out-of-phase loading is mentioned, it always refers to the case that multi-axial stress state is created by multi-axial loading.

When several stress components are operative at the same time at a material point, it can be categorized into two main groups. If one stress component increases and decreases proportionally in relation to another, it is naturally called proportional multi-axial stress state. For example, when a thin tube is under both sinusoidal tension and torsion without a phase different between them, the normal and shear stress components,

as shown in Fig. 1.3 (a) are then proportional to each other. As a result, the tube is subjected to proportional multi-axial stress histories. On the other side, if there is a phase shift between tension and torsion (Fig. 1.3(b)), the proportionality between these two stress components is lost. Naturally, it is named as non-proportional multi-axial loading. From a geometric point of view, if each stress component is plotted in a stress space, stress path for proportional multi-axial stress histories will be straight lines passing through the origin while non-proportional multi-axial fatigue paths can be arbitrary curves in stress space. From a mechanics point of view, non-proportional state of stress is characterized by rotation of principal stress and strain axes which will lead to quite different responses of materials and as a result, fatigue damage behavior in comparison with proportional multi-axial loading in which principal stress and strain axes directions remain unchanged during the whole loading process.

The multi-axial stress state arising from geometrical constrains such as a notch under uniaxial tension is generally proportional. Non-proportional multi-axial stress state is generally caused by the non-proportionality among multiple sources of loading such as illustrated in Fig. 1.1. As a further demonstration, Fig. 1.4 is a plot of measured micrstrain along 0°, 45° and 90° directions of a crankshaft [5] showing a clear non-proportional straining between 0° and 90° directions. For more complex real engineering structures under real variable amplitude loading histories, non-proportional loading can still be significant. Fig. 1.5 is a representative service loading histories plot recorded for lower wing skin of an aircraft with a variety of take-off, landing, and in-flight maneuvers represented [7]. One can observe from both stress history (Fig. 1.5 (a)) plot and load path

plot (Fig. 1.5(b)) that there exist noticeable non-proportionalities between axial and shear stress components.

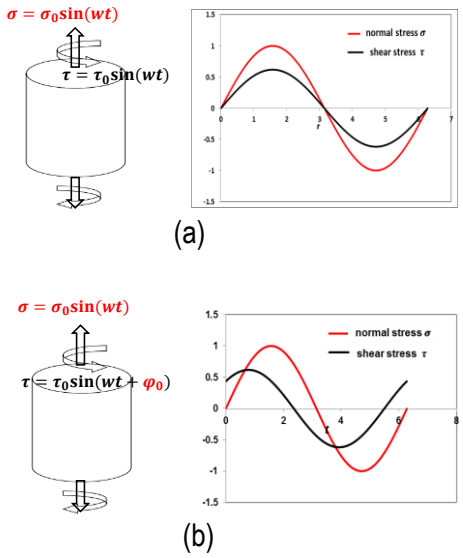

Fig. 1.3 Proportional (a) and non-proportional (b) multi-axial stress state introduced by in-phase and out-of-phase tension and torsion

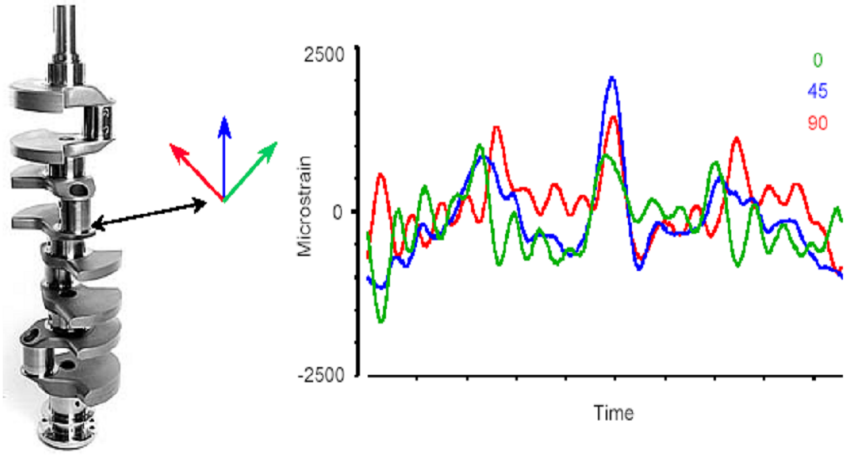

Fig. 1.4 Measured micrstrain along 0°, 45° and 90° directions of crankshaft [5]

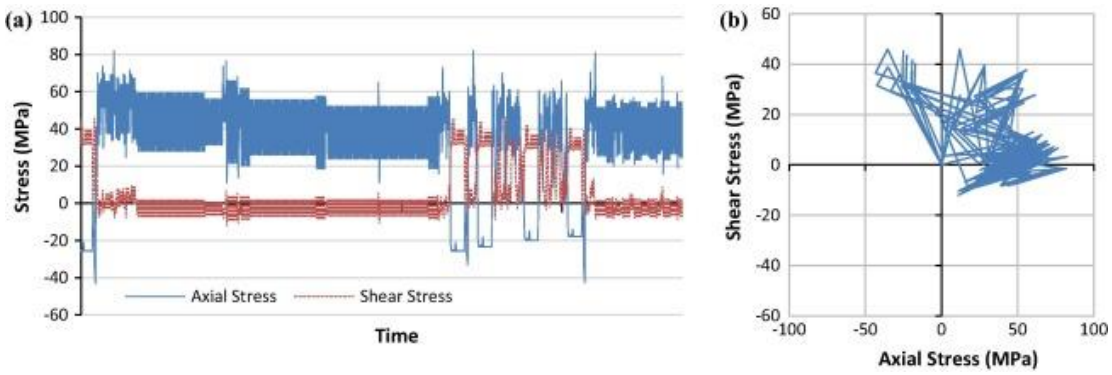

Fig. 1.5 Representative loading segment from the variable amplitude service loading history in terms of (a) applied stresses vs. time and (b) axial–shear stress path [7]

Compared with proportional multi-axial fatigue, two unique challenges exist for non-proportional multi-axial variable amplitude loading which is the most generic description of loading histories in real world. These two major issues will be elaborated in detail as follows since they are also the main challenges to be addressed by this thesis.

Firstly, which fatigue damage parameter can be used to describe fatigue damage under non-proportional loading histories? It is generally observed that classical S-N model and $\varepsilon - N$ model developed under uniaxial loading cases can be extended to proportional multi-axial fatigue loading based on certain types of equivalent stress definitions such Tresca stress or von Mises stress. For example, for tubular specimen (Fig. 1.3 (a)) under bi-axial fatigue loading, the effective stress range (von Mises stress) is defined as:

$$\Delta\sigma_e = \sqrt{\Delta\sigma^2 + 3\Delta\tau^2} \tag{1.1}$$

where $\Delta\sigma = 2\sigma_a$ and $\Delta\tau = 2\tau_a$ in which σ_a and τ_a are stress amplitudes of normal and shear stress component respectively. The above type of effective stress range definition is a reasonable choice for proportional multi-axial fatigue since both uniaxial loading, based

on which S-N and $\varepsilon - N$ curves are developed and proportional multi-axial loading share the commonality that principal stress axes remain unchanged during loading process. However, when Eq. 1.1 is applied to non-proportional bi-axial loading shown in Fig.1.3 (b), the effective stress range calculated is exactly the same as that of proportional loading (Fig. 1.3(a)). So the question then becomes: will the fatigue damage parameter still effective in predicting fatigue damage of non-proportional loading? The answer is no. Fig. 1.6 (b) is a plot of experimental fatigue life against effective (von Mises) stress ranges (Eq. 1.1) for pure bending, in-phase (proportional) bending and torsion, 90° out-of-phase (non-proportional) fatigue loading tested on welded tubular welded components (Fig. 1.6 (a)) done by Sonsino and Kueppers [8]. It clearly shows that when von Mises stress range is used for non-proportional loading (90° out-of-phase loading in this case), significant over prediction of fatigue life is observed. On the contrary, it gives a pretty good life estimation for proportional loading (in-phase loading in this case) since in-phase and uniaxial loading (pure bending in this case) test data tend to overlap with each other.

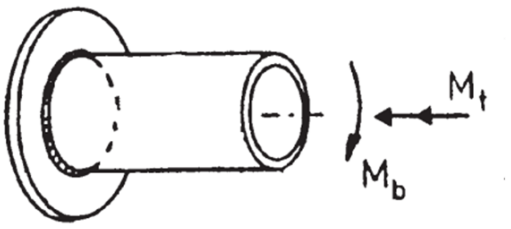

(a)

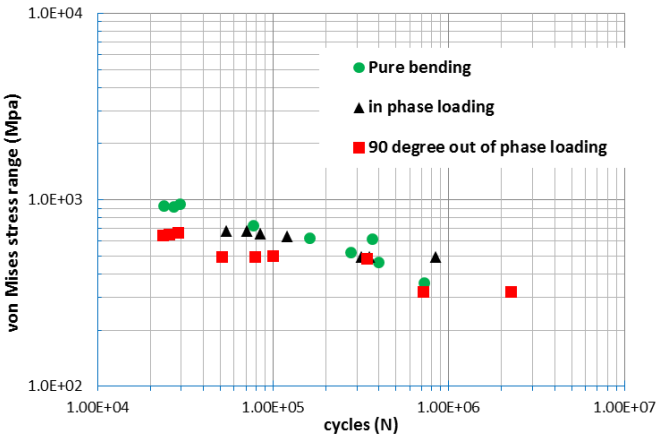

(b)

Fig. 1.6 Tubular welded componentss under pure bending, in-phase (proportional) bending and torsion and 90° out-of-phase (non-proportional) fatigue loading [8]: (a) tubular specimen test; (b) fatigue life plot in terms of von Mises stress range

As another case of demonstration, Fig. 1.7 presents proportional and non-proportional test data on tubular specimens made of Ti–6Al–4V [9]. Since fatigue tests are strain controlled in these cases, the test data (Fig. 1.7 (b)) are plotted in terms of von Mises strain range. Again, one can observe that for proportional (PP path and TP path) and non-proportional load paths (CP path) shown in Fig. 1.7 (a), non-proportional loadings lead to a much lower fatigue life than that of proportional loading and that the use of von Mises strain range as a fatigue damage parameter results in under-prediction of fatigue damage for CP path.

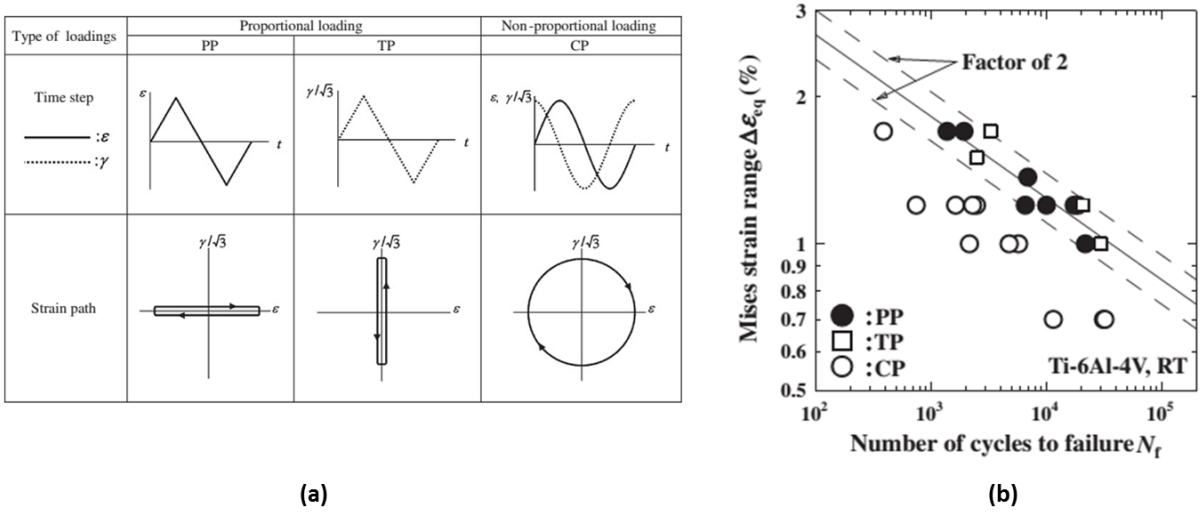

Fig. 1.7 Tubular non-welded specimen under strain-controlled proportional and non-proportional loading paths [9]: (a) three different strain paths employed; (b) plot of fatigue lives in terms of von Mises strain range

A large amount of experimental investigations, as will be reviewed in Sec. 1.2 reveal that non-proportional cyclic loading is generally more damaging than that of

proportional loading. Furthermore, the extent of non-proportional damage is dependent both on materials examined and load paths employed. Up to now, a fatigue damage model that is capable of taking into account of both material and load path dependent non-proportional damage is still a challenging and important topic that has not been fully addressed, especially considering the continuous push for cost reduction through lightweight design while at the same time having to meet more stringent product reliability requirement.

The second issue that is unique to non-proportional multi-axial fatigue damage is that a well-accepted multi-axial cycle counting procedure is still lacking. Realistic service loading histories are mostly variable amplitude, as demonstrated by Fig. 1.4 and Fig. 1.5. These non-proportional variable amplitude loading histories require a proper cycle counting procedure to break complex non-proportional loading histories into simple segments for which fatigue damage can be easily calculated and accumulated in order for total fatigue damage calculation. When it comes to uniaxial variable amplitude loading, rainflow cycle counting procedure is still the best we have got in spite of some other cycle counting procedures are also available [10]. As for proportional multi-axial fatigue loading, since one stress component can be simply scaled to the other, uniaxial cycle counting can be applied to any stress component for cycle counting purpose. A critical issue will emerge when one tries to implement rainflow cycle counting to non-proportional multi-axial variable amplitude loading histories. That is, which stress component should one make use of for cycle counting purpose, considering loading history of one stress component can be totally different from another? One typically case would be asynchronous loading between bending and torsion when they are applied

simultaneously to a tubular component shown in Fig. 1.8(a). For the two asynchronous normal and shear stress sinusoidal histories (Fig. 1.8(b)) with a frequency ratio of $f_t/f_b = 3$, where f_t and f_b are torsion and bending frequency respectively. One question that will arise naturally is: which load frequency should one make use of for fatigue life calculation? The same issue exists for more realistic and complex non-proportional variable amplitude loading histories as shown in Fig. 1.9. Therefore, further investigation on non-proportional multi-axial cycle counting is needed.

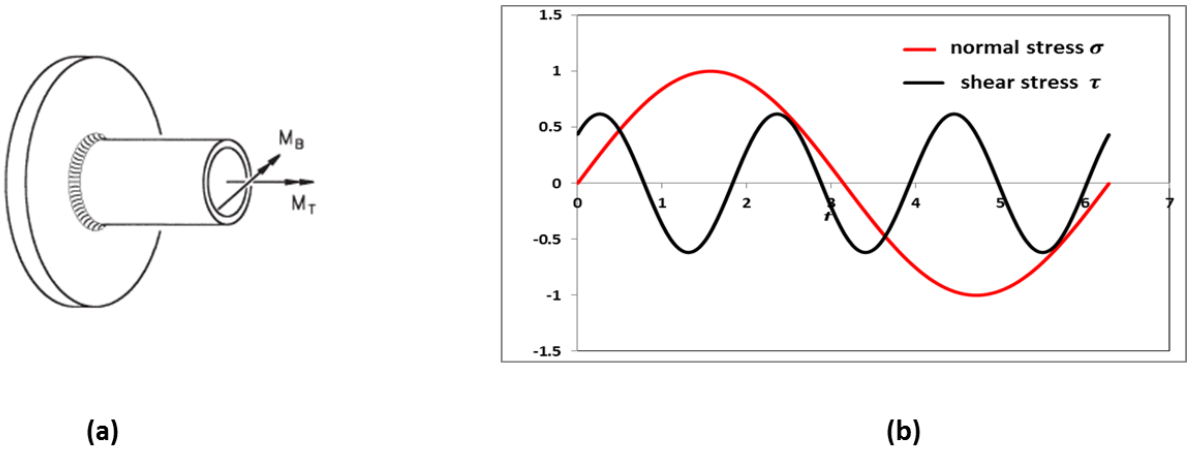

(a) **(b)**

Fig. 1.8 Tubular specimen under asynchronous bending and torsion with loading frequency ratio of 3 between torsional and bending moments: (a) Tubular specimen tested; (b) asynchronous stress histories of normal stress and shear stress components

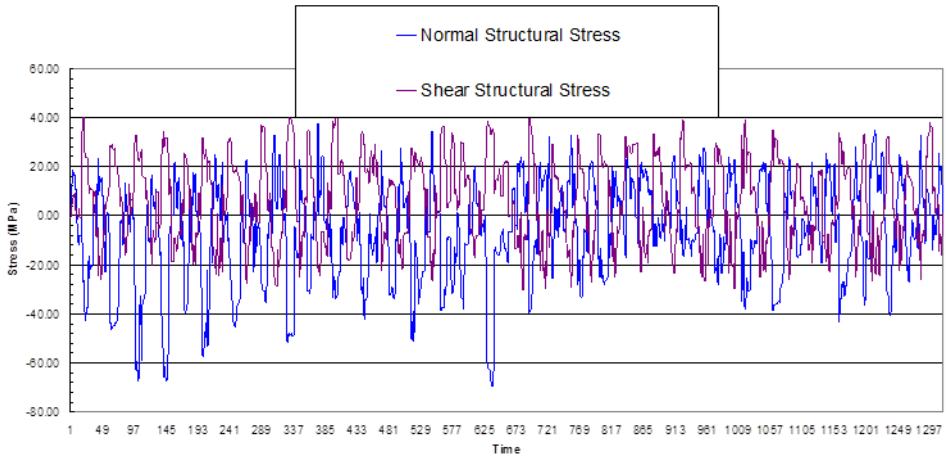

Fig. 1.9 Non-proportional multi-axial variable amplitude loading histories

In spite of that the above two major challenges of non-proportional multi-axial fatigue variable amplitude loading were illustrated separately; they are nevertheless closely inter-related with each other. As discussed by Dariusz in [6], some non-proportional fatigue damage models such as critical plane methods e.g. Fatemi-Socie model [11] might not need a multi-axial cycle counting procedure and uniaxial methods of cycle counting methods can be adapted to multi-axial counting based on the dominant failure mechanisms (shear stress/strain dominant or normal stress/strain dominant). On the other hands, spectral methods and continuum damage mechanics based models don't even need a separate cycle counting method. Therefore an integrated treatment of both fatigue damage model and non-proportional multi-axial cycle counting (very much dependent on fatigue model proposed) approach is needed for dealing with realistic variable amplitude histories.

It is worth mentioning that the above backgrounds on non-proportional multi-axial fatigue under variable amplitude loading and its two unique issues are not only applicable for non-welded metallic components/structures, but also for welded components for which fatigue failure mostly occur around weld joint location. In fact, Fig. 1.6 is a presentation of non-proportional fatigue of welded joint component. Since welded structures are so extensively used in off-shore, civil and transportation industries, treatment of non-proportional fatigue of welded components will also have to be examined and validated if any proposed fatigue damage model (in conjunction with multi-axial cycle counting) is claimed to be a robust one. Therefore, non-proportional

fatigue of welded joint will be covered in a separate chapter of this thesis. Furthermore, when a component with a pre-existing crack is subjected to non-proportional loading, it turns into a non-proportional mixed mode fatigue crack growth problem which is even more challenging. The aforementioned two major issues still exist with additional uncertainty involved such as crack branching and crack surface contact. An attempt will be made in an effort to deal with mixed mode fatigue crack growth under non-proportional loading in Chapter 5.

The following section will first present a detailed and updated literature review of major progresses that were made in an attempt to tackle the above discussed two unique issues. Our review covers various types of stress/strain definitions used in fatigue damage models for both non-welded and welded components, multi-axial fatigue damage parameters including mixed mode fatigue crack growth model and multi-axial cycle counting procedures proposed thus far.

1.2 Literature Review and Assessment

1.2. 1 Different Types of Constitutive Models and Stress/Strain Definitions used for Fatigue Life Prediction

Most of fatigue damage parameters are formulated in terms of certain kinds of stress and (or) strain definitions. Considering that only stress histories (for load controlled loading) or strain histories (for displacement controlled loading) are available in most cases, constitutive models are needed to derive from stress (strain) to strain (stress) for fatigue damage models that require both stress and strain as input. As a result, several cyclic constitutive models are reviewed in the following first subsection.

Even if a cyclic elastic-plastic constitutive equation is available, it would be impractical to implement elastic-plastic analysis for the whole load history examined. Therefore, a practical strategy is that elastic analysis is usually carried out first and then certain kinds of elastic-plastic corrections at locations such as notches are made to obtain local elastic-plastic strain. Furthermore, note that fatigue damage is a localized process occurring not only at the material point with the highest stress, but also within a neighboring volume of certain size. Therefore, how to come up with a local type of stress/strain definition for fatigue damage models is also essential. Therefore, various types of local stresses/stains that were used thus far for fatigue assessment are also briefly reviewed and commented for non-welded and welded components in separate subsections.

1.2.1.1 Constitutive Models for Cyclic Stress-Strain Relationship

Whenever we talk about constitutive relationship between stress and strain for fatigue, it generally refers to cyclic constitutive models. It is well known that monotonic stress-strain behavior of a material can be quite different from that of cyclic one because of material hardening or softening effect. However, as for very low cycle fatigue, making use of stabilized cyclic stress-strain can also be questionable because materials have not experienced enough cyclic loading before reaching stabilized stress-strain behavior, especially for cases when materials experience low cycle variable amplitude service loading.

For uniaxial cyclic loading, quite similar to that of monotonic stress-strain curve, cyclic stress-strain curve can be simply fitted in the form of Ramberg-Osgood equation [1]:

$$\varepsilon_a = \frac{\sigma_a}{E} + \frac{(\sigma_a)^{\frac{1}{n'}}}{K'} \quad (1.2)$$

where ε_a is strain amplitude and σ_a is applied stress amplitude. K' and n' are cyclic strength coefficient and cyclic hardening exponent.

For multi-axial fatigue, more complex cyclic plasticity model is needed to describe various types of effects [12] such as Bauschinger effect, cyclic hardening or softening effect, non-proportional hardening effect etc. Since most cyclic plasticity models are built upon classical incremental plasticity theories [13,14], the essential elements that are required of for plasticity models should also be in place for cyclic plasticity model. These are [6]:

(a) Initial yield surface definition to separate plastic region from elastic region in stress space.
(b) Flow rules describing the connection between plastic strain increment and increment of stress. The most common flow rule is called associated flow rule, in which plastic strain increment is normal to yield surface.
(c) Hardening rule: how a yield surface changes with accumulated plastic strain.
(d) Consistency requirement: when stress state changes on yield surface, there will be change to yield function.

Much effort is devoted to developing constitutive models to reflect the complex responses (e.g. non-proportional hardening) of materials under plastic deformation [14, 15] in the past few decades. These include multi yield surface model [16], two-surface model [17] and nonlinear kinematic hardening model developed by Amstrong and

Frederick [18] which was further refined by Chaboche [19]. More detailed descriptions of these models can be found in [14, 20]. As reviewed by Jiang and Kurath [21], since Armstrong-Frederick model is more suitable for modeling cyclic softening and hardening as well non-proportional hardening, only this model will be explained in detail here:

By assuming von Mises criterion as the initial yielding condition, yield surface in stress space is defined as:

$$F = \frac{3}{2}(\boldsymbol{S}-\boldsymbol{a}):(\boldsymbol{S}-\boldsymbol{a}) - \sigma_y^2(\varepsilon_e^p)=0 \tag{1.3}$$

in which $\boldsymbol{S}$ is deviatoric stress tensor, $\boldsymbol{a}$ is backstress and σ_y is yield surface as a function of effective plastic strain ε_e^p. The associated flow rule requires that plastic strain increment is normal to the yield surface:

$$d\boldsymbol{\varepsilon}^p = \frac{1}{K^p}(d\boldsymbol{\sigma}:\boldsymbol{n})\boldsymbol{n} \tag{1.4}$$

in which K^p is plastic modulus and the normal direction of yield surface is:

$$\boldsymbol{n} = \frac{\boldsymbol{S}-\boldsymbol{a}}{(\boldsymbol{S}-\boldsymbol{a}):(\boldsymbol{S}-\boldsymbol{a})} \tag{1.5}$$

the key part of Armstrong-Frederic model is that the backstress increment to describe the movement of yield surface is defined as:

$$d\boldsymbol{a} = \frac{2}{3}c_0 \cdot d\boldsymbol{\varepsilon}^p - \gamma_0 \boldsymbol{a} \cdot d\varepsilon_e^p \tag{1.6}$$

where c_0 and γ_0 are two material constants which can be functions of effective plastic strain. Finally, the plastic modulus K^p in Eq. 1.4 can then be obtained from consistency condition.

Chaboche [22] further suggested that backstress term in Eq. (1.6) can be further expressed as a series of backstress components:

$$\boldsymbol{a} = \sum_{i=1}^{M} \boldsymbol{a}^i \tag{1.7}$$

where each backstress component can be written in the same form as in Eq. (1.6).

For further including isotropic hardening effect, the radius of yield surface ($\sigma_y(\varepsilon_e^p)$) is a function of accumulated plastic strain. Jiang and Kurah [23] introduced the increment of yield surface as:

$$d\sigma_y\left(\varepsilon_e^p\right) = b_0\left(Q_0 - \sigma_y\left(\varepsilon_e^p\right)\right) d\varepsilon_e^p \tag{1.8}$$

where b_0 is a material constant and Q_0 is a function of hardening for both proportional and non-proportional loading with the following definition:

$$Q = A_T q_N + (1 - A_T) q_P \tag{1.9}$$

A_T in Eq. (1.9) is a measure of non-proportionality such as the one proposed by Tanaka [24] and q_N is hardening parameter for non-proportional loading while q_P is proportional hardening parameter.

It can be seen from the above explanations of well-recognized elastic-plastic constitutive model that many material parameters are needed in order to calculate plastic strain based on input of stress history. Especially when it comes to non-proportional loading, the load calculation of load path non-proportionality A_T in Eq. (1.9) would require a fourth rank tensor for Tanaka's model [24]. Therefore, the application of cyclic plasticity models to real engineering practice is not an easy job both owing to the

complexity of cyclic plasticity model and the many material parameters involved for determination.

The most important aspect of non-proportional loading is more slip planes and dislocations will be activated because of rotation of principal stress/strain axes. These different slip planes and dislocations interact with each other leading to quite different microstructures [25-28] when compared with that under proportional loading. From a mechanical point of view, additional cyclic hardening that is material-dependent is sometimes observed for some material under non-proportional loading. Therefore, to circumvent from the complexity of cyclic plastic constitutive model, simplified experiment-based empirical models were often used to describe additional cyclic hardening when non-proportional loading is applied. The most well-known one proposed by Kanazawa et al.[25] aimed at replacing cyclic strength coefficient (K') in Eq. (1.2) for uni-axial loading with the following one in case of non-proportional cyclic loading:

$$K'_{NP} = K'(1 + \alpha_I F_0) \tag{1.20}$$

in which K'_{NP} is cyclic coefficient for non-proportional loading and F is rotation factor of non-proportional path, which is defined as the ratio of shear strain range at 45° to maximum shear plane to maximum shear strain range.

α_I in Eq. (1.20) is a material dependent additional hardening coefficient [5,25] defined as:

$$\alpha_I = \frac{\sigma_{90^\circ} - \sigma_{0^\circ}}{\sigma_{0^\circ}} \tag{1.21}$$

where σ_{90° and σ_{0° are equivalent stress amplitudes for 90° out of phase and in phase loading (Fig. 1.10 (a)), respectively, with the same applied effective strain.

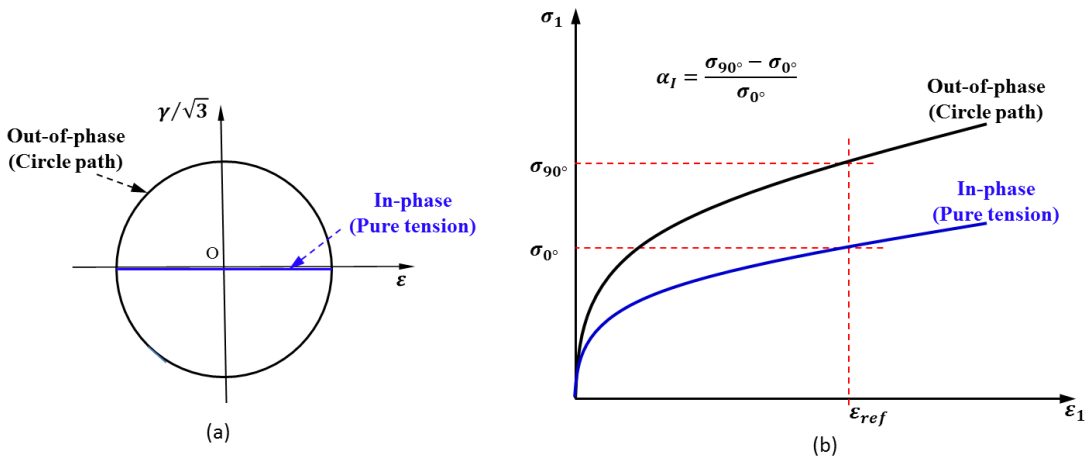

Fig. 1.10 Effective stress-strain curve for in and out of phase test: (a) 90° out of phase and in phase load path; (b) equivalent stress amplitude for same applied effective strain.

With Eq. (1.20) for estimating cyclic coefficient for non-proportional loading, additional cyclic hardening is generally taken into account [29] by Eq. (1.2). However, strictly speaking, the calculated α_I based on Eq. (1.21) is dependent upon the amplitude of effective strain used. This might be part of the reason why calculated stress based on the strength coefficient in Eq. (1.20) tends to over predict stress under non-proportional loading in some cases [29].

The sensitivities of materials to non-proportional hardening vary a lot for different materials [15, 28, 29] and are important parameters to be determined for calculation of additional cyclic hardening. Several attempts were made trying to build a connection between α_I and other material parameters that are easily available. One important finding [27, 28, 30] is that additionally hardening under non-proportional loading is closely related to stacking fault energy (SFE) of material examined. The lower the SFE, the higher the additional non-proportional hardening will be observed (e.g. stainless steel).

On the other hand, for materials with higher SFE, such as aluminum, minimal non-proportional hardening is found. On the other hand, Borodii and Shukaev [30] proposed an empirical relationship between non-proportional hardening coefficient and monotonic properties of materials:

$$lg(\alpha_I) = 0.705\beta - 1.22 \tag{1.22}$$

where $\beta = (\sigma_u/\sigma_y) - 1$, in which σ_u and σ_y is ultimate tensile strength and yield strength respectively.

Later on, Shamsaei and Fatemi [31] further suggested that additional cyclic hardening parameter α_I can be related with both uniaxial monotonic and cyclic deformation properties of a material.

It is conventionally believed until today that additional cyclic hardening coefficient α_I is directly related with fatigue life reduction under non-proportional loading. However recent researches [15, 29, 31, 32] clearly showed that in cases when there is negligible additional hardening effect, significant reduction of fatigue life under non-proportional loading is still observed, indicating that more than one mechanisms are responsible for non-proportional fatigue damage. This critical point will be further elaborated in following sections.

1.2.1.2 Stresses/Strains Typically Used for Non-Welded Components with Notches

Currently, applications of the above reviewed several types of constitutive models are mainly limited to simple specimens. However, in most structures and engineering components, localized fatigue damage caused by stress risers such as notches are of

major concern. For this purpose, several approaches used for estimating local stresses are briefly reviewed here.

As stated by Radaj [33]: "local approaches are assigned to the structural stress and strain approach, to the notch stress and strain approach and to the fracture mechanics approach. These local approaches supplement or substitute the older nominal stress approach which is of a global nature". Nominal stress approach implies that material effects, stress gradient effects caused by notches and surface finish effects are all grossly considered in a nominal S-N curve that is specific to one category of structural component. Additionally, it is only applicable to cases when nominal stress can be clearly defined. On the contrary, local approaches attempt to separate stress state experienced by materials from fatigue properties of materials such that only one S-N curve from uniaxial fatigue test on simple specimen is enough for fatigue design and assessment of different components as long as local stresses can be calculated.

(a) Notch stress/strain based approach

Generally, with a notch radius well defined and nominal stress known, the maximum elastic stress at the notch root is simply the nominal stress (σ_n) multiplied by stress concentration factor (K_t). However, because of stress gradient effect, stress drops sharply for materials away from the maximum notch stress location. Considering that real fatigue damage process occurs in a process zone, not only at the highest stress point, elastic notch stress $K_t\sigma_n$ will therefore always leads to an underestimation of fatigue life. To overcome this issue, Neuber [34] came up with a well-known fatigue notch factor (K_f):

$$K_f = 1 + \frac{K_t - 1}{1 + \sqrt{\frac{\rho}{r}}} \tag{1.23}$$

where r is the notch radius and ρ is a material dependent characteristic length reflecting the sensitivity of material to notch. The above relationship seems pretty reasonable in that notch radius is the most important available geometric parameter for a notch to take into account of stress gradient effect. However, the determination of characteristic length ρ will generally require an empirical equation.

Later on Peterson [35] proposed a similar equation to that of Neuber's:

$$K_f = 1 + \frac{K_t - 1}{1 + \frac{\rho'}{r}} \tag{1.24}$$

in which ρ' is a characteristic length of materials which also requires an empirical estimation.

Another type of notch stress is based on the theory of critical distance (TCD) [36, 37]. The essential idea of TCD is that the stress state of a notch can be represented by the stress state of a material point (point method) which is certain distance away from notch root or by averaging stress over certain length (line method) or certain area (area method) or volume (volume method). As an illustration, Fig. 1.11 shows the concept of line method and point method as representations of notch stress state.

However, all of the above critical distance based methods will also require a reference length (L) in order for satisfactory prediction [36]. One way of determining its value is by taking advantage of the relationship between fatigue crack threshold value and fatigue limit based on fatigue crack propagation of small cracks [38]:

$$L = \frac{1}{\pi}\left(\frac{\Delta K_{th}}{\sigma_f}\right)^2 \tag{1.24}$$

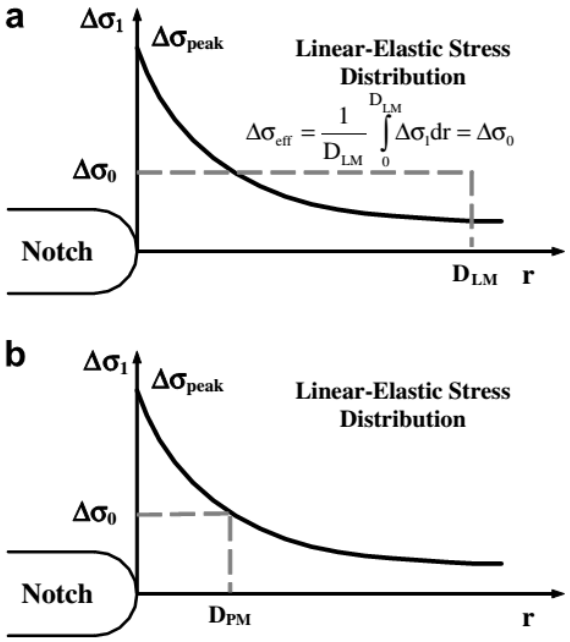

Fig. 1.11 Formalization of the line method (a) and the point method (b) [36] in theory of critical distance method

When local yielding occurs around notches, which is generally true for both low and medium-high cycle fatigue of structural components, elastic-plastic response has to be estimated instead of carrying out elastic-plastic finite element analysis for whole service loading histories. As mentioned in previous section, elastic analysis is done together with certain kind of plastic correction to achieve elastic-plastic stress/strain responses at notches. It should be noted that, as described above, which type of elastic notch stress definitions should be used for plastic correction is still a concern.

The most common notch stress-strain estimation is based on Neuber's rule [39]. It assumes that the geometric mean of stress and strain is equal to that of the elastic stress and strain when pure elastic analysis is carried out:

$$\sigma\varepsilon = \sigma^e\varepsilon^e = (K_t\sigma_n)(K_t\varepsilon_n) = \frac{K_t^2\sigma_n^2}{E} \tag{1.25}$$

where σ and ε are real elastic-plastic responses at notch root. σ^e and ε^e are pseudo stress and pseudo strain calculated elastic analysis. With Neuber's rule (in terms of range definition) and Ramberg-Osgood type of cyclic stress-strain curve in Eq. 1.2, the elastic-plastic histories of stress/strain responses can then be estimated.

It is worth noting that Neuber's rule was originally proposed for correction at the notch root point with largest stress. By replacing K_t with K_f in (Eq. 1.25), Topper et al. [40] found that better agreement with experimental results was achieved. As a further note for notch stress based analysis, when notch stress used is based on theory of critical distance is used, similar type of elastic-plastic correction is also needed when calculated stress is beyond yield stress.

There are also other types of notch stress/strain analysis rules such as strain energy density or Glinka's rule which assumes that the strain energy density at the notch is assumed to the same for linear elastic notch analysis and real elastic-plastic notch behavior. More detailed explanations can be found in [1, 41].

(b) Structural stress approach

To quote from a review paper from Radaj [33]: "an approach between the global and local versions is the structural stress approach which emphasizes the stress

concentrations caused by the macro-geometry, while the actual notch effect is definitely suppressed". The idea of structural stress/strain is to capture the macro (structural) level of stress/strain state subjected by components. This type of stress definition is particular important in that it is the structural stress/strain that determines the overall responses of structural components. Taking a notched component as an illustration, in spite of the fact that localized plastic deformation occurs at the notch root, its cyclic response is still mainly dominated (strain-controlled) by its surrounding overall elastic response, as long as localized plastic region is surrounded by a much larger elastic region. In this case, capturing the precise elastic-plastic response at the notch root is of less importance than representing its surrounding overall structural response. With the above argument, the much more challenging task of calculating localized elastic-plastic response can be avoided and capturing overall response a component by structural stress method is good enough for fatigue assessment purpose. Up to now, structural stress approach is only fully developed for welded structures which will be reviewed in detail shortly. Part of the reason can be attributed to the fact that a clearly defined characteristic length is lacking for non-welded components. To certain extent, the characteristic lengths defined in TCD based notch stress definitions can be viewed as attempts for achieving such a purpose. For smooth specimen, structural stress is then simply reduced to nominal stress. On the other hand, structural stress can be viewed as notch stress if its notch radius is large enough. Therefore, it is attempting to postulate that for characterizing structural stress of notched specimen, notch radius is an important factor to be considered.

To author's best knowledge, the most relevant work towards structural stress approach is done by Köttgen et al. [42] who proposed a structural yield surface concept

for notch analysis. The idea is that elastic analysis is first carried out to calculate pseudo stress (σ^e). Then a relationship between pseudo stress and notch strain is as a power function is built:

$$\varepsilon = \frac{\sigma^e}{E} + \left(\frac{\sigma^e}{K^*}\right)^{\left(\frac{1}{n^*}\right)} \tag{1.26}$$

in which notch strain ε is determined by Neuber's rule. The constants K^* and n^* represent the response of the structure examined and is determined by a fitting process. As a result, they are structure-dependent. With Eq. (1.26) and pseudo stress response, pseudo stress-local strain response can be obtained. Furthermore, strain controlled cyclic plasticity model is used to obtain the local strain - local stress response.

1.2.1.3 Stresses/Strains Typically Used for Welded Components

An independent section of literature review for welded joints is presented here not only because of welded joints are the most common fatigue failure locations of welded structures, but also because of several local approaches that were uniquely developed for fatigue analysis of welded components. Besides that, a separate chapter is devoted to multi-axial fatigue analysis of welded joints by comparing different types of local stress approaches. Four different types of widely used stress definitions, namely, nominal stress, notch stress, hot spot stress (geometric stress) and structural stress (traction based structural stress) will be briefly reviewed with special emphasis placed on traction based structural stress method.

(a) Nominal stress approach

Nominal stress is the stress calculated in the sectional area in the absence of structural discontinuity being considered. It is the most traditional and still a prevailing fatigue design approach. The essential idea is that welded joints are put into different classifications based on joint configurations and loading paths. Different S-N curves are assigned to various types of classifications. As long as nominal stress is available and welded joint examined can be viewed as belonging to one type of classification provided by codes and standards [43, 44] based on engineers' judgment, fatigue life can then be estimated based on the S-N curve that is specific to the joint classification. On example with two joints types and their separate S-N curves are shown Fig. 1.12

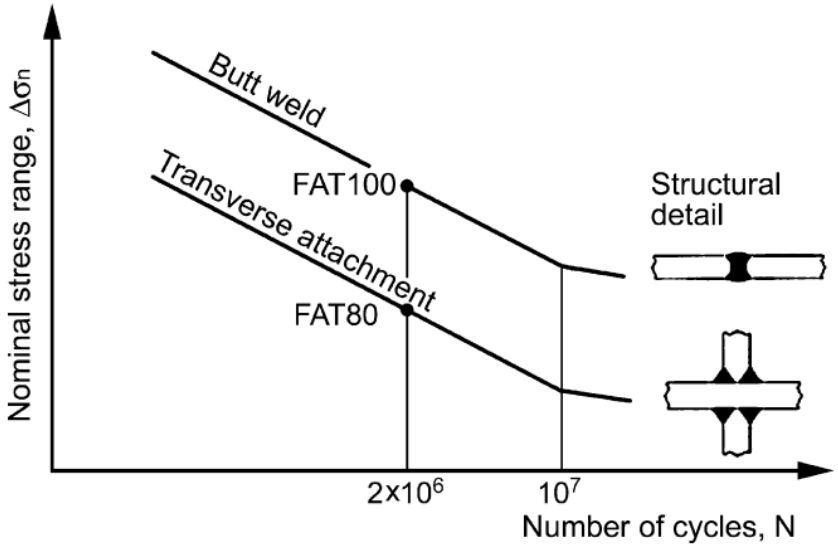

Fig. 1.12 Nominal stress based design S-N curves according to IIW recommendations for two different structural details [45]

Although dozens of typical welded joints are listed as cartoons in current standards [43, 44, 46] and their S-N curves are available, one clear drawback of nominal stress based fatigue design approach is that it is not always possible or an easy job to find

a proper classification to be assigned to for many new welded joint designs. What is worse, nominal stress cannot be easily defined for some complex structures/components, especially for FEA based design nowadays.

(b) Effective notch stress

Effective notch stress is the total and maximum stress at the root of a notch, taking into account of the variation of weld profile. Illustration of maximum notch stress in shown in Fig. 1.13. It is the most localized stress definition currently used for capturing all types of stress rising effects. Again, as mentioned previously, it is not always a good idea to try to include as much local details as possible since fatigue damage occurs in a process zone, not only at the material point with the highest stress. What's more, weld toe profile can hardly be modeled in an accurate manner. Fig.1.14 shows typical measurements of radius at different weld toe locations of a welded cruciform joint representing current level of manufacture practice [47], demonstrating that local weld toe radius can be quite random and can hardly be fully considered in real practice. Since a sharp notch will lead to singular stress distribution and real notch radiuses vary significantly, a fictitious notch radius (e.g. $\rho = 1.0mm$ from IIW [43]) is generally assumed for notch stress calculation of welded joints made of structural steels and aluminum alloys, as demonstrated in Fig. 1.15. There are several disadvantages of applying notch stress approach. First of all, very refined mesh is needed for notch stress calculation, thus making is less attractive for analyzing complex engineering structures. Secondly, an assumed fictitious notch radius introduces arbitrariness in calculated notch stress. Finally, notch stress does not capture stress gradient effect properly.

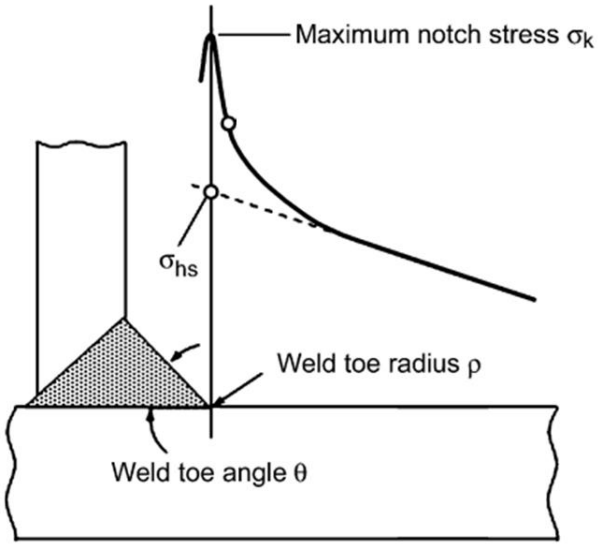

Fig. 1.13 Illustration of notch stress (σ_k) and hot spot stress (σ_{hs}) at weld toe location as toe radius of (ρ) [45]

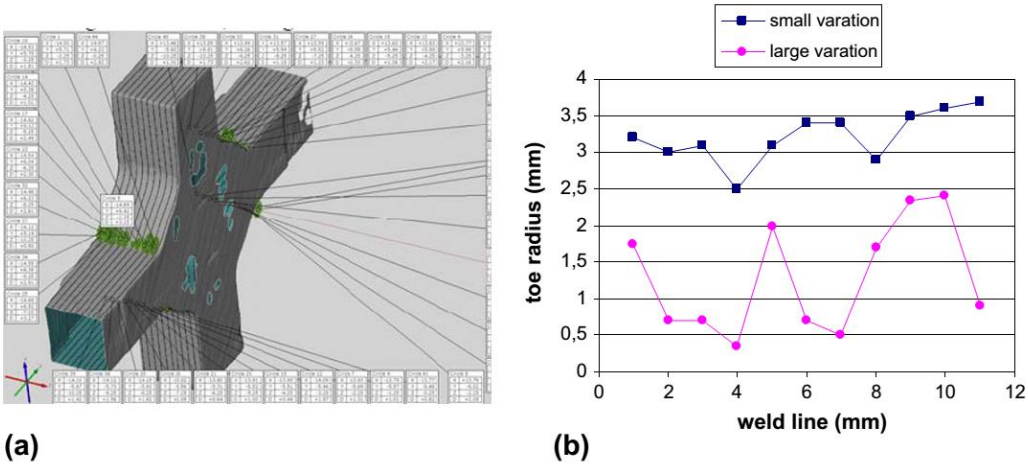

Fig. 1.14 Measurements of toe radius along weld a toe line: (a) 3D surface of weld, (b) results showing small and large variations in the measurements of the weld toe radius [47]

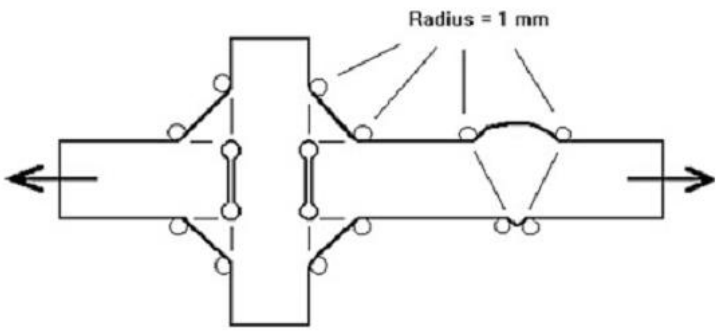

Fig. 1.15 Sketch of FEA model for notch stress calculation [43]

(c) Hot spot stress

Hot spot stress that we are referring to is also called structural or geometric stress (σ_{hs}). It includes all stress raising effects of a structural detail, but excluding that due to the local weld profile itself. It originates from structural strain measurement certain distance away from weld toe location and was used as a reference strain for strain state of weld toe location. With FEA model widely used nowadays, it gains further attention and leads to hot spot stress as a codified procedure for fatigue assessment [43]. For hot spot stress [43] calculation, surface stresses at prescribed evaluation points in front of a weld toe are extrapolated to the weld toe location. As a result, hot spot stress is also called extrapolated hot spot stress. As shown in Fig. 1.13, the hot spot stress is assumed to reflect overall geometrical inhomogeneity which is believed to lead to variation of surface stress some distance away from weld toe location. Different linear and non-linear extrapolation techniques from different locations requiring proper arrangement of element nodes and element sizes are recommended [43]. More details of recommended extrapolation procedures can be found in IIW. As a demonstration, three types of hot spot

stresses [48] are shown in Fig.1.15. With hot spot extrapolation procedures and several hot spot S-N curves recommended, fatigue assessment can then be carried out.

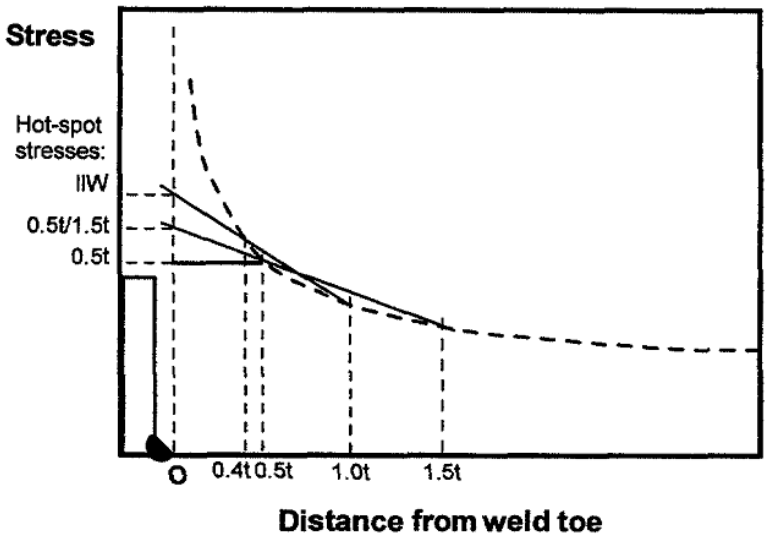

Fig. 1.16 Three different definitions of hot spot stress examined by Maddox [48]

Unfortunately, as demonstrated in Fig. 1.16 and plenty of examples in [49], hot spot stress calculated by using different extrapolation procedures and element types varies a lot and it is mesh sensitive. Also note that the implementation of hot spot stress method requires well-controlled element size near weld toe location, even though acknowledging that the requirement is less stringent than that of notch stress method. Most importantly, extrapolated hot spot stress by surface stress lacks mechanics-based interpretation and it does not reflect the stress gradient effect in thickness direction along which most of weld toe fatigue cracks grow.

(d) Traction based structural stress

Traction based structural stress developed by Dong, Dong et al. [49-51] is gaining popularity in recent years owing to its several important merits:

(i) It is a structural stress method, admitting that local structural stress along thickness direction is of primary importance and notch stress introduced by weld profile is of secondary importance. The effects of variation of weld toe profiles are captured by the scatter band of S-N curve.

(ii) Traction based structural stress is responsible for leading to fatigue crack growth failure along thickness direction and it is built on solid fracture mechanics theory. For this reason, both stress gradient and thickness effects are taken into account properly.

(iii) Nodal forces (moments) outputted from FEA model are directly used for calculation of structural stress, instead of adopting a stress linearization procedure. Since nodal forces (moments) in displacement based finite element method are of a higher order accuracy than outputted stress, traction based structural stress calculated from nodal forces (moments) demonstrates both element type and element size insensitivity. As a result, pretty coarse elements can be used for structural stress calculation.

(iv) Only one master S-N curve is needed for fatigue assessment of various types of welded joints. This single S-N curve is a consequence of the fact that traction based structural stress captures the essential fatigue failure mechanism of welded joints. That is, fatigue failure of a welded joint is dominated by fatigue crack growth process. Regardless of joint types and plate/tube thicknesses, traction

based structural stress is the only stress parameter that controls fatigue crack growth process.

Noting that traction based structural stress is the most prominent local stress definition for fatigue assessment and it will be used for multi-axial fatigue analysis of welded joints in Chapter 4. The methodology and procedures for traction based structural stress will therefore be reviewed here in a little bit more detail [52].

Traction based structural stress, as presented in [49 50, 53, 54] is formulated by representing stress state on a hypothetical crack plane in the form of membrane and bending stress components. Consider the stress state at a weld toe location along a through thickness hypothetical cut in Fig. 1.17 (a), the three stress components exposed by the cut is σ_x, τ_y and τ_z. Transverse shear τ_z is usually negligible in most cases. Within the context of structural mechanics, these stress components can be presented in the form of membrane (e.g. σ_m for normal membrane structural stress) and bending (e.g σ_b for normal bending structural stress) parts which can be directly related to their corresponding line forces and line moments if shell or plate theories are used. For 3D geometry, structural stress which is defined with respect to local coordinate along curved weld line is shown in Fig. 1.17 (b). Such a traction based structural stress definition is also consistent with fracture mechanics principle in view of the fact that stress intensity factors for a crack situated along the hypothetic plane in Fig. 1.17 (a) are fully described by the three traction components. Specifically, Mode I stress intensity factor is solely contributed by the normal structural stress σ_s, Mode II by the in-plane shear structural stress τ_s and Mode III by the transverse shear τ_z .

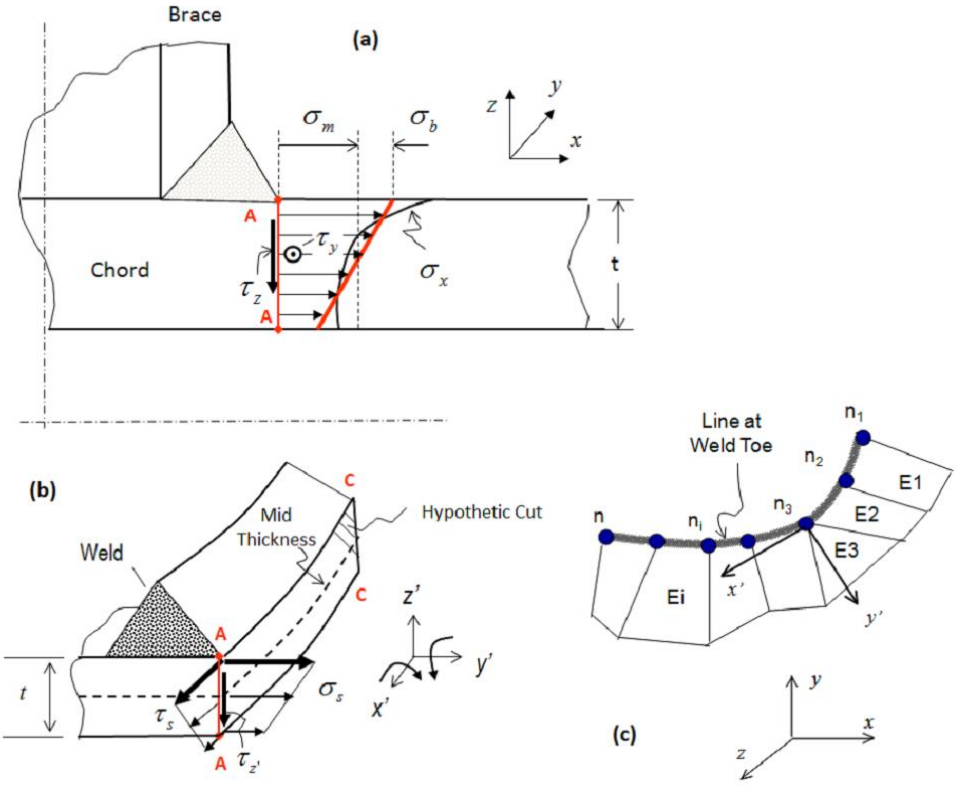

Fig. 1.17 Traction based structural stress definition [52] along weld toe through thickness direction: (a) 2D equilibrium equivalent stress definition with respect to Line A-A; (b) 3D Equilibrium-equivalent stress definition on a hypothetical cut surface (local x'-z' plane) encompassing Line A-A; (c) weld line definition and local coordinate system for structural stress calculation

In real practice of calculation, the traction stress along the hypothetical cut shown in Fig. 1.17 (b) can be calculated by extracting nodal forces and nodal moments from shell/plate finite element model or solid model. For example, global nodal forces and nodal moments are first rotated into local coordinated systems ($x' - y' - z'$) at each node, they are then transformed into work equivalent line forces and line moments defined with these local coordinate systems by matrix form of equations. For example, line forces in y' of Fig. 1.17 (c) contribute to membrane stress. Imposing work equivalent

argument for all nodal forces, one obtains the following matrix form of equations relating nodal forces in y'directions to line forces in y' directions:

$$\begin{Bmatrix} F_1 \\ F_2 \\ F_3 \\ \vdots \\ \vdots \\ F_{n-1} \end{Bmatrix}_{y'} = \begin{bmatrix} \frac{(l_1+l_{n-1})}{3} & \frac{l_1}{6} & 0 & 0 & \cdots & \frac{l_{n-1}}{6} \\ \frac{l_1}{6} & \frac{(l_1+l_2)}{3} & \frac{l_2}{6} & 0 & \cdots & 0 \\ 0 & \frac{l_2}{6} & \frac{(l_2+l_3)}{3} & \frac{l_3}{6} & 0 & \vdots \\ 0 & 0 & \ddots & \ddots & \ddots & 0 \\ \vdots & \ddots & 0 & \frac{l_{n-3}}{6} & \frac{(l_{n-3}+l_{n-2})}{3} & \frac{l_{n-2}}{6} \\ \frac{l_{n-1}}{6} & \cdots & 0 & 0 & \frac{l_{n-2}}{6} & \frac{(l_{n-2}+l_{n-1})}{3} \end{bmatrix} \begin{Bmatrix} f_1 \\ f_2 \\ f_3 \\ \vdots \\ \vdots \\ f_{n-1} \end{Bmatrix}_{y'} \tag{1.27}$$

where $F_1, \ldots F_n, F_{n-1}$ are nodal forces in y' directions in the local coordinate systems. Line forces $f_1, \ldots f_n, f_{n-1}$ are line forces in y' directions and $l_1, \ldots l_n, l_{n-1}$ are edge length of elements. In a similar manner, line moments along a weld line can also be calculated.

With line force ($f_{y'}$) in y' direction and line moment ($m_{x'}$) in x' direction at each node calculated, traction based normal structural stress is:

$$\sigma_s = \frac{f_{y'}}{t} - \frac{6m_{x'}}{t^2} \tag{1.28}$$

Similarly, in-plane shear structural stress based on line force ($f_{x'}$) and line moment ($m_{y'}$) is calculated as:

$$\tau_s = \frac{f_{x'}}{t} + \frac{6m_{y'}}{t^2} \tag{1.29}$$

Traction based normal structural stress and in-plane shear structural stress will be used for non-proportional fatigue analysis of welded joints in Chapter 4. One thing to be

noticed is that when non-welded components without notches are examined, as seen in Chapter 2 and Chapter 3, structural stress is simply reduced to nominal stress and nominal strain.

1.2. 2 Multi-Axial Fatigue Damage Models

Previous section surveyed various types of stress/strain definitions for non-welded and welded components and elastic-plastic models (if needed) that are commonly used in constructing fatigue damage parameters. This section will review various types of multi-axial fatigue damage models with an emphasis on their capabilities of taking account of non-proportional damage effects. Based on our survey and interpretation, multi-axial fatigue damage models can be categorized into three groups: static strength (equivalent stress) based fatigue models; critical plane based fatigue damage models and recently developed new approaches for non-proportional multi-axial fatigue. These three groups of multi-axial fatigue damage parameters will be reviewed separately.

1.2.2.1 Static Strength Based Fatigue Damage Models

For equivalent stress or strain based models, fatigue damage prediction is based on different ways of combining stress or strain components into one parameter that is equivalent to the one used for uniaxial fatigue loading. It is still a prevailing way of dealing with multi-axial fatigue owing to its simplicity and the mechanics basis associated with it.

(a) Gough Ellipse Model

Among the early researchers, Gough [55] performed extensive combined bending and torsion experiments on several materials to establish fatigue limits of different

bending/torsion ratios. The classical formulation, also called Gough Ellipse is of the following form:

$$\left(\frac{\Delta\sigma}{\sigma_f}\right)^2 + \left(\frac{\Delta\tau}{\tau_f}\right)^2 = 1 \tag{1.30}$$

where σ_f is the fatigue limit under tension and τ_f is the fatigue limit under torsion. This original version of Gough Ellipse is only applicable to proportional multi-axial fatigue and cannot take into account of non-proportional loading effect.

(b) Static yield strength criteria based fatigue models

This type of criteria borrows from the static yield strength parameter and is based on the reasoning that fatigue damage is controlled by plastic deformation. Yield criteria that describe plastic deformation should then also be applicable for describing plastic deformation during fatigue loading. The three most common forms of yield strength based fatigue models are stress ranges defined in terms of maximum principal stress, maximum shear stress, and octahedral shear stress (von Mises criterion). Their specific forms are:

$$\Delta\sigma_{eq}^{I} = \Delta\sigma_1 \tag{1.31}$$

$$\Delta\tau_{eq} = \frac{\Delta\sigma_1 - \Delta\sigma_3}{2} \tag{1.32}$$

$$\Delta\sigma_{von} = \frac{1}{\sqrt{2}}\sqrt{(\Delta\sigma_1 - \Delta\sigma_2)^2 + (\Delta\sigma_2 - \Delta\sigma_3)^2 + (\Delta\sigma_3 - \Delta\sigma_1)^2} \tag{1.33}$$

The von Mises effective stress range can also be written in terms of stress components:

$$\Delta\sigma_{von} = \frac{1}{\sqrt{2}}\sqrt{(\Delta\sigma_{11} - \Delta\sigma_{22})^2 + (\Delta\sigma_{22} - \Delta\sigma_{33})^2 + (\Delta\sigma_{33} - \Delta\sigma_{11})^2 + 6(\Delta\sigma_{12}^2 + \Delta\sigma_{23}^2 + \Delta\sigma_{31}^2)} \quad (1.34)$$

The von Mises stress range is the most widely used one and it can be both related to changes of distortion energy and shear stress on octahedral planes when multi-axial loading is proportional. Therefore, for ductile materials under multi-axial proportional loading, von Mises stress range is still a pretty reasonable choice, except for a few cases reported [56]. Again, as demonstrated in Fig.1.6, von Mises stress range cannot take into account of non-proportional damage effect. At the same time, stress range definitions by Eq. 1.31 to Eq. 1.32 lose their mechanics based interpretations since principal stress axes rotates during non-proportional loading.

(c) Sine model

Sines [57] proposed a linear combination of the amplitude of second deviator stress invariant (also called octahedral shear stress) and hydrostatic pressure for proportional multi-axial fatigue:

$$\frac{\Delta\tau_{oct}}{2} + \alpha\left(3\sigma_{hyd}\right) = \vartheta \quad (1.35)$$

where $\Delta\tau_{oct} = \frac{\sqrt{2}}{3}\Delta\sigma_{von}$ and σ_{hyd} is the mean hydrostatic stress in a cycle. By comparing the von Mises stress range in Eq.1.34, one can tell that in spite of Sine's model takes into account of mean stress effect in terms of hydrostatic stress, it is still not applicable for non-proportional fatigue.

Crossland [58] proposed a very similar form of equation like Sines's. However, the mean stress effect is taken into account by the maximum value of hydrostatic stress that occurs in a cycle:

$$\frac{\Delta\tau_{oct}}{2} + \alpha\left(3\sigma_{hyd,max}\right) = \vartheta' \tag{1.36}$$

(d) Octahedral shear strain

Strain based parameters are usually used in the regime of low cycle fatigue where significant plasticity occurs. The most popular form of equivalent strain parameter is octahedral shear strain range, also called von Mises strain range:

$$\Delta\varepsilon_{von} = \frac{1}{\sqrt{2}(1+\upsilon)}\sqrt{(\Delta\varepsilon_{11}-\Delta\varepsilon_{22})^2+(\Delta\varepsilon_{22}-\Delta\varepsilon_{33})^2+(\Delta\varepsilon_{33}-\Delta\varepsilon_{11})^2+\frac{3}{2}(\Delta\varepsilon_{12}^2+\Delta\varepsilon_{23}^2+\Delta\varepsilon_{31}^2)} \tag{1.37}$$

As will be seen in later chapters, equivalent strain in terms of von Mises strain will be often used as a reference for comparison with our proposed non-proportional equivalent strain whenever strain controlled test data are examined.

To summarize, none of the above static strength based type of fatigue damage parameters are capable of taking into account of non-proportional fatigue damage. However, they are easy to implement and are reasonable choices for proportional loading cases.

1.2.2.2 Critical Plane Based Fatigue Damage Models

Quite different from equivalent stress or equivalent strain concept which is an average or an overall representation of stress/strain state of a small volume of material at the location of our interest, critical plane models assume that fatigue damage is directional and mainly occurs on certain preferred planes, depending on which kind of failure mechanism is a dominant one. According to parameters used for fatigue assessment, critical plane approaches can also be classified into three categories, stress based criterion, strain based criterion and a combination of both stress and strain (e.g. energy criterion) parameters. The obvious benefit of a critical plane method is that it is able to predict fatigue failure planes. On the other hand, the additional complexity involved in a critical plane approach is that additional search process is needed for finding those critical planes. As a result, critical plane models are computationally-intensive than equivalent stress or strain methods. This is especially the case when it comes to fatigue assessment of large and complex engineering structures under complex variable amplitude loading histories.

(a) Findley's stress based critical plane model

Findely [59] suggested that the critical plane for fatigue crack initiation and growth is dependent on both alternating shear stress and maximum normal stress. The combined effects of shear stress and normal stress are responsible for fatigue damage. Linear combination of shear stress and normal stress is used as a damage parameter in the following way:

$$\left(\frac{\Delta\tau}{2} + k\sigma\right)_{max} = \sqrt{1+k^2}\,\tau_f'\left(2N_f\right)^{b_0} \tag{1.38}$$

where k is a material dependent parameter reflecting the effect of normal stress on fatigue damage. τ_f' and b_0 are shear fatigue strength coefficient and exponent, respectively.

(b) Mc Diarmid 's stress based critical plane model

The McDiarmid Criterion [60] defines the critical plane as the plane with largest shear stress range. The maximum shear stress range and maximum normal stress within a cycle is combined as fatigue damage parameter. The criterion is:

$$\frac{\Delta\tau_{max}}{2} + \tau_{A,B}\frac{\sigma_{n,max}}{2\sigma_u} = \tau_f'\left(2N_f\right)^b \tag{1.39}$$

In the above equation $\sigma_u$is ultimate tensile strength and $\tau_{A,B}$ is shear fatigue strength for two different types of cracking, one is the case with shear crack propagates along the surface of a component and the other for shear crack propagating into a component from surface.

Both Findely's and McDiarmid's models only have stress components involved. They are more suitable for fatigue life prediction in high cycle fatigue regime in which stresses are dominated by elastic components.

(c) Brown-Miller strain based critical plane model

In the low cycle regime, Brown and Miller [61] proposed a model in which maximum shear strain range $\Delta\gamma_{max}$ and the range of normal strain $\Delta\varepsilon_n$ that act on the maximum shear strain range plane are two damage factors. A linear combination of them is established:

$$\frac{\Delta\gamma_{max}}{2} + S\,\Delta\varepsilon_n = f(N_f) \tag{1.40}$$

In the above equation, S is a material-dependent parameter that represents the influence of the normal strain on fatigue crack growth and is determined by correlating uniaxial tension and pure torsion fatigue test results. When elastic and plastic strains are considered separately, the fatigue damage model is of the following form:

$$\frac{\Delta\gamma_{max}}{2} + S\,\Delta\varepsilon_n = A\frac{\sigma_f'}{E}\left(2N_f\right)^b + B\varepsilon_f'\left(2N_f\right)^c \tag{1.41}$$

In the above equation, σ_f' is fatigue strength coefficient and ε_f' is shear ductility coefficient, b and c are fatigue strength exponent and fatigue ductility exponent, respectively. It can be observed that several material parameters are involved for correlation.

Brown-Miller's model is applicable to low cycle fatigue since fatigue is a strain controlled process in low cycle regime and it cannot take into account of mean normal strain effect

(d) Fatemi-Socie's critical plane model

Fatemi and Socie [11] built on the work of Brown and Miller and suggested that instead of using normal strain range, normal stress should be included to reflect crack closure effect:

$$\frac{\Delta\gamma_{max}}{2}\left(1 + k\frac{\sigma_{n,max}}{\sigma_y}\right) = \frac{\tau_f'}{G}\left(2N_f\right)^b + \gamma_f'\left(2N_f\right)^c \tag{1.42}$$

$\Delta\gamma_{max}$ is the maximum shear strain range on any possible plane and $\sigma_{n,max}$ is the maximum normal stress on the plane with maximum shear strain range within one cycle. The sensitivity of a material to normal stress is reflected in the value of k. Fatemi-Socie model is becoming very popular and effective for fatigue assessment [62-64] since it contains both stress (with mean stress effect of normal stress component considered) and strain requiring a constitutive model for characterizing material behavior. Therefore, the model is capable of capturing non-proportional hardening effect. Again for the application of the above equation, plenty of material constants have to be known in advance for both constitutive equation and fatigue damage model in Eq. 1.42.

(e) Smith-Watson-Topper (SWT) critical plane model

The Brown-Miller and Fatemi-Socie's models are developed primarily for shear dominated fatigue failure and the critical plane is generally defined as the plane with maximum shear strain range. In contrast, SWT [65] was developed for materials that fail predominantly by crack growth on the plane with maximum principal strain range:

$$\sigma_{n,max}\frac{\Delta\varepsilon_1}{2} = \frac{\sigma_f'^2}{E}\left(2N_f\right)^{2b} + \sigma_f'\varepsilon_f'\left(2N_f\right)^{b+c} \tag{1.43}$$

Since $\sigma_{n,max}$ in Eq. 1.43 is defined on the plane with maximum principal strain range, mean stress effect is also included. However, for non-proportional loading with rotation of principal strain axes, the definition of principal strain range $\Delta\varepsilon_1$ seems questionable since at the two moments with the largest principal strain range between them, their principal strain axes may not be in the same direction.

There are also several energy-based critical plane models [5] in which strain energy is defined with respect to potential fatigue planes. Detailed explanations can be found in [5].

As a critical assessment, critical plane methods are advantageous in their capability of locating the specific direction along which maximum fatigue damage occurs. However, both cycle counting and fatigue damage accumulation have to be carried out on each potential critical plane for each material point of concern. Therefore, the computational cost would be one order of magnitude higher than that of conventional methods. Admittedly, critical plane methods are generally capable of taking into account of non-proportional loading effect in the process of searching for various potential critical planes. Taking Fatemi-Socie's model as an illustration, Fig.1.18 is a plot of Fatemi-Socie's fatigue damage parameter and its components as well as equivalent strain (von Mises equivalent strain) as a function of plane orientation [32] under in-phase and 90° out-of-phase fatigue loading on a titanium alloy BT9. The non-proportional effect between in-phase and out-of-phase is captured by the different values of Fatemi-Socie's parameter on their respective most critical planes (planes with largest value of Fatemi-Socie's parameter). Nevertheless, one issue that emerges is how to define shear stress/strain ranges (e.g. $\Delta\tau_{max}$ in Findley's model and $\Delta\gamma_{max}$ in Fatemi-Socie's model) for potential critical planes in real practice. This question arises from the fact that shear stress/strain is a vector and its trace can be of arbitrary shapes (e.g. Fig. 1.19) during non-proportional loading. Therefore, we can then argue that a proper shear stress/strain range definition that includes the effect of non-proportional loading is still lacking for critical

plane methods. Some empirical approximations that have been proposed trying to achieve such a purpose will be briefly explained in the next section.

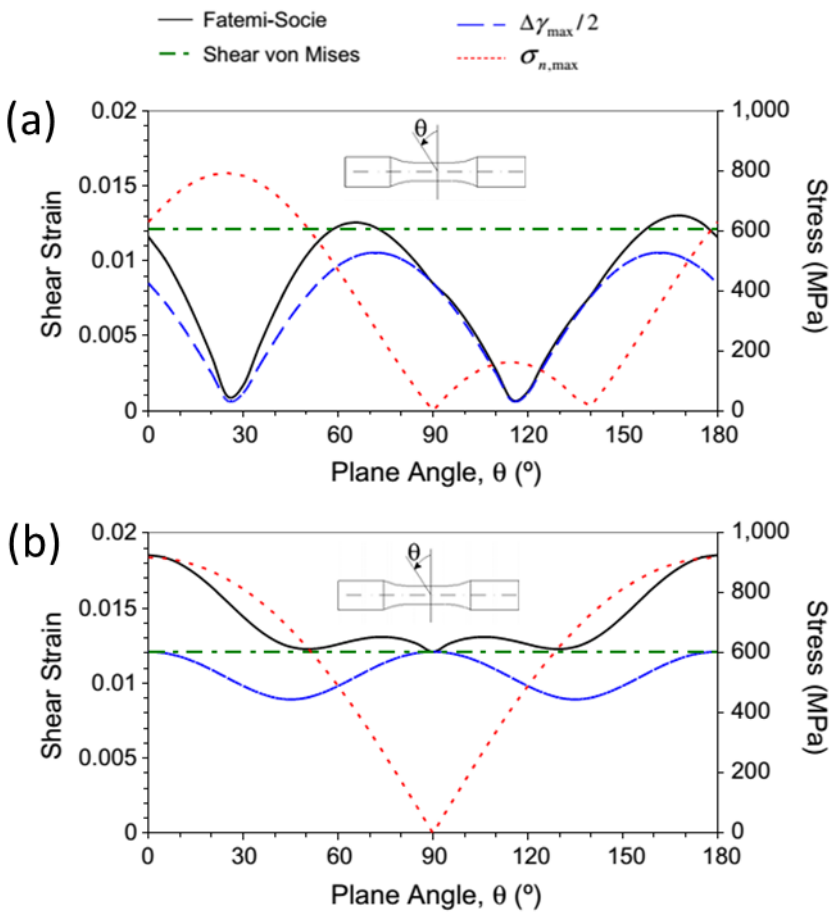

Fig. 1.18 Variation of damage components with plane orientation for titanium alloy BT9 for (a) in-phase axial–torsion, and (b) 90°out-ofphase axial–torsion loadings with same equivalent strain amplitude [32]

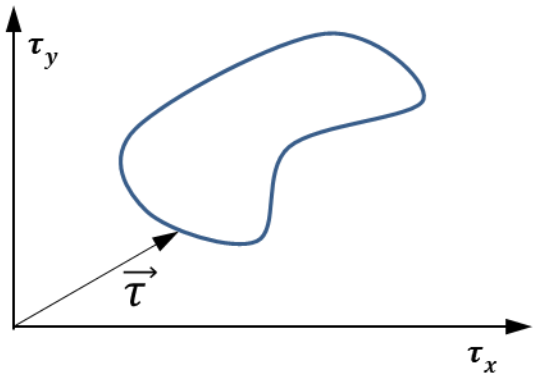

Fig.1.19. The shear stress vector on a potential critical plane in one non-proportional loading cycle

1.2.2.3 Recently Developed Models for Taking into Account of Non-Proportional Effect

Besides the above reviewed well-known classical and critical plane models, some other less known models which were specifically proposed for incorporating non-proportional damage effect will be examined here since these are most relevant to the theme of this dissertation.

(a) Modified Gough ellipse

For non-proportional loading with clearly defined phase angle between sinusoidal tension and torsion, Dong and Hong [66] hypothesized a modified form of Gough ellipse equation:

$$\left(\frac{\Delta\sigma}{\sigma_f}\right)^2 + \left(\frac{\Delta\tau}{\tau_f}\right)^2 = \left(F(\delta)\right)^2 \tag{1.44}$$

where $F(\delta)$ is a dimensionless parameter as a function of phase angle δ. The case $\delta = 0°$ $(F(\delta) = 1)$ corresponds to original Gough's ellipse equation. For a given phase angle

δ, The von Mises expression used in ASME Boiler and Pressure Vessel code can be applied to define $F(\delta)$:

$$F(\delta)=\frac{\Delta\sigma_{VM}(\delta)}{\Delta\sigma_{VM}(\delta=0)}=\frac{1}{\sqrt{2}}\sqrt{1+\sqrt{1-\frac{4\beta\left(\Delta\sigma_s\right)^2\left(\Delta\tau_s\right)^2\sin^2\delta}{\left[\left(\Delta\sigma_s\right)^2+\beta\left(\Delta\tau_s\right)^2\right]^2}}} \tag{1.45}$$

Good correlation was achieved by examining non-proportional loading of welded joints [8, 67, 68]. However, $F(\delta)$ is only applicable to non-proportional loading with clearly defined phase angle between normal and shear stress components.

(b) Effective equivalent stress hypothesis (EESH) by Sonsino

The application of EESH method [8] is also limited to out of phase loading with clearly defined phase angle. To overcome the incapability of von Mises stress in dealing with out-of-phase loading cases, non-proportional effect in EESH model is taken into account by the following steps (combined bending and torsion for illustration):

i. For bending stress and torsion stress with an out-of-phase angle (δ) between them, the normal and shear stresses are

$$\sigma_x=\sigma_0\sin(wt)$$
$$\sigma_y=\sigma_0\sin(wt) \tag{1.46}$$
$$\tau_{xy}=\tau_0\sin(wt+\delta)$$

ii. The shear stress on the plane defined by angle φ with respect to x axis can be written as:

$$\tau_n(\varphi)=\tau_{xy}(\cos^2\varphi-sin^2\varphi)-(\sigma_x-\sigma_y)\cos(\varphi)\sin(\varphi) \tag{1.47}$$

iii. The total effect of shear stress could be expressed by an integral form:

$$F = \frac{1}{\pi}\int_0^{\pi} \tau_n(\varphi) d\varphi \tag{1.48}$$

In the above equation, EESH assumes that failure of ductile materials is initiated by shear stress $\tau_n(\varphi)$. The reason for decreased fatigue life when principal stress direction rotates is the interaction of shear stresses $\tau_n(\varphi)$ on various planes. So the non-proportional effect could be reflected by ratio of the integral in Eq. 1.48 to that of in-phase loading, The EESH stress is then defined as:

$$\sigma_{eq}(\delta) = \sigma_{eq}(\delta = 0)\frac{F(\delta)}{F(\delta=0°)}\sqrt{G\ exp(1 - \left(\frac{\delta-90°}{90°}\right)^2)} \tag{1.49}$$

Detailed explanation of each parameter in Eq. 1.49 can be found in [8]. EESH provides a reasonable way of describing non-proportional loading effect. Nevertheless, it is currently only applicable to out of phase loading cases with the same loading frequency between tension and torsion.

(c) Itoh et al.'s principal strain based critical plane model

Pure strain based model proposed by Itoh et al. [69] makes the use of the principal strain range and take it as the basis of their proposed non-proportional fatigue damage parameter. To include non-proportional loading effect, a path-dependent non-proportional factor and a material parameter are involved. With different variables illustrated in Fig. 1.20, the main procedures needed for finding the maximum principal strain range within one loading block are as follows:

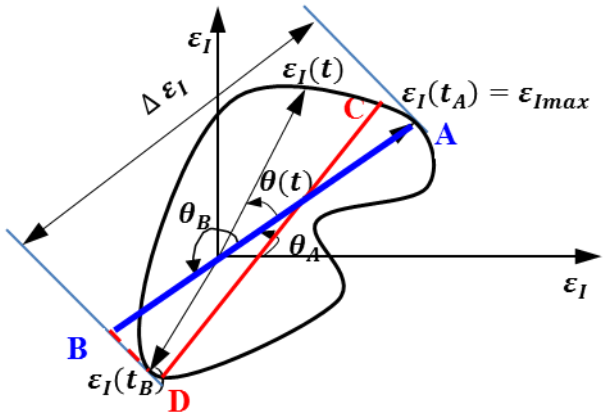

Fig. 1.20 Polar coordinate plot of max principal strain history in Itoh et al.'s model

i. Search for the plane with the maximum absolute value of principal strain (ε_{Imax}) and its direction (θ_A) within a whole loading block.

ii. At any time t in a loading block, calculate the largest magnitude of principal strain and its direction (θ) with respect to θ_A. Plot the principal strain and its direction in polar coordinate shown in Fig. 1.20 for the whole loading block. The largest magnitude of principal strain is defined as:

$$\varepsilon_I(t) = \begin{Bmatrix} \varepsilon_1(t) & for\ \varepsilon_1(t) \geq |\varepsilon_3(t)| \\ |\varepsilon_3(t)| & for |\varepsilon_3(t)| > \varepsilon_1(t) \end{Bmatrix} \quad (1.50)$$

iii. Project principal strain $\varepsilon_I(t)$ at any time t to the plane with largest principal strain ε_{Imax}, and calculate the largest difference between ε_{Imax} and projected length of $\varepsilon_I(t)$ which is:

$$\Delta\varepsilon_I = \max(\varepsilon_{Imax} - \varepsilon_I \cos(\theta)) \quad (1.51)$$

iv. $\Delta\varepsilon_I$ in Eq. 1.51 is then defined as the principal strain range, the non-proportional effect is defined as time integration of principal strain $\varepsilon_I(t)$ projected to the plane

perpendicular to the plane of ε_{Imax} over a load block. The normalized form, also called non-proportionality factor is:

$$f_{NP} = \frac{\pi}{2\varepsilon_{Imax}} \int \varepsilon_I(t) |\sin(\theta)| \, dt \tag{1.52}$$

v. The proposed non-proportional equivalent strain is then defined as:

$$\varepsilon_{NP} = (1 + a_I f_{NP}) \Delta\varepsilon_I \tag{1.53}$$

where a_I is a material constant to reflect the sensitivity of a material to non-proportional hardening as defined in Eq. 1.21 and Fig. 1.10. Later on, recognizing that including non-proportional hardening effect by a_I still fails to achieve satisfactory data correlation [70], another material parameter (α^*) based on fatigue damage equivalence is adopted. The authors [70] continues to attempt to link non-proportional damage sensitivity parameter (α^*) with additional non-proportional hardening coefficient (a_I) which is further believed to be related with static yield and tensile strength properties of metals. As mentioned before, it is a conventional belief, as exemplified here by the attempt carried out by Itoh and Yang [70] that additional non-proportional hardening is the root cause for non-proportional damage. Contrary to this common belief, recent researches [32, 71] reveal that materials with little or no strain hardening may still exhibit a significant amount of fatigue life reduction under non-proportional loading conditions. These contradictory observations have not yet attracted enough attention up to now.

The fatigue model in Eq. 1.53 is built on principal strain range ($\Delta\varepsilon_I$) which is believed to be more suitable for fatigue assessment of brittle materials (note that SWT model is also constructed with a term of $\Delta\varepsilon_I$). On the other hand, by taking ε_{Imax} within a load block as reference for maximum principal stain range calculation, it may have the potential to miss the real maximum principal strain range. As shown in Fig. 1.20, the

maximum principal strain range may be not between A (corresponds to ε_{Imax} location) and B, but between C and D. Finally, for the application of Itoh et al.'s method to complex loading blocks, how to break complex loading path into simple load segments for damage accumulation purpose is still unresolved. Other critical assessments of Itoh's method can be found in Section 1.3.

In spite of that further improvement of Eq. 1.53 is needed, the formulation structure of fatigue damage parameter is enlightening in that its simple form combines two independent key parameters to be considered for taking into account of non-proportional damage: a load path related parameter to characterize load path non-proportionality and a material parameter to reflect material-dependent response under external non-proportional loading. How to capture these two parameters in a more reasonable manner in our proposed model will be presented in Chapter 2 and Chapter 3.

(d) Path length based fatigue damage parameter

Recently, Dong [72] and Wei and Dong [73-74] proposed a path length based stress range definition which measures the accumulated path length of a loading trace in stress space:

$$\Delta S_{path} = \int_{\frac{1}{2}cycle} d\overline{S}, \qquad d\overline{S} = \left[(d\sigma_s)^2 + \beta (d\tau_s)^2 \right]^{\frac{1}{2}} \tag{1.54}$$

The significance of this new definition is that it can be used for arbitrary loading path. The physical basis of path length based equivalent stress was also explained by Wei and Dong [73-74]. Before calculating path length based equivalent stress, Path Dependent Maximum Range (PDMR) cycle counting procedure will have to be implemented to

break complex loading path into simple segements. PDMR cycle counting procedure will be explained in detail in the next section.

It has been shown that path length based stress range is very effective in correlating non-proportional fatigue data [72-74]. However, our recent study has shown that ΔS_{path} is still incapable of correlating non-proportional fatigue test data [69] in certain special cases, especially for cases of different load paths with the same path length. One such example is illustrated graphically as follows:

Tests for different non-proportional strain paths with the same path length were done by Itoh et al. [69] and three of these load paths having exactly the same path length are shown in Fig.1.21. It is expeirmentally proven that the three load cases have quite different non-proportional damaging effects. Case 6 is the least damaging one, having almost the same fatigue life as proportional loading path while Case 8 is the most damging one among the three paths. It can be seen that path length as a non-proportional fatigue damage parameter is incapable of differentiting the different extent of non-proportional damage among the three paths. Thus, we conclude that path length based equivalent stress range fails to reflect path dependent behavior of non-proportional loading in some cases and further improvement is needed.

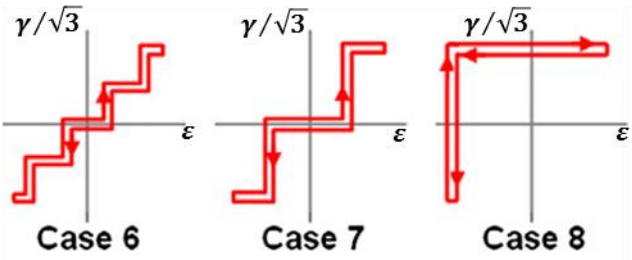

Fig.1.21. Three tested non-proportional strain paths on $\varepsilon - \gamma/\sqrt{3}$ plane with the same path length [69].

(e) Other stress/strain range definitions for non-proportional loading paths

The specific procedures for calculating equivalent stress and strain for non-proportional fatigue models such as Modified Gough Ellipse, EESH models and Itoh's model are already explained above. For other cases, especially for critical plane methods discussed at the end of Section 1.2.2.2, researchers are also met with the task of finding a proper definition of shear stress/strain range on potential critical planes since shear stress may change both its direction and magnitude on the plane of our interest (see Fig.1.19). This section will review several proposed methods including Longest Projection (LP), Longest Chord (LC), minimum circumscribed circle (MCC) and minimum circumscribed ellipse (MCE) for estimating stress/strain ranges and mean values for non-proportional loading paths. Each of them will be illustrated here briefly.

(i) Longest Projection method (LP) [75]

The longest projection method searches for a direction so that the length of the path projected onto this direction is the longest. Half of the projected length is defined as amplitude while the distance between the segment's center and the origin defines the mean stress.

(ii) Longest Chord method (LC) [75]

The longest chord inscribed in a path is searched, the length of the longest chord is defined as stress range and the distance from the middle of the chord to reference point is the mean value of stress.

(iii) Minimum circumscribed circle (MCC) [75]

It involves finding a minimum circle that circumscribes the loading path, the diameter of the circle is stress range and the center of the circle determines the mean stress.

(iv) Minimum circumscribed ellipse (MCE) [76]

Li et al. [76] proposed to use a minimum ellipse (Fig. 1.22) instead of a circle to circumscribe a non-proportional loading path as shown in Fig.1.22. Its long axis is R_D and short axis is R_d. The stress amplitude calculated by MCE method is:

$$\tau_a = \sqrt{R_D^2 + R_d^2} \tag{1.55}$$

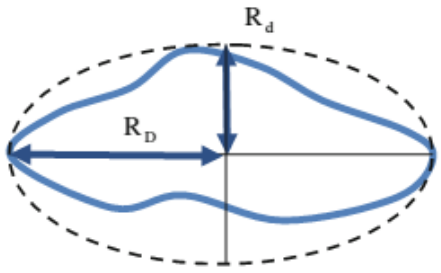

Fig.1.22. Minimum circumscribed ellipse for stress range definition by Li et al. [76]

Fig. 1.23 illustrates each approximation method graphically on $\sigma - \sqrt{\beta}\tau$ plane which is generally used for plotting non-proportional load path when two stress

components (σ and τ) are operative. It can be seen that, for arbitrary loading path, none of LP, LC, and MCC methods could be able to differentiate between a proportional loading path and a non-proportional loading path. Although MCE is able to differentiate between proportional and non-proportional loading paths to some extent in Fig.1.23, it fails in many cases between different non-proportional paths. One simple example is shown in Fig.1.24. It can be seen that even though Path 1 and Path 2 are totally different, their circumscribed ellipse is identical. As a result, MCE fails to predict the different non-proportional damage between these two paths.

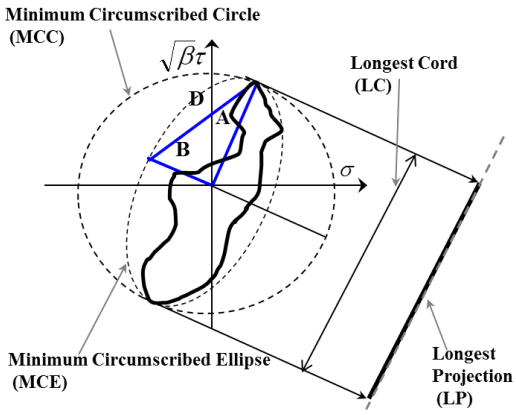

Fig.1.23 Different ways of approximating stress ranges for non-proportional load path.

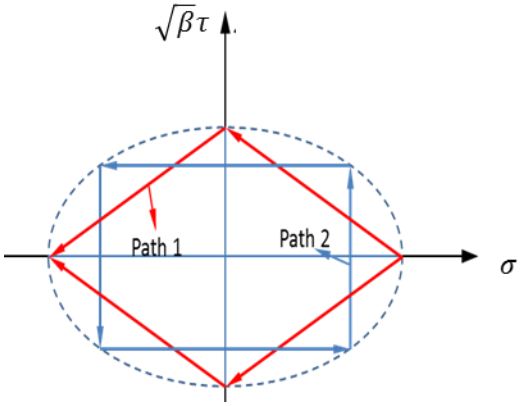

Fig.1.24 Two different non-proportional paths circumscribed by one ellipse.

To briefly summarize recently developed models proposed thus far for non-proportional fatigue, we find that non-proportional fatigue has attracted much attention and quite a few researches were done toward the direction of including non-proportional effects into consideration. As reviewed in this section, some models such as modified Gough Ellipse and EESH hypothesis are only applicable to cases when there is a clearly defined phase angle between two independent stress components. Itoh et al.'s definition of principal strain based equivalent strain is a pretty attractive one in terms of both its simple form and the inclusion of non-proportional effect by two separate parameters with one characterizing load path non-proportionality (as a result of external loading) and the other reflecting material responses. Nevertheless, further improvement is needed considering principal strain range used in Itoh et al.'s model is more suitable for brittle material and material sensitivity parameter to non-proportional loading is not necessarily related with additional hardening effect. With PDMR as a cycle counting procedure, which will be explained shortly, path length as a non-proportional fatigue damage parameter is proven to be quite effective for many, but not all cases. Other stress range definitions based on MCE, MCC only have limited capabilities to take into account of non-proportional loading effect.

1.2. 3 Multi-Axial Cycle Counting Procedures

When it comes to complex variable amplitude fatigue loading histories, a proper cycle counting procedure is needed to break them into simple cycles/reversals of different amplitudes before fatigue damage can be accumulated. In spite of that rainflow cycle

counting is widely used for variable amplitude fatigue life prediciton, its application is generally limited to uniaxial and proportional loading cases. The fact that peak values of stress or strain components of non-proportional loading histories do not necessarily occur at the same time renders rainflow method difficut to be adopted. In this non-proportional loading case, one is faced with more than one independent loading history. A natural question would be: which stress component history should one make use of for cycle counting? Multi-axial cycle counting method is aimed at offering a reasonable solution to this challenging issue. Unfortunately, only a few multi-axial cycle counting procedures (if they are truly applicable) were proposed till now. This section presents three popular methods for cycle counting of non-proportional variable amplitude loading histories: one developed by Bannantine and Socie [77], another by Wang and Brown [78] and the third one is Path Dependent Maximum Range (PDMR) cycle counting procedure [72-74]. Since PDMR will be adopted in our research for cycle counting purpose, it will be explained and demonstrated in more detail in this section.

(a) Bannantine and Socie's multi-axial cycle counting method [77]

This method was originally proposed for cycle counting purpose needed for critical plane based fatigue models and it is essentially a modified version of rainflow cycle counting to the application of critical plane models. The essential idea is that fatigue failures are categorized into two main groups: tensile stress dominated and shear stress dominated fatigue failure. Taking Fatemi and Socie's critical plane method (Eq. 1.42) for an illustration, shear strain range is believed to be the primary controlling parameter for fatigue damage and normal stress is of secondary importance by opening crack face. Therefore, shear strain history will be viewed as the primary channel. As a

result, rainlflow cycle counting will be applied to shear strain history for cycle counting purpose. For instance, Fig.1.25 [79] demonstrates rain flow cycle counting applied to shear strain history. Counted cycle results are also listed in Fig. 1.25. As for normal stress history, it is only viewed as auxiliary channel and no cycle counting is needed. Auxiliary channel is used to find the maximum normal stress within the time domain of each counted cycle of shear strain. So shear strain range and maximum normal stress can be identified for each counted cycle. One thing to be criticized is that within each counted cycle, the normal stress history can vary significantly without having any influence on the specific value fatigue damage parameter calculated in Eq. 1.42 as long as the maximum normal stress remains the same. Based on the above analysis, it can be argued that Fatemi-Socie's critical plane method may fail to capture certain amount of non-proportional loading effect when Bannantine and Socie's multi-axial cycle counting is used.

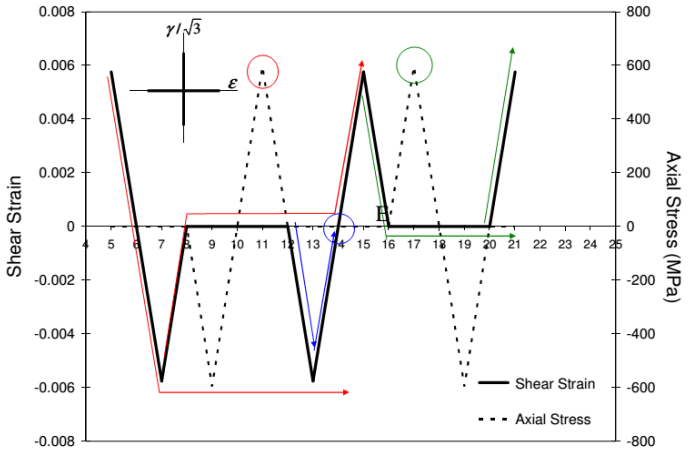

Number of Cycles	Shear Strain Range	Maximum Normal Stress, MPa
1	0.0116	600
1	0.0058	0
1	0.0058	600

Fig.1.25 Example of Bannantine and Socie's multi-axial cycle counting for Fatemi-Socie's critical plane method with shear strain as primary channel [79]

It can be seen that Bannantine and Socie's cycle counting method is essentially rainflow counting of the primary stress or strain history that is viewed as the dominant role in fatigue damage process. In fact, which stress/strain component plays a dominant role is not always clear since fatigue life of one component can either be dominated by shear cracking or tensile cracking depending on loading amplitude, loading mode and environment. Engineering judgment is needed for determining primary and auxiliary channels.

(b) Wang-Brown's cycle counting [78]

Wang-Brown's multi-axial cycle counting method is based on von Mises equivalent strain ε_{von}. The history of equivalent strain serves to define loading cycles. However, since the problem with the equivalent strain is that it is always positive, stress component signs are lost in calculation. To overcome the problem, a relative equivalent strain value is proposed. The method begins with searching the largest value of equivalent strain ε_{von}^{max} within a loading history, then the equivalent strain history is organized in such a way that the ε_{von}^{max} is the starting point for cycle searching. The relative value of strain components with respect to their reference points, which correspond to ε_{von}^{max} is used to calculate relative von Mises strain history. The path it takes for relative equivalent strain $\varepsilon_{von}^{rel}(t)$ to increase monotonically from zero to maximum is counted as a half cycle.

The procedure for Wang-Brown method is as follows:

(i) Find the largest equivalent strain history, arrange the stress history in such a way it start with the largest value.

(ii) Calculate the relative strain components history by taking the point with largest equivalent strain as reference.

(iii) Calculate the relative equivalent strain history based on relative strain components history $\varepsilon_{von}^{rel}(t) = \varepsilon_{von}(t) - \varepsilon_{von}^{max}$

(iv) Search for the path it takes for relative equivalent strain increasing monotonically from zero to maximum. This path is counted a half cycle.

(v) Eliminate the counted cycle, and go to step (1) to search for next cycle.

Wang-Brown's method provides a reasonable way of cycle counting for multi-axial non-proportional loading. Nevertheless, the relative equivalent strain concept may not be able to find the real maximum equivalent strain/stress range. This will be illustrated by the example shown in Fig. 1.26.

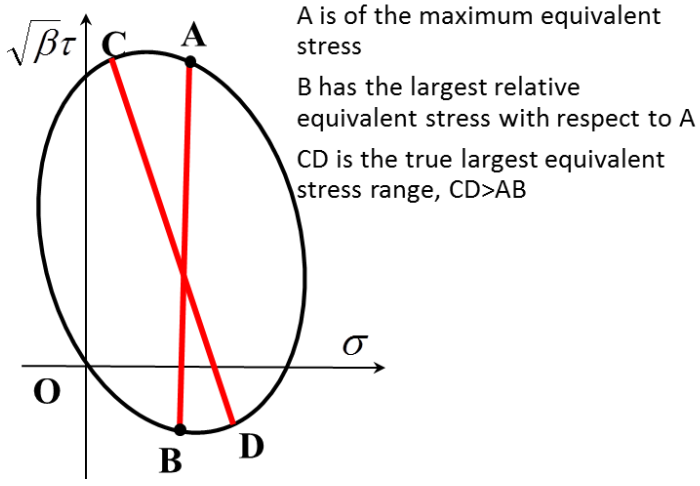

Fig. 1.26 A Sketch showing how Wang-Brown's method fails to find maximum equivalent stress range

Point A in Fig. 1.26 has the largest equivalent stress value, which is the distance from A to the origin O. Taking Point A as reference, the largest relative equivalent stress is, let's say, AB in Fig. 1.26. Thus the first largest range found by Wang-Brown would be AB. However, the true largest equivalent stress range may be actually between C and D. The key reason for Wang-Brown's failure in this case is that the point with largest equivalent stress is taken as the start point for searching the largest relative equivalent stress whereas the largest range does not necessarily have to be related with the point with absolute value of largest equivalent stress.

(c) Path Dependent Maximum Range (PDMR) cycle counting procedure [72-74]

The previous two methods aim at dealing with multi-axial cycle issue by focusing on loading histories. A pretty new perspective of tackling multi-axial cycle counting in PDMR is by focusing on load path in stress space. Therefore, stress plane ($\sigma - \sqrt{\beta}\tau$ plane), which were already shown in Fig. 1.23, Fig. 1.23, Fig. 1.26 for bi-axial stress sate will be explained here.

Consider von Mises type of effective stress definition in Eq. 1.1 for plane stress problem with $\sigma = \sigma_x, \sigma_y = 0$ and $\tau_{xy} = \tau$, the case $\sigma_A \neq 0, \tau_A = 0$ is equivalent to the case $\sigma_B = 0, \tau_B \neq 0$ in terms of σ_e when $\sigma_A = \sqrt{\beta}\tau_B$ where $\beta = 3$. In other words, it can be said that σ_A is equivalent to $\sqrt{3}\tau_B$ when von Mises type of effective stress definition is concerned. Similarly, σ_A is equivalent to $\sqrt{4}\tau_B$ in terms of equivalent Tresca stress. When we plot the two stress components on $\sigma - \sqrt{\beta}\tau$ plane, the distance of any stress point on the plane to the origin will be σ_e, if $\beta = 3$ is assumed. With τ scaled by $\sqrt{\beta}$, normal and

shear stresses can then be treated equivalently in a coordinate system (i.e. $\sigma - \sqrt{\beta}\tau$ plane) in which simple mathematical operations (e.g. distance between two points) can be done without losing its mechanics-based implication.

When it comes to fatigue, let's assume that a pure tension test with stress range of $\Delta\sigma$ has a fatigue life of N and a shear stress range of $\Delta\tau$ with $\Delta\sigma = \sqrt{\beta}\Delta\tau$ under pure shear fatigue loading is needed for achieving such a fatigue life. We can then argue that $\Delta\sigma$ is equivalent to $\sqrt{\beta}\Delta\tau$ in terms of their fatigue damage. Therefore, $\sqrt{\beta}$ can then be viewed as a fatigue equivalency parameter between normal stress and shear stress. In spite of that $\sqrt{\beta}$ can be determined based on its definition, which is more generic for different materials, β=3 generally yields pretty good data correlation in most cases for ductile metals, indicating that von Mises form of equivalent stress range is still the most useful form of equivalent stress definition for fatigue problems under uniaxial loading or proportional loading.

Note that the concept of $\sigma - \sqrt{\beta}\tau$ plot can be extended in a similar manner to strain space in terms of $\varepsilon - \sqrt{\beta^{\varepsilon}}\gamma$ where $\sqrt{\beta^{\varepsilon}}$is a fatigue equivalency parameter between ε and γ and it generally takes the value of $1/\sqrt{3}$, corresponding to von Mises type of equivalent strain definition. For mixed mode fatigue crack growth problems in which stress intensity factors of Mode I, Mode II and Mode III are most frequently used, a similar plane could be defined in terms of K_I, K_{II} or K_{III} , i.e. $K_I - \sqrt{\beta^{K}}K_{III}$ plane for mixed Mode I and Mode III fatigue crack problem where $\sqrt{\beta^{K}}$is a fatigue equivalency parameter between K_I and K_{III}. These types of stress/strain/stress intensity factor planes in different terms for dealing with different problems will be demonstrated in this thesis.

Finally, the above mentioned stress space definition can be further extended to five-dimensional stress space [80-81] when a stress tensor is needed for describing stress state at a point. Five-dimensional stress space is enough for stress state characterization since only deviatoric stress components are needed in most cases.

For fatigue problems, it is well-known that range definition (stress range, strain range or stress intensity factor range), especially the maximum range is the most important parameter to characterize fatigue damage process. Therefore, a reasonble cycle counting procedure should first be able to count the maximum range reliably. Based on the above understanding, searching for the maximum range on stress space (e.g. $\sigma - \sqrt{\beta}\tau$) is the key of PDMR multi-axial cycle counting. For achieving such a purpose, it is also necessary to define some terminologies such as turning points, projected points and virtual path. This will be illustrated in Fig. 1.27. In searching for the maximum range with respect to a reference point, there are possibly more than one local maximum range points, following which the distance to the reference point is decreasing. These types of points are termed as turning points. In Fig. 1.27, it can be seen that a turning point, denoted as R is the local maximum with reference point O. After the turning points, the distance to reference point is actually decreasing, till another point denoted as R^* having the same distance as turning point R is reached. Pretty much like local hysteresis loop in uniaxial loading, the loading history RSR^* is a local hysteresis in terms of their distance to reference point. Thus, during the search for the maximum stress range, once a turning point is found, it will be projected to a point on the loading path with the same distance to reference point. The projected point is therefore called projected turning point. Point R^* in Fig. 1.27 is one such projected turning point. The straight line or arc (RR^*) that

connects turning point R and projected turning point R^* is called virtual path. The virtual path is not the real path, but it does reflect the change of stress state from R to R^*.

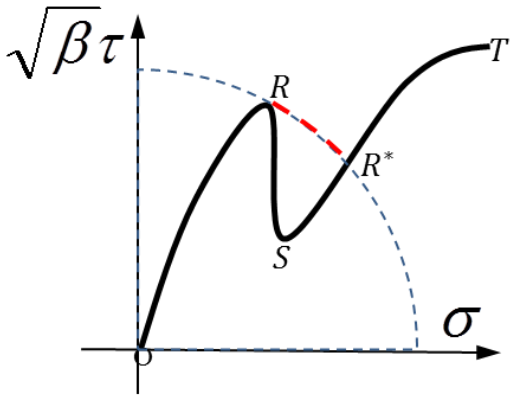

Fig. 1.27. Turning point (R), projected turning point (R^*) and virtual path (RR^*)) definition

The main aim of PDMR is to find the maximum range consecutively in each searching step until all paths are counted and counted only once. The general procedures for PDMR are as follows:

(i) Search for the maximum range between any two points of a whole loading path in stress plane, denoting the starting point as A and ending point as B for this maximum range. Noting that starting point and ending points don't have to be at the start and the end of the whole path. Thus, one or two parts of the whole load path may be removed to the next stage of searching.

(ii) For the load path between A and B, take the starting point A as reference and calculate the distance of following points to A. Once a turning point is found, PDMR then searches for its corresponding projected turning point. The loading

path (such as RSR^* in Fig. 1.27) between a turning point and a projected point, also called local hysteresis path is then removed for next stage of searching. The virtual path (RR^* in Fig. 1.27 for illustration) is counted as part of path history for maximum range AB. This type of searching for turning point and removing local hysteresis paths is repeated until no turning point is left between AB. The monotonically increasing load path left between A and B, possibly including many virtual paths is counted as half a cycle with the maximum range.

(iii) For the counted load path segment with maximum range between A and B identified by step (i) and (ii), different non-proportional fatigue models can be used for damage calculation.

(iv) Repeat the steps (i)-(iii) for each load path that is removed during step (i) and turning point projection in step(ii)

With PDMR searching procedures elaborated, a specific example of cycle counting for the very simple load path in Fig. 1.27 will be demonstrated here. As discussed, the maximum range is between O and T. There is one turning point and one projected turning point between OT. Therefore, the local hysteresis (RSR^*) between R and R* is removed to next stage of cycle counting. The first cycle counted is path ORR^*T shown in Fig. 1.28 (a). Note that the virtual path RR^* has to be taken into account for path length based fatigue damage parameter calculation since non-proportional stress state transition occurs from state R to R^*.

The remaining loading path left after first cycle counting is RSR^* in Fig. 1.28(b). Starting from R, it is clear that the maximum range is from R to S with no turning points

in between. Thus, the second counted cycle is simply path RS in red in Fig. 1.28 (b). Finally, the last path left is SR^* shown in Fig. 1.28(c).

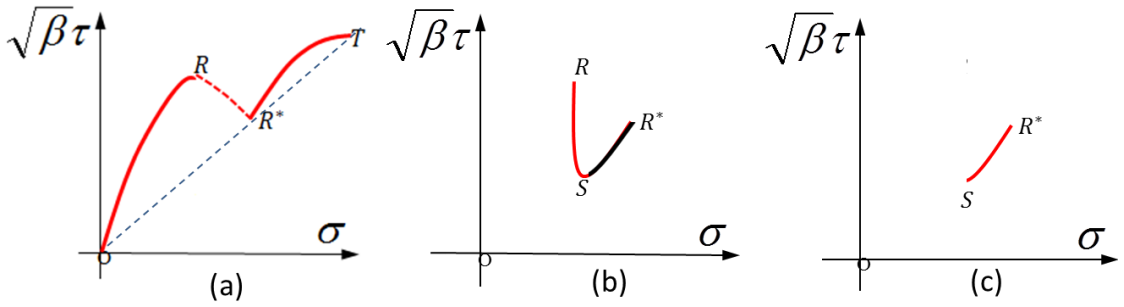

Fig.1.28. PDMR cycle counting for loading path of Fig. 1.27 with each counted path plotted in red. (a) first counted half cycle for maximum range path ORR^*T ; (b) second half cycle RS; (c) third half cycle SR^*

With the above half cycles of different ranges counted, different fatigue damage parameters such as path length [72-74] can be used directly for fatigue assessment. As far as critical plane methods are concerned such as Findely's model [59], the above multi-axial cycle counting procedure is equally applicable.

It is worth mentioning that another multi-axial cycle counting procedure named as the Modified Wang–Brown method was proposed by Marco Antonio Meggiolaro [80-81]. It essentially shares the same idea of PDMR in that it also searches for the maximum distance in stress space. The progress made in the publication is that it further extends multi-axial cycle counting procedures to five-dimensional stress space.

PDMR based cycle counting procedures as well as further developments by [80-81] provide a new framework for multi-axial cycle counting by identifying maximum range in stress space. Therefore, it was adopted in our research for cycle counting purpose. As will be seen later, a pretty good and straightforward integration of our

proposed fatigue damage model is made with PDMR cycle counting for dealing with non-proportional multi-axial variable amplitude loading.

1.2. 4 Fatigue Damage Accumulation Rules

Once non-proportional variable amplitude loading histories are broken into various segments by multi-axial cycle counting procedures (see Section. 1.2.3), their damage calculated by various damage models (see Section 1.2.2) has to be summed up for total damage assessment. Fatigue damage accumulation rules can be categorized into linear rule, namely Palmgren-Miner rule (or Miner's rule), [82, 83] and non-linear rules. A comprehensive review of various types of damage accumulation rules can be found in [84].

In most cases, fatigue damage at a certain stress/strain range is defined as the ratio of cycles experienced in service over the total number of cycles that are needed for fatigue failure under the fixed stress/strain range. For instance, if a stress loading history of interest is counted into many different cycles (n_i) with stress levels ($\Delta\sigma_i$), the fatigue damage of each stress level is:

$$D_i = \frac{n_i}{N_i} \tag{1.56}$$

in which N_i is the number of cycles associated with fatigue failure when constant stress range ($\Delta\sigma_i$) is applied. The specific number of N_i for stress range of $\Delta\sigma_i$ can be found by checking with S-N curve. When total fatigue damage reaches to $D = 1$, final fatigue failure will occur.

Linear damage accumulation rule is the most widely adopted one in practice. It assumes that there is no damage interaction among various stress/strain levels and the total damage is calculated by adding fatigue damage of different stress levels linearly:

$$D = \sum_{i=1}^{n} \frac{n_i}{N_i} \tag{1.57}$$

Linear damage accumulation rule will be used in our data analysis for variable amplitude loading histories. Note that as commented by Fatemi and Shamsaei[29], some of the inaccuracies attributed to linear damage accumulation rule may not be actually due to damage rule itself, but to the fatigue damage model used. On the other hand, non-linear damage accumulation rule would require extra material constant to be determined in advance.

For some typically used load blocks as those employed in research studies [69, 85], it is usually convenient to combine several load path segments counted within one block into one equivalent cycle with a corresponding stress range based on Miner's rule for data correlation purpose [72]. The reason for combining them into one equivalent cycle is that most of experimentalists conventionally take it as one cycle for one load block. Taking an applied loading block consisting of one cycle with an equivalent stress range of $\Delta\sigma_e^1$ and one cycle with an equivalent stress range of $\Delta\sigma_e^2$ as an example, the way of deriving such an Miner's rule based equivalent stress range for one load block is as follows:

For power-law type of S-N curve, we have

$$\Delta\sigma_e^1 = C \cdot N_1^{-1/m} \tag{1.58}$$

$$\Delta\sigma_e^2 = C \cdot N_2^{-1/m} \tag{1.59}$$

where N_1 and N_2 are the fatigue lives corresponding to $\Delta\sigma_e^1$ and $\Delta\sigma_e^2$. Based on Miner's rule, since one load block in current case is assumed to consist of one cycle with stress range of $\Delta\sigma_e^1$ and another cycle with range of $\Delta\sigma_e^2$, the total fatigue damage within one load block is $1/N_1 + 1/N_2$. Suppose that the number of load blocks needed for fatigue failure is N, we thus have

$$N \cdot \left(\frac{1}{N_1} + \frac{1}{N_2}\right) = 1 \tag{1.60}$$

Based on S-N curve, the effective stress range corresponding to N loading blocks is:

$$\Delta\sigma_{eff} = C \cdot N^{-1/m} \tag{1.61}$$

From Eq. 1.58 to Eq.1.61, the effective stress range can then be expressed as:

$$\Delta\sigma_{eff} = (\Delta\sigma_1^m + \Delta\sigma_2^m)^{-1/m} \tag{1.62}$$

Similar steps can be applied to calculate effective stress of a complex loading block after cycle counting for the block is done. This type Miner's rule based effective stress/strain range definition will be used when needed for data correlation purpose in later chapters.

1.2. 5 Mixed Mode Fatigue Crack Growth

The reviewed fatigue damage models in Sec. 1.2.2 are mainly associated with fatigue damage assessment in terms of stress and strain which are suitable for characterization of fatigue behavior of components/materials before a fatigue crack reaches to macro scale. In other words, stress or stain based fatigue models are most

commonly used for cases when fatigue lives are primarily consumed by the stage of fatigue crack initiation and small crack growth until a technical crack size (around 1 mm scale [1]) is observed. However, in many cases, especially when fatigue damage tolerance based design is concerned, fatigue life spent on macro scale fatigue crack growth might take a large portion of total fatigue life. This is especially true when initial defects introduced by manufacturing processes exist even before engineering structures are put into service. As a result, macro-scale fatigue crack growth has to be considered for such cases and stress intensity factors can be used instead of stress/strain for characterizing fatigue crack growth.

A majority of fatigue crack growth researches focus on mode I type of crack under uniaxial tensile loading. In this case, a fatigue crack will always grow in a self-similar manner maintaining its original crack growth direction. However, as far as multi-axial stress state is concerned, a fatigue crack will be subjected to combined mixed mode I, mode I and mode III types of loading. Compared with pure mode I types of crack growth, both the direction of crack growth and an effective stress intensity factor have to be determined for mixed mode loading. When non-proportional mixed mode fatigue loading is applied, the task becomes even more challenging. This section will briefly review some typical research progresses made on predicting crack grow direction and effective stress intensity factors proposed thus far. More detailed literature reviews of this part can be found in [86-89].

(a) Criteria for mixed mode crack growth direction

One of the earliest and most widely adopted model for predicting crack growth direction under mode I and mode II loading is proposed by Erdogan and Sih [90]. It assumes that crack will propagate in the direction perpendicular to the maximum tangential stress ($\sigma_{\theta\theta}$) (MTS) in the polar coordinate system defined with the origin located at a crack tip. In other words, a crack will grow in the direction with the largest crack opening force. When only the singular term of elastic stress field, i.e. K_I and K_{II} are considered, the MTS criterion will lead to the following equation for determining crack growth direction:

$$K_I \sin\theta_c + K_{II}\,(3\cos\theta_c - 1) \tag{1.63}$$

in which θ_c is the angle of maximum tangential stress.

Later on, Sih [91] came up with minimum strain energy density criterion (S-criterion). This criterion assumes that a crack will propagate in a direction with minimum local strain energy density around the crack tip. The total strain energy under mode I and mode II loading can be written as:

$$S = \frac{1}{16\pi\mu}(a_{11}K_I^2 + 2a_{12}K_IK_{II} + a_{22}K_{22}^2) \tag{1.64}$$

where a_{11}, a_{12} and a_{22} are functions of angle θ and can be found in [91]. By letting the first derivative of Eq. 1.64 be zero, the crack propagation direction can then be determined.

Another criterion directly related with energy release rate concept was developed by Hussain and Pu [92]. It attempts to represent stress intensity factors ($K_I^{(2)}$ for mode I and $K_{II}^{(2)}$ for mode II) of an assumed kinked crack in θ direction in terms of stress

intensity factors (K_I for mode I and K_I for mode II) of current configuration. The energy release rate of an assumed kinked crack is:

$$G = \frac{1}{E'}\left(\left(K_I^{(2)}\right)^2 + \left(K_{II}^{(2)}\right)^2\right) \tag{1.65}$$

Then true direction of the crack will be the direction of maximum energy release rate (MERR) which can be determined by letting the first order of derivative of Eq. 1.65 with respect to angle θ be zero.

Detailed and more comprehensive review of crack growth direction can be found in [86]. Overall, most of current well-known criteria tend to predict a crack will generally deflect to the direction along which mode I cracking is maximized and mode II cracking is minimized [93]. This is in general agreement with the usual observation that a crack will generally propagate to a direction such that only mode I type of crack is operative.

However, there are cases when macro cracks have been shown to propagate on maximum shear planes or planes when both tensile and shear loading exist [5]. Based on MTS criterion, the deflection angle would keep on increasing with the increase of mode mixity (the ratio of K_{II} to K_I). However, experiments by Maccagno and Knott [94] showed that with an increase of mode mixity, crack deflection angle first increases and then decreases back to its initial crack direction, demonstrating that crack growth along maximum shear stress plane by pure mode II loading is also possible. Similar observations of crack mode transition between mode I and mode II were also reported in [95-97]. Therefore, another criterion named as maximum shear stress criterion (MSSC) was suggested by Maccagno and Knott [94] and its competition with MTS criterion dictates the final direction of crack growth. More researches on the competition between

tensile dominated and shear dominated crack growth can be found in [89, 98, 99]. For mixed mode fatigue crack growth, the general observation is that the preferred crack growth plane depends on materials, load mixities and loading magnitudes.

As can be seen from the above review, crack growth direction under mixed mode loading is complicated by many factors such as loading level and load mixity in spite of some well-known criteria are available. Furthermore, most of the above researches into mixed mode crack direction only consider the case of proportional mixed mode loading. Crack direction determination under non-proportional mixed mode loading [89] has not been well understood yet.

(b) Effective stress intensity factor definition under mixed mode loading

When a fatigue crack grows under mixed mode loading, a proper definition of stress intensity factor range is needed for incorporating the effect of different modes on fatigue crack growth. The most common type of stress intensity factor is effective stress intensity factor based on different assumptions. Some popular ones are reviewed here.

The earliest proposition of effective stress intensity factor range for mixed mode I, II and III fatigue loading from Tanaka [100] is based on crack tip displacement and has the following form:

$$\Delta K_e = \left(\Delta K_I^4 + 8\Delta K_{II}^4 + \frac{8\Delta K_{III}^4}{1-\nu}\right)^{\frac{1}{4}} \tag{1.66}$$

Tanaka's effective stress intensity factor range definition has been found to show good correlation [101] for fatigue crack growth test under mixed mode I and II loading with different ratios between K_{II} and K_I.

Energy release rate based effective stress intensity factor assumes that its energy release rate is equal to the summation of the release rate of each individual part. As a result:

$$\Delta K_e = (\Delta K_I^2 + \Delta K_{II}^2 + (1+\nu)\Delta K_{III}^2)^{\frac{1}{2}} \tag{1.67}$$

Another type of recently proposed definition is from Richard et al.[102]:

$$\Delta K_e = \frac{\Delta K_I}{2} + \frac{1}{2}\sqrt{\Delta K_I^2 + 4(\eta \Delta K_{II}^2)} \tag{1.68}$$

where η is a material constant.

It should be noted that all of the above proposed effective stress intensity factor range definitions are only applicable (if they are) for proportional mixed mode fatigue crack loading and cannot be extended to the application of non-proportional mixed mode crack growth. Furthermore, loading ratio (R-ratio) effects are not taken into account. As for non-proportional mixed mode fatigue crack growth, plenty of experiment evidences [103-105] demonstrate that crack growth under non-proportional mixed mode loading is much faster than that of proportional case. However, few attempts are made toward this direction. To author's best knowledge, only two models dealing with non-proportional mixed mode fatigue growth models for small cracks are available. The first one is by Socie et al. [106] in terms of normal and shear strain ranges:

$$K_e = ((Y_{II} G \Delta\gamma_{max})^2 + (Y_I E \Delta\varepsilon_n)^2)^{\frac{1}{2}}\sqrt{\pi a} \tag{1.69}$$

where $\Delta\varepsilon_n$ is the normal strain range to the plane with the maximum shear strain range $\Delta\gamma_{max}$ and Y_I and Y_{II} are geometric factors for mode I and mode II respectively. By

applying the model to different loading conditions, pretty good correlations were reported [106].

By following similar form of critical plane based fatigue damage model proposed by Fatemi and Socie [11], Reddy and Fatemi [107] also introduced an effective strain intensity factor of the following form:

$$K_e = G\Delta\gamma_{max}(1 + k\frac{\sigma_{n,max}}{\sigma_y})\sqrt{\pi a} \tag{1.70}$$

The advantage of Eq. 1.69 and Eq. 1.70 is that both the direction and fatigue life can be predicted for small crack growth regardless of load path proportionality.

As can be seen, an equivalent stress intensity factor model that is applicable for macro scale fatigue crack growth under both proportional and non-proportional mixed mode loading is not yet available based on our assessment in spite of the fact that recent test results [104,105] clearly indicated that non-proportional loading leads to a faster fatigue crack growth rate. It should be noted that the above observations were reported in the absence of crack surface interaction (e.g. surface pressure, friction and rubbing between upper and lower crack surfaces). Things can be further complicated if such factors are taken into account. Recent attempts to include crack surface interaction can be found on papers [108].

1.3 Existing Major Challenges

1.3.1 A Proper Stress/Strain Definition for Fatigue Analysis of both Non-Welded and Welded Components

Which type of stress/strain definition should one make use of is the first step for constructing a reliable fatigue damage model. Extensive literature review in Section 1.2 indicates that besides a proper consideration of constitutive relationship between stress and strain (if needed), how to come up with a stress/strain definition that reflects the overall response of components, not the response of one specific material point, is an important concern for fatigue assessment of notched components. For non-welded components, progresses made on critical distance theory and structural yield surface model are the few attempts made along this direction. For welded joints, notch stress approach and hot spot approach are pretty commonly used nowadays by researchers and engineers. Nevertheless, the assumption of a fictitious notch radius in notch stress approach and different surface stress extrapolation techniques in hot spot stress approach lack of solid physical and mechanical basis. Traction based structural stress/strain is proven to be more suitable for fatigue analysis of welded joints subjected to dominantly uniaxial loading. Its potential for fatigue assessment under non-proportional multi-axial loading has not been fully explored yet.

1.3.2 An Integrated Approach for Non-Proportional Fatigue Modeling and Multi-Axle Cycle Counting

Both non-proportional fatigue models and multi-axial cycle counting are challenging issues for fatigue research community. The majority of researchers only focus on one of them as their research topic. For instance, Fatemi and Socie's work [11]

lies on proposing different fatigue damage parameters without paying much attention on cycle counting issue. Similarly, Itoh et al. [69] proposed a new formulation of non-proportional fatigue damage parameter only for the case of simple load blocks and no recommendation was made on how to apply the proposed damage model to complex variable amplitude loading involving multi-axle cycle counting issue, leading to the applicability of Itoh et al. model only limited to simple cases at current stage. On the other hand, Wang-Brown's work [78] mainly focused on procedures needed for non-proportional multi-axial cycle counting.

One important progress towards integrating fatigue damage parameter with multi-axial cycle counting procedures was made by Dong et al.[72], Dong and Wei [73,74]. They proposed a PDMR cycle counting procedure and at the same time made use of path length of each counted load path segment as a fatigue damage parameter. This integrated treatment of non-proportional fatigue is enlightening. Nonetheless, as reviewed in Section 1.2.3, there are cases and experimental evidences indicating that path length is not always effective in capturing non-proportional damage effect. Furthermore, path length as a fatigue damage parameter cannot reflect the fact that different materials under the same load path may have different sensitivities in terms of their damage to non-proportional loading. Therefore, further improvement of the integrated approach is needed.

1.3.3 Characterization of Material Sensitivity to Non-Proportional Loading

The most conventional belief that has been persisting in research community of non-proportional multi-axial fatigue is that the much more damaging effect of non-proportional loading than that of proportional loading is caused by additional hardening in non-proportional case. As a result, much effort is devoted to coming up with complex

cyclic elastic-plastic constitutive models for calculation of stress or strain responses. As a consequence, additional cyclic hardening coefficient is always used to reflect material sensitivity to non-proportional loading [69, 109] in the construction of non-proportional fatigue damage parameters. However, as commented by Skibicki [6], additional hardening is not the only factor in contributing to non-proportional damage. The above argument is supported by recent experiments on Titanium alloys and steels [15, 29, 31 32] demonstrating that non-proportional fatigue damage is still significant with minimal non-proportional hardening. Furthermore, this observation tends to be further supported by Itoh et al.'s researches showing that replacing material sensitivity parameter with additional hardening coefficient will not lead to a satisfactory correlation. Therefore, a proper definition of material sensitivity parameter and a procedure for its determination have to be in place for any proposed non-proportional fatigue damage models.

1.3.4 Validation of Non-Proportional Fatigue Model by Extensive Test Data of Various Materials Available in Literature

For validations of any proposed fatigue model, satisfactory correlation of test data collected within one research group is far from enough. Unfortunately, except of those well-accepted fatigue models as reviewed in Section 1.2, the majority of various types of proposed fatigue damage models spreading through different publications did not undergo sufficient validations by a large amount of test data from different sources. As a result, the robustness and applicability of these models are questionable if were used in different scenarios or for different materials. It would be best if a fatigue model can be validated by different materials with different material properties. This can be achieved by examining a vast amount of test data of other types of materials available in literature.

1.3.5 Extension of Non-Proportional Fatigue Model to Fatigue Crack Growth Regime

A majority of non-proportional fatigue researches are dedicated to fatigue crack initiation stage (Stage I) of total fatigue life. Stress and (or) strain are used for the construction of fatigue damage model at this stage. When it comes to the stage of macro scale fatigue crack growth (Stage II) which might consume a significant portion of fatigue life, little efforts were made to capture non-proportional loading effect of Stage II crack growth till today. In other words, in contrary to experimental evidences [104, 105], current available effective stress intensity factors cannot differentiate between proportional and non-proportional mixed mode fatigue crack growth. Two strain based intensity factors [106,107] originated from critical plane methods are only applicable to small crack growth and are the only achievements made so far to extend the application of Stage I non-proportional fatigue model to the early stage of Stage II. It would be great if a consistent type of non-proportional fatigue damage definition is applicable to both fatigue crack initiation and macro scale fatigue crack growth stages. Unfortunately, little progress was made along this direction.

1.4 Motivation and Objectives of Current Researches

After a comprehensive review of state-of-the-art developments in various aspects of non-proportional fatigue modeling and summarizing current major challenges that have not been fully resolved, the author is motivated to come up with a new model for modeling of non-proportional fatigue under variable amplitude loading conditions with special focus on the following topics:

i. Proper selection of a suitable stress/strain definition that represents the overall cyclic stress/strain state at fatigue failure locations of interest as the starting point for a formulation of non-proportional fatigue damage parameter.

ii. Formulation of a non-proportional fatigue damage model which is integrated into PDMR multi-axle cycle counting procedures for fatigue assessment of both non-welded and welded structures/components under non-proportional multi-axial variable amplitude loading.

iii. A proper characterization of material sensitivity and a specific procedure for its determination for different materials.

iv. Extension of non-proportional damage model defined in terms of stress/strain to non-proportional mixed mode fatigue crack growth in terms of stress intensity factors.

v. Validation of proposed non-proportional fatigue model by a large amount of low cycle and high cycle test data available from different well-documented literatures at both material and structural component levels.

1.5 Outline of Dissertation

The dissertation begins with an introductory background of non-proportional multi-axial fatigue and extensive literature review of state-of-the-art developments relevant to our research topics. Chapter 1 starts with a quick overview of stress-strain constitutive modeling which has been a focal point of many researchers and detailed evaluation of various types of stress/strain definitions for non-welded and welded components. Such a detailed assessment of different stress/strain definitions originates from our understanding that a proper definition of stress/strain that captures overall

responses (or structural responses) of structural components under fatigue loading is much more important than employing complex constitutive models to capture stress/strain state at one specific material point. As a result, structural stress/strain is used as our building block of proposed fatigue damage models when it comes to analysis of welded components. After that, a comprehensive review of three main groups of multi-axial fatigue models, namely, equivalent stress/strain based, critical plane based as well as recently developed new models are critically assessed in terms of their capabilities in taking into account of non-proportional damage effects. For dealing with variable amplitude loading, three types of currently available multi-axial cycle counting procedures are explained with emphasis placed on PDMR cycle counting since it will be integrated into our proposed non-proportional model. Finally, as a special category of non-proportional fatigue problem, mixed mode crack growth under non-proportional loading is also reviewed in detail since it is also a topic we are going to address as a part of our work. With critical assessments of several reviewed topics and major challenges summarized, our research objectives emerge in Section 1.4 of Chapter 1.

Chapter 2 proposes a moment of load path (MLP) based non-proportional fatigue damage model which is integrated into PDMR cycle counting procedure for dealing with complex variable amplitude loading. The essential assumptions related with damage decomposition and non-proportional damage representation are presented for the purpose of characterizing load path non-proportionality which finally leads to a MLP based equivalent structural stress/strain definition. The physical interpretation of the non-proportional damage model is given in terms of weighted form of strain energy density and the procedures for material sensitivity determination are suggested. As a second

major part of Chapter 1, various types of structural steels, including both welded and non-welded components in low and high cycle fatigue regimes are examined to validate the proposed model.

Following proposed model in Chapter 2, Chapter 3, 4 and Chapter 5 focus on applications of MLP model to different areas. It is important to note that since separate papers are now already published on peer-reviewed international journals for each application area, these chapters are therefore composed of published journals with minimal modifications. As a result of the entirety of these journal papers, some background introduction and model description of the proposed model may also occur in each of these chapters. However, these seemingly overlapping contents do serve different purposes in the context of each chapter.

The application of MLP model to different series of aluminum alloys is presented in Chapter 3. A vast amount of currently available aluminum alloys test data is examined in this chapter. Since a majority of non-proportional fatigue data is from out-of-phase tests corresponding to elliptical load paths, an analytical form of load path non-proportionality for arbitrary elliptical load path is given first. Furthermore, detailed procedures with a specific example for determining material sensitivity are illustrated. With material sensitivity parameters calculated for all separate groups of test data, the effectiveness of data correlation by MLP model for each group and as a whole is examined. Finally, the linkage between material ductility and material sensitivity are explored.

Chapter 4 focuses on how MLP based equivalent stress can be used for non-proportional fatigue of welded components. With structural stress definition introduced, a majority of well-documented proportional and non-proportional multi-axial fatigue test data which are grouped into residual stress relieved and as-welded are examined. With MLP based structural stress, a new equivalent stress parameter that further takes into account of thickness effect, bending ratio effect is employed for data correlation of these two separate groups. The correlations for stress relieved and as welded test data are then compared with hot spot stress based effective stress definition by following Eurocode 3 and IIW recommendations. Finally, an overall correlation is presented with mean stress (R-ratio) considered and its plot against master S-N curve adopted in ASME is presented and discussed.

Further extension of MLP model application to macro-scale mixed mode fatigue crack growth problem is made in Chapter 5. A MLP based effective stress intensity factor is first constructed in K plane by following exactly the same manner as proposed in Chapter 2. Two additional issues are addressed in this chapter. One is how mean stress effect can be represented with respect to K plane. Secondly, a two-parameter fatigue crack growth model to allow for mean stress effect is proposed. As a demonstration, stainless steel and structural steel data from non-proportional mixed mode I and mode III fatigue loading of disc specimens are examined by proposed two-parameter fatigue crack grow model.

An overall summary for the whole dissertation is presented in Chapter 6. Some key and original findings from previous four chapters are reviewed. Furthermore,

suggestions are made on how MLP model can be improved and which direction can be further explored for future research.

References

[1] Stephens R. I., Ali Fatemi, Robert R. Stephens, Henry O. Fuchs. *Metal fatigue in engineering*. John Wiley & Sons, 2000.

[2] ASTM E1823-10. Standard Terminology Relating to Fatigue and Fracture Testing. 2010

[3] Suresh S. Fatigue of materials. Cambridge university press, 1998.

[4] The Alexander L. Kielland accident, Report of a Norwegian public commission appointed by royal decree of March 28, 1980, presented to the Ministry of Justice and Police March, 1981

[5] Socie D F, Marquis G. Multiaxial fatigue. Warrendale, PA: Society of Automotive Engineers; 1999.

[6] Skibicki D. Phenomena and computational models of non-proportional fatigue of materials. Springer; 2014.

[7] Gates N, Fatemi A. Multiaxial variable amplitude fatigue life analysis including notch effects. Int J Fatigue 2016; 91:337-351.

[8] Sonsino C M, Kueppers M. Multiaxial fatigue of welded joints under constant and variable amplitude loadings. Fatigue Fract Eng Mater Struct 2001;24:309–327.

[9] Nakamura H, Takanashi M, Itoh T, Wu M, Shimizu Y. Fatigue crack initiation and growth behavior of Ti-6Al-4V under non-proportional multiaxial loading. Int J Fatigue 2011;33:842–848.

[10] ASTM Standard E1049-85, Standard Practices for Cycle Counting in Fatigue Analysis, in: Annual Book of ASTM Standards. ASTM International, West Conshohocken, PA. 2009.

[11] Fatemi A, Socie DF. A Critical Plane Approach to Multiaxial Fatigue Damage Including out-of-Phase Loading. Fatigue Fract Eng Mater Struct 1988;11:149–165.

[12] Jiang Y, Zhang J. Benchmark experiments and characteristic cyclic plasticity deformation. Int J Plast 2008;24:1481–1515.

[13] Hill, R. The mathematical theory of plasticity. Oxford university press; 1998.

[14] Khan, A. S., Huang, S. Continuum theory of plasticity. John Wiley & Sons; 1995.

[15] Shamsaei N, Fatemi A, Socie DF. Multiaxial cyclic deformation and non-proportional hardening employing discriminating load paths. Int J Plast 2010;26:1680–701.

[16] Mróz Z. On the description of anisotropic workhardening. J Mech Phys Solids 1967;15:163–175.

[17] Dafalias, Y F., Popov E P. Plastic internal variables formalism of cyclic plasticity. J. App. Mech. 1976; 98: 645-651.

[18] Armstrong, P.J., Frederick, C.O. A mathematical representation of the multi-axial Bauschinger effect (Report RD/B/N 731). Central Electricity Generating Board. 1966

[19] Chaboche, J. L. Viscoplastic constitutive equations for description of cyclic and anisotropic behavior of metals. Bulletin De L Academie Polonaise Des Sciences-Serie Des Sciences Techniques, 1977; 25:39-48.

[20] Lee, Y. L., Barkey, M. E., Kang, H. T. Metal fatigue analysis handbook: practical problem-solving techniques for computer-aided engineering. Elsevier. 2011

[21] Jiang, Y., Kurath, P. Characteristics of the Armstrong-Frederick type plasticity

models. Int. J. Plast. 1996; 12: 387–415.

[22] Chaboche J L. On some modifications of kinematic hardening to improve the description of ratchetting effects. Int J Plast 1991;7:661–678.

[23] Jiang Y, Kurath P. Nonproportional cyclic deformation: critical experiments and analytical modeling. Int J Plast 1997;13:743–763.

[24] Tanaka E. A nonproportionality parameter and a cyclic viscoplastic constitutive model taking into account amplitude dependences and memory effects of isotropic hardening. Eur J Mech A- Solids 1994;2:155–173.

[25] Kanazawa K., Miller K J., Brown, M.W. Cyclic deformation of 1% Cr-Mo-V steel under out-of-phase loads. Fatigue Fract Eng Mater Struct 1979;2:217–228.

[26] Kida S, Itoh T, Sakane M, Ohnami M, Socie DF. Dislocation structure and non-proportional hardening of Type 304 stainless steel. Fatigue Fract Eng Mater Struct 1997;20:1375–1386.

[27] Zhang J, Jiang Y. An experimental investigation on cyclic plastic deformation and substructures of polycrystalline copper. Int. J. Plast. 2005;21:2191–2211.

[28] Doong S.H., Socie D.F., Robertson I.M. Dislocation sub-structures and nonproportional hardening ASME J Eng Mater Technol. 1990;112:456–464.

[29] Fatemi A, Shamsaei N. Multiaxial fatigue: An overview and some approximation models for life estimation. Int J Fatigue 2011;33:948–958.

[30] Borodii, M. V., Shukaev, S. M. Additional cyclic strain hardening and its relation to material structure, mechanical characteristics, and lifetime. Int J Fatigue, 2007;29(6):1184-1191.

[31] Shamsaei, N., Fatemi, A. Effect of microstructure and hardness on non-proportional cyclic hardening coefficient and predictions. J. Mater. Sci. Eng. A 2010; 527:3015–3024.

[32] Shamsaei N, Gladskyi M, Panasovskyi K, Shukaev S, Fatemi A. Multiaxial fatigue of titanium including step loading and load path alteration and sequence effects. Int J Fatigue 2010;32:1862–1874.

[33] Radaj, D. Review of fatigue strength assessment of nonwelded and welded structures based on local parameters. Int J Fatigue. 1996; 18(3): 153-170.

[34] Neuber H. Theory of notch stresses: principles for exact calculation of strength with reference to structural form and material. 2nd ed. Berlin: Springer Verlag; 1958

[35] Peterson R E. Notch sensitivity. Metal fatigue. New York: McGraw Hill; 1959; 293–306.

[36] Susmel, L. The theory of critical distances: a review of its applications in fatigue. Eng Fract Mech. 2008; 75(7):1706-1724.

[37] Taylor D. The theory of critical distances. Eng Fract Mech 2008;75:1696–17705.

[38] Haddad E I, Smith K N, Topper T H. Fatigue Crack Propagation of Short Cracks. J Eng Mater Technol 1979;101:42–46.

[39] Neuber, H. Theory of stress concentration for shear-strained prismatical bodies with arbitrary nonlinear stress-strain law. J. App. Mech. 1961; 28(4): 544-550.

[40] Topper, T. H., Wetzel, R. M., Morrow, J. Neuber's rule applied to fatigue of notched specimens. ILLINOIS UNIV AT URBANA DEPT OF THEORETICAL AND APPLIED MECHANICS. 1967.

[41] Molski K, Glinka G. A method of elastic-plastic stress and strain calculation at a notch root. Mater Sci Eng 1981;50:93–100.

[42] Köttgen, V. B., Barkey, M. E., & Socie, D. F. Pseudo stress and pseudo strain based approaches to multiaxial notch analysis. Fatigue Fract Eng Mater Struct. 1995; 18(9): 981-1006.

[43] Hobbacher A F. IIW recommendations for fatigue design of welded joints and components. Springer; 2015

[44] BS7910, B. S. Guidance on methods for assessing the acceptability of flaws in metallic structures. British Standards Institution. 2005.

[45] Radaj D, Sonsino C M, Fricke W. Recent developments in local concepts of fatigue assessment of welded joints. Int J Fatigue 2009;31:2–11.

[46] Eurocode 3, design of steel structures-Part 1–9: Fatigue, CEN;2005

[47] Barsoum Z, Jonsson B. Influence of weld quality on the fatigue strength in seam welds. Eng Fail Anal 2011;18:971–979.

[48] Maddox, S. J. Recommended hot-spot stress design SN curves for fatigue assessment of FPSOs. The Eleventh International Offshore and Polar Engineering Conference. International Society of Offshore and Polar Engineers, 2001.

[49] Dong P, Hong J K, Osage D A, Dewees D J, Prager M. "The Master S-N Curve Method: An Implementation in 2007 ASME Div 2 International Codes for Boilers and Pressure Vessels," Welding Research Council Bulletin, No. 523, 2010.

[50] Dong P. A structural stress definition and numerical implementation for fatigue analysis of welded joints. Int J Fatigue 2001;23:865–876.

[51] Dong, P. A robust structural stress method for fatigue analysis of offshore/marine structures J. Offshore Mech. Arct. Eng 2005; 127(1): 68-74.

[52] Dong, P., Pei, X., Xing, S. A Structural Strain Method for Fatigue Evaluation of Welded Components. 33rd International Conference on Ocean, Offshore and Arctic Engineering. ASME 2014.

[53] Dong P, Hong J K. Fatigue Of Tubular Joints: Hot Spot Stress Method Revisited. J Offshore Mech Arct Eng 2012;134:12

[54] Nie, C., Dong, P. A Traction Stress Based Shear Strength Definition for Fillet Welds. Int. J. of Strain Analysis, 2012; 47(8):562-575.

[55] Gough, H. J. Engineering steels under combined cyclic and static stresses. Proceedings of the Institution of Mechanical Engineers.1949; 160(1): 417-440.

[56] Gladskyi M, Fatemi A. Notched fatigue behavior including load sequence effects under axial and torsional loadings. Int J Fatigue 2013;55:43–53.

[57] Sines, G. "Behaviour of metals under complex static and alternating stresses". In Metal Fatigue Edited by: Sines, G. and Waisman, J. L. 145–169. New York: McGraw-Hill. 1959.

[58] Crossland, B. Effect of large hydrostatic pressures on the torsional fatigue strength of an alloy steel. In Proc. Int. Conf. on Fatigue of Metals (vol:138). Institution of Mechanical Engineers London.1956.

[59] Findley, W. N. A theory for the effect of mean stress on fatigue of metals under combined torsion and axial load or bending. Engineering Materials Research Laboratory, Division of Engineering, Brown University. 1958.

[60] McDiarmid D L. A shear-stress based critical-plane criterion of multiaxial fatigue failure for design and life prediction. Fatigue Fract Eng Mater Struct 1994;17:1475–1484.

[61] Brown M W, Miller K J. A theory for fatigue failure under multiaxial stress–strain conditions. Proc Inst Mech Eng. 1973; 187(1):745-755.

[62] Park J, Nelson D. Evaluation of an energy-based approach and a critical plane approach for predicting constant amplitude multiaxial fatigue life. Int J Fatigue 2000;22:23–29.

[63] Gao Z, Qiu B, Wang X, Jiang Y. An investigation of fatigue of a notched member. Int J Fatigue 2010;32:1960–1969.

[64] Kim K S, Park J C. Shear strain based multiaxial fatigue parameters applied to variable amplitude loading. Int J Fatigue 2000;21:475–483.

[65] Smith K N, Watson P, Topper T H. Stress-Strain Function for the Fatigue of Metals. J Mater 1970;5:767–778.

[66] Dong P, Hong J, A Robust Structural Stress Parameter for Evaluation of Multiaxial Fatigue of Weldments. J ASTM Int 2006;3(7):206-222.

[67] Siljander A, Kurath P, Lawrence FV. Nonproportional fatigue of welded structures. In Advances in fatigue lifetime predictive techniques. ASTM Int. 1992; 319-338.

[68] Yousefi F, Witt M, Zenner H. Fatigue strength of welded joints under multiaxial loading: experiments and calculations. Fatigue Fract Eng Mater Struct 2001;24:339–355.

[69] Itoh T, Sakane M, Ohnami M, Socie DF. Nonproportional low cycle fatigue criterion for type 304 stainless steel. J Eng Mater Technol 1995;117:285–292.

[70] Itoh T, Yang T. Material dependence of multiaxial low cycle fatigue lives under non-proportional loading. Int J Fatigue 2011;33:1025–1031.

[71] Shamsaei N, Fatemi A, Socie D F. Multiaxial fatigue evaluation using discriminating strain paths. Int J Fatigue 2011;33:597–609.

[72] Dong P, Wei Z, Hong J K. A path-dependent cycle counting method for variable-amplitude multi-axial loading. Int J Fatigue 2010;32:720–734.

[73] Wei Z., Dong P. A generalized cycle counting criterion for arbitrary multi-axial fatigue loading conditions. J Strain Anal Eng Des 2014;49:325–341.

[74] Wei Z, Dong P. Multiaxial fatigue life assessment of welded structures. Eng Fract Mech 2010;77:3011–3021.

[75] Papadopoulos I. Critical plane approaches in high-cycle Fatigue: on the definition of the amplitude and mean value of the shear stress acting on the critical plane. Fatigue Fract Eng Mater Struct 1998;21:269–285.

[76] Li B, Reis L, de Freitas M. Comparative study of multiaxial fatigue damage models for ductile structural steels and brittle materials. Int J Fatigue 2009;31:1895–1906.

[77] Bannantine, J. A., Socie, D. F. A variable amplitude multiaxial fatigue life prediction methods. In ICBMFF3. 2013.

[78] Wang C H, Brown M W. Life Prediction Techniques for Variable Amplitude Multiaxial Fatigue - Part 1: Theories. J Eng Mater Technol 1996;118:367–370.

[79] Shamsaei, N. Multiaxial Fatigue and Deformation Including Non-proportional

Hardening and Variable Amplitude Loading Effects (Ph.D. Dissertation). 2010. The University of Toledo, Toledo, OH.

[80] Meggiolaro MA, De Castro JTP. An improved multiaxial rainflow algorithm for non-proportional stress or strain histories - Part I: Enclosing surface methods. Int J Fatigue 2012;42:217–26.

[81] Meggiolaro MA, De Castro JTP. An improved multiaxial rainflow algorithm for non-proportional stress or strain histories – Part II: The Modified Wang–Brown method. Int J Fatigue 2012;42:194-206.

[82] Palmgren, A. Die Lebensdauer von Kugellagern. Verfahrenstechinki Berl. 1924; 68:

339–341.

[83] Miner, M.A Cumulative damage in fatigue. J. Appl. Mech. 1945; 67: A159–A164.

[84] Fatemi a., Yang L. Cumulative fatigue damage and life prediction theories: a survey of the state of the art for homogeneous materials. Int J Fatigue 1998;20:9–34.

[85] Socie D. Multiaxial Fatigue Damage Models. J Eng Mater Technol 1987;109:293–298.

[86] Qian J, Fatemi A. Mixed mode fatigue crack growth: A literature survey. Eng Fract Mech 1996;55:969–990.

[87] Shamsaei, N. Multiaxial Fatigue and Deformation Including Non-proportional

Hardening and Variable Amplitude Loading Effects (Ph.D. Dissertation). 2010. The University

of Toledo, Toledo, OH.

[88] Gates R. G. Fatigue Behavior under Multiaxial Stress States Including Notch Effects and

Variable Amplitude Loading (Ph.D. Dissertation). 2016. The University of Toledo, Toledo, OH.

[89] Highsmith Jr, S. Crack path determination for non-proportional mixed-mode fatigue (Ph.D. Dissertation). 2016. Georgia Institute of Technology, Atlanta, GA.

[90] Erdogan F, Sih G C. On the Crack Extension in Plates Under Plane Loading and Transverse Shear. J Basic Eng 1963;85:519–525.

[91] Sih G C. Strain-energy-density factor applied to mixed mode crack problems. Int J Fract 1974;10:305–321.

[92] Hussain M, Pu S L, Underwood J. Strain Energy Release Rate for a Crack Under Combined Mode I and Mode II. Fract Anal 1974;560:2–28.

[93] Maccagno T M, Knott J F. The low temperature brittle fracture behaviour of steel in mixed modes I and II. Eng Fract Mech 1991;38:111–128.

[94] Maccagno T M, Knott J F. The mixed mode I/II fracture behaviour of lightly tempered HY130 steel at room temperature. Eng Fract Mech 1992;41:805–820.

[95] Hallbäck, N., Nilsson, F. Mixed-mode I/II fracture behaviour of an aluminium alloy. J Mech. Phys. Solids, 1994;42(9);1345-1374.

[96] Tanaka, K. Small crack propagation in multiaxial notch fatigue, in: Carpinteri, A., Iacoviello, F., Pook, L.P., Susmel, L. (Eds.), Proceedings of the 4th International Conference on Crack Paths. Gruppo Italiano Frattura, Gaeta, Italy, 2012; 31 –45.

[97] Donne, C. D., Doeker, H. Plane stress crack resistance curves of an inclined crack under biaxial loading. In Multiaxial fatigue and deformation testing techniques. ASTM International,1997.

[98] Chao, Y. J., Liu, S. On the failure of cracks under mixed-mode loads. Int. J. Fract. 1997; 87: 201-223.

[99] Kfouri, A. P. Brown, M. W. A fracture criterion for cracks under mixed-mode loading. Fatigue Fract Eng Mater Struct. 1995; 18(9):959–969.

[100] Tanaka, K., Fatigue crack propagation from a crack inclined to the cyclic tensile axis. Eng. Fract. Mech. 1974: 6; 493–507.

[101] Zhang, H., Fatemi, A. Short fatigue crack growth behaviour under mixed-mode loading. Int. J. Fract. 2010; 165: 1 –19.

[102] Richard H A, Fulland M, Sander M. Theoretical crack path prediction. Fatigue Fract Eng Mater Struct 2005;28:3–12.

[103] Shamsaei N, Fatemi A. Small fatigue crack growth under multiaxial stresses. Int J Fatigue 2014;58:126–135.

[104] Fremy F, Pommier S, Poncelet M, Raka B, Galenne E, Courtin S, et al. Load path effect on fatigue crack propagation in I+II+III mixed mode conditions – Part 1: Experimental investigations. Int J Fatigue 2014;62:104–112.

[105] Feng, M., Ding, F., Jiang, Y., A Study of Loading Path Influence on Fatigue Crack Growth under Combined Loading," Int J Fatigue. 2006;28(1):19-27.

[106] Socie, D.F., Hua, C.T., Worthem, D.W. Mixed mode small crack growth. Fatigue Fract. Eng. Mater. Struct. 1987: 10: 1 –16.

[107] Reddy, S.C., Fatemi, A., Small Crack Growth in Multiaxial Fatigue, in: Advances in Fatigue Lifetime Predictive Techniques, ASTM STP 1122. American Society for Testing and Materials, Philadelphia 1992; 276–298.

[108] Gates N, Fatemi A. Friction and roughness induced closure effects on shear-mode crack growth and branching mechanisms. Int J Fatigue 2016;92:442–58.

[109] Lee Y, Tjhung T, Jordan A. A life prediction model for welded joints under multiaxial variable amplitude loading histories. Int J Fatigue 2007;29:1162–73.

Chaper 2.

A New Path-Dependent Fatigue Damage Model for Non-Proportional Multi-Axial Loading

Abstract

This paper presents a new path-dependent multi-axial fatigue damage model which is formulated based on an incremental form of moment of load path (MLP) on either $\sigma - \sqrt{\beta}\tau$ stress plane or $\varepsilon - \sqrt{\beta^{\varepsilon}}\,\gamma$ strain plane. The resulting MLP-based fatigue damage parameter can be shown to be related to an integral form of strain energy densities contributed by normal and shear deformation and each weighted by a path-dependent function. Then, the MLP-based damage parameter in terms of either equivalent stress range or strain range, in conjunction with path-dependent maximum-range cycle counting procedure (Dong et al., 2010 and Wei and Dong, 2010), has been shown effective in correlating a large amount of test data obtained under non-proportional multi-axial loading conditions both for welded joints under stress-controlled conditions in high cycle fatigue regime and non-welded components under strain-controlled conditions in low-cycle regime.

Keywords: *Multi-axial fatigue, multi-axial cycle counting, non-proportional loading, fatigue damage modeling, welded joints*

2.1 Introduction

Engineering structures are often subjected to multi-axial cyclic stresses during service [1-3]. One common type of multi-axial stress state occurs where there is a sudden change of geometry such as at notches or welded joints, as a result of geometric constraints. Another source for multi-axial stress state is due to external multi-axial loading conditions leading to a stress state that is multi-axial in nature, such as that in a shaft component under both bending and torsion. The first type of multi-axial stress state is largely proportional, in which stress components vary proportionally with each other over time and the corresponding principal stress directions remain unchanged. Since the peaks and valleys of each stress component history occur at the same time for proportional loading, an effective stress range formulated using component stress ranges, e.g., in the form of von Mises stress range have been shown to be effective in fatigue damage modeling, as shown by [1,4-5]. Furthermore, conventional cycle counting methods such as Rainflow cycle counting can still be used by tracking a given time history of one of the stress components and scaling the rest. If stress components at a given material point vary independently or with a clearly defined phase shift angle in sinusoidal variation over time, non-proportionality effects on fatigue damage must be considered, as pointed out by numerous researchers, such as by Sonsino and Kueppers [6] and Yousefi et al. [7] for welded joints and Itoh et al. [8] on plain tube specimens, among others.

It has been observed that non-proportional loading induced fatigue damage depends upon both load path and material [5-15]. Various experimental studies [6-10] have shown that fatigue damage as a result of load-path non-proportionality can be more

significant in some materials and to a less degree or even showing a reduced damage in others [13-15]. To deal with the complexity of non-proportional multi-axial fatigue, two key questions must be addressed: (a) how to formulate an effective fatigue damage parameter that is capable of capturing both load path and material effects; (b) how to perform cycle counting against independent component stress histories. To a large extent, both questions are inter-related and must be addressed concurrently when dealing with general variable amplitude multi-axial stress histories.

2.1.1 Fatigue Damage Parameter

Within the confine of constant amplitude multi-axial loading conditions, such as sinusoidal stress histories of shear and normal stress components with a clearly defined phase shift between them, or some simple path patterns that are repeated during fatigue testing, various fatigue damage parameter definitions have been investigated by numerous researchers [6, 8-9, 16-18] in the literature. Among them, Dong and Hong [18] proposed a Modified Gough Ellipse model in which a fatigue damage parameter is analytically formulated as a function of phase angle (δ) shift between normal and shear stress histories, if both stress histories can be expressed as synchronous sinusoidal wave forms. A good correlation was achieved by examining both proportional and non-proportional test data [6-7, 19] obtained from welded joints. However, the Modified Gough Ellipse model is only applicable to constant amplitude non-proportional loading conditions with a clearly defined phase angle. Sonsino and Kueppers [6] showed that non-proportionality induced fatigue damage can be captured by an integral formulation of shear stress over all planes, referred as an Effective Equivalent Stress Hypothesis (EESH). Again, the proposed parameter in [6] can only be applied to constant amplitude sinusoidal

loading with a known phase angle between two stress components. Itoh et al. [8] proposed an equivalent non-proportional strain range definition based on principal strain range. A non-proportionality related parameter that takes into account of the rotation of the principal strain axis was used to formulate their fatigue damage parameter. Although a reasonable correlation of non-proportional low cycle fatigue data was demonstrated by Itoh et al. [8], it should be pointed out that their cycle definition for some of the load cases seems questionable, e.g., for similar type of "cross" load patterns, some cases being considered as two cycles while others as one cycle [8]. In addition, their material sensitivity parameter may only be applicable for low cycle fatigue applications.

Without directly addressing the need for a consistent cycle-counting procedure, one important category of non-proportional fatigue damage models is of critical plane type. Among various proposed critical plane models, Findely's stress-based model [20], Brown-Miller's strain-based model [21] and Fatemi-Socie's strain-stress-based model [17] are perhaps the most widely investigated ones. However, a common and non-trivial issue associated with these critical plane models is how to determine shear stress range, $\Delta\tau$ or shear strain range, $\Delta\gamma$ on a potential critical plane since both shear stress and shear strain change their magnitudes and directions along non-proportional load path. As a case in point, a closed irregular load Path $\widetilde{AB}$ (thick lines) shown in Fig. 2.1 represents non-proportional load path of shear stresses on one potential critical plane. It is not straightforward and an easy task to determine $\Delta\tau$ for load path $\widetilde{AB}$ in Fig. 2.1. Various approximate methods [22] such as Minimum Circumscribed Circle (MCC), Longest Chord (LC) and Longest Projection (LP) have been proposed. However, none of these methods could truly differentiate between a proportional path i.e., $\overline{AB}$ and the actual non-

proportional load path $\widetilde{AB}$ as illustrated in Fig. 2.1. For instance, consider non-proportional path $\widetilde{AB}$ in Fig. 2.1, MCC method involves finding a minimum circle that circumscribes the load path, which yields a radius (R) as the shear stress amplitude. However, as can be seen in Fig. 2.1, the use of the radius (R) for representing fatigue damage caused by the non-proportional load path $\widetilde{AB}$ ignores all non-proportional path excursions away from the straight line load path $\overline{AB}$. Li et al. [23] proposed a Minimum Circumscribed Ellipse (MCE), also shown in Fig. 2.1 for shear stress range calculation. Then, an equivalent shear stress amplitude is defined as the root mean square of the semi-major axis (denoted as a in Fig. 2.1) and semi-minor axis (denoted as b in Fig. 2.1). However, as shown by Skibicki [3], MCE has been demonstrated to be inadequate in differentiating various non-proportional load paths that share the same MCE. Therefore, an effective path-dependent fatigue damage parameter within the context of critical plane methods remains to be fully resolved.

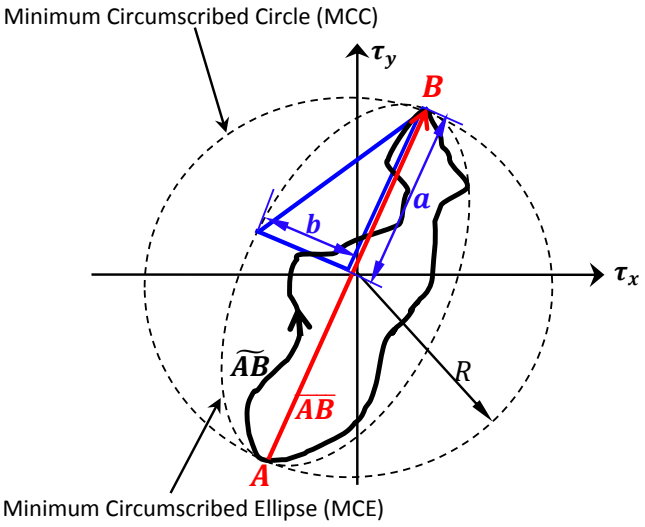

Fig. 2.1 MCC and MCE methods for calculating effective shear stress range $\Delta\tau$ in critical plane based multi-axial fatigue models

2.1.2 Fatigue Cycle Definition

Another fundamental question in the treatment of multi-axial fatigue damage in non-proportional variable amplitude loading is how to define a fatigue cycle. In the context of critical plane approach, Bannantine and Socie [24] proposed that component stress or strain histories can be classified as primary channel and auxiliary channel based on their dominance over fatigue damage and Rainflow cycle counting method can then be carried out only on the primary channel. Therefore, Bannantine and Socie's multi-axial cycle counting is essentially an uniaxial Rainflow cycle counting method applied to a pre-determined dominant stress or strain component out of multiple stress or strain components varying over time. One major issue of Bannantine and Socie's approach is that it is somewhat arbitrary and empirical in identifying one stress or strain component as the primary channel especially when several stress/strain components are operative. In directly dealing with multiple stress components and their time histories as a whole, Wang and Brown [16] outlined a more rational procedure for searching a maximum relative effective stress or strain range parameter and associated cycle definition that can be directly used for non-proportional variable amplitude loading histories. Their proposed relative effective stress or strain range parameters overcome the sign issue in using von Mises stress definition. However, it was demonstrated recently by Dong et al. [25] that Wang and Brown's multi-axial cycle counting procedure may fail to identify the maximum effective range available in non-proportional variable amplitude loading histories.

2.1.3 An Integrated Approach

In an attempt of addressing both damage parameter and cycle definition in an integrated manner for treating non-proportional variable amplitude multi-axial fatigue, Dong et al. [25] and Wei and Dong [26-27] recently developed a path-dependent cycle counting method referred to as Path-Dependent Maximum Range (PDMR) method that searches successively the maximum ranges available in a given multi-axial stress or strain histories mapped onto a stress ($\sigma - \sqrt{\beta}\tau$) plane or strain ($\varepsilon - \sqrt{\beta^{\varepsilon}}\gamma$) plane and counts their occurrences as half cycles. In the meantime, PDMR also tracks accumulative path length traversed within each counted half cycle. In their approach, path length accumulated in stress space or strain space in completing one half cycle was used directly as a fatigue damage parameter for correlating non-proportional multi-axial fatigue test data.

However, the use of accumulative path length as multiaxial fatigue damage parameter as given in Dong et al. [25], Wei and Dong [26-27], can be shown to have limitations in dealing with certain types of non-proportional loading conditions such as a few load cases studied by Itoh et al. [8]. For illustration purpose, consider three load path scenarios from P to Q in Fig. 2.2, in which Path A represents a semi-circular path with a radius of R; Path B is a series of semi-circular load paths with a radius $r = R/n$, where n is an integer and larger than unity, and Path C is a straight line, corresponding to a proportional load path. Based on PDMR method, all these three load path scenarios form their own one-half cycles from P to Q. In addition, it should be noted that Path A and Path B share the same accumulative path lengths, suggesting that fatigue damages for the two load cases should be the same if path length is adopted as a fatigue damage

parameter. However, it is not difficult to visualize that as n increases, fatigue damage corresponding to Path B should approach to that represented by Path C which is a proportional load path. Therefore, an improved fatigue damage parameter model is needed to address such a deficiency illustrated in Fig. 2.2.

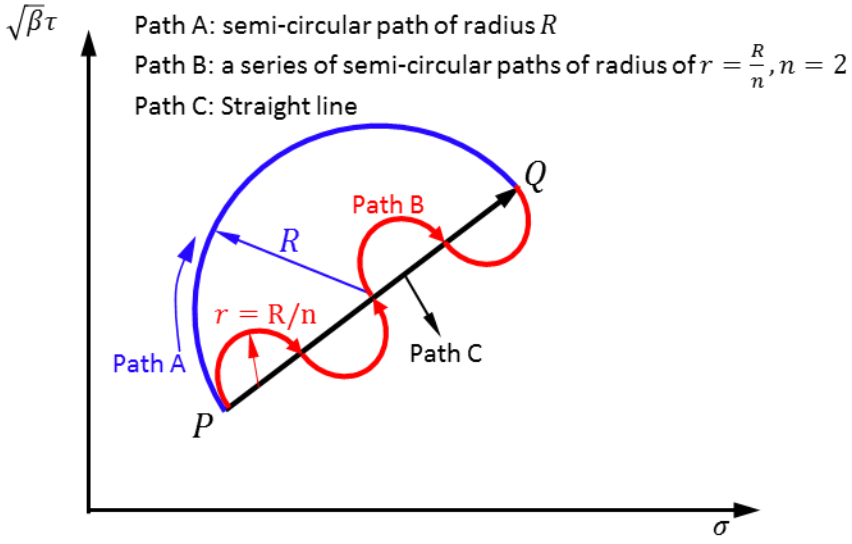

Fig. 2.2 Schematic illustration of one deficiency of path-length-based fatigue damage parameter for characterizing non-proportionality induced fatigue damage

With the above discussions as a starting point, this paper presents a new fatigue damage parameter based on an accumulative Moment of Load Path (MLP) concept, for which fatigue cycle definition remains the same as that determined by PDMR cycle counting method. The physical meaning underlying the newly proposed model can then be shown to be related to accumulative strain energy density contributed by normal and shear stresses, with each term being weighted by a path-dependent function. This new damage parameter can be consistently applied with respect to stress plane ($\sigma - \sqrt{\beta}\tau$ plane) or strain plane ($\varepsilon - \sqrt{\beta^{\varepsilon}}\,\gamma$ plane). Its validity in effectively correlating a

large amount of non-proportional multi-axial fatigue test data is then demonstrated with respect to $\sigma - \sqrt{\beta}\tau$ stress plane in high cycle regime and $\varepsilon - \sqrt{\beta^{\varepsilon}}\,\gamma$ strain plane in low cycle regime.

2.2 A Damage Model Based on Moment of Load Path

2.2.1 Hypothesis and Formulation

Consider a non-proportional load path from *A* to *B*, i.e., $\widetilde{AB}$, on $\sigma - \sqrt{\beta}\tau$ plane illustrated in Fig. 2.3, which can be shown to constitute one half cycle according to PDMR cycle counting procedure. We then postulate that multi-axial fatigue damage for any given non-proportional load path $\widetilde{AB}$ can be decomposed into two parts:

$$D = D_P + D_{NP} \tag{2.1}$$

in which D_P represents fatigue damage caused by the reference proportional loading event from *A* to *B* (i.e., $\overline{AB}$), which can be directly related to distance from *A* to *B*, or the effective stress range $\Delta\sigma_e$. D_{NP} represents load path non-proportionality induced fatigue damage due to any excursions of load path $\widetilde{AB}$ deviating from reference proportional load path ($\overline{AB}$). One intuitive and effective way of characterizing the extent of load path excursion away from its reference proportional load path is to consider the moment of non-proportional load path $\widetilde{AB}$ with respect of its reference path $\overline{AB}$. Therefore, the load path non-proportionality related damage along Path $\widetilde{AB}$ can be stated as follows, in an incremental form:

$$dD_{NP} = r'\left|sin\,(\theta)\right|ds' \tag{2.2}$$

as shown in Fig. 2.3 in $x' - y'$ local coordinate system in which dD_{NP} measures not only load-path non-proportionality, but also its extent of its deviation ($r'|sin(\theta)|$) from its reference proportional load path $\overline{AB}$. The total load path non-proportionality induced fatigue damage (D_{NP}) along Path $\widetilde{AB}$ then becomes, in an integral form:

$$D_{NP} = \int_{AB} r' \cdot |\sin(\theta)| ds' \tag{2.3}$$

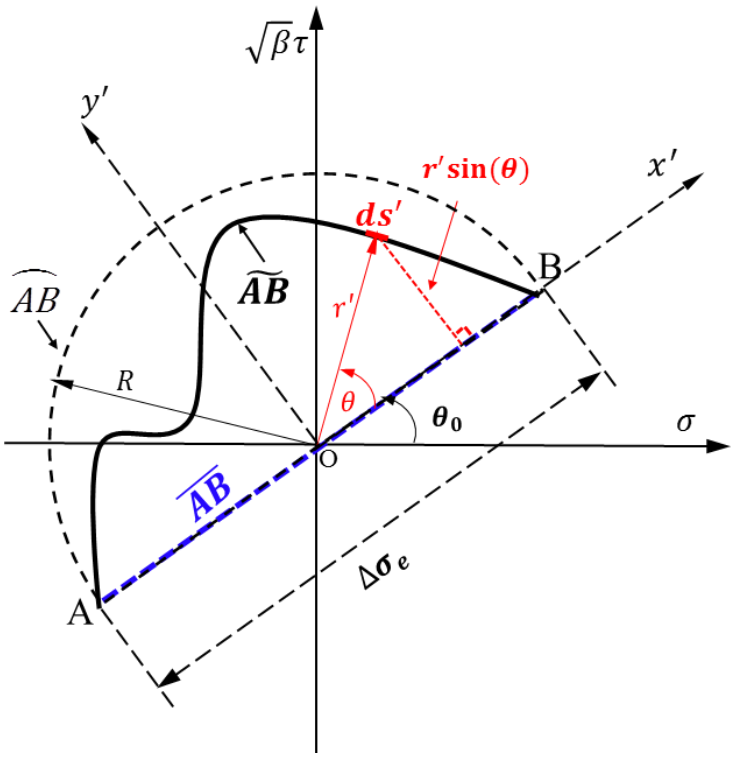

Fig. 2.3 Non-proportional load path $\widetilde{AB}$, non-proportional semi-circular load path $\overset{\frown}{AB}$ and reference (proportional) load path $\overline{AB}$

2.2.2 Dimensionless Representation

It is convenient to represent the damage parameters in Eq. (2.1) in a dimensionless form. To do so, it is natural to introduce a reference non-proportional load path AB that yields the maximum non-proportional damage within all possible non-

proportional paths with the same effective range $\Delta\sigma_e$ while satisfying one-half cycle definition according PDMR [25-27]. Such a non-proportional load path becomes the semi-circular load path AB represented by the dash line in Fig. 2.3, as supported by both existing test data and available multi-axial fatigue damage theories by various researchers [17, 28-29]. Along this line, a dimensionless formulation of load path non-proportionality induced damage can be expressed as follows:

$$g_{NP} = \frac{D_{NP}}{D_{Max}} = \frac{\int_{AB} r' \left|\sin(\theta)\right| ds'}{\int_{AB} R \left|\sin(\theta)\right| ds'} = \frac{\int_{AB} r' \left|\sin(\theta)\right| ds'}{2R^2} \tag{2.4}$$

where D_{Max} represents the maximum possible non-proportional fatigue damage induced by the semi-circular load path represented by dashed lines in Fig. 2.3. Then, g_{NP} in Eq. (2.4) can be referred as a normalized load path non-proportionality damage factor with respect to the maximum possible damage D_{Max}, noting that g_{NP} varies from zero corresponding to the proportional load path $\overline{AB}$ to unity corresponding to the semi-circular load path AB in Fig. 2.3.

As a result, Eq. (2.1) can be written in terms of effective stress range $\Delta\sigma_e$ corresponding to reference load path and normalized non-proportionality factor g_{NP} as:

$$\Delta\sigma_{NP} = \Delta\sigma_e(1 + \alpha \cdot g_{NP}) \tag{2.5}$$

The equivalent stress $\Delta\sigma_{NP}$ incorporating load-path non-proportionality induced fatigue damage effects along path $\widetilde{AB}$ can be referred to as a MLP-based equivalent stress range. Note a material-dependent non-proportionality sensitivity parameter α defined in

stress space is inserted into Eq. (2.5) to accommodate the fact that studies have shown that some materials are more sensitive to non-proportional multi-axial loading than others, depending on the ductility of materials examined [13-15,30].

It's worth mentioning that although it shares a similar form with that proposed by Itoh et al. [8], Eq. (2.5) differs from Itoh et al.'s model in two major aspects. Firstly, the dimensionless non-proportionality factor g_{NP} in Eq. (2.5) is calculated with respect to $\sigma - \sqrt{\beta}\tau$ stress plane while Itoh et al.'s non-proportional damage factor is defined with respect to a polar coordinate based maximum principal strain plane as a function of its direction (angle). Secondly, the non-proportionality factor g_{NP} in Eq. (2.5) is defined with respect to the reference semi-circular load path which corresponds to conditions yielding the maximum possible damage among all possible paths between any two positions forming one half cycle in $\sigma - \sqrt{\beta}\tau$ plane, while Itoh et al.'s damage factor is calculated with respect to the maximum principal strain within a loading event.

Eq. (2.5) can also be rephrased with respect to strain space, e.g., $\varepsilon - \sqrt{\beta^{\varepsilon}}\gamma$ plane, in which $\sqrt{\beta^{\varepsilon}}$ is a fatigue equivalency parameter between pure cyclic tensile strain and pure shear strain fatigue test results,

$$\Delta\varepsilon_{NP} = \Delta\varepsilon_e(1 + \alpha^{\varepsilon} \cdot g_{NP}^{\varepsilon}) \tag{2.6}$$

In Eq. (2.6), α^{ε} is a material-dependent non-proportionality sensitivity parameter defined in strain space and g_{NP}^{ε} is evaluated according to Eq. (2.4) on $\varepsilon - \sqrt{\beta^{\varepsilon}}\gamma$ plane.

2.2.3 Material Sensitivity Parameter Determination

Material sensitivity parameter α in stress space (or α^{ε} in strain space) can be determined by performing two types of simple multi-axial loading tests: one type is in-phase tests and the other simple out-of-phase tests with a circular load path, as illustrated in Fig. 2.4 (a). The resulting S-N test data can be plotted in Fig. 2.4 (b) in terms of effective stress range ($\Delta\sigma_e$) as defined in $\sigma - \sqrt{\beta}\tau$ plane shown in Fig. 2.4 (a). Two separate S-N curves can then be determined by curve fitting, i.e., (A) and (B) in Fig. 2.4 (b), which may or may not be parallel to each other. At a given reference fatigue life (N_{ref}), equating their respective MLP-based equivalent stress ranges (i.e., $\Delta\sigma_{NP}^{(A)} = \Delta\sigma_{NP}^{(B)}$) results in (see [31] for further details):

$$\alpha = \frac{\Delta\sigma_e^{(A)}}{\Delta\sigma_e^{(B)}} - 1 \tag{2.7}$$

It is important to point out here that the above procedure for determining α is not restricted to the case with a circular load path for which $g_{NP} = 1$, which is required by other non-proportional fatigue damage models available to date (e.g. Itoh et al. [8], Lee et al.[32]). The procedure presented here is also applicable for any elliptical load paths and Eq. (2.7) can be generalized as:

$$\alpha = \frac{\left(\frac{\Delta\sigma_e^{(A)}}{\Delta\sigma_e^{(B)}} - 1\right)}{g_{NP}} \tag{2.8}$$

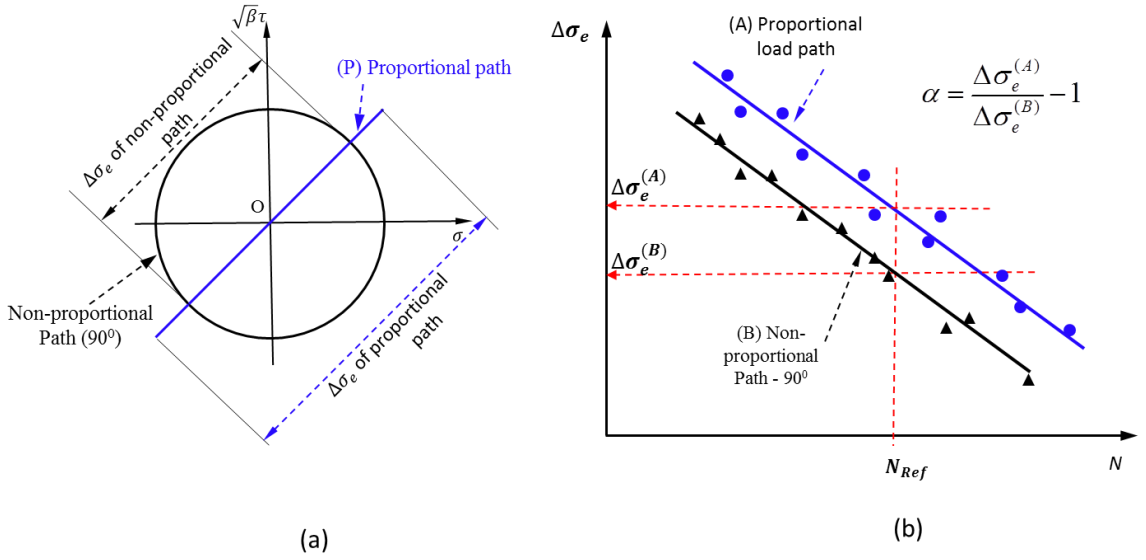

Fig. 2.4 Procedure for determining material sensitivity parameter α, (a) proportional and non-proportional circle load paths for fatigue testing; (b) Calculation of material sensitivity parameter α from S-N curves corresponding two load paths

When strain-based fatigue tests are considered, the corresponding material sensitivity parameter is defined as α^{ε} as given in Eq. (2.6) can be calculated in the same manner as demonstrated in Fig. 2.4, except it is now on $\varepsilon - \sqrt{\beta^{\varepsilon}}\,\gamma$ plane.

As illustrated by Fig. 2.4 (b) when $\Delta\sigma_e^{(A)} > \Delta\sigma_e^{(B)}$, $\alpha > 0$, material is considered as being more damaging to non-proportional loading. When $\Delta\sigma_e^{(A)} \leq \Delta\sigma_e^{(B)}$, $\alpha \leq 0$, the material is neutral to or even beneficial from the presence of non-proportional loading, as reported by Kueppers and Sonsino [13-14] on a series of tests of 6000 series of aluminum alloys. Further discussions on interpretation of test data as well as characterization of material sensitivity parameter for different series of aluminum alloys in terms of either α using stress-life data or α^{ε} using strain-life data are given in a separate paper [31]. In the present study on structural steel components and specimens, both α and α^{ε} are assumed

as being unity in order to focus our attention on examination of the effectiveness of non-proportionality factor g_{NP} formulated.

2.2.4 Physical Interpretation

For simplicity, consider the non-proportional load path $\widetilde{AB}$ in $\sigma - \sqrt{\beta}\tau$ plane shown in Fig. 2.3 with its origin being situated at mid-point of proportional load path $\overline{AB}$, i.e., assuming that any mean stress effects are negligible. With respect to $x' - y'$ local coordinate system in Fig. 2.3, the non-proportionality induced fatigue damage D_{NP} can be expressed as:

$$D_{NP} = \int_{AB} |y'| ds' = \int_{AB} |y'| \sqrt{(dx')^2 + (dy')^2} \tag{2.9}$$

Note that local coordinates could be expressed in terms of global coordinates as:

$$x' = x\cos(\theta_0) + y\sin(\theta_0) \tag{2.10}$$

$$y' = -x\sin(\theta_0) + y\cos(\theta_0) \tag{2.11}$$

Also note that

$$\sqrt{(dx')^2 + (dy')^2} = \sqrt{(dx)^2 + (dy)^2} \tag{2.12}$$

Then, the non-proportionality induced damage $D_{NP}$with respect to the global coordinate system can now be expressed as:

$$D_{NP} = \int_{AB} \left| -x\sin(\theta_0) + y\cos(\theta_0) \right| \sqrt{dx^2 + dy^2} \tag{2.13}$$

By replacing x by σ and y by $\sqrt{\beta}\tau$ and noting that $d\sigma = Ed\varepsilon$ and $d\tau = Gd\gamma$, where E (Young's modus), G (shear modulus) and υ (Poisson's ratio) are related in terms of $G = E/(2(1+\upsilon))$, the non-proportional damage D_{NP} can then be written as:

$$D_{NP} = E\int_{AB} \left| p(\sigma,\tau)\sigma d\varepsilon + q(\sigma,\tau)\tau d\gamma \right| \tag{2.14}$$

where

$$p(\sigma,\tau) = -sin\left(\theta_0\right)\sqrt{1+\beta\left(\frac{d\tau}{d\sigma}\right)^2} \tag{2.15}$$

$$q(\sigma,\tau) = \frac{1}{2(1+\upsilon)}\beta cos\left(\theta_0\right)\sqrt{1+\frac{1}{\beta}\left(\frac{d\sigma}{d\tau}\right)^2} \tag{2.16}$$

It can be seen from Eq. (2.15) and Eq. (2.16) that the weight function $p(\sigma,\tau)$ and $q(\sigma,\tau)$ in Eq. (2.14) are dimensionless. The integrand of Eq. (2.15) has a dimension of strain energy densities contributed by normal and shear stresses, with each being weighted by a path-dependent function, i.e., $p(\sigma,\tau)$ and $q(\sigma,\tau)$, respectively, over a given non-proportional load path ($\widetilde{AB}$) from A to B in Fig. 2.3.

Then, the dimensionless load path non-proportionality factor g_{NP} in Eq. (2.4) can be written as:

$$g_{NP} = \frac{D_{NP}}{D_{Max}} = \frac{\int_{AB} \left| p(\sigma,\tau)\sigma d\varepsilon + q(\sigma,\tau)\tau d\gamma \right|}{\int_{A'B'} \left| p'(\sigma,\tau)\sigma d\varepsilon + q'(\sigma,\tau)\tau d\gamma \right|} \tag{2.17}$$

where $p'(\sigma,\tau)$ and $q'(\sigma,\tau)$ are dimensionless weight functions of reference semi-circular load path (dashed semi-circle path in Fig. 2.3). It can be seen that non-proportionality factor g_{NP} can be interpreted as the ratio of weighted form of strain energy densities between an actual load path of interest and maximum damage reference load path.

For proportional loading case, we have $\widetilde{AB} = \overline{AB}$, $\sqrt{\beta}\tau = k\sigma$, where $k = \sin(\theta_0)/\cos(\theta_0)$. All terms in Eq. (2.14) cancel out, resulting in $D_{NP} = 0$, as it must be. As a case of demonstration, consider a uniaxial load path $\overline{AOB}$ along σ axis shown in Fig. 2.5, one can easily see from Eq. (2.15) that $p(\sigma,\tau) = 0$ and shear strain energy density term in Eq. (2.14) vanishes, resulting in:

$$D_{NP} = \int_{\overline{AOB}} 0 \cdot dx = 0 . \tag{2.18}$$

However, if semi-circular load path $\widetilde{ACB}$ shown Fig. 2.5 is considered, Eq. (2.14) becomes:

$$D_{NP} = G\int_{ACB}\left(\sqrt{\left(\frac{d\sigma}{d\tau}\right)^2+1}\right)\left|\tau d\gamma\right| = G\int_{ACB}\left(\frac{1}{\left|\cos(\theta)\right|}\right)\left|\tau d\gamma\right| = G\int_{ACB}\left|R^2 Sin(\theta)\right| d\theta \tag{2.19}$$

It can be seen that D_{NP} in Eq. (2.19) now depends on shear strain energy density $\tau d\gamma$ weighted by a dimensionless function that is now dependent on current position of load path increment ds and attains its maximum when $\theta = 90°$.

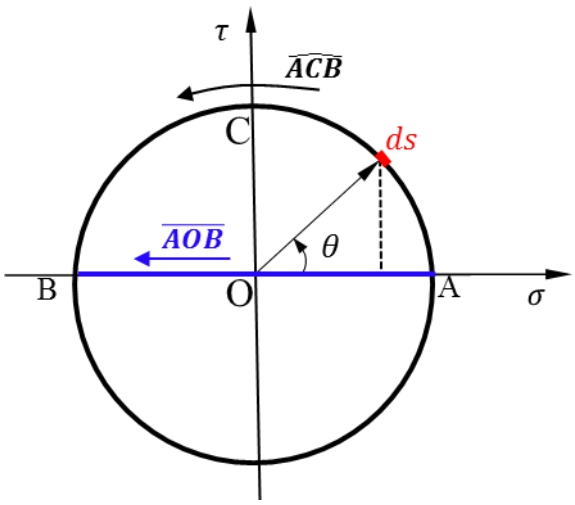

Fig. 2.5 Illustration of proportional load path $\overline{AOB}$ and semi-circular load path $\widehat{ACB}$ in terms of D_{NP} calculation

2.3 Analysis of Test Data

In this section, the MLP-based multi-axial fatigue damage parameter discussed in the previous section in combination with PDMR-based multi-axial cycle counting procedure will be used to demonstrate their effectiveness in correlating a large amount of well-documented test data in the literature. Two types of non-proportional multi-axial fatigue test data are considered here. The first type consists of test data on filet-welded tube-to-plate joints by Sonsino and Kueppers [6] using combined sinusoidal bending and torsion stresses with a phase shift in introducing non-proportionality effects and by Yousefi et al. [7] on a similar joint type by changing the frequency ratio between sinusoidal bending and torsion. The second type involves strain-based multi-axial test data [8, 9], in which un-welded thin-wall tubular specimens subjected to different non-proportional load path patterns, e.g., “diamond”, “cross”, and “staircase” etc. defined respect to strain plane.

2.3.1 Tube-to-Plate Fillet Weld Test Data

2.3.1.1 Tests by Sonsino and Kueppers

Sonsino and Kueppers [6] reported a series of test results of tube-to-plate fillet-welded joints made of StE460 steel under four sinusoidal loading conditions: pure bending, pure torsion, combined proportional bending and torsion (in-phase) and non-proportional (out-of-phase) bending and torsion with a phase shift angle of 90°. The test specimen and set up are shown in Fig. 2.6. Based on the nominal stresses given in [6], the load paths on nominal stress plane ($\sigma_n - \sqrt{\beta}\tau_n$ plane) are illustrated in Fig. 2.7 (a), in which the out-of-phase loading case forms a circular load path and $\beta = 3$. As demonstrated in [33-34], both nominal stresses and hot spot stresses are inadequate to differentiate the stress concentration effects on fatigue for this joint type, particularly when dealing with combined loading. Here, we directly adopt the stress concentration factor results calculated using a mesh-insensitive structural stress method [33-34] at weld toe, which are referred here as normal structural stress $\sigma_s = 1.7\sigma_n$ corresponding to applied nominal bending stress σ_n and in-plane shear structural stress $\tau_s = 1.1\tau_n$ corresponding applied nominal shear stress τ_n. As a result, the nominal stress based circular load path in Fig. 2.7 (a) becomes an elliptical load path on the structural stress plane ($\sigma_s - \sqrt{\beta}\tau_s$ plane) in Fig. 2.7 (b). Among the four paths used by Sonsino and Kueppers [6], only the elliptical path has non-zero non-proportionality factor g_{NP} according to Eq. (2.4), which can be analytically integrated as [31]:

$$g_{NP} = \frac{\eta}{2}\left(\eta + \frac{\arcsin(\sqrt{1-\eta^2})}{\sqrt{1-\eta^2}}\right) \tag{2.20}$$

where η is the ratio of minor axis over major axis of elliptical load path.

Then, Eq. (2.5) can be used to calculate MLP-based equivalent stress range $\Delta\sigma_{NP}$ for all load cases, noting that $\Delta\sigma_e$ being the maximum distance traversed in $\sigma_s - \sqrt{\beta}\tau_s$ plane. The results are shown in Fig. 2.8.

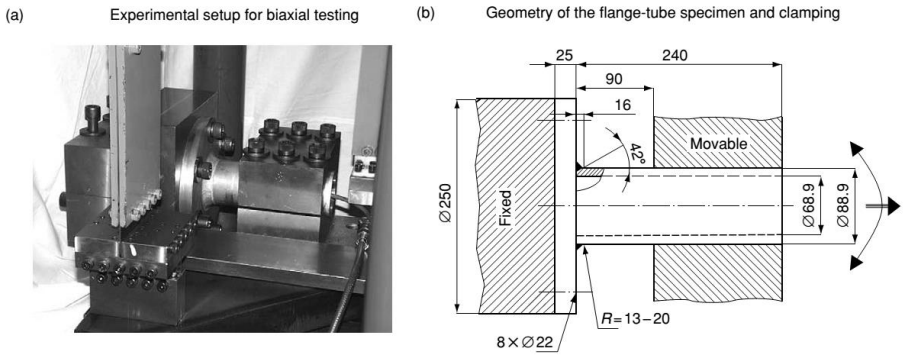

Fig. 2.6 Experimental setup (a) and specimen geometry (b) of Sonsino and Kueppers' test [6]

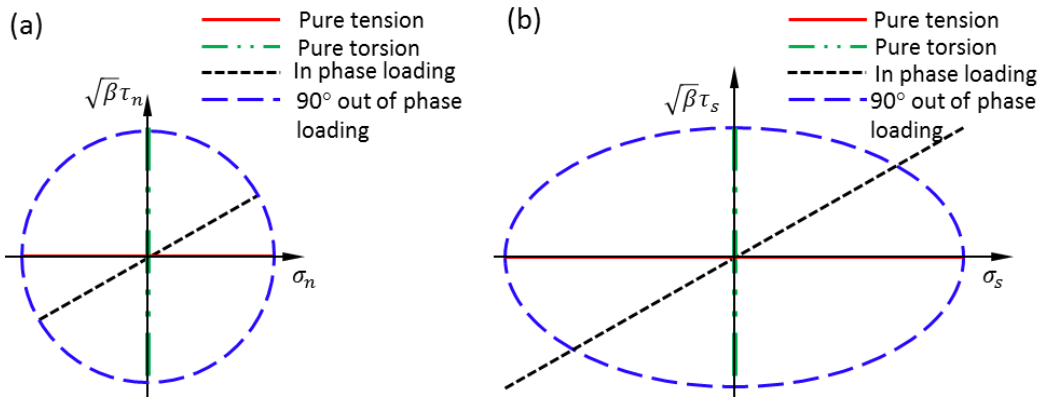

Fig. 2.7 Load paths used by Sonsino and Kueppers [6]: (a) Load paths on nominal stress based $\sigma_n - \sqrt{\beta}\tau_n$ plane; (b) load paths in structural stress based load path on $\sigma_s - \sqrt{\beta}\tau_s$ plane

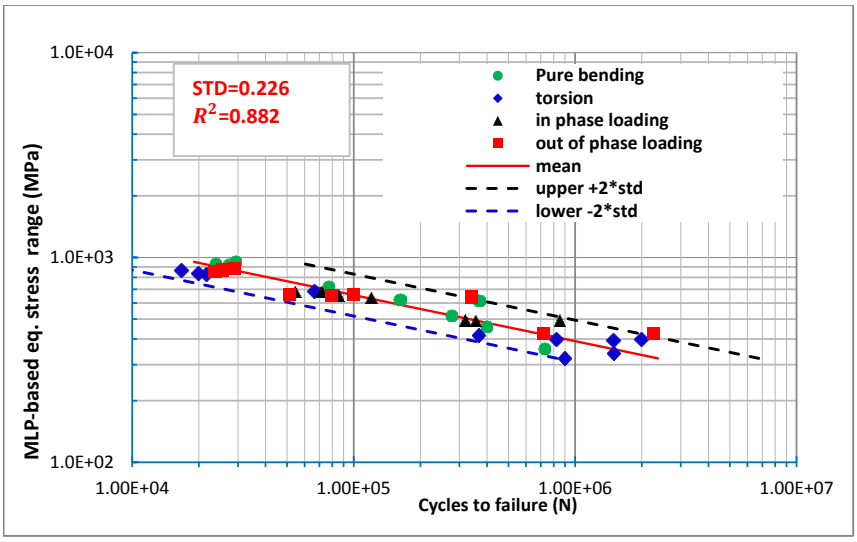

Fig. 2.8 Correlation of test data reported by Sonsino and Kueppers' test data [6] using MLP-based equivalent stress range

As shown in Fig. 2.8, the MLP-based equivalent stress range yields an excellent correlation of the test data with a standard deviation of 0.226, without relying on any other empirical parameters. It should be pointed out that Sonsino [4] and Sonsino and Kueppers [6] introduced an EESH approach which shows a correlation similar to Fig. 2.8. However, their EESH approach was based on notch stress calculated by assuming a fictitious weld toe notch radius of 0.45mm [6] and two other empirical parameters (one was related to size effects and the other as related stress gradient). As a result, the applicability of the EESH parameter may be limited. Such a limitation seemed to be confirmed by their own results [6] when applying the EESH parameter for correlating multi-axial fatigue test results between constant amplitude and variable-amplitude loading conditions, in which Palmgren-Miner's rule based damage parameter (D) had to be set as 0.35 (or $D = 0.35$). With a PDMR path length based equivalent stress parameter in conjunction with the structural stress definition, both the constant and variable

amplitude multi-axial test data fall into the same narrow band with $D = 1$, as presented in [25].

2.3.1.2 Tests by Yousefi et al.

Yousefi et al. [7] performed non-proportional multi-axial fatigue tests on fillet-welded tube-to-plate joints shown in Fig. 2.9. The most interesting aspect of these tests is that they examined asynchronous loading between sinusoidal bending and torsion with a frequency ratio of $f_b/f_t = 1/5$ and $f_b/f_t = 5$ where f_b represents the frequency of applied sinusoidal bending stress and f_t of applied sinusoidal torsional stress. Again, the nominal stresses used by Yousefi et al. [7] are converted into the mesh-insensitive structural stresses given by Dong et al. [33-35] as $\sigma_s = 1.73\sigma_n$ and $\tau_s = 1.1\tau_n$. The nominal bending and shear stress histories used by Yousefi et al. [7] can be then be represented in Fig. 2.10 in terms of normalized bending structural stress and shear structural stress, both of which are normalized by shear structural stress amplitude. With this normalization, PDMR-based cycle counting and MLP-based equivalent stress calculation can be performed with respect to the normalized load path. Then, MLP-based equivalent stresses under given load levels can be obtained by simply scaling the normalized MLP-based equivalent stresses by corresponding shear structural stress amplitude.

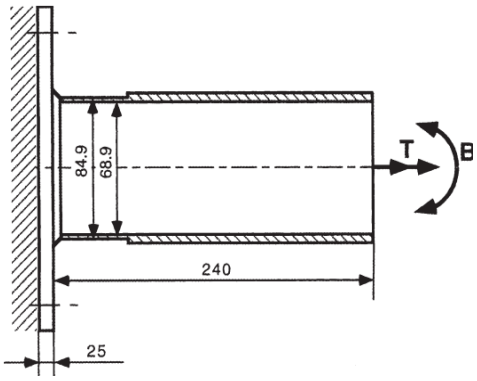

Fig. 2.9 Tube-to-plate joints tested by Yousefi et al. [7]

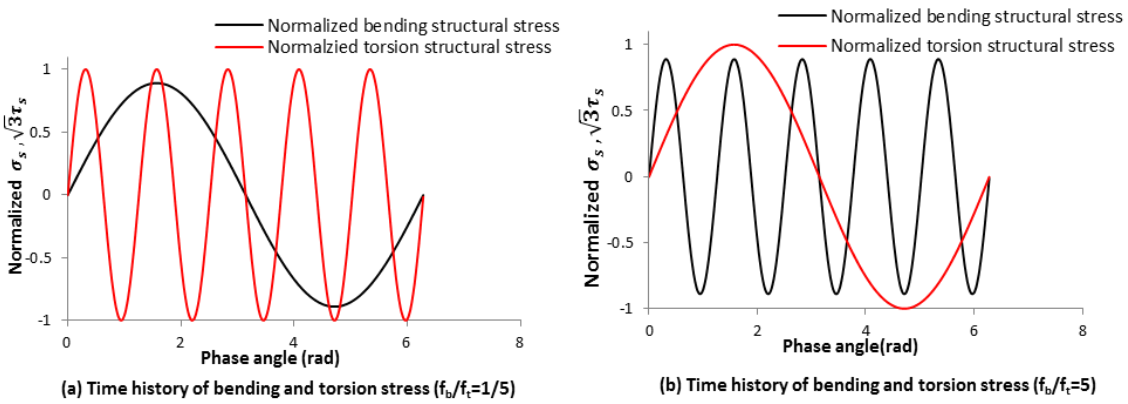

Fig. 2.10 Normalized asynchronous sinusoidal bending and torsion structural stress histories corresponding to test conditions used by Yousefi et al [7]: (a) bending/torsion ratio equals to 1/5 ($f_b/f_t = 1/5$); (b) bending/torsion ratio equals to 5 ($f_b/f_t = 5$)

It should be pointed out here that Yousefi et al. [7] did not address how to consistently define a fatigue cycle for these asynchronous load cases shown in Fig. 2.10. Instead, they presented their test data in S-N plots with N being defined as cycles accumulated by the stress component with a higher frequency [7]. As a result, the loading history block shown in Fig. 2.10 (a) and Fig. 2.10 (b) were considered as consisting of five fatigue cycles by Yousefi et al. [7].

In applying MPL-based approach for treating the load cases shown in Fig. 2.10, both cycle definition and non-proportional damage parameter calculation can be clearly illustrated by considering the load case in Fig. 2.10 (a). After mapping the normalized stress histories onto $\sigma_s - \sqrt{\beta}\tau_s$ plane in Fig. 2.11, the time history depicted in Fig. 2.10 (a) becomes the load path represented by the solid line starting from A to B and then back to A in Fig. 2.11. Consider the load path segment from A to B for PDMR cycle counting illustration purpose, the maximum stress range (AB) available is first identified by following load path segments indicated by dashed lines (i.e., $AC - CC^* - C^*E - EE^* - E^*B$) while monotonically increasing the distance measured with respect to starting position A. This constitutes the first half cycle. Note that CC^* and EE^* are referred to as virtual load paths [25-27]. Apply the same procedure for the remaining segmented load paths (i.e., $C - D - C^*$, $E - F - E^*$, etc.) so that all segmented load paths are all counted and counted only once. The final cycle counting results are summarized in Table 2.1. Then, normalized MLP-based equivalent stress range can be computed along load paths (including virtual load paths) corresponding to each cycle counted. This can be demonstrated by considering the half cycle giving the maximum effective stress range shown by dashed lines in Fig. 2.11 and re-plotted in Fig. 2.12 for clarity for illustration purpose. MLP-based fatigue damage parameter described in Eq. (2.5) can be readily calculated through numerical integration. Following the same procedure, MLP-based equivalent stress ranges for the remaining load path segments can be calculated, as summarized in Table 2.1. Since the values of MLP-based equivalent stress in Table 2.1 is normalized by shear structural stress amplitude, the true values of MLP-based equivalent

stress for different load amplitudes can be easily calculated scaling the normalized equivalent stress by the amplitude of shear structural stress.

Finally, for facilitating S-N based data plotting, each load block (e.g. solid line in Fig. 2.11, corresponding to time history block in Fig. 2.10 (a)) can be treated as one equivalent cycle with respect to which a Palmgren-Miner's rule based equivalent stress is calculated by linearly accumulating MLP-based equivalent stress ranges contributed by cycles counted within one load block (see [25]).

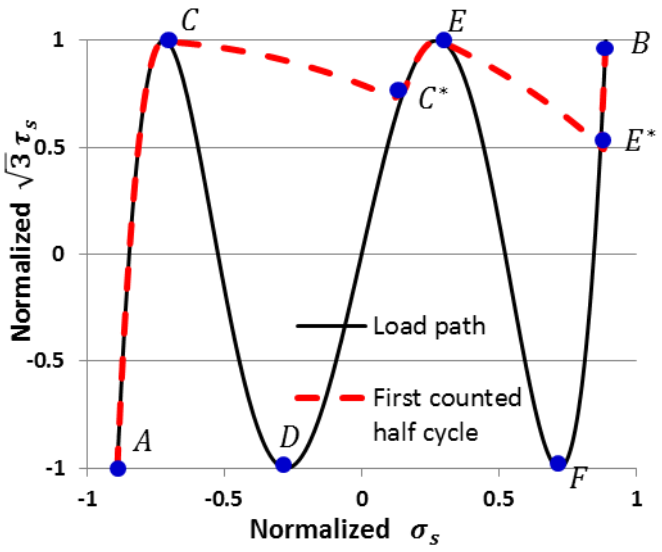

Fig. 2.11 Load path representation of Fig. 2.10 (a) on normalized $\sigma_s - \sqrt{3}\tau_s$ plane and illustration of PDMR based path determination (red dashed lines) for the 1st half cycle exhibiting the maximum stress range

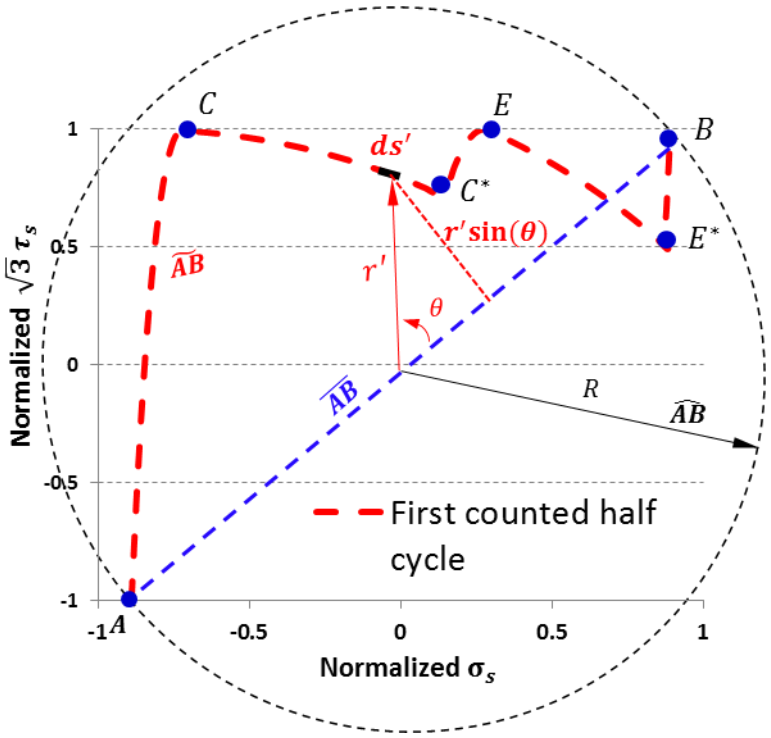

Fig. 2.12 Illustration of MLP-based non-proportional damage factor calculation for load path AC-CC*-C*E-EE*-E*B, determined by PMDR in Fig. 2.11

Table 2.1 PDMR counted cycles (N_i), effective stress ranges ($\Delta\sigma_{e,i}$), non-proportionality factor $g_{NP,i}$ and MLP-based equivalent stress ($\sigma_{NP,i}$) for asynchronous loading case with frequency ratio of $f_b/f_t = 1/5$

ID (i)	Counted cycles (N_i)	Effective stress range ($\Delta\sigma_{e,i}$)		Load path	Non-proportional factor($g_{NP,i}$)	MLP-based equivalent stress ($\Delta\sigma_{NP,i}$)
		Stress range	Range value			
1	1	AB	2.67	AC-CC*-C*E-EE*-E*B	0.66	4.4322
2	1	CD	2.04	CD	0.1	2.244
3	1	EF	2.03	EF	0.1	2.233
4	1	DC*	1.8	DC*	0.09	1.962
5	1	FE*	1.45	FE*	0.08	1.566

For comparison purpose, the test data from [7] are first plotted in log-log scale, as shown in Fig. 2.13, based on nominal stress range and the cycle definition used in [7]. As

expected, the scatter band is rather large, with a standard derivation of 0.45. When MLP-based equivalent stress is used in conjunction with PDMR-based cycle definition (as shown in Table 2.1), a significant improvement can be seen in Fig. 2.14, with a standard deviation of 0.314. It is worth noting that the two sets of data with different bending and torsional loading frequency ratios (i.e., $f_b/f_t = 1/5$ versus $f_b/f_t = 5$) are distributed closely around the mean line in Fig. 2.14.

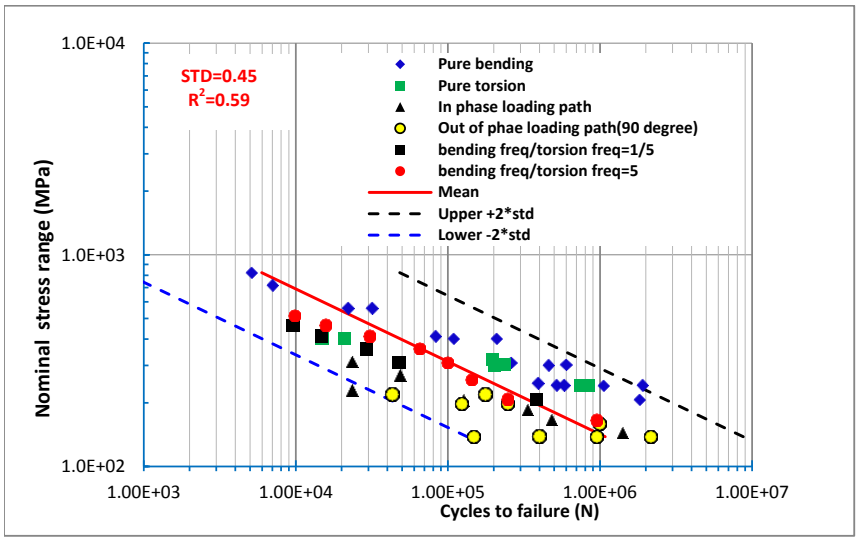

Fig. 2.13 Correlation of test data obtained by Yousfei et al. [7] by means of nominal stress range

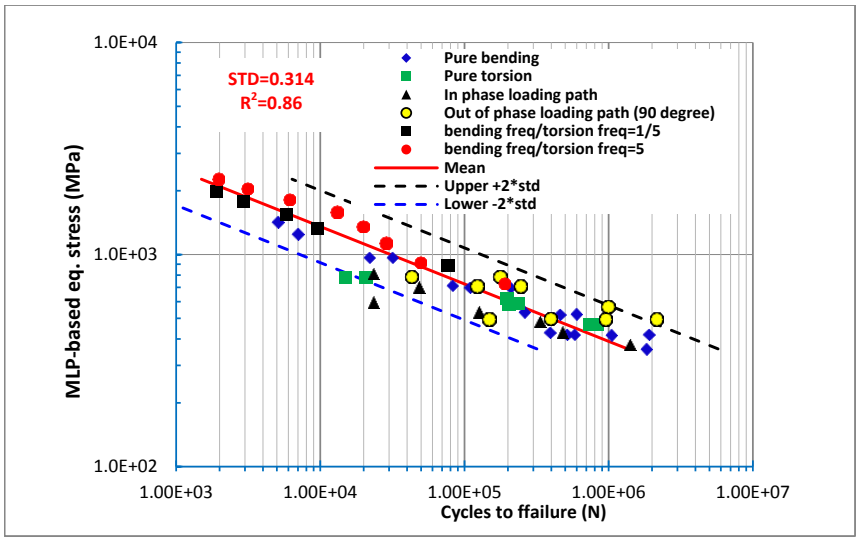

Fig. 2.14. Correlation of test data obtained by Yousfei et al. [7] by means of MLP-based equivalent stress

As a further demonstration of the generality of MLP-based equivalent stress parameter for correlating independent multi-axial fatigue test data from different authors, Fig. 2.15 combines the test data from Sonsino and Kueppers (Fig. 2.8) and those from Yousefi et al. (Fig. 2.14), showing that both sets of test data correlate reasonably well with each other, exhibiting essentially the same trend. This suggests that MLP-based fatigue damage parameter developed in this study offers data transferability, not only from proportional to non-proportional loading conditions, from synchronized to non-synchronized sinusoidal multi-axial loading conditions, but also from one joint geometry to another.

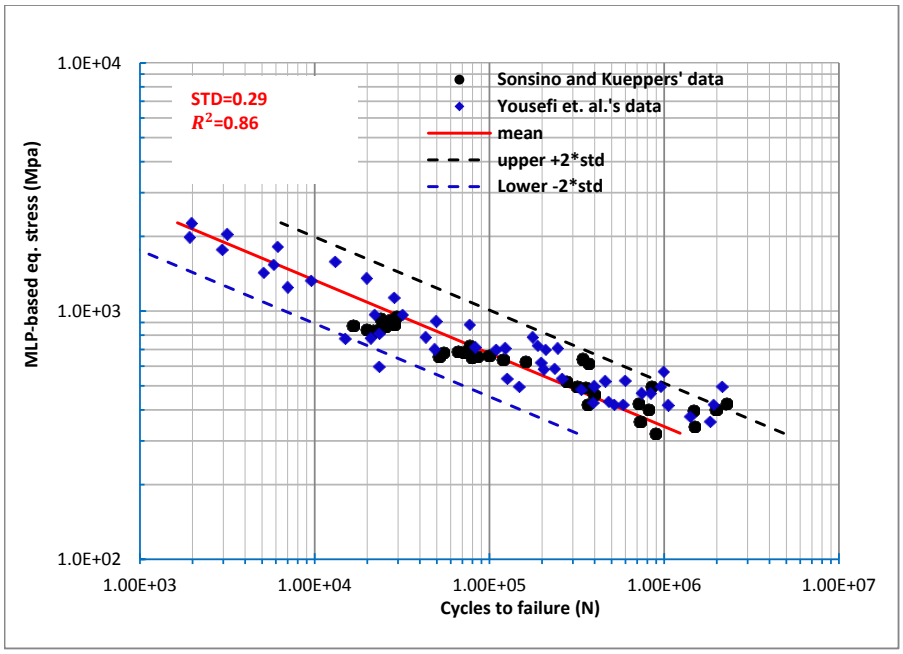

Fig. 2.15. MLP base equivalent stress for fatigue correlation of test data from both Yousefi et al. (see Fig. 2.14) and Sonsino and Kueppers (see Fig. 2.8)

2.3.2 Low Cycle Fatigue Data of Un-Welded Specimens

2.3.2.1 Tests by Itoh et al.

Strain-controlled multi-axial fatigue tests were carried out by Itoh et al. [8] on 304 stainless steel specimens (Fig. 2.16 (a)). Tubular specimens were subjected to a combined push-pull and reversed torsion, by following various strain paths given Fig. 2.16 (b). After demonstrating the inability of the equivalent stress method based on ASME Code (i.e., a relative von Mises strain range) [36] in effectively correlating their test data, Itoh et al. [8] proposed an equivalent non-proportional strain range parameter that incorporates effects of both maximum principal strain axis rotation and material cyclic strain-hardening response. Although showing an improved correlation for the same data (see Fig. 2.17), their material sensitivity parameter (to non-proportional loading)

determined from cyclic strain-hardening response may not be generally applicable. For instance, it is recently found that materials without exhibiting noticeable additional cyclic strain-hardening effect, such as Titanium alloy [37] and 1050 QT steel [38], non-proportional load path is still found to be much more damaging than proportional load path. Also note that when it comes to cycle counting, it is assumed by Itoh et al.'s that "one cycle is defined as a full straining for both axial and shear strain" which is not applicable for complex loading conditions such as Yousefi et al.'s asynchronous load cases [7].

In analyzing the same set of test data by MLP-based equivalent strain range according to Eq. (2.6), PDMR-based cycle counting are performed consistently for all cases except for Cases 0 and 5, for which no cycle counting is needed. For each identified one half cycle, MLP-based equivalent strain range is calculated by Eq. (2.6) (assuming $\alpha^{\varepsilon} = 1$) with respect to $\varepsilon - \sqrt{\beta^{\varepsilon}}\gamma$ plane given in Fig. 2.16(b) where $\beta^{\varepsilon} = 1/3$. Without relying on any material cyclic hardening related parameters, Fig. 2.18 shows the MLP-based correlation results for the same data shown in Fig. 2.17, clearly showing the effectiveness of the proposed fatigue damage parameter in addition to its simplicity, even though the two models give a rather similar correlation and standard deviation with ours being slightly better. It's worth mentioning that as already demonstrated in Sec. 3.1, the MLP model is equally effective in correlating stress-life multi-axial test data in high-cycle fatigue regime while Itoh et al.'s model has not been demonstrated in stress space for high cycle fatigue.

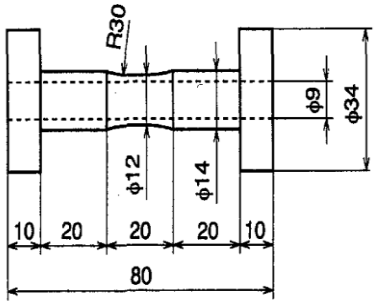

(a) Hollow cylinder specimen geometry

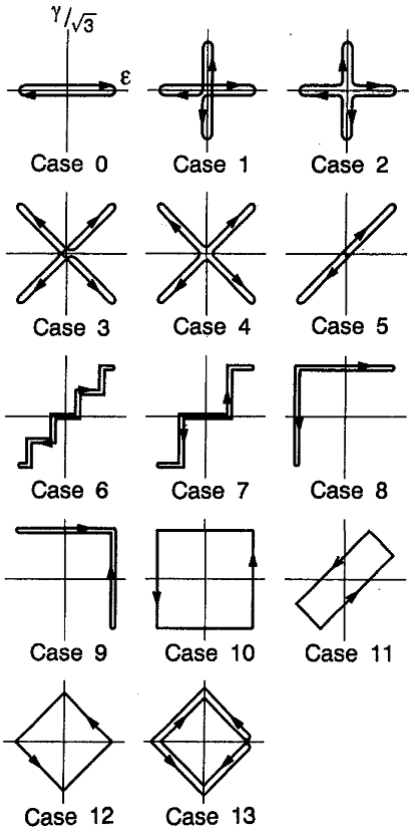

(b) strain-controlled load paths

Fig. 2.16 Strain-controlled multi-axial fatigue tests reported by Itoh et al. [8]: (a) thin tubular specimen geometry; (b) strain-controlled load paths

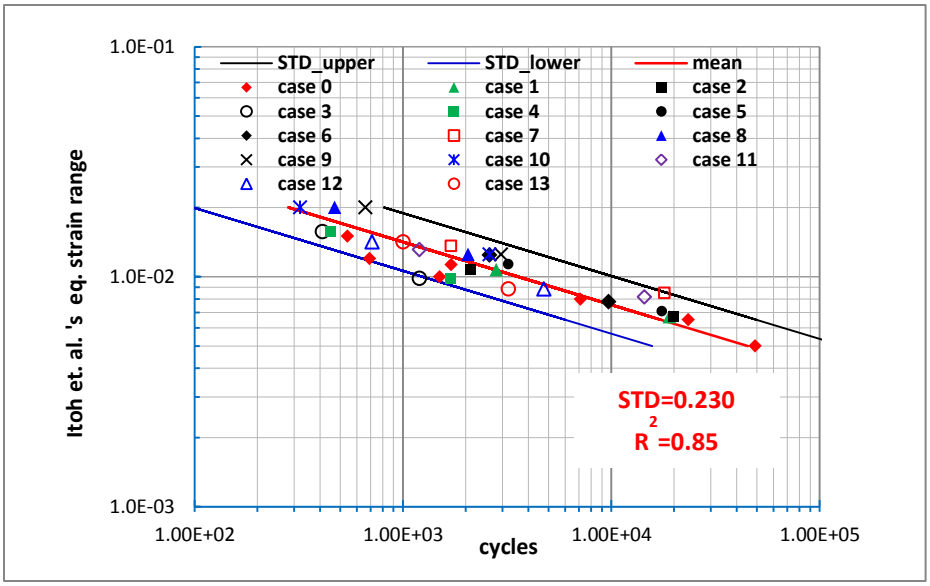

Fig. 2.17 Fatigue life correlation of test data [8] by Itoh et al.'s [8] model

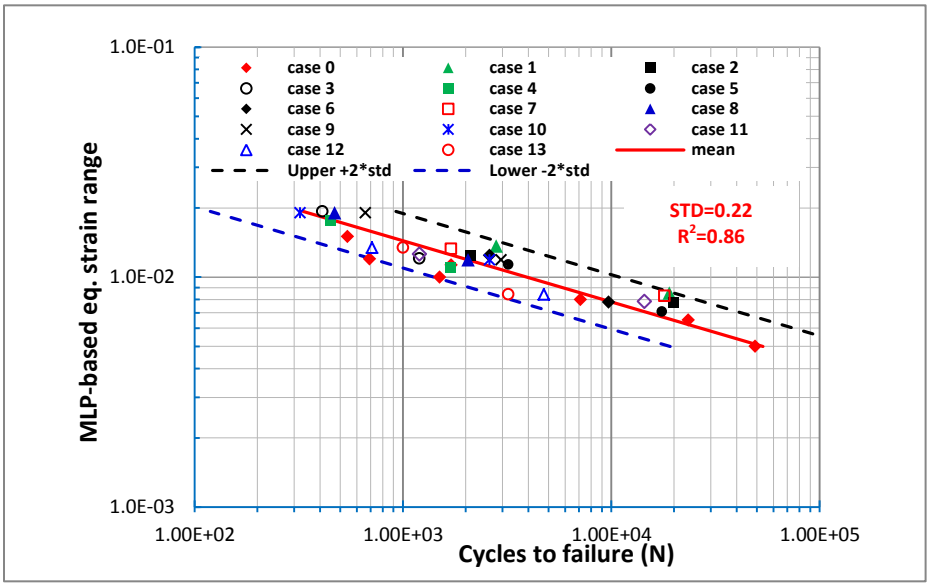

Fig. 2.18 Data correlation of test data [8] by MLP-based equivalent strain range

Of the fourteen load patterns shown in Fig. 2.16 (b), it is important to note that Cases 6-8 possess the same load-path length as well as the same effective strain range ($\Delta\sigma_e$) and constitute one full fatigue cycle according to Dong et al. [25], and Wei and

Dong [26-27]. As shown in Fig. 2.19, path-length based equivalent strain parameter fails to correlate the test data among the three load patterns (Cases 6-8). Once the MLP-based equivalent strain definition according Eq. (2.6) is used, the three sets of test results show an excellent correlation, as shown in Fig. 2.20, which is a replot of the same test data in Fig. 2.18 here for clarity. The corresponding load path non-proportionality factor g_{NP} for the three load patterns are also provided in Table 2.2 for a quantitative comparison purpose.

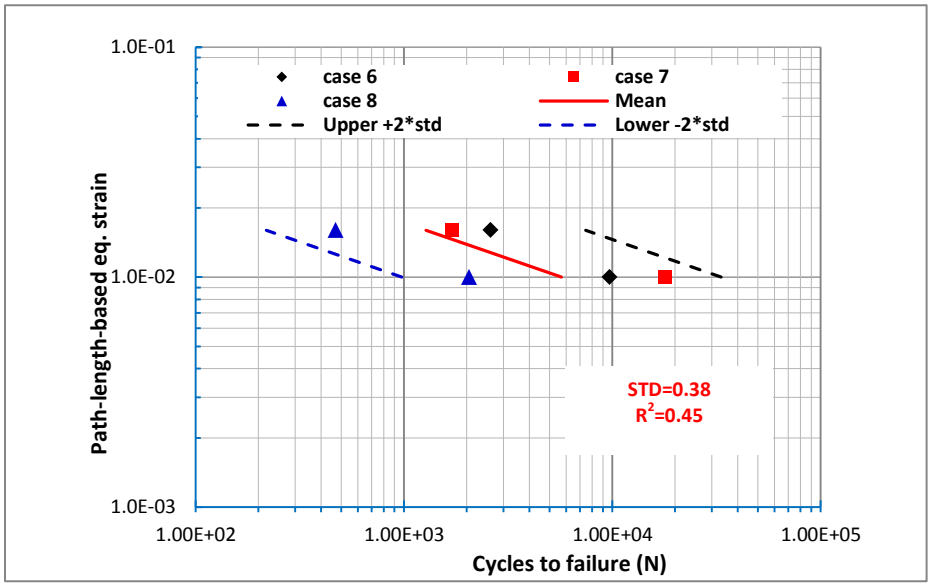

Fig. 2.19 Data correlation using path-length-based equivalent strain for load patterns Cases 6-8 shown in Fig. 2.16 (b).

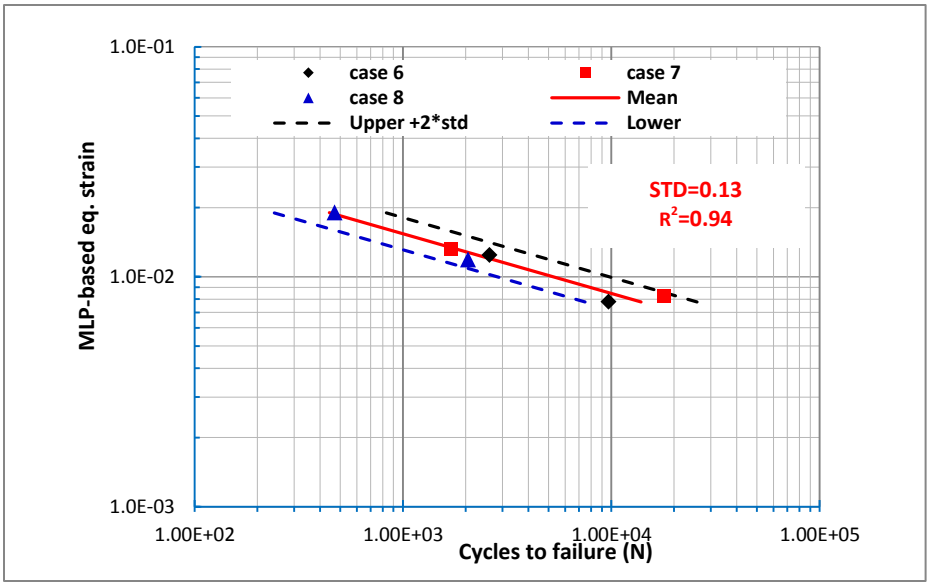

Fig. 2.20 Data correlation using MLP-based equivalent strain range for Cases 6-8 shown in Fig. 2.16 (b).

Table 2.2. Comparison of path-length and MLP-based non-proportionality factors

Load pattern [8]	Path-length based non-proportionality damage factor	MLP-based non-proportionality damage factor
Case 6	0.41	0.1
Case 7	0.41	0.17
Case 8	0.41	0.68

2.3.2.2 Tests by Socie

Socie [9] also reported both proportional and non-proportional fatigue test results on 304 stainless steel. Tubular specimens with an internal diameter of 25mm and a wall thickness of 3.8mm were subjected to strain-controlled load paths as illustrated in Fig. 2.21. Smith-Watson-Topper (SWT) critical plane model [39] was used for data analysis and the maximum principal strain plane was defined as the critical plane. With four

material parameters being determined in advance, a reasonably good correlation was demonstrated by Socie [9].

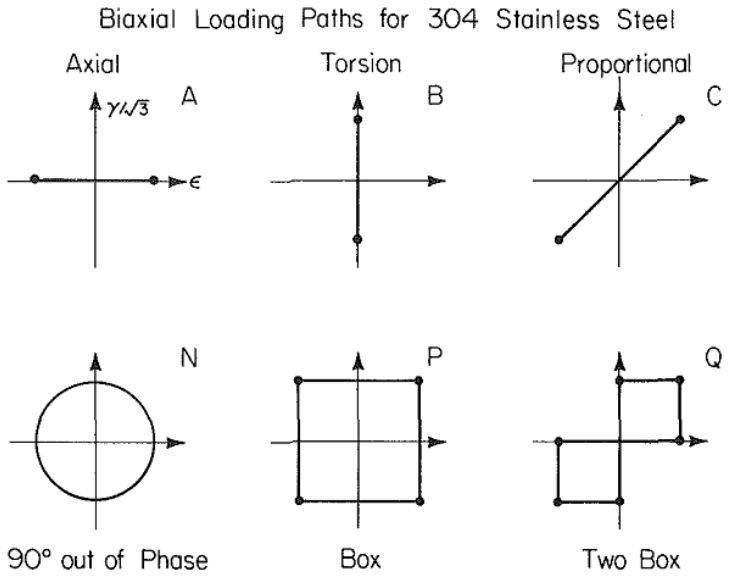

Fig. 2.21 Loading paths used by Socie [9] for 304 stainless steel test

To demonstrate the simplicity and effectiveness of the approach developed in this study, the same test data by Socie [9] are analyzed here using MLP-based equivalent strain parameter in the same way as was used for analyzing Itoh et al.'s test data discussed in the previous section. Without introducing any material related parameter in Eq. (2.6), i.e., setting $\alpha^{\varepsilon} = 1$, the results are shown in Fig. 2.22.

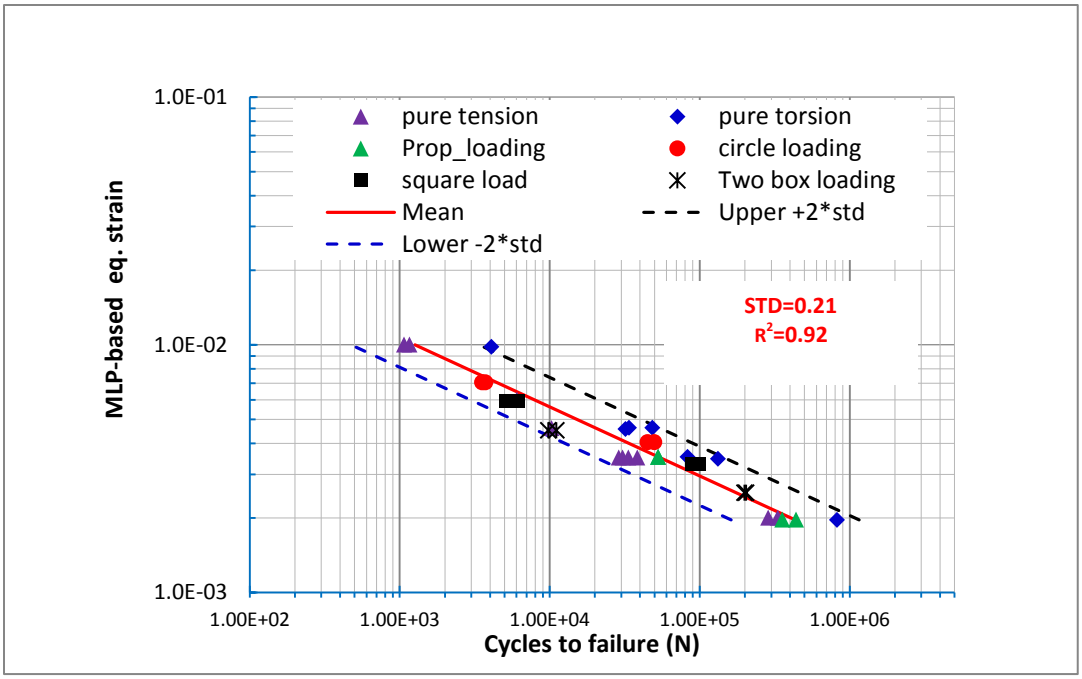

Fig. 2.22 MLP-based equivalent strain correlation of Socie's data [9]

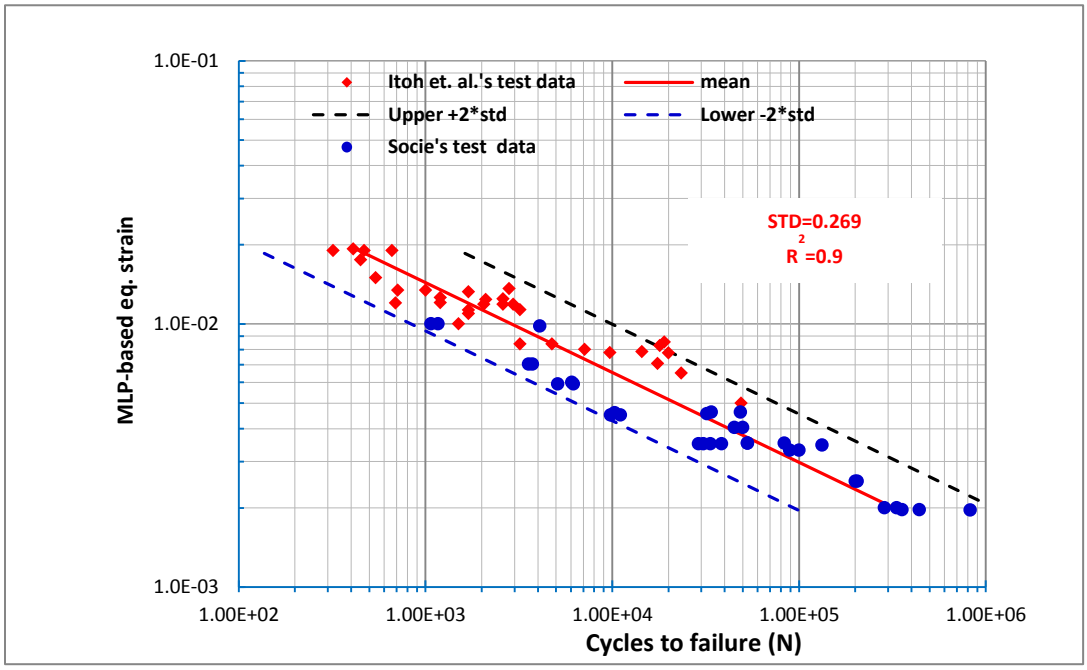

Fig. 2.23 MLP-based equivalent strain correlation of both test data from Itoh et al. [8] and Socie [9]

Furthermore, it should be interesting to compare the test data by Itoh et al. [8] and those by Socie [9] using MLP-based equivalent strain parameter. Fig. 2.23 shows the results, indicating a rather reasonable agreement between the test data from the two sources. Note that Itoh et al. [8] and Socie [9] used different methods and different material-related parameters. The present MLP-based approach as shown in Fig. 2.23, again, did not use any material-related parameter, i.e., $\alpha^{\varepsilon} = 1$ is assumed in Eq. (2.6). This should not be interpreted as suggesting that material behavior under multi-axial loading conditions is not important. Rather, the intent of such a comparison shown in Fig. 2.23 (as well as that shown in Fig. 2.15) is to highlight the reasonableness of the formulation of the MLP-based damage parameter. It suffices to say that if a best fit of material parameter α^{ε} is introduced here, a further improved correlation should be expected, which is not the focus on this study.

2.4 Conclusions

In this study, a new non-proportional fatigue damage parameter, referred to as MLP-based equivalent stress or strain parameter, is proposed and applied for correlating a large amount of multi-axial fatigue test data obtained using numerous load-path patterns in either stress-plane in high cycle fatigue regime or in strain-plane in low-cycle fatigue regime. Major findings can be stated as follows:

(1) The MLP-based fatigue damage parameter, in conjunction with PDMR-based cycle counting procedure, is effective in correlating a large amount of non-proportional multi-axial test data obtained from numerous authors with diverse load-path patterns.

(2) The MLP-based parameter can be shown to be related to an integral form of strain energy densities contributed by normal and shear deformation and each weighted by a path-dependent function, over a given non-proportional load path.

(3) The dimensionless non-proportionality damage factor (g_{NP}) can be readily calculated along a load-path or accumulated path segments corresponding each one-half cycle determined by PDMR cycle counting method.

(4) Once determined, the dimensionless non-proportionality damage factor (g_{NP}) can be used for calculating MLP-based equivalent stress or strain parameter for data correlation or fatigue life correlation purpose in stress-space or strain space under variable amplitude multi-axial fatigue loading conditions.

Acknowledgments

The authors acknowledge the support of this work through a grant from the National Research Foundation of Korea (NRF) Grant funded by the Korea government (MEST) through GCRC-SOP at University of Michigan under Project 2-1: Reliability and Strength Assessment of Core Parts and Material System. P. Dong acknowledges the financial support made possible by Traction Power National Key Laboratory Open Competition Grant (No. TPL 1605). The authors are also grateful to fruitful discussions with Dr. Zhigang Wei of Tenneco Automotive during the course of this investigation.

References

[1] Socie DF, Marquis G. Multiaxial fatigue. Warrendale, PA: Society of Automotive Engineers; 1999.

[2] Susmel L. Multiaxial Notch Fatigue. Elsevier; 2009.

[3] Skibicki D. Phenomena and computational models of non-proportional fatigue of materials. Springer; 2014.

[4] Sonsino C. Multiaxial fatigue of welded joints under in-phase and out-of-phase local strains and stresses. Int J Fatigue 1995;17:55–70.

[5] Fatemi A, Shamsaei N. Multiaxial fatigue: An overview and some approximation models for life estimation. Int J Fatigue 2011;33:948–958.

[6] Sonsino CM, Kueppers M. Multiaxial fatigue of welded joints under constant and variable amplitude loadings. Fatigue Fract Eng Mater Struct 2001;24:309–327.

[7] Yousefi F, Witt M, Zenner H. Fatigue strength of welded joints under multiaxial loading: experiments and calculations. Fatigue Fract Eng Mater Struct 2001;24:339–355.

[8] Itoh T, Sakane M, Ohnami M, Socie DF. Nonproportional low cycle fatigue criterion for type 304 stainless steel. J Eng Mater Technol 1995;117:285–292.

[9] Socie D. Multiaxial Fatigue Damage Models. J Eng Mater Technol 1987;109:293–298.

[10] Shamsaei N, Fatemi A, Socie DF. Multiaxial cyclic deformation and non-proportional hardening employing discriminating load paths. Int J Plast 2010;26:1680–701.

[11] Maddox SJ, Razmjoo GR. Interim fatigue design recommendations for fillet welded joints under complex loading. Fatigue Fract Eng Mater Struct 2001;24:329–337.

[12] Sonsino CM. Multiaxial fatigue assessment of welded joints - Recommendations for design codes. Int J Fatigue 2009;31:173–187.

[13] Kuppers M, Sonsino CM. Critical plane approach for the assessment of the fatigue behaviour of welded aluminum under multiaxial loading. Fatigue Fract Eng Mat Stru 2003;26:507–513.

[14] Kueppers M, Sonsino CM. Assessment of the fatigue behavior of welded aluminum joints under multi-axial spectrum loading by a critical plane approach. Int J Fatigue 2006;28:540–6.

[15] Sonsino CM. Influence of material's ductility and local deformation mode on multiaxial fatigue response. Int J Fatigue 2011;33:930–947.

[16] Wang CH, Brown MW. Life prediction techniques for variable amplitude multiaxial fatigue—Part 1: Theories 1996;118:367–370.

[17] Fatemi a, Socie DF. Critical plane approach to multiaxial fatigue damage including out-of-phase loading. Fatigue Fract Eng Mater Struct 1988;11:149–165.

[18] Dong P, Hong J, A Robust Structural Stress Parameter for Evaluation of Multiaxial Fatigue of Weldments. J ASTM Int 2006;3:100348.

[19] Siljander A, Kurath P, Lawrence F V. Nonproportional Fatigue of Welded Structures. ASTM STP 1992;1122:319–338.

[20] Findley WN. A theory for the effect of mean stress on fatigue of metals under combined torsion and axial load or bending. J Eng Ind 1959;81:301–306.

[21] Brown MW, Miller KJ. A theory for fatigue failure under multiaxial stress–strain conditions. Proc Inst Mech Eng 2006;187:745–755.

[22] Papadopoulos I. Critical plane approaches in high-cycle Fatigue: on the definition of the amplitude and mean value of the shear stress acting on the critical plane. Fatigue Fract Eng Mater Struct 1998;21:269–285.

[23] Li B, Reis L, de Freitas M. Comparative study of multiaxial fatigue damage models for ductile structural steels and brittle materials. Int J Fatigue 2009;31:1895–1906.

[24] Bannantine JA, Socie D. A variable amplitude multiaxial fatigue life prediction methods. ICBMFF3, 2013.

[25] Dong P, Wei Z, Hong JK. A path-dependent cycle counting method for variable-amplitude multi-axial loading. Int J Fatigue 2010;32:720–734.

[26] Wei Z, Dong P. A generalized cycle counting criterion for arbitrary multi-axial fatigue loading conditions. J Strain Anal Eng Des 2014;49:325–341.

[27] Wei Z, Dong P. Multiaxial fatigue life assessment of welded structures. Eng Fract Mech 2010;77:3011–3021.

[28] Kanazawa K, Miller KJ, Brown MW. Low-cycle fatigue under out-of-phase loading conditions. J Eng Mater Technol 1977;99:222–228.

[29] Pejkowski Ł, Skibicki D, Sempruch J. High cycle fatigue behavior of austenitic steel and pure copper under uniaxial, proportional and non-proportional loading. Stroj Vestn - J Mech Eng 2014;60:549–560.

[30] Itoh T, Nakata T, Sakane M, Ohnami M. Nonproportional low cycle fatigue of 6061 aluminum alloy under 14 strain paths. Eur Struct Integr Soc 1999;25:41–54.

[31] Mei J, Dong P. Modeling of non-proportional multi-axial fatigue damage in aluminum alloys. ASTM Selected Technical Papers. Submitted.

[32] Lee Y-L, Tjhung T, Jordan A. A life prediction model for welded joints under multiaxial variable amplitude loading histories. Int J Fatigue 2007;29:1162–73.

[33] Dong P. A structural stress definition and numerical implementation for fatigue analysis of welded joints. Int J Fatigue 2001;23:865–876.

[34] Dong, P. A robust structural stress method for fatigue analysis of offshore/marine structures

J. Offshore Mech. Arct. Eng 2005; 127(1): 68-74.

[35] Dong, P., and J. K. Hong. "The master SN curve approach to fatigue of piping and vessel welds." Welding in the World 48.1-2 (2004): 28-36.

[36] ASME Code, Case N-47-23 of ASME Boiler and Pressure Vessel Code, American Society of Mechanical Engineers, (1988)

[37] Shamsaei N, Gladskyi M, Panasovskyi K, Shukaev S, Fatemi A. Multiaxial fatigue of titanium including step loading and load path alteration and sequence effects. Int J Fatigue 2010;32:1862–1874.

[38] Shamsaei N, Fatemi A, Socie DF. Multiaxial fatigue evaluation using discriminating strain paths. Int J Fatigue 2011;33:597–609.

[39] Smith K, Topper TH, Watson P. A stress-strain function for the fatigue of metals(Stress-strain function for metal fatigue including mean stress effect). J Mat. 1970;5:767-778.

Chaper 3.

Modeling of Path-Dependent Multi-Axial Fatigue Damage in Aluminum Alloys

Abstract

This paper presents a comprehensive investigation into non-proportional loading induced multi-axial fatigue damage in wrought aluminum alloys using a recently developed multi-axial fatigue damage parameter. The moment of load path (MLP) based fatigue damage parameter is formulated in a form of an equivalent stress or strain range that measures both the extent of load-path deviation from proportionality within a fatigue cycle and material sensitivity to load-path non-proportionality. The use of such a fatigue damage parameter for correlating a large amount of test data is given in a recent publication by Mei and Dong (2016) for structural steels that are deemed very sensitive to non-proportional loading. This study examines another class of materials such as various types of wrought aluminum alloys (including 2000, 5000, 6000 and 7000 series) that are typically viewed as being less sensitive to non-proportional loading. A generalized procedure for extracting material sensitivity parameter from stress-life or strain-life test data under simple multi-axial loading conditions is first presented. After obtaining material sensitivity parameter for each of the wrought aluminum alloys examined in this study, It is found that material sensitivity parameter can be related to material ductility (in

terms of percentage of elongation from tensile tests) in an approximately linear manner in both low-cycle and high cycle regimes. An excellent agreement (mostly within a factor of 3) is achieved between model-estimated fatigue lives and test lives for all materials under various non-proportional multi-axial loading conditions considered in this study.

Keywords: *Multi-axial fatigue, wrought aluminum alloys, non-proportional loading, fatigue damage modeling, damage parameter, material sensitivity. cycle counting*

3.1 Introduction

Over the past few decades, there has been a great deal of experimental evidence [1-10] documenting that additional fatigue damage can be introduced under non-proportional multi-axial cyclic loading conditions, depending on both load paths and materials. Therefore, a fatigue damage model capable of both effectively capturing non-proportional load path in its driving force formulation and consistently representing material resistance to load-path non-proportionality in terms of a material sensitivity parameter has been sought after by researchers [1, 3, 11-14] in order to achieve reliable fatigue life estimation for engineering structures.

As for modeling of load-path non-proportionality in fatigue driving force formulation, past investigations include Kanazawa et al. [11] who proposed a shear plane based rotation factor (F) as a measure of load-path non-proportionality, which was defined as a ratio of shear strain range acting on a plane of 45° away from the maximum shear plane to the maximum shear strain range; Itoh et al.[1] introduced a normalized load-path non-proportionality factor (f_{NP}) for measuring the extent of rotation of the principal strain axis during one multi-axial loading event; Sonsino and Kueppers [3]

considered an integrated form of shear stresses over all planes corresponding to out-of-phase loading and defined its ratio over the value corresponding proportional loading as a non-proportionality factor. It should be pointed out that the model by Sonsino and Kueppers [3] is only applicable for non-proportional loading condition in which there exists a clearly defined phase angle.

When it comes to material sensitivity to non-proportional loading induced fatigue damage, most of researchers tend to attribute it to additional strain hardening resulted from non-proportional loading. Along this line, Doong et al. [12] pointed out there exist a significant difference in dislocation movements between proportional and non-proportional loadings in copper and stainless steel. The degree of non-proportional hardening was proposed to be measured by the difference in equivalent yield stresses between cyclic out-of-phase (90^0 degree) loading and cyclic in-phase loading conditions at a specified equivalent plastic strain amplitude. Following a similar concept, Itoh et al. [1] proposed material sensitivity parameter (α_I) to load-path non-proportionality in their multiaxial fatigue damage model, which can be determined by comparing cyclic stress-strain curves generated under non-proportional and proportional loading conditions, respectively. Recognizing that unsatisfactory data correlation may occur for some applications and difficulties may exist for variable amplitude loadings, Itoh and Yang [13] and Itoh et al. [14] later proposed an alternative method by using monotonic strain-hardening properties for determining material sensitivity to load-path non-proportionality.

However, the very assumption that load-path non-proportionality induced fatigue damage is solely related to material hardening behavior have been challenged by recent studies [6, 15-16] that have shown that materials with little or no strain hardening can still

exhibit a significant amount of fatigue life reduction under non-proportional loading conditions. Similar observations can be made when examining high cycle fatigue test data subjected to load-path non-proportionality, in which any plastic deformation can be considered insignificant or negligible while additional fatigue damage due to non-proportional loading is seen being as significant as that in low cycle regime. As a result, a more appropriate definition of material sensitivity parameter is required for modeling multi-axial fatigue damage resulted from non-proportional loading.

In order to construct an effective equivalent stress/strain based model for consistently capturing non-proportional multi-axial fatigue damage under general loading conditions, both loading-related non-proportionality and material-related parameters must be considered simultaneously and properly (see Mei and Dong [17]). In recognizing such a need, the authors have recently proposed a "moment of load path" (MLP) based multi-axial fatigue damage model which contains both a dimensionless load-path non-proportionality factor and a material sensitivity parameter. The path-dependent proportionality factor is determined with respect to the load path of one fatigue cycle defined by means of the path-dependent maximum range (PDMR) cycle counting method proposed by Dong et al. [18] and Wei and Dong [19-20], while the material sensitivity parameter to non-proportional loading can be determined by comparing two sets of fatigue test data, of which one is under in-phase multi-axial loading and the other is under out-of-phase. As shown in [17], this MLP-based model proves to be quite effective in correlating a large amount of multi-axial fatigue test data obtained from welded components made of structural steels and non-welded components of stainless steels in both low cycle and high cycle regimes.

It should be noted that when applying MLP-based model for analyzing structural steel and stainless steel test data [17], a material sensitivity parameter to load-path non-proportionality was assumed to be unity and it results in a good correlation of all test data analyzed. As mentioned earlier, there also exists another class of materials, such as some wrought aluminum alloys [21-23] which may exhibit less sensitivity to load-path non-proportionality. Therefore, the effectiveness of the MLP-based model remains to be demonstrated for applications in this class of materials. It is important to point out that the observations on material sensitivity made by above cited studies [21-23] are rather qualitative in nature without introducing a clearly defined effective stress or strain parameter in comparing test data between those under proportional and those under non-proportional loading conditions. In addition, there exist quite a few non-proportional multi-axial fatigue test data on non-welded tubular specimens made of 2000, 5000, 6000 and 7000 series of wrought aluminum alloys, as reported by other researchers [24-31]. These test data have not been analyzed for quantitatively establishing material sensitivity to non-proportional load paths due to the lack of an effective framework on which the data can be cross-compared.

As a sequel to the recently published paper [17] on a MLP-based model, the purpose of this paper is to demonstrate how this model can be effectively used for characterizing non-proportional loading effects on multi-axial fatigue damage in a wide range of wrought aluminum alloys. This includes the determination of material sensitivity to non-proportional loading in a consistent manner for different aluminum alloys in order for its usage in fatigue test data correlation. A particularly emphasis will be given to establishing a relationship between material sensitivity and material ductility (i.e.

elongation) for wrought aluminum alloys examined in this study. A comprehensive collection of non-proportional multi-axial fatigue test data on aluminum alloys [24-31] are considered here, which include 2000, 5000, 6000 and 7000 series of wrought aluminum alloys exhibiting a wide range of ductility.

3.2 Multi-Axial Fatigue Damage Parameter

3.2.1 Formulation

As presented in detail by the same authors in [17], consider a non-proportional load path (see Fig. 3.1) from A to B, i.e., $\widetilde{AB}$, on $\sigma - \sqrt{\beta}\tau$ plane where that $\sqrt{\beta}$ represents a fatigue equivalence parameter between S-N curves obtained by performing pure normal stress and pure shear stress cyclic testing [18-20]. The total multi-axial fatigue damage (D) for any given non-proportional load path $\widetilde{AB}$ is assumed to consist of two parts:

$$D = D_P + D_{NP} \tag{3.1}$$

in which D_P represents damage caused by the reference proportional loading event from A to B (i.e., $\overline{AB}$), which can be directly related to distance from A to B, or the effective stress range $\Delta\sigma_e$, and D_{NP} represents load path non-proportionality caused fatigue damage due to any excursions of load path $\widetilde{AB}$ deviating from the reference proportional path ($\overline{AB}$). Therefore, one assumed way of representing the load path non-proportionality related damage along Path $\widetilde{AB}$ can be stated as follows, with respect to local $x' - y'$ coordinate system, as:

$$D_{NP} = \int_{AB} r' \cdot \left|\sin(\theta)\right| ds' \tag{3.2}$$

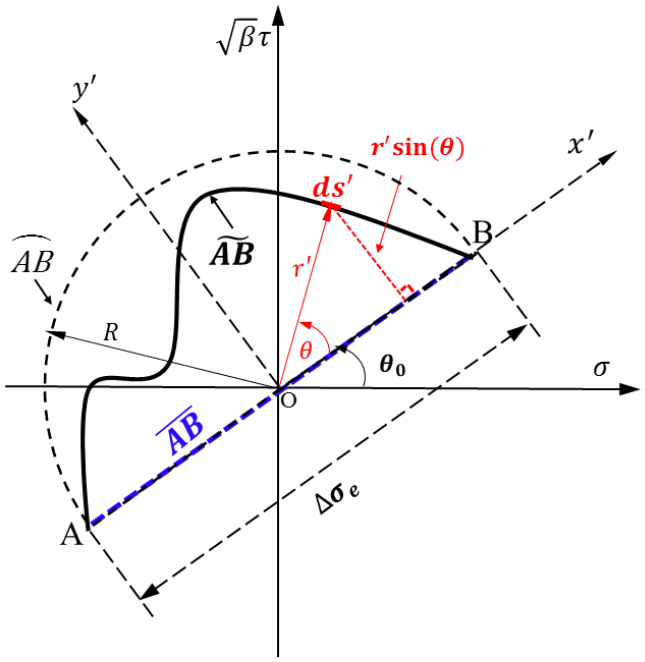

Fig. 3.1 Non-proportional load path $\widetilde{AB}$, non-proportional circular load path $_{AB}$ and reference (proportional) load path $\overline{AB}$

It can then be shown [17] that, a dimensionless form of load path non-proportionality induced damage parameter can be expressed as, with respect to the local $x' - y'$ coordinate system:

$$g_{NP} = \frac{D_{NP}}{D_{Max}} = \frac{\int_{AB} r' \left|\sin(\theta)\right| ds'}{\int_{AB} R \left|\sin(\theta)\right| ds'} = \frac{\int_{AB} r' \left|\sin(\theta)\right| ds'}{2R^2} \tag{3.3}$$

where D_{Max} represents the maximum possible non-proportional fatigue damage caused by the semi-circular load path denoted by dashed lines in Fig. 3.1. Then, g_{NP} in Eq. (3.3) can be referred as a normalized load-path non-proportionality damage factor with respect

to the maximum possible damage D_{Max}, noting that g_{NP} varies from zero (corresponding to the proportional load path $\overline{AB}$) to unity (corresponding to the semi-circular load path AB). Then, an equivalent stress range parameter (MLP-based equivalent stress range) taking into account of non-proportional load path induced damage can be written as:

$$\Delta\sigma_{NP} = \Delta\sigma_e(1 + \alpha \cdot g_{NP}) \tag{3.4}$$

Note that a material sensitivity parameter α is inserted in Eq. (3.4) to accommodate the fact that some materials are more sensitive to non-proportional multi-axial fatigue loading than others as observed in [21-23].

Eq. (3.4) can also be rephrased with respect to strain space for analyzing strain-life based multi-axial test data, e.g., $\varepsilon - \sqrt{\beta^{\varepsilon}}\gamma$ plane, in which β^{ε} is a fatigue equivalency parameter determined by comparing two $\varepsilon - N$ curves generated using pure normal strain ε and pure shear strain γ cyclic tests, respectively. Consistent with $\beta = 3$ in stress space, β^{ε}=$1/3$ has being shown to be valid for most multi-axial strain-life based test data correlation. Then, an equivalent strain range parameter (MLP-based equivalent strain range) incorporating non-proportional load-path induced damage can be written as:

$$\Delta\varepsilon_{NP} = \Delta\varepsilon_e(1 + \alpha^{\varepsilon} \cdot g_{NP}^{\varepsilon}) \tag{3.5}$$

In Eq. (3.5), $\Delta\varepsilon_e$ is effective strain range which can be directly related to distance between two points on $\varepsilon - \sqrt{\beta^{\varepsilon}}\gamma$ plane. α^{ε} is a material-dependent non-proportionality sensitivity parameter defined in terms of cyclic strain fatigue test results and g_{NP}^{ε} can be evaluated according to Eq. (3.3) on $\varepsilon - \sqrt{\beta^{\varepsilon}}\gamma$ plane.

3.2.2 Closed Form Solution of g_{NP} for Elliptical Load Paths

In performing laboratory multi-axial fatigue tests, it is common that both normal and shear components are represented in a sinusoidal wave form with a phase shift angle (δ), e.g.,

$$\begin{aligned} \sigma &= \sigma_0 \sin(\theta) \\ \tau &= \tau_0 \sin(\theta - \delta) \end{aligned} \tag{3.6}$$

which form an elliptical load path in $\sigma - \sqrt{\beta}\tau$ plane (see Fig. 3.2 as an illustration when $\delta \neq 0$), The semi-major axis (A) and semi-minor axis (B) of the elliptical load path can be expressed analytically as:

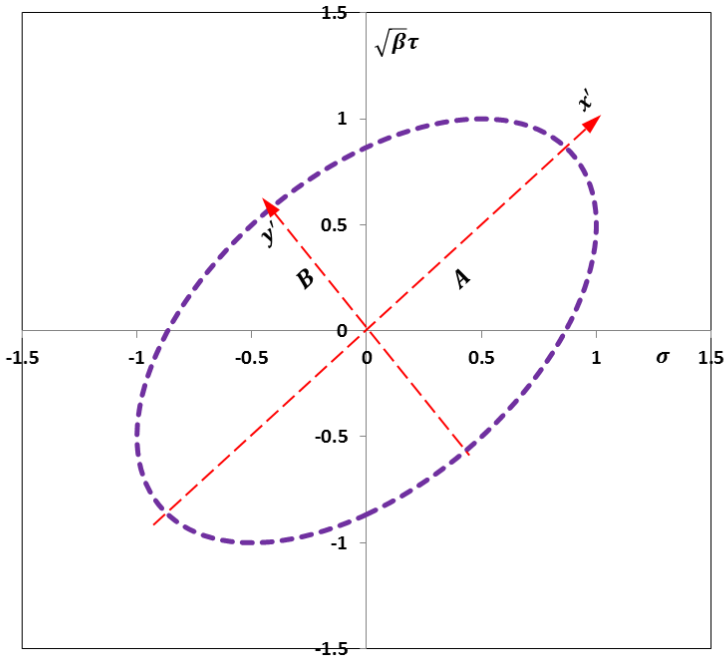

Fig.3.2 Illustration of an elliptical load path with its semi-major axis (A) and semi-minor axis (B) with respect to local coordinate system $x' - y'$

$$A=\sqrt{\frac{2\beta\sigma_0^2\tau_0^2\sin^2\delta}{\left(\sigma_0^2+\beta\tau_0^2\right)-\sqrt{\left(\sigma_0^2+\beta\tau_0^2\right)^2-4\beta\sigma_0^2\tau_0^2\sin^2\delta}}} \tag{3.7}$$

$$B=\sqrt{\frac{2\beta\sigma_0^2\tau_0^2\sin^2\delta}{\left(\sigma_0^2+\beta\tau_0^2\right)+\sqrt{\left(\sigma_0^2+\beta\tau_0^2\right)^2-4\beta\sigma_0^2\tau_0^2\sin^2\delta}}} \tag{3.8}$$

Then, by introducing a parametric representation of the ellipse in terms of $x' = Acos(\theta)$ and $y' = Bsin(\theta)$, it can be shown that the integration of non-proportional damage D_{NP} of Eq. (3.2) for the elliptical path will lead to:

$$D_{NP}=2AB\int_0^1\sqrt{1-e^2x^2}dx=AB\left(\sqrt{1-e^2}+\frac{\arcsin(e)}{e}\right) \tag{3.9}$$

where $e=\sqrt{(A^2-B^2)/A^2}$. Substituting Eq. (3.9) into Eq. (3.3) results in the non-proportionality factor of an elliptical load path as:

$$g_{NP}(\sigma_0,\tau_0,\delta)=\frac{\eta}{2}(\eta+\frac{\arcsin(\sqrt{1-\eta^2})}{\sqrt{1-\eta^2}}) \tag{3.10}$$

where,

$$\eta=\frac{B}{A}=\sqrt{\frac{\left(\sigma_0^2+\beta\tau_0^2\right)-\sqrt{\left(\sigma_0^2+\beta\tau_0^2\right)^2-4\beta\sigma_0^2\tau_0^2\sin^2\delta}}{\left(\sigma_0^2+\beta\tau_0^2\right)+\sqrt{\left(\sigma_0^2+\beta\tau_0^2\right)^2-4\beta\sigma_0^2\tau_0^2\sin^2\delta}}} \tag{3.11}$$

One important application of the closed form solution given in Eq. (3.10) is that it makes the determination of material sensitivity parameter α rather convenient once fatigue test data for proportional loading (represented by $\Delta\sigma_e$) and those for non-

proportional loading with a phase angle (δ) represented by $\Delta\sigma_{NP}$ become available, as discussed in the next section.

3.2.3 Determination of Material Sensitivity Parameter α

To determine the material sensitivity (a) to non-proportional loading, one only need to conduct two sets of relatively simple multi-axial fatigue tests: one is under in-phase (proportional) loading labeled as (P) and the other is under out-of-phase (e.g., with a phase angle of 90°) labeled as (Q), with the two respective load paths illustrated in Fig. 3.3(a). When their corresponding S-N test data are plotted as illustrated in Fig. 3.3(b) in terms of effective stress range ($\Delta\sigma_e$), two separate mean S-N curves can then be determined. Now consider a reference fatigue life (N_{ref}), the MLP-based equivalent stress range for both in-phase loading case (Case A) and 90° out-of-phase loading case (Case B) should be of the same values, each represented by $\Delta\sigma_{NP}^{(A)}$, and $\Delta\sigma_{NP}^{(B)}$ respectively. For the in-phase case (Case A), since $g_{NP}^{(A)} = 0$, $\Delta\sigma_{NP}^{(A)}$ can be written as, according to Eq. (3.4):

$$\Delta\sigma_{NP}^{(A)} = \Delta\sigma_e^{(A)}\left(1 + \alpha \cdot g_{NP}^{(A)}\right) = \Delta\sigma_e^{(A)} \tag{3.12}$$

For the out-of-phase case (Case B) for which $g_{NP}^{(B)} = 1$ by definition (see Eq. (3.3) as applied to the circular load path shown in Fig. 3.3(a)), $\Delta\sigma_{NP}^{(B)}$ is formulated as:

$$\Delta\sigma_{NP}^{(B)} = \Delta\sigma_e^{(B)}\left(1 + \alpha \cdot g_{NP}^{(B)}\right) = \Delta\sigma_e^{(B)}(1 + \alpha) \tag{3.13}$$

Since $\Delta\sigma_{NP}^{(A)}$ and $\Delta\sigma_{NP}^{(B)}$ correspond to the same fatigue life (N_{ref}), it follows that $\Delta\sigma_{NP}^{(A)} = \Delta\sigma_{NP}^{(B)}$. By equating Eq. (3.12) with Eq. (3.13), α can then be expressed as:

$$\alpha = \frac{\Delta\sigma_e^{(A)}}{\Delta\sigma_e^{(B)}} - 1 \tag{3.14}$$

As can be seen, when $\Delta\sigma_e^{(A)} > \Delta\sigma_e^{(B)}$, $\alpha > 0$, material is considered as being sensitive and more damaging to non-proportional loading compared with proportionally loaded; when $\alpha < 0$, material is sensitive but less damaging to non-proportional loading; When $\alpha = 0$, material is neutral to the presence of non-proportional loading.

It is important to point out here that the above procedure for determining α is not restricted to the availability of test data obtained using a circular load path for which $g_{NP} = 1$. The procedure presented here is also applicable for any elliptical load paths for which, Eq. (3.14) can be generalized as:

$$\alpha = \frac{\left(\frac{\Delta\sigma_e^{(A)}}{\Delta\sigma_e^{(B)}} - 1\right)}{g_{NP}} \tag{3.15}$$

in which g_{NP} is determined through Eq. (3.10) for given σ_0, τ_0 , and δ.

For strain-life based multi-axial data correlation, the corresponding material sensitivity parameter α^{ε} given in Eq. (3.5) can be determined in exactly the same manner, but with respect to $\varepsilon - \sqrt{\beta^{\varepsilon}}\,\gamma$ plane. It is tempting to seek a direct relationship between α and α^{ε} so that once one is determined, e.g., α in stress space, can be used to infer the other (i.e. α^{ε} in strain space (α^{ε}) or vice versa. Such a relationship would require considerations of material cyclic constitutive relationship under non-proportional loading conditions in both high cycle and low cycle regime, which is a subject of on-going study by the authors.

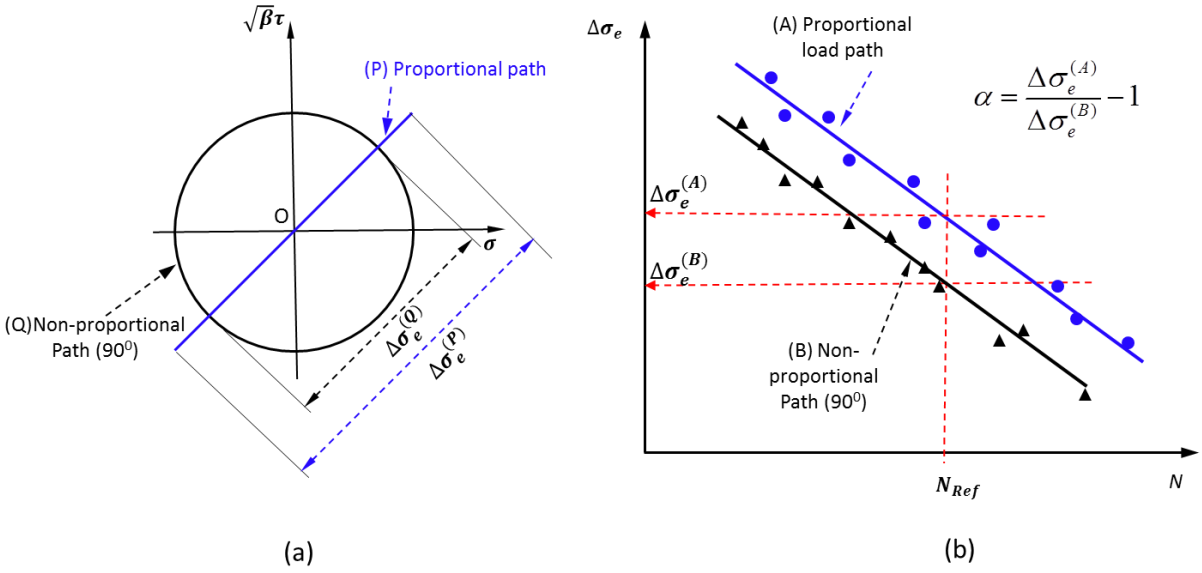

Fig. 3.3. Procedure for determining material sensitivity parameter α, (a) proportional and non-proportional circular load paths for fatigue testing; (b) Calculation of material sensitivity parameter α with respect to reference fatigue life N_{ref}

3.3 Analysis of Fatigue Test Data

3.3.1 Determination of α or α^{ε}

A total of seven groups [24-31] of multi-axial (including both proportional and non-proportional) test data obtained from four types of wrought aluminum alloys are considered here, which are designated as 2000, 5000, 6000 and 7000 series. As an illustration for applying the procedure described in Sec. 2.3, Fig. 3.4 is a plot of strain-life curves for hollow tube specimen (see Fig. 3.5) test results obtained from aluminum alloy 7075-T6 [24-25] in terms of effective strain range versus cycles to failure, in which the effective strain range is the distance on $\varepsilon - \sqrt{\beta^{\varepsilon}}\gamma$ plane, where $\beta^{\varepsilon} = 1/3$, as discussed in Sec. 2. The two sets of test data can then be represented by the two mean lines, respectively, through a simple curve fitting. Since the two lines have slightly different

slopes, a mid-range life, i.e., $N_{ref} = 100$ in this case is chosen here for determining α^{ε} which will be used for analyzing test data obtained under more complex non-proportional load paths. Substituting $\varepsilon_e^{(A)}$ and $\varepsilon_e^{(B)}$ into exactly the same form of Eq. (3.15) but in terms of strain, α^{ε} is found to be 0.35 (i.e. $\alpha^{\varepsilon} = 0.35$).

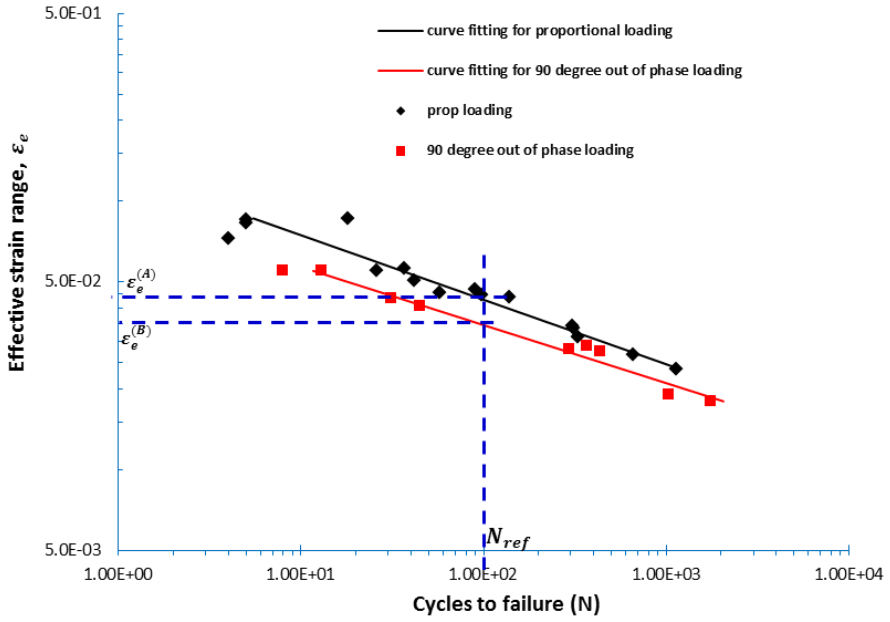

Fig.3.4 Determination of α^{ε} using proportional and non-proportional (phase angle of 90^0) test data - aluminum alloy 7075-T6

Following the same procedure, α^{ε} for another independent set of 7075-T651 multi-axial fatigue tests data [26] using tubular specimens is also calculated as $\alpha^{\varepsilon} = 0.35$. Table 3.1 summarizes material sensitivity parameters α (for load-controlled tests) or α^{ε} (for strain-controlled tests) calculated by comparing simple proportional and non-proportional (circle load path) multi-axial fatigue test results for all the seven groups of wrought aluminum alloys except for Itoh et al.'s test data [27] in which pure torsion test data is compared with out-of-phase data since only a few in-phase data points are

available. Also listed in Table. 3.1 is material ductility in terms of elongation for each group of aluminum alloys examined. By observing the material sensitivity parameters (α or α^{ε}) and elongation of all aluminum alloys listed in Table. 3.1, the following interesting observations can be made:

(a) Material sensitivity parameter α determined from stress-life data or α^{ε} determined from strain-life data seem to have a similar value, such as shown for 2000 and 7000 series alloys.

(b) For each type of aluminum alloy, there exists a reasonable degree of consistency in α or α^{ε} values determined from tests conducted independently by different researchers, suggesting that α or α^{ε} indeed can be interpreted as a material constant.

(c) For the four types of aluminum alloys investigated, the values of α and α^{ε} are found to be in the range of 0.35-0.55, much less than those found for structural steels and steel weldment tests, which were treated as unity (i.e. $\alpha = \alpha^{\varepsilon} = 1$) in [17].

(d) For aluminum alloys showing a relatively higher ductility, such as 2000 series aluminum alloys in Table 3.1, they tend to possess a higher α or α^{ε} value, indicating more sensitivity to non-proportional loading than those with a smaller value of ductility (e.g., 7000 series). Such a trend that seems consistent for all types of aluminum alloys examined here will be further discussed in a later section.

Table 3.1. Summary of material sensitivity parameters α or α^{ε} determined for different groups of wrought aluminum alloys

Series of Aluminum	Aluminum alloys	Loading types	Ductility (Elongation, %)	α or α^{ε}
7000 series alloys	7075-T651 [24-25]	Strain controlled	9.7	α^{ε}=0.35
	7075-T6 [26]	Strain controlled	11	α^{ε}=0.35
6000 series alloys	6061-T6 [27]	Strain controlled	12	α^{ε}=0.4
	6082-T6 [28]	Load controlled	8	α=0.35
5000 series alloys	5083 [29]	Strain controlled	20	α^{ε}=0.48
2000 series alloys	2024-T4 [30]	Load controlled	18	α=0.5
	2024-T4 [31]	Strain controlled	20	α^{ε}=0.5

The validity of the material sensitivity parameters in term of either α or α^{ε} summarized in Table 3.1 will be further substantiated by its effectiveness in correlating the corresponding multi-axial fatigue test data obtained under various forms of non-proportional load paths in the form of MLP-based model in the next section.

3.3.2 MLP-Based Correlation of Multi-Axial Test Data

3.3.2.1 7000 Series Aluminum Alloy

Zamrick [24], Zamrick and Frishmuth [25] studied non-proportional multi-axial low cycle fatigue of 7075-T6 aluminum alloys by testing a large number of hollow-tube specimens shown in Fig. 3.5. Their strain-controlled tests involved pure tension, pure torsion, combined tension and torsion loading with a phase angle (δ) being 0^{o}, 30°, 45°, 60° and 90° (see Eq. (3.6)), respectively. Note that the material sensitivity parameter α^{ε} for this aluminum alloy has already been determined, as given in Table 3.1. The corresponding load-path non-proportionality damage factor g_{NP} corresponding to each

phase angle δ can be determined by Eq. (3.10). Then Eq. (3.5) can be used to calculate the MLP-based equivalent strain $\Delta\varepsilon_{NP}$ at any applied effective strain range $\Delta\varepsilon_e$. As such, all test data in [24] can be converted to MLP-based equivalent strain ranges versus cycles to failure, as shown in Fig. 3.6, indicating an excellent correlation among all test data with a standard deviation of 0.26 and a correlation coefficient of 0.86. It is worth noting that most of fatigue life estimated using MLP-based model is within a factor of two of test lives except for those with extremely low-cycle lives ($N < 10$) cases which may have tube buckling involved [24].

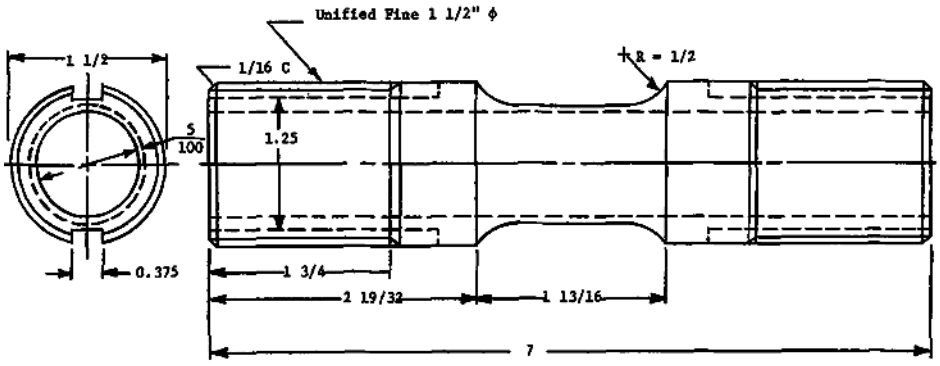

Fig. 3.5 Thin-walled tubular specimen test by Zamrick [24], Zamrick and Frishmuth [25]

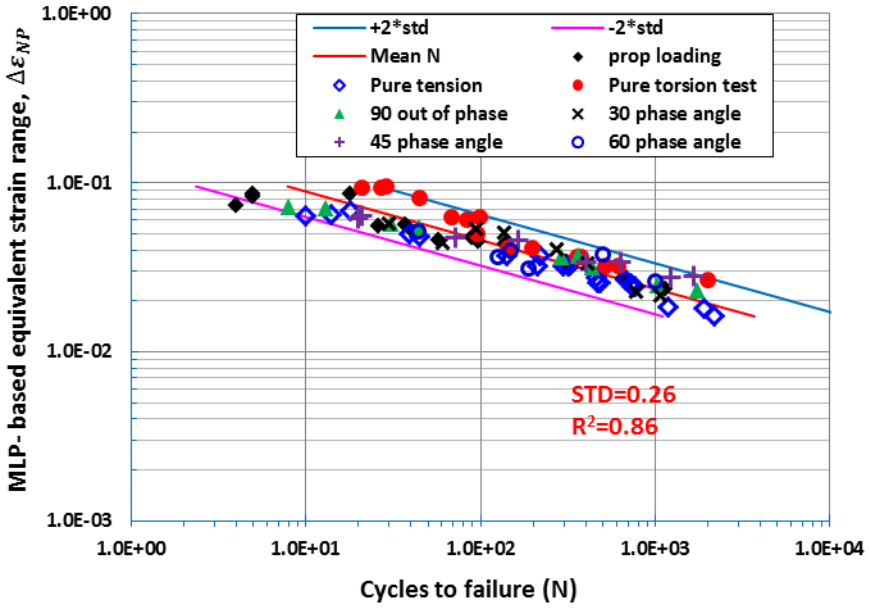

Fig. 3.6 Fatigue data correlation of 7075-T6 aluminum alloy [24-25] using MLP-based model

More recently, Zhao and Jiang [26] reported a series of non-proportional multi-axial fatigue tests on 7075-T651 aluminum alloy using hollow tube specimens with fully reversed strain-controlled load paths shown in Fig. 3.7. Note that the load case with non-zero mean effective stress given in [26] is not considered here since it would require additional treatment, which is under investigation and will be reported separately in the near future. Load paths (d) and (e) in Fig. 3.7 correspond to asynchronous loading with torsion/tension frequency ratios of 2 and 4, respectively, which require a proper cycle counting, such as using PDMR [18-20]. In addition, the authors in [26] did not discuss how their test data among these load cases in Fig. 3.7 should be correlated. In this study, PDMR based cycle counting is performed first to break the load blocks (i.e., load paths (d) and (e)) into multiple cycles (see examples given in [17-20]). These counted cycles are then treated as one equivalent cycle corresponding to Palmgren-Miner's rule based

equivalent strain range for correlation with other load cases, i.e., (a) through (c). The test data from [26] are then represented by MLP-based equivalent strain range versus cycles to failure in Fig. 3.8. It can be seen that all proportional and non-proportional test data are now situated in a narrow band around its mean curve, demonstrating the effectiveness of the MLP-based equivalent strain range, especially when integrated with PDMR cycle counting procedures.

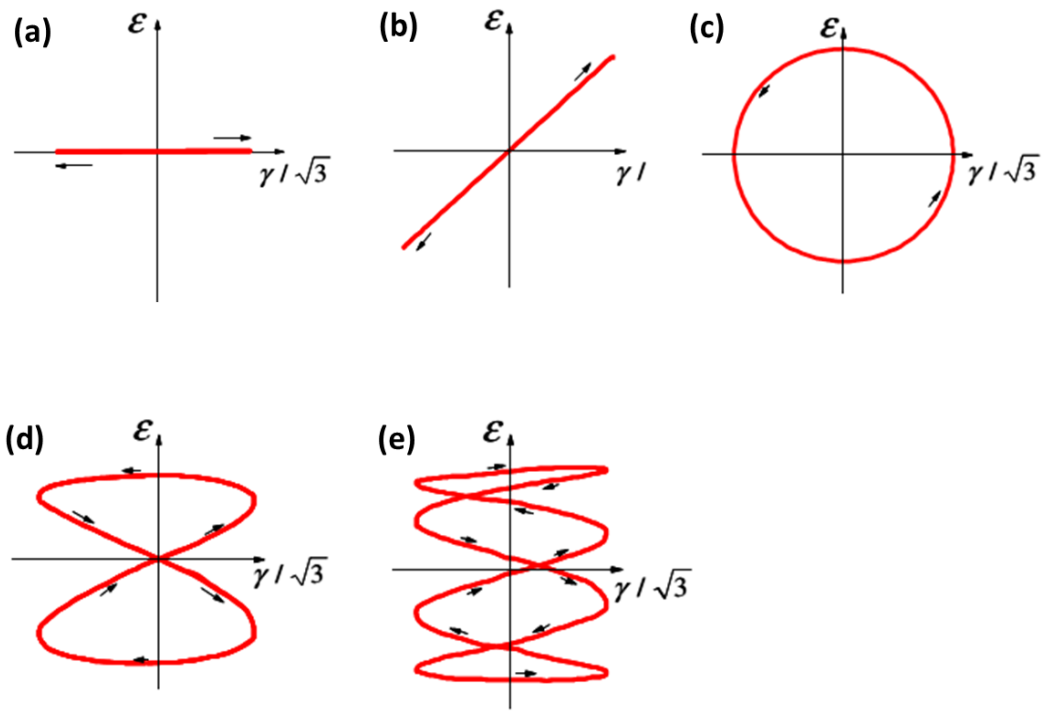

Fig. 3.7 Load paths used in [26] for tube specimen testing under combined cyclic tension and torsion

Another way of demonstrating the effectiveness of MLP-based model is by comparing MLP-based prediction of the same test data with SWT-based model prediction [32], as shown in Fig. 3.9 (a) and Fig. 3.9(b) respectively. The dashed lines in Fig. 3.9 (a) and Fig. 3.9 (b) represent a factor-of-five in life prediction from the mean line. It can be

clearly seen that all but one data point fall within a factor of 5 in life when MLP-based model is used, showing a significant improvement over SWT-based prediction presented by Zhao and Jiang [26] as shown in Fig. 3.9 (b).

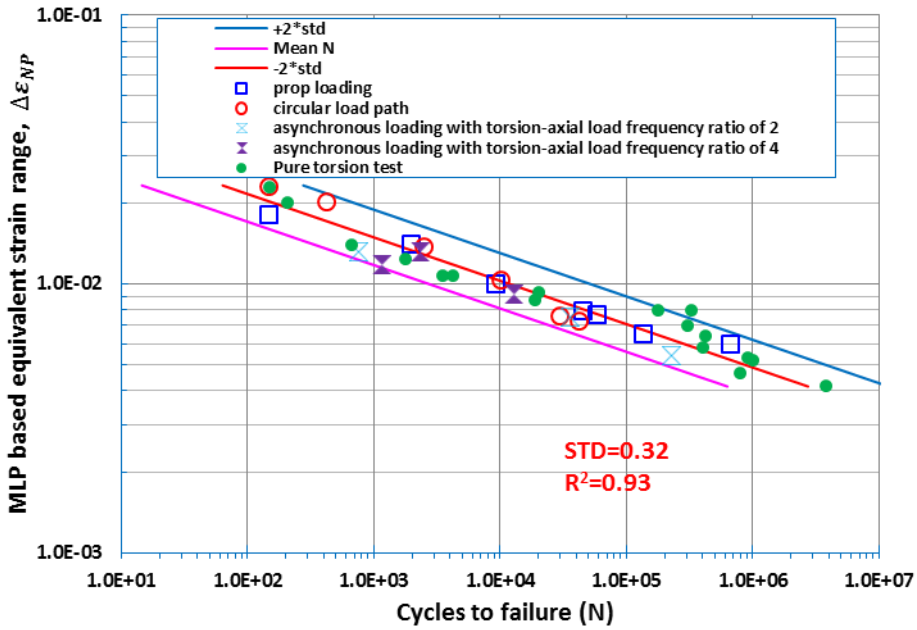

Fig. 3.8 MLP-based equivalent strain range correlation of Zhao and Jiang's 7075-T651 [26] aluminum alloy test data

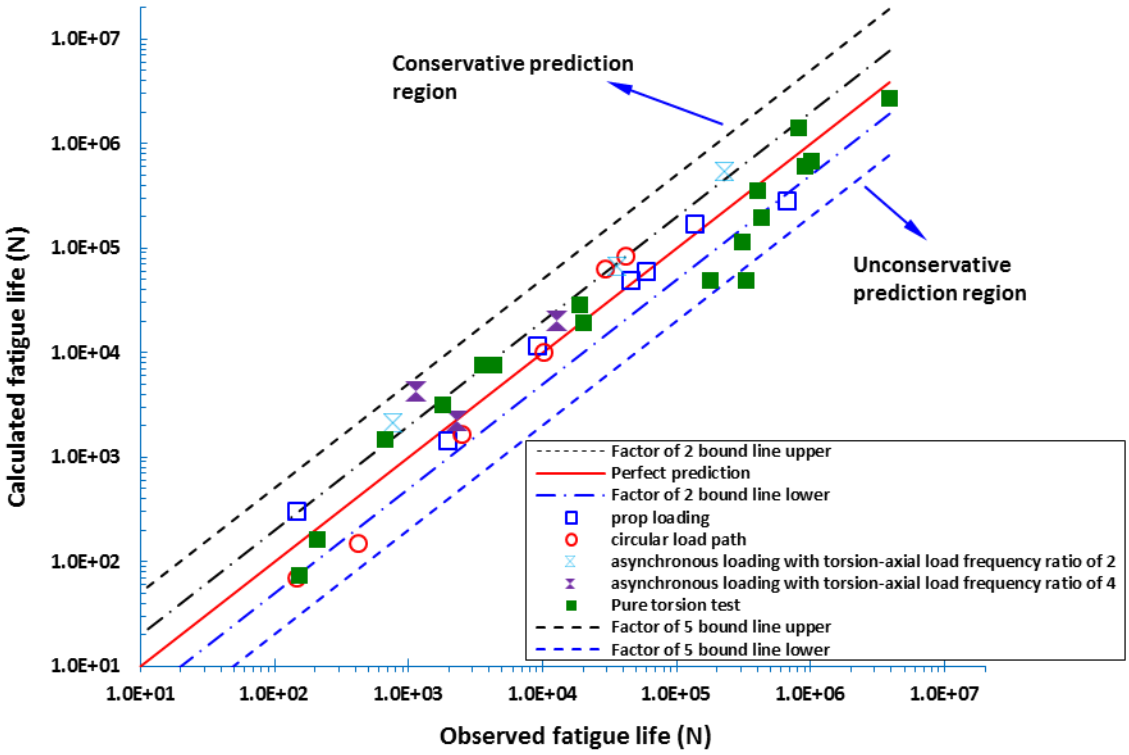
Conservative prediction region
Unconservative prediction region
Calculated fatigue life (N)
Observed fatigue life (N)
1.0E+01
1.0E+02
1.0E+03
1.0E+04
1.0E+05
1.0E+06
1.0E+07
Factor of 2 bound line upper
Perfect prediction
Factor of 2 bound line lower
prop loading
circular load path
asynchronous loading with torsion-axial load frequency ratio of 2
asynchronous loading with torsion-axial load frequency ratio of 4
Pure torsion test
Factor of 5 bound line upper
Factor of 5 bound line lower

Fig. 9(a)

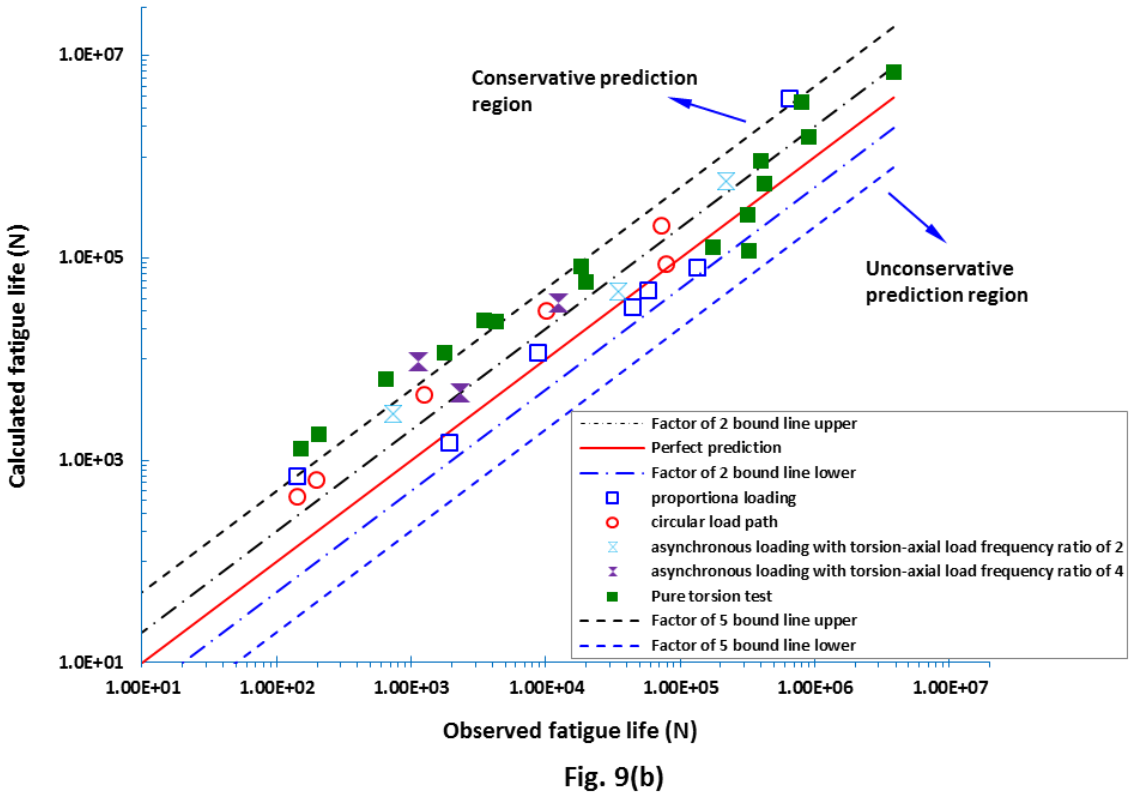

Fig. 3.9 Comparison of fatigue life calculation versus actual test data [26] of 7075-T651 aluminum alloy (a) MLP-based model; (b) SWT-based model

3.3.2.2 6000 Series Aluminum Alloy

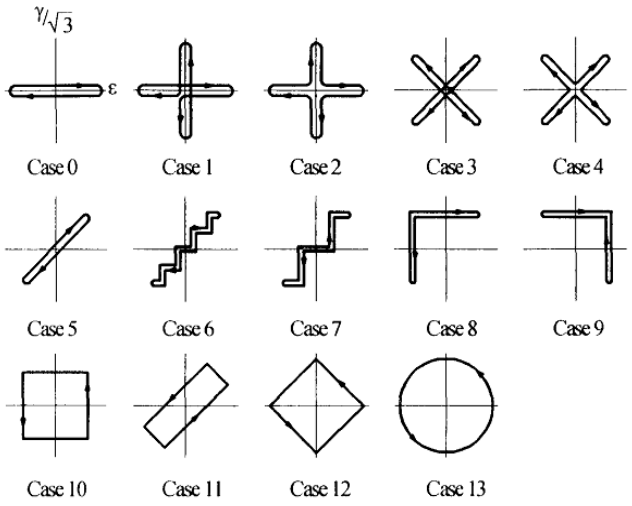

Fig. 3.10 Strain paths used by Itoh et al. [27] for performing multi-axial fatigue tests on 6061 aluminum alloy

Itoh et al. [27] examined non-proportional low cycle fatigue behaviors of 6061-T6 aluminum alloy by conducting strain-controlled fatigue testing using 14 types of strain paths shown in Fig. 3.10. As mentioned in Sec. 3.1, the material sensitivity parameter α^{ε} is determined using test data corresponding to Case 0 and Case 13. The use of Case 0 rather than Case 5 is due to the consideration that there are only two data points of Case 5 available and it is statistically insufficient for the purpose of determining α^{ε}. Also note that PDMR cycle counting procedure is used for Case 1 to Case 4 to determine the numbers of fatigue cycles each case represents, for which detailed PDMR cycle counting details can be found in [17-20]. Fig. 3.11 summarizes all test data by Itoh et al.[27] in terms of MLP-based equivalent strain range versus cycles to failure, showing an excellent correlation, with a standard deviation of 0.17 (i.e., STD=0.17). Among a total of 21 tests, 19 of them fall within a factor of 2 about the mean curve.

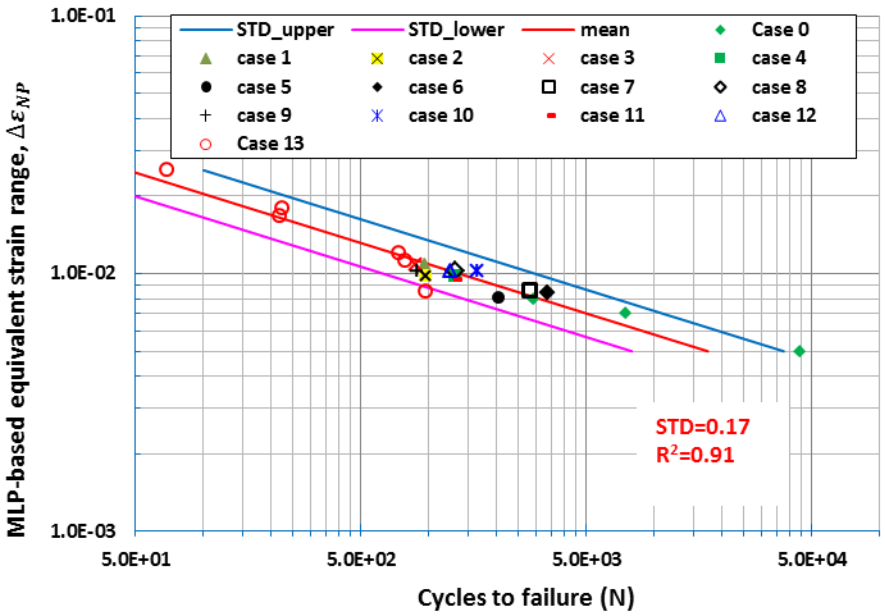

Fig. 3.11 MLP-based equivalent strain range versus cycles to failure - 6061 aluminum alloy test data by Itoh et al.[27]

By considering a similar aluminum alloy 6082-T6, Susmel and Petrone [28] performed a series of load-controlled multi-axial fatigue tests (pure torsion, pure bending, combined torsion and bending with specified phase angle of 0^0 (in-phase), 90^o and 126^o (out-of-phase), respectively. Solid round bar specimens were used in all these tests (see Fig. 3.12). By following the same analysis procedure described earlier (note that material sensitivity parameter α is determined as 0.35 as given in Table 3.1), the test data [28] can then be presented as MLP-based equivalent stress range versus cycles plot, as shown in Fig. 3.13. A good correlation of all these test data can be seen, with a standard deviation of around 0.21.

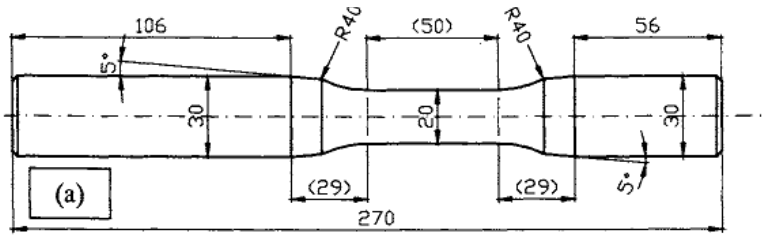

Fig. 3.12 Solid round bar specimen used by Susmel and Petrone [28] for multi-axial fatigue test of 6082-T6 aluminum alloy

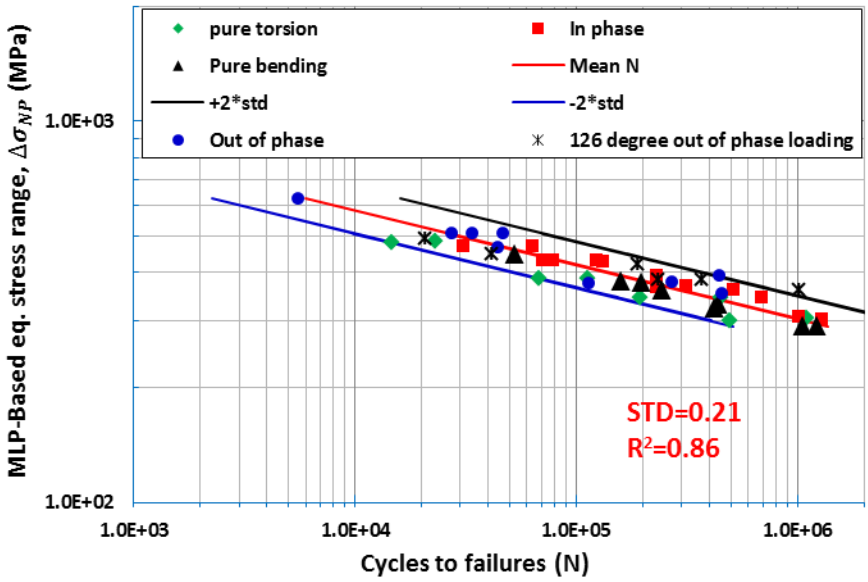

Fig. 3.13 MLP-based equivalent stress range versus cycles to failure - 6082-T6 aluminum alloy test data by Susmel and Petrone's [28]

3.3.2.3 5000 Series Aluminum Alloy

Hoffmeyer et al. [29] carried out non-proportional multi-axial fatigue tests on 5083 aluminum alloy with different typical strain paths illustrated in Fig. 3.14 in which asynchronous loading paths (Fig.3.14(e) and Fig.3.14(f)) were also investigated to demonstrate applicability of their proposed short crack growth model. Here, the authors' short crack based strain life data are converted into MLP-based equivalent strain range

versus cycles to failure corresponding the same short crack definition, in which material sensitivity parameter is calculated by comparing data using proportional path (Fig.3.14(a)) and circular path (Fig.3.14(b)), as given in Table. 3.1. The MLP-based correlation results are given in Fig. 3.15, again showing a very good correlation among different load paths with a standard deviation as small as 0.237.

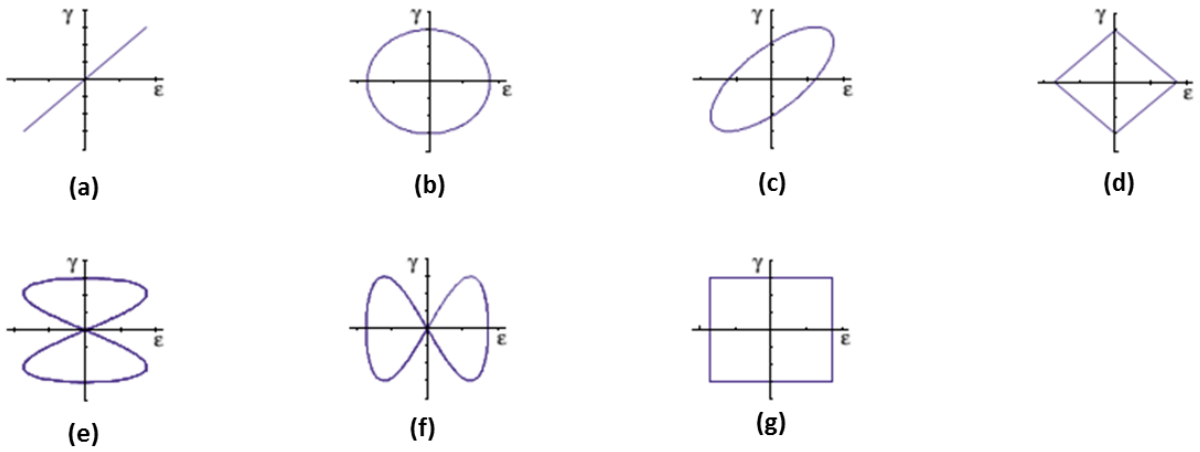

Fig. 3.14 Strain paths employed by Hoffmeyer et al [29] for multi-axial fatigue testing of Al 5083 aluminum alloy

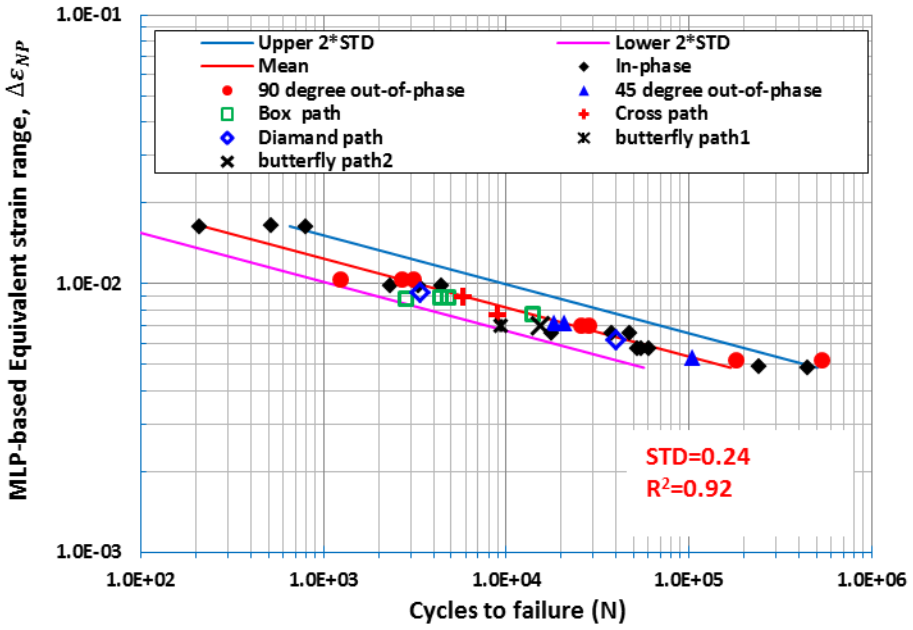

Fig. 3.15 MLP-based equivalent strain range versus cycles to failure for Al 5083 test data [29]

3.3.2.4 2000 Series Aluminum Alloy

Xia and Yao [30] recently conducted load-controlled non-proportional multi-axial fatigue tests on 2024-T4 aluminum alloys with phase angles between tension and torsion set at 30^o, 45^o, 60^o, and 90^o, respectively. Their objective was mainly focused on examination of cumulative damage rules for dealing with multi-axial block loading spectrums. For the purpose of this investigation, only "Single Stage" test data in [30] are considered here for demonstrating the effectiveness of MLP-based model for data correlation. The results are given in Fig. 3.16 which clearly shows an excellent correlation among test data under different non-proportional loading conditions with different phase angles.

For the same type of aluminum alloy, strain-controlled non-proportional fatigue test data were also reported by Wang et al. [31]. The MLP-based equivalent strain range versus cycles to failure for this set of strain controlled data is given in Fig. 3.17. It is interesting to note that material sensitivity parameter α^{ε} for the strain-controlled tests is calculated as $\alpha^{\varepsilon} = 0.5$, being the same as (i.e., $\alpha = 0.5$) the load controlled test data generated by Xia and Yao [30]. In both cases, a good data correlation can be seen, as shown in Figs. 16 and Fig. 3.17, respectively. The estimated fatigue life using MLP-based model is within a factor of 2 from the mean curve for data reported by Xia and Yao's [30] while within a factor of about 3 is found for data reported by Wang et al.[31].

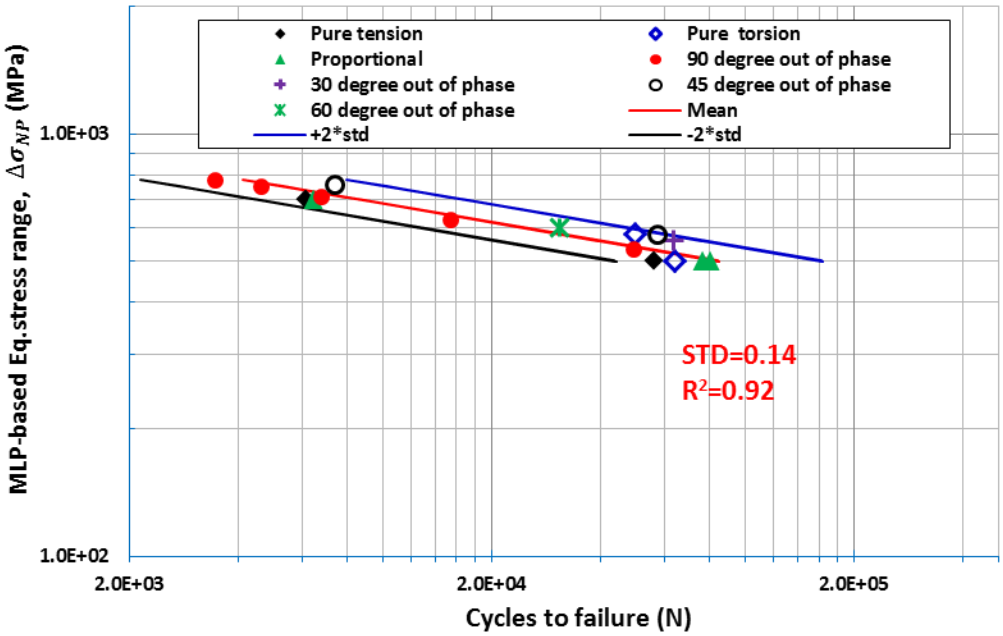

Fig. 3.16 MLP-based equivalent stress range versus cycles to failure - 2024-T4 aluminum alloy test data by Xia and Yao's [30]

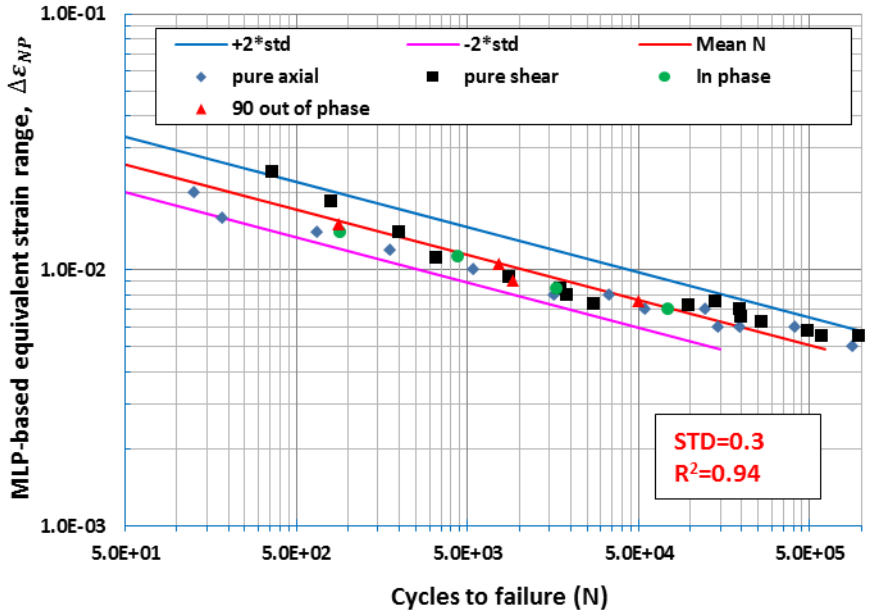

Fig. 3.17 MLP-based equivalent strain range versus cycles to failure - 2024-T4 aluminum alloy test data by Wang et al. [31]

3.4 Discussions

3.4.1 Effects of Strain Hardening and Ductility

Material sensitivity parameter to non-proportional loading, i.e., α given in Eq. (3.4) or α^{ε} given in Eq. (3.5) is determined directly through the comparison of fatigue test data under proportional and simple non-proportional loading conditions as illustrated in Section 3.1. A similarly defined parameter (α_I), first introduced by Itoh et al. [1] in the context of a maximum principle strain range was determined by comparing two cyclic stress-strain curves generated under proportional and non-proportional cyclic loadings, respectively. This is illustrated in Fig. 3.18, which is re-plotted from Itoh et al. [1]. In doing so, they attributed additional fatigue damage of non-proportional loading to additional material hardening at a reference strain amplitude level (i.e., ε_{ref} in Fig. 3.18). A number of issues may arise in using this approach, such as:

(a) In high cycle fatigue regime in which any plastic deformation or strain hardening effects are typically negligible, it has been shown that load path non-proportionality can cause significant fatigue damage (see Mei and Dong [17]). Under such conditions, the material sensitivity parameter as defined in Fig. 3.18 in [1] seems no longer applicable.

(b) In low cycle regime under strain-controlled loading conditions, the approach in Fig. 3.18 may only be applicable for constant amplitude loading, say with a given strain amplitude given as ε_{ref}. This also suggests that material sensitivity parameter so determined is strain amplitude dependent. Under variable amplitude

loading conditions, it would require a cycle-by-cycle determination of the material sensitivity parameter, which can be rather inconvenient in practice.

(c) It has been well-established that some materials that may not exhibit any noticeable non-proportional hardening (see Ref [6,15-16]) still show significant fatigue damage due to load path non-proportionality. The procedure illustrated in Fig. 3.18 seems not able to capture load non-proportionality induced fatigue damage for these materials.

Some of the concerns seem to be confirmed by a more recent publication by Itoh and Yang [13]. They compared material sensitivity parameter (α*) determined by comparing strain life test data between proportional and non-proportional load paths metals with body-centered cubic (BCC) and face-centered cubic (FCC) lattice structures. They showed that in order to correlate their fatigue test results, α* for BCC type metals should be about twice as much as the material sensitivity value α_I determined by the procedure in Fig. 3.18.

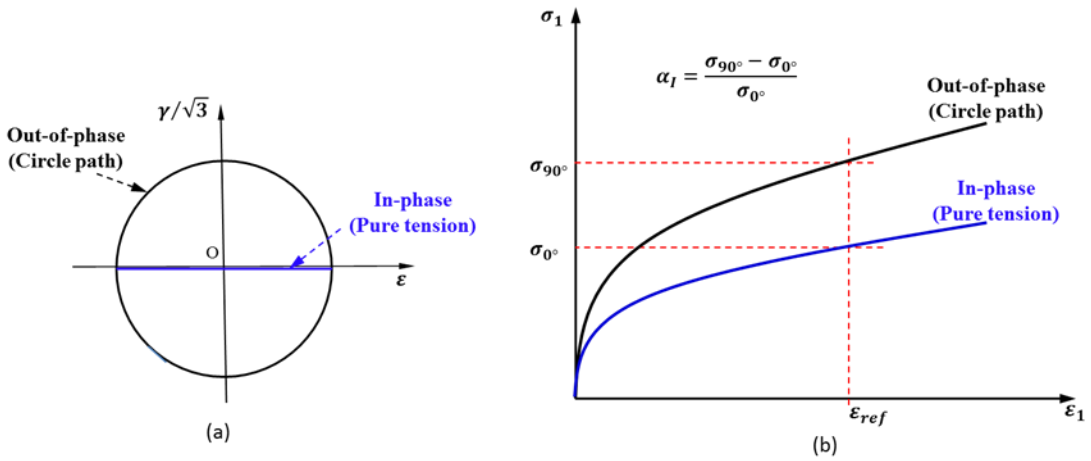

Fig. 3.18 Determination of non-proportional cyclic hardening material constant (α). (a) proportional and non-proportional loading path and (b) cyclic stress-strain curve of two load paths

Instead of relating material sensitivity parameter to non-proportional loading induced additional cyclic hardening behavior, as presented by Itoh et al. [1, 27], Sonsino [23], after a review of a large amount of non-proportional multi-axial test data ranging from cast irons, structural steels, aluminum alloys, as well as magnesium alloys, pointed out that material ductility seems to have a decisive contribution to fatigue damage development under non-proportional loading conditions. He then defined three groups of materials based on their ductility level and sensitivity to non-proportional loading, as follows: (a) "Ductile materials", such as structural steels, tend to show a significant sensitivity to non-proportional loading by showing a reduction of fatigue lives comparing with those under proportional loading; (b) Materials with "low-ductility", such as cast iron or cast aluminum alloys, were shown to exhibit an increase in fatigue life when subjected to non-proportional loading; (c) "Semi-ductile" materials, such as cast steel, tend to be neutral or insensitive to non-proportional loading. It should be noted that most of the above observations were based on S-N plots of test data using component stress in terms of either nominal or a local stress definition) with corresponding shear stress being applied at a fixed ratio. However, the author [23] did not provide a quantitative relationship between material ductility and sensitivity to non-proportional damage.

With the present developments given in Sections 2.1 and 3.1, it would be interesting to relate the material sensitivity parameters determined for various wrought aluminum alloys in Section 3.1 to their respective ductility parameters (i.e., uniaxial

elongation test results). The results are given in Fig. 3.19, showing an approximately linear relationship. Note that for the cases of Al 6061 [27] and Al 2024-T4 [31], their respective ductility values in terms of elongation were not given by their respective authors and were taken from ASM material handbook [33] for the purpose of generating Fig. 3.19. It should be pointed out here that two additional sets are included in Fig. 3.19, i.e., cast aluminum alloy [34] with a low ductility and Al welded joint [21], both of which are not included in the discussions in Sec. 3.2 due to space limitation. The total of nine groups of multi-axial fatigue test data from 9 independent sources, as shown in Fig. 3.19, seem to suggest the existence of an approximately linear relationship between material sensitivity parameter (α or α^{ε}) to non-proportional fatigue loading and material ductility. Mechanistically, such a dependency may be explained as follows:

(a) In a ductile material, the likelihood of fatigue damage in the form of intrusion and extrusion through dislocation movement/cross slip/interaction along preferential slip planes [35-36] should be significantly increased at the presence of load-path non-proportionality due to the rotation of maximum shear stress/strain plane within one fatigue loading cycle.

(b) In a brittle material with less ductility, the same amount of rotation of maximum shear stress/strain plane during a fatigue loading cycle has a lesser effect on fatigue damage due to a lack of preferential shear slip planes and dislocation mobility.

If the relationship in Fig. 3.19 can be further proven for a broader category of materials, it can significantly simplify the efforts for determining material sensitivity parameter α in Eq. (3.14) or α^{ε} for non-proportional multi-axial fatigue evaluation in

practice, by reducing or eliminating the needs for systematic fatigue testing described in Fig. 3.3. To that end, the results from an on-going research by the authors on titanium alloys and magnesium alloys will be published in the near future.

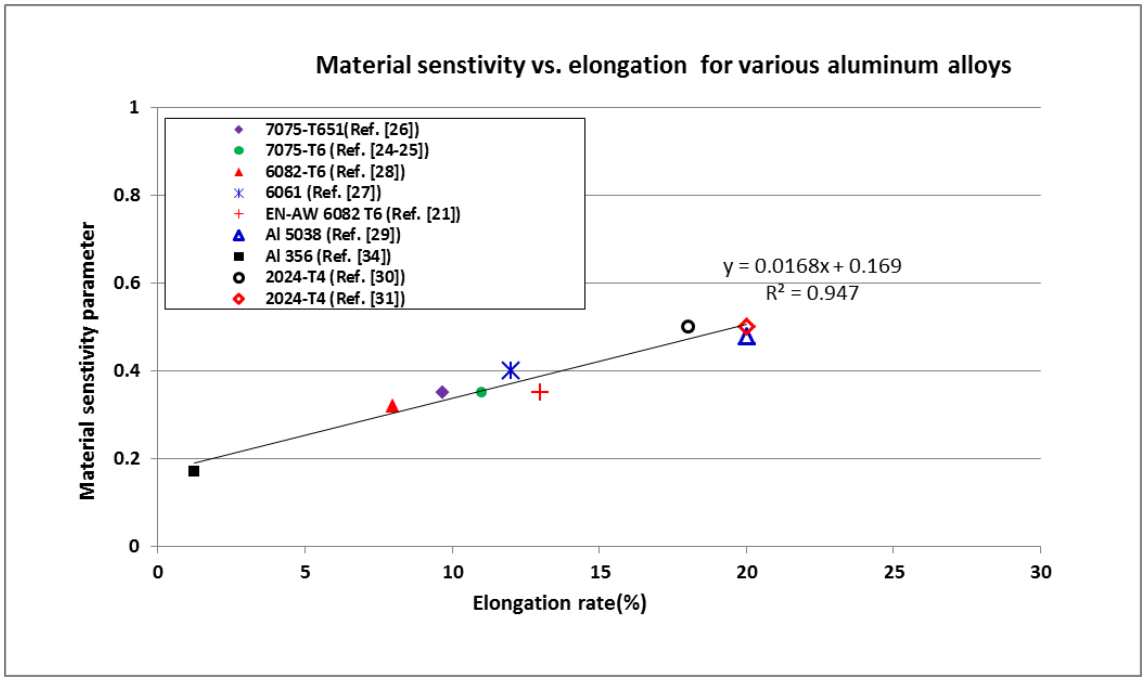

Fig. 3.19 Relationship between material sensitivity parameter α or α^{ε} and and material ductility characterized by e.g. elongationfor various types of aluminum alloys.

3.4.2 Overall Effectiveness of MLP-Based Model

Finally, in order to quantitatively assess the effectiveness of the MLP-based model in correlating test data over all wrought aluminum alloys investigated in this study (see Sec. 3.2), Fig. 3.20 plots MLP-based fatigue life estimations versus fatigue life test results. Fig. 3.20 contains a total of 274 multi-axial fatigue test results of seven wrought aluminum alloys from different sources. Except for only a few data points, most of calculated fatigue lives are within a factor of 3 of actual tested fatigue lives, demonstrating the effectiveness and robustness of the MLP-based fatigue damage

parameter in both low cycle and high cycle regime with load paths from simple to complex ones which require cycle counting using PDMR method.

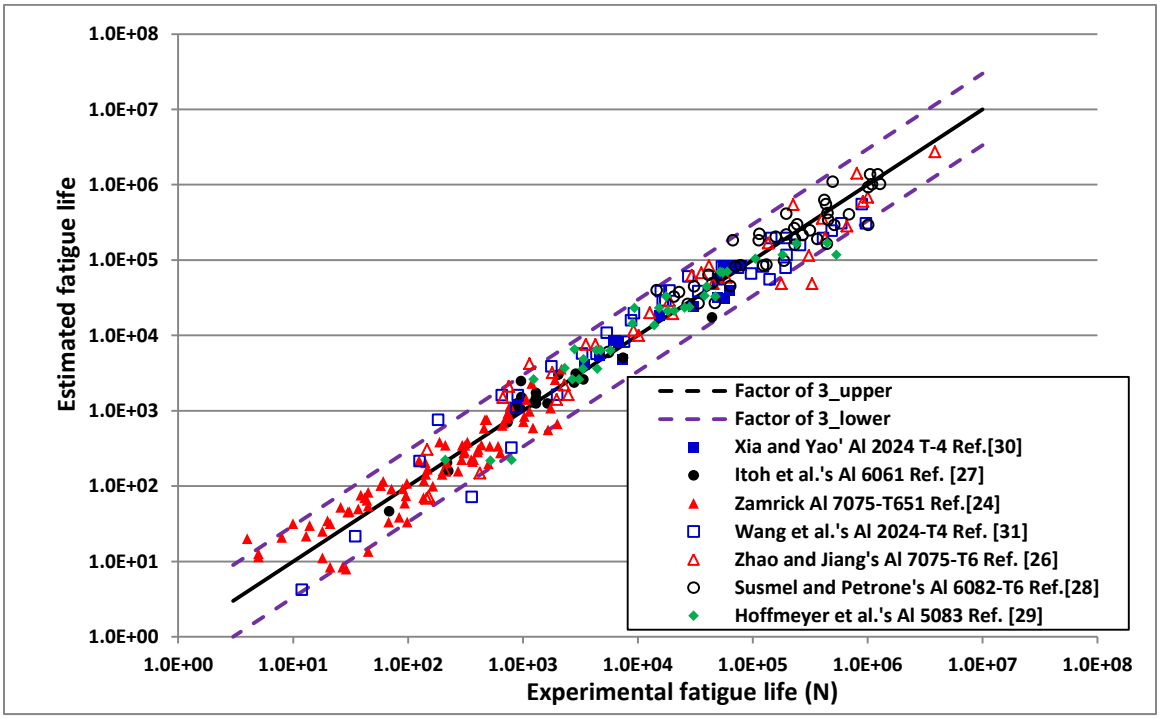

Fig. 3.20 Estimated fatigue lives versus experimental fatigue lives for different series of wrought aluminum alloys from seven independent research groups.

3.5 Conclusions

This paper presents a detailed investigation into non-proportional loading induced multi-axial fatigue damage in a series of wrought aluminum alloys using a recently developed multi-axial fatigue damage model. Major findings can be stated as follows:

(a) All of the wrought aluminum alloys studied in this paper show a less degree of sensitivity to non-proportional loading comparing structural steels recently reported by the same authors, with material sensitivity parameter (α defined with respect to stress plane and α^{ε} to strain plane) ranging from 0.35 to 0.5, much

smaller than that of structural steels which were found to be around unity (i.e. $\alpha \approx \alpha^{\varepsilon} \approx 1$)

(b) Within the same aluminum alloy type, it is found that material sensitivity parameter (α) calculated on stress plane using stress-life test data is rather close to the values calculated in strain plane using strain-life data (i.e., α^{ε})

(c) With the material sensitivity parameter (α or α^{ε}) being determined, MLP-based equivalent stress range (defined on $\sigma - \sqrt{\beta}\tau$ plane) or equivalent strain range (on $\varepsilon - \sqrt{\beta^{\varepsilon}}\,\gamma$ plane) are shown to be effective in correlating a large amount of multi-axial fatigue test data subjected to a varying degree of load-path non-proportionality.

(d) An approximately linear relationship between material sensitivity parameter to non-proportional loading and material ductility (in terms of percentage of elongation obtained standard tensile tests) is observed for wrought aluminum alloys examined in this study.

Acknowledgments

The authors acknowledge the support of this work through a grant from the National Research Foundation of Korea (NRF) Grant funded by the Korea government (MEST) through GCRC-SOP at University of Michigan under Project 2-1: Reliability and Strength Assessment of Core Parts and Material System. P. Dong acknowledges the financial support made possible by Traction Power National Key Laboratory Open Competition Grant (No. TPL 1605).

References

[1] Itoh T, Sakane M, Ohnami M, Socie DF. Nonproportional low cycle fatigue criterion for type 304 stainless steel. J Eng Mater Technol 1995;117:285–292.

[2] Sonsino C. Multiaxial fatigue of welded joints under in-phase and out-of-phase local strains and stresses. Int J Fatigue 1995;17:55–70.

[3] Sonsino CM, Kueppers M. Multiaxial fatigue of welded joints under constant and variable amplitude loadings. Fatigue Fract Eng Mater Struct 2001;24:309–327.

[4] Yousefi F, Witt M, Zenner H. Fatigue strength of welded joints under multiaxial loading: experiments and calculations. Fatigue Fract Eng Mater Struct 2001;24:339–355.

[5] Socie D. Multiaxial Fatigue Damage Models. J Eng Mater Technol 1987;109:293–298.

[6] Nakamura H, Takanashi M, Itoh T, Wu M, Shimizu Y. Fatigue crack initiation and growth behavior of Ti–6Al–4V under non-proportional multiaxial loading. Int J Fatigue 2011;33:842–848. doi:10.1016/j.ijfatigue.2010.12.013.

[7] Exel N, Sonsino CM. Multiaxial fatigue evaluation of laserbeam-welded magnesium joints according to IIW-fatigue design recommendations. Weld World 2014;58:539–545. doi:10.1007/s40194-014-0139-6. [8] Yu Q, Zhang J, Jiang Y, Li Q. Multiaxial fatigue of extruded AZ61A magnesium alloy. Int J Fatigue 2011;33:437–47. doi:10.1016/j.ijfatigue.2010.09.020.

[9] Fatemi A, Shamsaei N. Multiaxial fatigue: An overview and some approximation models for life estimation. Int J Fatigue 2011;33:948–958.

[10] Sonsino CM. Multiaxial fatigue assessment of welded joints - Recommendations for design codes. Int J Fatigue 2009;31:173–187.

[11] Kanazawa K, Miller KJ, Brown MW. Cyclic deformation of 1% Cr-Mo-V steel under out-of-phase loads. Fatigue Fract Eng Mater Struct 1979;2:217–228.

[12] Doong SH, Socie DF, Robertson IM. Dislocation Substructures and Nonproportional Hardening. J Eng Mater Technol 1990;112:456–464. doi:10.1115/1.2903357.

[13] Itoh T, Yang T. Material dependence of multiaxial low cycle fatigue lives under non-proportional loading. Int J Fatigue 2011;33:1025–1031. doi:10.1016/j.ijfatigue.2010.12.001.

[14] Itoh T, Sakane M, Ohsuga K. Multiaxial low cycle fatigue life under non-proportional loading. Int J Press Vessel Pip 2013;110:50–56. doi:10.1016/j.ijpvp.2013.04.021.

[15] Shamsaei N, Gladskyi M, Panasovskyi K, Shukaev S, Fatemi A. Multiaxial fatigue of titanium including step loading and load path alteration and sequence effects. Int J Fatigue 2010;32:1862–1874.

[16] Shamsaei N, Fatemi A, Socie DF. Multiaxial fatigue evaluation using discriminating strain paths. Int J Fatigue 2011;33:597–609.

[17] Mei J, Dong P. A new path-dependent fatigue damage model for non-proportional multi-axial loading. Int J Fatigue 2016;90:210–221. doi:10.1016/j.ijfatigue.2016.05.010.

[18] Dong P, Wei Z, Hong JK. A path-dependent cycle counting method for variable-amplitude multi-axial loading. Int J Fatigue 2010;32:720–734.

[19] Wei Z, Dong P. A generalized cycle counting criterion for arbitrary multi-axial fatigue loading conditions. J Strain Anal Eng Des 2014;49:325–341.

[20] Wei Z, Dong P. Multiaxial fatigue life assessment of welded structures. Eng Fract Mech 2010;77:3011–3021.

[21] Kuppers M, Sonsino CM. Critical plane approach for the assessment of the fatigue behaviour of welded aluminum under multiaxial loading. Fatigue Fract Eng Mat Stru 2003;26:507–513.

[22] Kueppers M, Sonsino CM. Assessment of the fatigue behavior of welded aluminum joints under multi-axial spectrum loading by a critical plane approach. Int J Fatigue 2006;28:540–546.

[23] Sonsino CM. Influence of material's ductility and local deformation mode on multiaxial fatigue response. Int J Fatigue 2011;33:930–947.

[24] Zamrik SY. (1972). An investigation of strain cycling behavior of 7075-T6 aluminum under combined state of strain: The effects of out-of-phase, biaxial strain cycling on low cycle fatigue. Technical Report, Pennsylvania State University, Department of Engineering Mechanics, 1972.

[25] Zamrik SY, Frishmuth RE. The Effects of Out-of-phase Biaxial-strain Cycling 1973;13:204–208.

[26] Zhao T, Jiang Y. Fatigue of 7075-T651 aluminum alloy. Int J Fatigue 2008;30:834–49. doi:10.1016/j.ijfatigue.2007.07.005.

[27] Itoh T, Nakata T, Sakane M, Ohnami M. Nonproportional Low Cycle Fatigue of 6061 Aluminum Alloy Under 14 Strain Paths. 5th Int Conf Biaxial/Multiaxial Fatigue Fract 1997:173–187.

[28] Susmel L, Petrone N. Multiaxial fatigue life estimations for 6082-T6 cylindrical specimens under in-phase and out-of-phase biaxial loadings. Eur Struct Integr Soc 2003;31:83–104.

[29] Hoffmeyer J, Döring R, Seeger T, Vormwald M. Deformation behaviour, short crack growth and fatigue lives under multiaxial nonproportional loading. Int J Fatigue 2006;28:508–20. doi:10.1016/j.ijfatigue.2005.05.014.

[30] Xia T, Yao W. Comparative research on the accumulative damage rules under multiaxial block loading spectrum for 2024-T4 aluminum alloy. Int J Fatigue 2013;48:257–65. doi:10.1016/j.ijfatigue.2012.11.004.

[31] Wang X, Gao Z, Qiu L, Wang L, Jiang Y. Multiaxial Fatigue of 2024-T4 Aluminum Alloy. Chinese J Mech Eng 2011;24:1–7. doi:10.3901/CJME.2011.

[32]Smith KN, Watson P, Topper TH. Stress-Strain Function for the Fatigue of Metals. J Mater 1970;5:767–778.

[33] ASM Handbook Online, Properties and Selection: Nonferrous Alloys and Special-Purpose Materials, Vol. 2, ASM International, 2010

[34] Zhu Z, He G, Chen C, Ding X, Liu D. Study on Multi-axial low cycle fatigue properties for under non-proportional loading of cast aluminum alloys. Foundry 2006; 55:1275-1279.

[35] Sonsino C.M. Grubisic, V., Fatigue behavior of cyclically softening and hardening steels under multiaxial elastic-plastic deformation. Multiaxlal Fatigue, ASTM STP 853, 1985, 586-605.

[36] Nishino S., Hamada N., Sakane M., Ohnami M., Matsumura N., Tokizane, M. Microstructural study of cyclic strain hardening behaviour in biaxial stress states at elevated temperature. Fatigue Fract Eng Mat Struct 1986; 9(1):65-77.

Chaper 4.

An Equivalent Stress Parameter for Multi-Axial Fatigue Evaluation of Welded Components Including Non-Proportional loading effects

Abstract

This paper presents a comprehensive investigation into non-proportional multi-axial fatigue of welded components by introducing an equivalent structural stress parameter that takes into account of load-path non-proportionality in addition to plate thickness and stress state effects. This is accomplished by formulating a "moment of load-path" or "MLP" based fatigue damage parameter that provides a consistent treatment of load-path non-proportionality under arbitrary multi-axial loading conditions for which cycle counting can be consistently performed by means of a previously developed path-dependent maximum range (PDMR) cycle counting procedure. To examine its broad applicability and effectiveness, non-proportional multi-axial test data obtained using different components, joint types, and loading conditions from various sources are analyzed using the newly developed equivalent stress parameter. The results show that the new equivalent stress parameter enables not only an effective consolidation of all multi-axial test data (up to about 300 tests) analyzed in this paper into a narrow band, but also the demonstrated transferability between the master S-N curve (dominated by test data under uniaxial cyclic loading conditions) adopted by the 2007 ASME Div 2 and API 579 RP/ASME FFS-1 Codes and the consolidated S-N curve dominated by

severe non-proportional multi-axial cyclic loading conditions. As a result of the present development, a unified fatigue evaluation procedure based on the newly proposed effective stress parameter and a single master S-N curve can be implemented for arbitrary cyclic loading conditions regardless of stress multi-axiality or load path proportionality.

Keywords: *Multi-axial fatigue, welded joints, non-proportional loading, fatigue damage parameter, mesh-insensitive method, traction stress, structural stress, master S-N curve*

4.1 Introduction

Multi-axial fatigue loading conditions [1, 2] are typically classified into two categories, i.e., proportional versus non-proportional loading, depending on if principal stress/strain directions rotate or not during one loading cycle. Non-proportional multi-axial loading has been found more damaging than proportional loading by numerous researchers through experimental studies [3-13], being strongly dependent upon load paths applied and material examined [5,7-9, 13-16].

Most of the early studies on non-proportional multi-axial fatigue have been focused on non-welded components [3-13]. Among them, Itoh et al. [5], after carrying out extensive experimental investigations on structural steels, aluminum alloys and titanium alloys, proposed an equivalent strain parameter for modeling fatigue damage caused by principal strain axis rotation and additional hardening as a result of non-proportional loading. However, some recent studies [7, 17] found that non-proportional fatigue damage can still be significant in some materials that exhibit minimal non-proportional strain hardening. In addition to material response, another major challenge in modeling non-proportional multi-axial fatigue damage is how to consistently break

down a complex multi-axial load path into fatigue cycles (or half cycles) on which an effective stress or strain range can be calculated for measuring fatigue damage unambiguously [18]. Along this line, different stress or strain range definitions [19-20] have been proposed, such as minimum circumscribed circle (MCC), or minimum circumscribed ellipse (MCE), as a fatigue damage parameter for modeling non-proportional fatigue loading. As discussed in [18, 21], these type of stress range definitions often fail in reliably capturing effects of load-path dependency on fatigue damage. Furthermore, these researchers did not provide any consistent procedures for performing cycle counting for dealing with non-proportional loading conditions. As far as critical plane based methods [22-25] are concerned, uniaxial rainflow cycle counting method is generally used against a dominant stress/strain component with the critical plane being determined by searching all potential planes in terms of fatigue damage.

As for multi-axial fatigue damage in welded components, although not as extensive as for non-welded components in terms of both experimental and theoretical studies, past investigations [26-37] have clearly demonstrated the importance of an appropriate treatment of non-proportional loading induced fatigue damage. Consistent with major findings in non-welded components, test data to date have showed that non-proportional loading can cause significant additional fatigue damage, as much as up to a factor of 10 [32] when compared with proportional loading. In an attempt to formulate an effective stress range parameter that captures non-proportional loading induced damage, Dong and Hong [37] proposed a Modified Gough Ellipse based model. Their model enables the development of an equivalent stress based fatigue damage parameter as a function of phase angle between normal and shear stress histories that can be expressed

as sinusoidal wave forms of the same frequency. A good correlation was achieved by examining both proportional and non-proportional test data [27, 29-30] obtained from welded joints. However, the Modified Gough Ellipse model is only applicable to constant amplitude non-proportional loading conditions with a clearly defined phase angle. Sonsino and Kueppers [27] showed that non-proportionality induced fatigue damage can be captured by an integral form of shear stress over all planes, referred as an Effective Equivalent Stress Hypothesis (EESH). Again, the proposed parameter in [27] is only applicable to constant amplitude sinusoidal loading with a clearly defined phase angle between two stress components.

Bäckström and Marquis [38] analyzed multi-axial test data available in literature by means of hot spot stress method and presented a comparative analysis of available multi-axial test results using various existing interaction equations between normal and shear stress components. The resulting scatter bands seem too large to be useful for performing reliable fatigue design and evaluation. More recently, Pedersen [39] carried out a similar evaluation of existing test data but using a notch stress approach and showed that an overall data correlation remains unsatisfactory. In addition to the lack of an adequate treatment of non-proportional loading, the large scatter bands resulted from both studies [38, 39] may also be attributed to stress definitions these researchers used, which may introduce variability in stress concentration calculations as a result of mesh sensitivity [40] in finite element computations. Furthermore, local notch stress based approaches require introducing an effective notch radius (e.g., 1 mm according to the International Institute of Welding (IIW) recommendation [41]) which in reality can vary in a significant manner, as demonstrated by systematic measurements given in [42-43]

and discussions [44-45]. With the recent developments in mesh-insensitive structural stress method based on the use of nodal forces and moments [40], it would be tempting to examine both how and how well such a traction stress based method can be used to correlate the same multi-axial test data.

Existing codes and standards as well as recommended practices tend to vary in stipulating stress definitions and their combinations to be used for treating non-proportional multi-axial fatigue loading. In Eurocode 3 [46], in addition to the traditional nominal stress based method in conjunction with joint classifications, geometric (i.e., hot spot) stress can also be used. For a chosen stress definition, multi-axial fatigue based design and evaluation according to Eurocode 3 uses an interaction equation in which the fatigue damage caused by normal and shear stress components are calculated separately based on their respective uniaxial S-N curves. One obvious limitation is that fatigue damage due to interactions between normal and shear stress components are not taken into account at cycle by cycle level, which is particularly important when load-path non-proportionality is involved [18]. The IIW Recommendations [41] considers the use of a stress definition among nominal stress, hot spot stress, and notch stress as a user's choice. Multi-axial fatigue is assessed by using a Gough-Pollard ellipse type interaction equation. It is worth mentioning regardless of the severity in load-path non-proportionality involved in an actual load path, the sum of total damage (D) in its interaction equation is fixed at D=0.5 while being as D=1.0 for proportional loading. Although being rather qualitative for treating non-proportional loading conditions, the IIW procedure represents an improvement over the one in Eurocode 3.

ASME BPVC 2007 SECTION VIII Division 2 [47] and API 579 RP-1/ASME FFS-1 [48] adopted a traction-based structural stress method as an alternative method since 2007. As has been demonstrated in [40, 49-50], traction structural stress calculated using nodal forces from finite element analysis results is insensitive to element size used, which lead to the development of the master S-N curve method by effectively collapsing about 1000 large scale fatigue tests of welded components into a narrow band. However, its treatment of multi-axial fatigue is still based on the modified Gough ellipse developed by Dong and Hong [37], which is not suitable for applications in general non-proportional loading conditions in which a phase shift often cannot be clearly defined. Moreover, the applicability of its master S-N curve to multi-axial fatigue design of welded joints remains to be demonstrated.

With the above discussions, the purpose of this paper is to establish an effective fatigue damage parameter that is capable of modeling fatigue damage under general non-proportional loading conditions for welded components. It is highly desirable that such a parameter can be presented in a form that can be conveniently adopted by some of the Codes and Standards for finite element based fatigue evaluation of complex welded components. To do so, we start with a brief discussion on the traction-based structural stress definition and its applications for characterizing multi-axial stress state, and then followed by a short description of a recently developed "moment of load path (MLP)" model for calculating fatigue damage due to load-path non-proportionality. To enable the incorporation of effects of plate thicknesses and stress distribution (i.e., membrane and bending content), advantage is taken of the structure of the equivalent structural stress parameter adopted by the 2007 ASME Code [47] by recasting it in the context of non-

proportional multi-axial loading. The resulting equivalent stress parameter is then validated by demonstrating its ability in effectively correlating non-proportional multi-axial fatigue test data obtained by multiple sources on different component types and joint geometries. Finally, the effectiveness of the newly proposed equivalent stress parameter is compared with hot spot stress based multi-axial fatigue evaluation procedures given by Eurocode 3 [46] and IIW [41].

4.2 Path-Dependent Equivalent Stress Parameter

4.2.1 Stress Definition

For welded components, a traction-based structural stress method has been shown effective in correlating a large amount of test data obtained from different joint geometries, plate thicknesses, and loading conditions. The structural stresses computed by means of nodal forces/moments with respect to a hypothetical cut plane are mesh-insensitive [40, 50]. The method has also been shown capable of extracting two shear stress components on the same cut plane, which can be used to describe multi-axial fatigue behavior under both proportional and non-proportional loading conditions [18, 37]. For instance, such a traction stress state relevant to weld toe cracking in a tube-to-flange joint can be illustrated in Fig. 4.1(a), in which the component is subjected to both remote cyclic bending (M_y) and torsion (M_z) in global coordinate system ($x-y-z$). The hypothetical cut into tube thickness simulating weld toe cracking (Fig. 4.1(b)) exposes three traction stress components that are responsible for fatigue crack growth behavior in the context of fracture mechanics. These components are referred to as normal, in-plane shear, and transverse shear stress components i.e., $\sigma_s(t), \tau_s(t)$ and $\tau_z(t)$ defined with respect to the cut plane ($x'-z'$ plane) along weld toe, as illustrated in Fig.

4.1(b). As given in [40], these traction stress components with respect to the local coordinate system can be directly related to line force and line moments obtained from nodal forces and nodal moments at each nodal position in shell or plate finite element model by:

$$\sigma_s = \sigma_m + \sigma_b = \frac{f_{y'}}{t} - \frac{6m_{x'}}{t^2} \tag{4.1}$$

$$\tau_s = \tau_m + \tau_b = \frac{f_{x'}}{t} + \frac{6m_{y'}}{t^2} \tag{4.2}$$

$$\tau_z = \frac{f_{z'}}{t} \tag{4.3}$$

In Eqs. (4.1) through (4.3), $f_{x'}, f_{y'}, f_{z'}$ represents line forces and $m_{x'}, m_{y'}$ line moments with respect to local coordinate system $x'-y'-z'$, respectively, as shown in Fig. 4.1 (b). These lines forces/moments can be solved by means of a system of simultaneous equations using nodal forces/moments obtained from finite element analysis [40, 50]. If 3D solid element models are used, a pre-processing procedure for converting nodal forces on a cut plane to nodal forces and nodal moments with respect to mid-thickness of the section is given by Nie and Dong [51].

For most applications, transverse shear component (τ_z) is usually negligible and only normal and in-plane shear components are often dominant when dealing with multi-axial fatigue modeling, such as the cases considered in this paper.

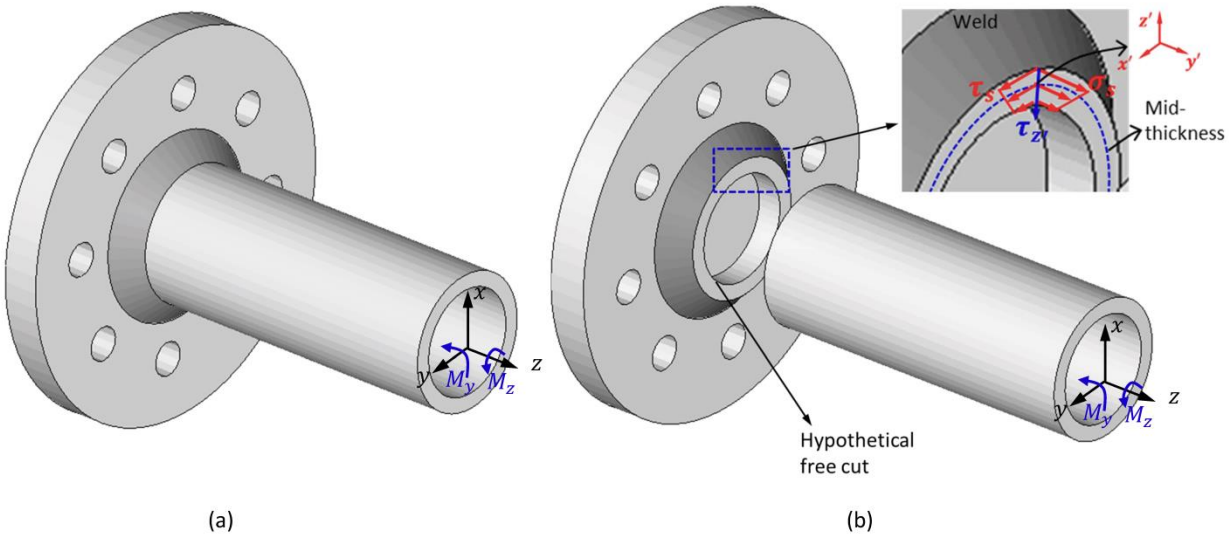

Fig. 4.1 Illustration of traction-based structural stress definition: (a) Tube-to-flange specimen subjected to both bending and torsion; (b) hypothetical free cut along weld toe and traction structural stress components exposed

4.2.2 Load Path Non-Proportionality

4.2.2.1 Load Path Representation

Any given load path depicted on a nominal stress based plane (i.e. $\sigma_n - \sqrt{\beta}\tau_n$ plane) can be mapped onto a traction structural stress based plane (i.e., $\sigma_s - \sqrt{\beta}\tau_s$ plane), where $\sqrt{\beta}$ can be interpreted as a fatigue equivalency parameter between S-N data obtained under pure bending and pure torsion, typically taking on a value of $\sqrt{3}$.

As an illustration, the multi-axial fatigue tests on tube-to-flange joint specimens (see Fig. 4.1) by Sonsino and Kueppers [27] were carried out by applying bending and torsion in synchronized sinusoidal wave forms with a phase shift (δ) difference, i.e.,

$$\sigma_n = \frac{1}{2}\Delta\sigma_0 \sin(\theta) \tag{4.4}$$

$$\tau_n = \frac{1}{2}\Delta\tau_0 \sin(\theta - \delta) \tag{4.5}$$

where $\Delta\sigma_0$ and $\Delta\tau_0$ are nominal stress ranges corresponding to remote bending and remote torsion, respectively. The resulting load paths for pure bending ($\Delta\sigma_0 \neq 0, \Delta\tau_0 = 0, \delta = 0°$), pure torsion ($\Delta\sigma_0 = 0, \Delta\tau_0 \neq 0, \delta = 0°$), in-phase loading ($\Delta\sigma_0 = k\Delta\tau_0, \delta = 0°$) and out-of-phase loading (e.g. $\Delta\sigma_0 = 0.58\,\Delta\tau_0, \delta = 90°$) are shown in Fig. 4.2(a). It is worth noting that the multi-axial loading conditions described in Eqs. (4.4) and (4.5) yield the same maximum effective stress range regardless of phase angle according to:

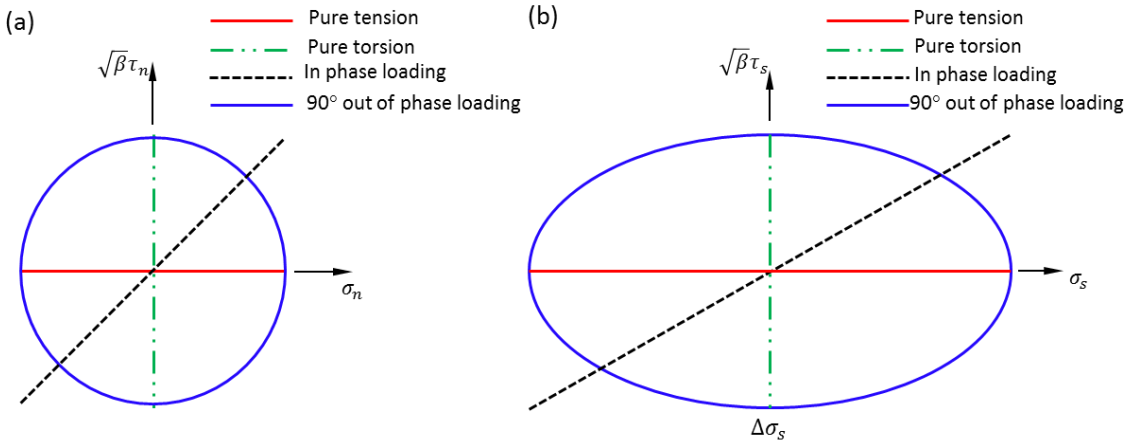

Fig. 4.2 Comparison of load paths between nominal and traction structural stress plane based representations: (a) nominal stress plane; (b) structural stress plane

$$\Delta\sigma_{n,e} = \sqrt{\Delta\sigma_0^2 + \beta\Delta\tau_0^2} \tag{4.6}$$

After mapping the load paths depicted in $\sigma_n - \sqrt{\beta}\tau_n$ plane (Fig. 4.2(a)) onto $\sigma_s - \sqrt{\beta}\tau_s$ plane, a shape change in load path often occurs, as shown in Fig. 4.2(b), since stress concentration for normal stress component is typically much higher than that for

shear stress, as to be further elaborated in Sec. 3. An alternative effective structural stress range, similar to longest chord concept [19] defined as:

$$\Delta\sigma_e = \max\{\sqrt{(\sigma_s^C - \sigma_s^D)^2 + \beta(\tau_s^C - \tau_s^D)^2}\} \tag{4.7}$$

can be introduced for measuring the maximum range experienced by these load paths shown in Fig. 4.2(b), where σ_s^C , σ_s^D , τ_s^C and τ_s^D are normal and shear structural stress components on $\sigma_s - \sqrt{\beta}\tau_s$ plane at any two points C and D that maximize the effective stress range $\Delta\sigma_e$. As such, the actual effective stress range ($\Delta\sigma_e$) incurred along the in-phase path should be the length of the straight line while the one incurred along an elliptical path should be the length of the long axis of the ellipse. They take on different values as shown in Fig.4.2 (b), which has been used in formulating a Moment of Load Path (MLP) based fatigue damage parameter for modeling load-path non-proportionality effects [18, 52] and will be further discussed in the next section.

4.2.2.2 Non-Proportionality Damage Parameter

As presented in detail by the same authors in a recent paper [18], consider a non-proportional load path from A to B, i.e., $\widetilde{AB}$, on $\sigma_s - \sqrt{\beta}\tau_s$ plane illustrated in Fig. 4.3, which can be shown to constitute one half cycle according to PDMR cycle counting procedure (see more detailed discussions by Dong et al [53] and Wei and Dong [54-55] in the context of PDMR cycle counting method). A multi-axial fatigue damage parameter D for any given non-proportional load path $\widetilde{AB}$ is assumed to consist of two parts:

$$D = D_P + D_{NP} \tag{4.8}$$

in which D_P represents damage caused by the reference loading event from A to B (i.e., $\overline{AB}$), which can be directly related to distance from A to B, or the effective stress range $\Delta\sigma_e$ defined in Eq. (4.7). D_{NP} represents load path non-proportionality caused fatigue damage due to any excursions of load path $\widetilde{AB}$ deviating from the reference load path ($\overline{AB}$). Therefore, one possible way of representing load path non-proportionality related damage along Path $\widetilde{AB}$ can be stated as follows, with respect to local $x' - y'$ coordinate system, as:

$$D_{NP} = \int_{AB} r' \cdot |\sin(\theta)| ds' \tag{4.9}$$

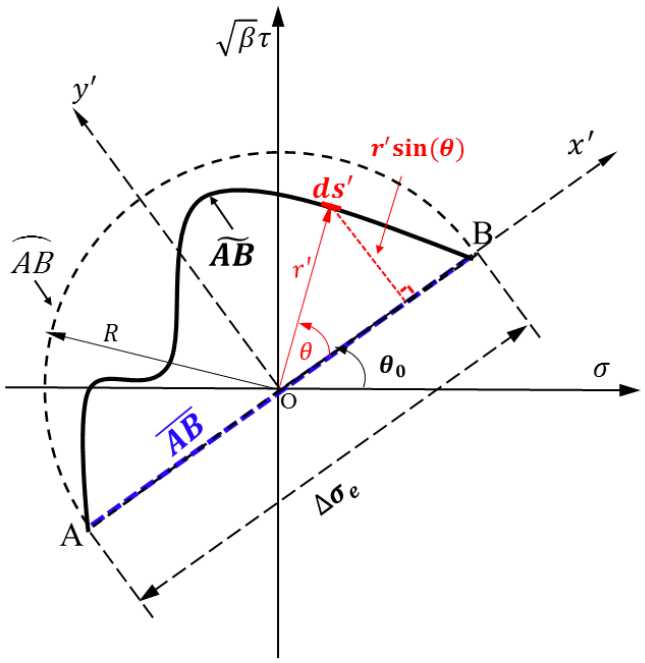

Fig. 4.3 Non-proportional load path $\widetilde{AB}$, non-proportional circular load path $\overset{\frown}{AB}$ and reference (proportional) load path $\overline{AB}$

It can then be shown [18] that, a dimensionless form of load path non-proportionality induced fatigue damage factor can be expressed as:

$$g_{NP} = \frac{D_{NP}}{D_{Max}} = \frac{\int_{AB} r' \left|\sin(\theta)\right| ds'}{\int_{AB} R \left|\sin(\theta)\right| ds'} = \frac{\int_{AB} r' \left|\sin(\theta)\right| ds'}{2R^2} \tag{4.10}$$

where D_{Max} represents the maximum possible non-proportional fatigue damage caused by the semi-circular load path [15-16] represented by dashed lines in Fig. 4.3 Then, g_{NP} in Eq. (4.10) can be referred as a normalized load-path non-proportionality damage factor with respect to the maximum possible damage D_{Max}, noting that g_{NP} varies from zero (corresponding to the proportional load path $\overline{AB}$) to unity (corresponding to the semi-circular load path AB). Then, a stress range parameter taking into account of non-proportional load path induced damage can be written as:

$$\Delta\sigma_{NP} = \Delta\sigma_e(1 + \alpha \cdot g_{NP}) \tag{4.11}$$

where $\Delta\sigma_e$ is defined as in Eq. (4.7) and it is the effective stress range of proportional reference path. Note that a material sensitivity parameter α is inserted in Eq. (4.11) to accommodate the fact that some materials are more sensitive to non-proportional multi-axial fatigue loading than others, as observed in [14, 52]. For various structure steels investigated [18], it is generally found that $\alpha \approx 1$ gives a reasonable correlation and will therefore be used in non-proportional multi-axial fatigue analysis of weld joints in the following sections. For aluminum alloys range from 2000 to 7000 series, they are observed to be less sensitive to non-proportional loading than structural steel and their material sensitivity parameter α vary from 0.35 to 0.5 depending on the ductility of aluminum alloys examined [52]. The specific procedures for material sensitivity determination can be found in [52].

Most of non-proportional fatigue tests considered in this paper employed a circular or elliptical load path (i. e. out-of-phase path in Fig. 4.2(b)) with a clearly defined phase angle between normal and shear stress component. For an elliptical load path defined by Eqs. (4.4) and (4.5), the non-proportionality damage factors (g_{NP}) can be analytically expressed as [52]:

$$g_{NP}(\sigma_0, \tau_0, \delta) = \frac{\eta}{2}\left(\eta + \frac{\arcsin(\sqrt{1-\eta^2})}{\sqrt{1-\eta^2}}\right) \tag{4.12}$$

where,

$$\eta = \frac{B}{A} = \sqrt{\frac{\left(\Delta\sigma_0^2 + \beta\Delta\tau_0^2\right) - \sqrt{\left(\Delta\sigma_0^2 + \beta\Delta\tau_0^2\right)^2 - 4\beta\Delta\sigma_0^2\Delta\tau_0^2\sin^2\delta}}{\left(\Delta\sigma_0^2 + \beta\Delta\tau_0^2\right) + \sqrt{\left(\Delta\sigma_0^2 + \beta\Delta\tau_0^2\right)^2 - 4\beta\Delta\sigma_0^2\Delta\tau_0^2\sin^2\delta}}} \tag{4.13}$$

in which *A* and B are major semi-axis length and minor semi-axis length of an elliptical load path.

4.2.3 Thickness and Bending Ratio Effects

Based on a two-stage crack growth model [40, 56], an equivalent normal structural stress parameter (ΔS_σ) taking into account of both plate thicknesses and bending ratio effect is given by Dong et al. [40] under normal traction stress dominated loading conditions as:

$$\Delta S_\sigma = \frac{\Delta\sigma_s}{t^{*\frac{2-m}{2m}} I(r_\sigma)^{\frac{1}{m}}} \tag{4.14}$$

In Eq. (4.14), $\Delta\sigma_s$ is traction structural stress range defined in Eq. (4.1); t^* is a relative thickness with respect to a reference thickness (t_{ref}), i.e., $t^* = t/t_{ref}$, which enables the

transferability of the resulting S-N curve for using a different reference thickness value such as those used in BS 7608 [57] etc. For the present discussions, $t_{ref} = 1mm$ is used here, which is consistent with the 2007 ASME Code [47]. Also note that $m = 3.6$ which was obtained by correlating both short and long crack growth data [40] under Mode I loading conditions. The integral $I(r_\sigma)$ is a dimensionless function of bending ratio r_σ, defined as:

$$r_\sigma = \frac{|\Delta\sigma_b|}{|\Delta\sigma_m|+|\Delta\sigma_b|} \tag{4.15}$$

The specific form of $I(r_\sigma)$ can be found in [40, 47], developed under dominantly uniaxial fatigue loading conditions. For treatment of multi-axial fatigue, we postulate that an equivalent structural stress parameter takes a similar form, as:

$$\Delta S_e = \frac{\Delta\sigma_e}{t^{*\frac{2-m}{2m}} I(r_e)^{\frac{1}{m}}} \tag{4.16}$$

where $\Delta\sigma_e$ is shown in Eq. (4.7) and r_e is defined as:

$$r_e = \frac{|\Delta\sigma_{b,e}|}{|\Delta\sigma_{m,e}|+|\Delta\sigma_{b,e}|} \tag{4.17}$$

in which

$$\Delta\sigma_{b,e} = \sqrt{\Delta\sigma_b^2 + \beta\Delta\tau_b^2} \tag{4.18}$$

$$\Delta\sigma_{m,e} = \sqrt{\Delta\sigma_m^2 + \beta\Delta\tau_m^2} \tag{4.19}$$

since $\Delta\tau_b$ is small in all cases studied in this paper (see Table 4.2), r_e can be written as, by ignoring $\Delta\tau_b$ term in the denominator of Eq. (4.17):

$$r_e = \frac{\sqrt{\Delta\sigma_b^2 + \beta\Delta\tau_b^2}}{\sqrt{\Delta\sigma_m^2 + \beta\Delta\tau_m^2} + |\Delta\sigma_b|} \tag{4.20}$$

Note that m in Eq. (4.16) is assumed to be the same as the one developed for Mode I crack growth crack growth, i.e., $m = 3.6$ due to lack of comprehensive short crack and long crack growth data under Mode III loading conditions at this time.

With load path dependency considered by Eq. (4.11), the final form of proposed equivalent stress parameter that takes into account of load path non-proportionality, thickness and bending ratio effect for non-proportional multi-axial fatigue loading becomes:

$$\Delta S_{NP} = \frac{\Delta\sigma_{NP}}{t^{*\frac{2-m}{2m}} I(r_e)^{\frac{1}{m}}} \tag{4.21}$$

In the following Section, the effectiveness of Eq. (4.21) in correlating well-documented non-proportional multi-axial fatigue test data will be examined.

4.3 Analysis of Test Data

4.3.1 Data Sources and Assessment

It is important that any proposed new multi-axial fatigue parameter such as the one given in Eq. (4.21) be validated with a large amount of test data from different joint geometries, different multi-axial loading conditions, and multiple sources. In doing so, some essential requirements must be imposed to ensure that test data considered in such a validation effort were documented with sufficient details for determining parameters involved in Eq. (4.21) and consistent failure mode and failure criteria for comparison

purposes. These requirements and considerations for including a particular set of existing test data are as follows:

(a) Specimen geometry and testing conditions: To facilitate the computation of traction stress based SCFs (see Sec. 3.2), detailed specimen geometry and dimensions must be available for creating a sufficiently detailed finite element model, including specimen mounting and loading conditions

(b) Weld toe failure mode: Only test data that exhibit weld toe failure are considered in this study since weld root or throat failures would require more detailed information on weld size and penetration in each specimen, as discussed recently by Xing et al. [58]

(c) As-welded versus stress-relieved conditions: Test data to be considered in this paper should have a clear indication on if welded components had gone through post-weld heat treatment (PWHT) based stress-relief prior to testing. A cursory review of existing multi-axial test data indicates that there exist noticeable differences in S-N data between as-welded and stress-relieved conditions

(d) Through-thickness failure definition: Consistent with the formulation of the equivalent structural stress parameter in Eq. (4.21), recalling through-thickness hypothetical cut in Fig. 4.2, test data to be considered here should also have a similar through-thickness based failure criterion (or there is evidence suggesting applicability of a similar failure criterion that can be inferred from test conditions reported) and adequate monitoring procedure for determining when to stop in fatigue testing.

After a comprehensive literature search and detailed critical assessments, various component types, loading conditions, test sources [27-36] to be considered for further examination in this study are illustrated in Fig. 4.4 under stress-relieved and Fig. 4.5 under as-welded conditions, respectively. Additional test details are given in Table 4.1.

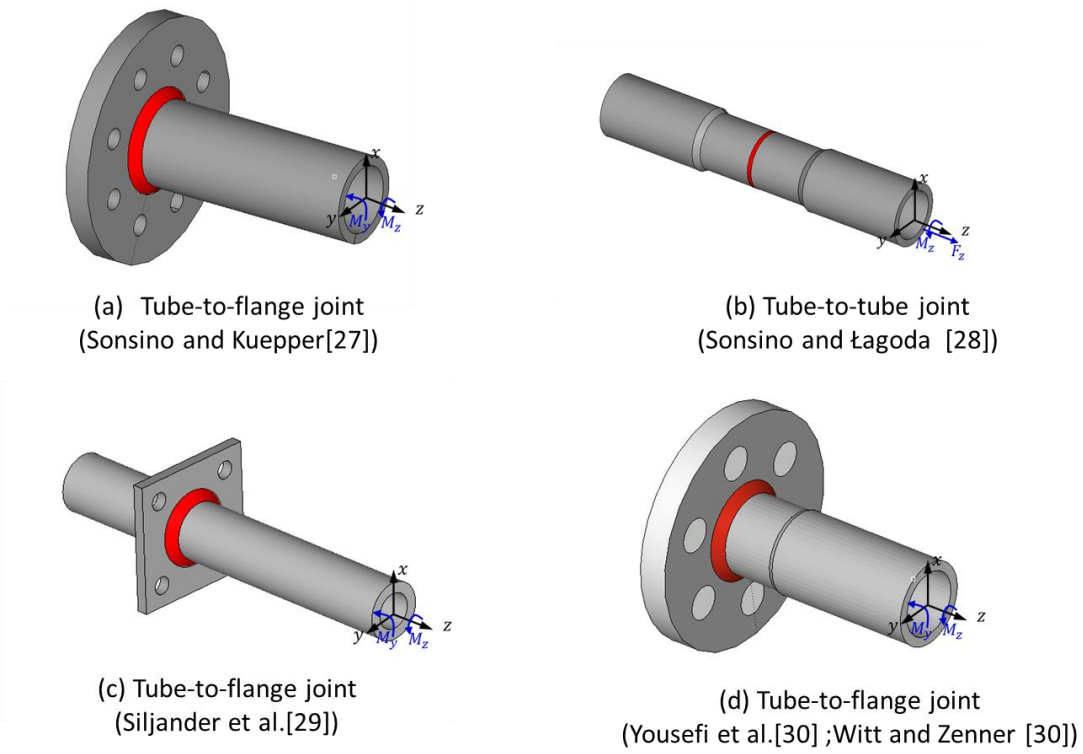

Fig. 4.4 Residual-stress-relieved multi-axial fatigue test specimens

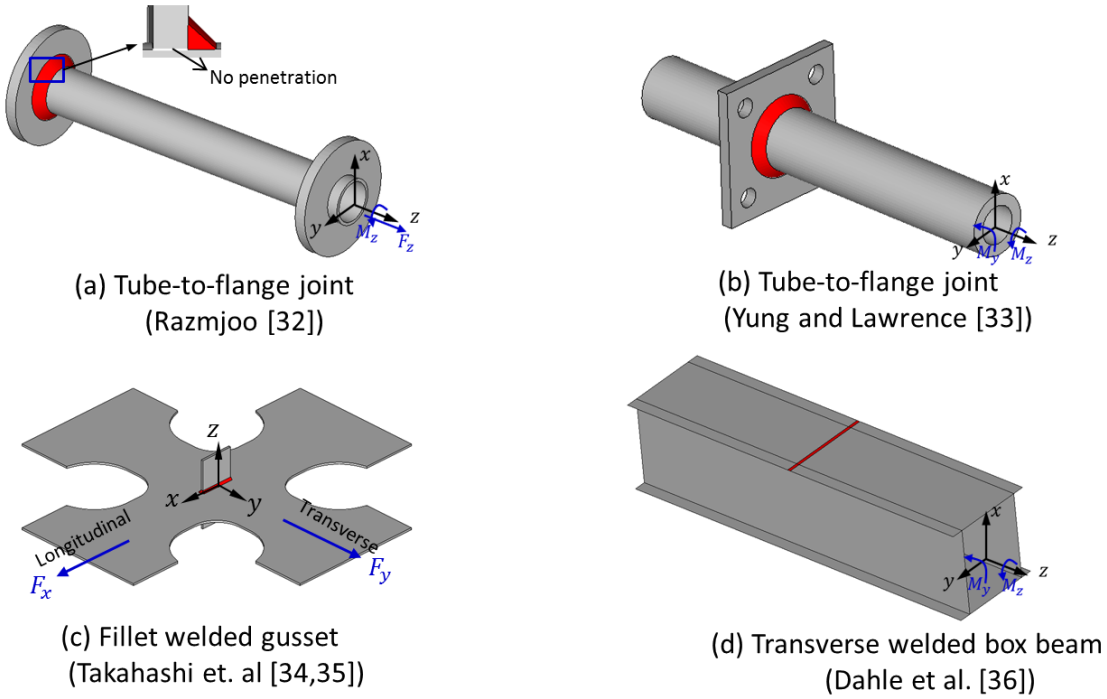

Fig. 4.5 As-welded multi-axial fatigue test specimens and loading conditions

Table.4.1 A summary of multi-axial fatigue tests and test details to be examined in this paper

Multi-axial fatigue test	**Joint type**	**Steels types**	**thickness**	**Load combinations**	**R ratio**	**Shear stress R ratio**	**Residual stress state**
Sonsino and Kueppers[27]	tube-to-flange	StE460	10	Bending, torsion	-1	-1	relieved
Sonsino and Łagoda [28]	tube-to-tube	StE460	6	Tension, torsion	-1	-1	relieved
Siljander et al.[29]	tube-to-plate	ASTM A519	7.95	Bending, torsion	-1, 0	-1, 0	relieved
Yousefi et al.[30]	tube-to-flange	P 460	8	Bending, torsion	-1, 0	-1, 0	relieved
Witt and Zenner [31]	tube-to-flange	StE 460M	8	Bending, torsion	-1	-1	relieved
Razmjoo [32]	tube-to-flange	BS4360 Grade 50E	3.2	Tension, torsion	0	0	as-welded

Yung and Lawrence [33]	tube-to-plate	ASTM A519	7.95	Bending, torsion	-1	-1	as-welded
Takahashi et al. [34,35]	fillet welded gusset	JIS SM400 B	6	Tension, Tension	0	0	as-welded
Dahle et al. [36]	butt weld box structure	Domex 350	10	Bending, torsion	-1	0	as-welded

4.3.2 Traction Structural Stress Analysis

For all test data determined fit for the criteria given in the previous section (see Table 4.1), traction structural stress analysis is performed for each joint type to extract structural stress based SCF. As a calculation example for demonstration purpose, Fig. 4.6 shows a solid finite element model used for computing traction stress based SCF for the tube-to-flange fillet weld specimens tested by Sonsino and Kueppers [27], which is also shown in sketches in Fig. 4.1. Nodal forces gathered along weld toe line into tube thickness are first transformed to mid-wall thicknesses (see Nie and Dong, 2012 [51]). Then simultaneous equations are solved for line forces and line moments along mid-thickness positions, which enter Eqs. (4.1)-(4.2) for calculating traction structural stress based SCFs, as follows:

$$K_{\sigma_s} = \frac{\sigma_s}{\sigma_n} \tag{4.22}$$

$$K_{\tau_s} = \frac{\tau_s}{\tau_n} \tag{4.23}$$

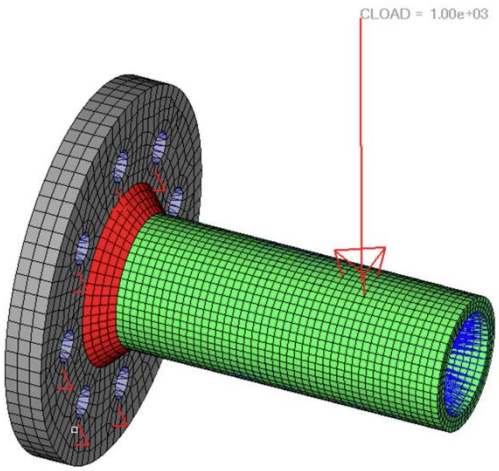

Fig. 4.6 3D solid finite element model for structural stress calculation of tube-to-flange joint used by Sonsino and Keuppers [27]

where K_{σ_s} with respect to applied remote bending stress (σ_n) and K_{τ_s} with respect to applied remote shear stress (τ_n) are found to be 1.71 and 1.1. These SCF values are presented in terms of their membrane and bending parts, as given in Table 4.2. For all other test components shown in Fig. 4.4 and Fig. 4.5, their corresponding SCF results are also listed for comparison purposes in Table. 4.2. It is important to note that the normal structural stress SCF for specimens tested by Siljander et al. [29] (see Fig.4.4(c) and Yung and Lawrence [33] (see Fig. 4.5(b)) is significantly less than those from tube-to-flange weld specimens by Sonsino and Kueppers [27], Yousefi et al.[30] and Witt and Zenner [31]. This is because in the former, the tube section on the backside of the flange is also clamped during fatigue loading, carrying a part of applied load. A relatively higher stress concentration in tube-to-flange welded specimens tested by Razmjoo [32] can be attributed to the fact that there exists a root gap behind the fillet weld between tube and flange (see Fig. 4.5 (a)), which only allows load transfer from tube wall through fillet weld to flange plate under remote tension conditions.

For all specimens examined, it can be observed that shear traction stress SCF contributed by τ_b is relatively small comparing with normal traction stress component σ_b. These computed K_{σ_s} and K_{τ_s} along with time histories in terms of applied nominal stress components given by each data source enable the generation of load path descriptions in structural stress plane ($\sigma_s - \sqrt{\beta}\tau_s$), as illustrated in Fig. 4.2(b). These results can then be used to compute both effective stress range ($\Delta\sigma_e$) through Eq. (4.7) and the corresponding load path non-proportionality damage factor through Eq. (4.10), as described in the next section.

In addition, hot spot stress based SCFs using surface extrapolation procedures given in IIW [41] for test specimens shown in Figs. 4.4 and 4.5 are also listed in Table 4.2. These values will be used in the next section for evaluating multi-axial fatigue evaluation procedures given Eurocode 3 and IIW as a comparison with the new method proposed in this study. Note that the majority of hot spot SCFs listed in the last two columns of Table 4.2 can are taken from [38] and the rest of them are calculated within this study.

Table. 4.2 Structural stress based SCFs calculated for test specimens/conditions described in Table. 4.1

Multi-axial fatigue test	Structural stress SCF - normal stress $(\sigma_m + \sigma_b)/\sigma_n$		Structural stress SCF - shear stress $(\tau_m + \tau_b)/\tau_n$		Hot spot SCF - normal stress σ_h/σ_n	Hot spot SCF - shear stress τ_h/τ_n
	Membrane part σ_m/σ_n	Bending part σ_b/σ_n	Membrane part τ_m/τ_n	Bending part τ_b/τ_n		
Sonsino and Kueppers[27]	0.925	0.79	0.97	0.13	2.2	1.1
Sonsino and Łagoda [28]	1.0	0	1.0	0	1.0	1.0
Siljander et	0.83	0.59	0.95	0.15	1.25	1.1

al.[29]						
Yousefi et al.[30]	0.80	0.89	0.97	0.13	1.37*	1.1*
Witt and Zenner [31]	0.80	0.89	0.97	0.13	1.37*	1.1*
Razmjoo [32]	0.94	0.96	0.96	0.14	1.4	1.1
Yung and Lawrence [33]	0.83	0.59	0.95	0.15	1.25	1.1
Takahashi et. al [34,35]	1.41	0.54	0	0	1.73*	0
Dahle et al. [36]	1	0	1	0	1.0	1.0

*: Hot spot SCF is calculated in this study according to IIW [41]

4.3.3 Non-Proportionality Damage Factor Calculation

The calculation of non-proportionality damage factor g_{NP} in Eq. (4.21), defined in Eq. (4.10), will be demonstrated using two non-proportional multi-axial load cases given in Tables 4.1: One is the test done by Sonsino and Kueppers [27] and the other involving a more complex non-proportional loading generated by asynchronous sinusoidal wave forms of bending and shear stress components [30].

Consider the elliptical load path case shown in Fig. 4.2(b). For the calculation of the load path non-proportionality damage factor g_{NP}, the corresponding reference proportional load path (solid line along horizontal axis) and the reference non-proportional load path giving the maximum non-proportionality (i.e., the circular load path shown as dashed lines) is plotted in Fig. 4.7. The load path non-proportionality factor $g_{NP} = 0.6$ can be calculated directly from Eq. (4.13) for the actual elliptical load path (long dashed lines) used by Sonsino and Kueppers [27]. Geometrically, the dimensionless non-proportionality factor (g_{NP}) as a result of the elliptical load path is

simply the ratio of the moment of the elliptical load path with respect to its major axis to that of the circular load path in the structural stress plane.

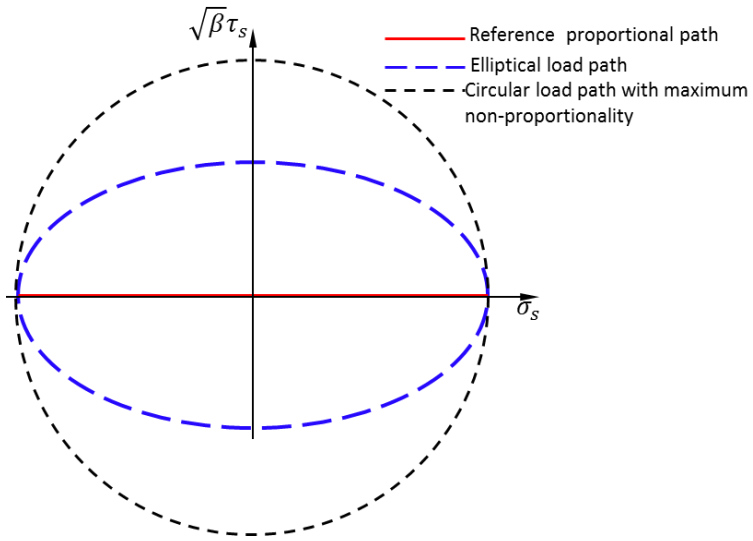

Fig. 4.7 Illustration of calculation procedure for non-proportionality factor – elliptical load path used by Sonsino and Kueppers [27].

As a second load case, consider one load path involving asynchronous loading of bending and torsion with a frequency ratio of $f_b/f_t = 1/5$ where f_b represents the frequency of applied sinusoidal bending and f_t of applied sinusoidal torsion (see solid line in Fig. 4.8), as used by Yousefi et al.[30]. Before computing g_{NP}, fatigue cycles involved in the load path need to be determined, which can be done by PDMR method [53-55]. As a result, the first counted half cycle can be determined by monotonically searching along the path formed by $AC - CC^* - C^*E - EE^* - E^*B$, which yields the largest effective stress range as the distance between Positions A and B. The calculation of load path non-proportionality of the counted half cycle with the largest effective stress range is illustrated in Fig. 4.9 in which reference proportional path is represented by $\overline{AB}$

and maximum non-proportional damage path denoted by dotted circle. By following Eq. (4.10), the numerically calculated load path non-proportionality for this counted half cycle is 0.66. All the other PDMR counted load path segments and their load path non-proportionality damage factors for the whole loading block (Fig.4.8) are listed in Table. 4.3. More details on the analysis of such an asynchronous load path can be found in [18].

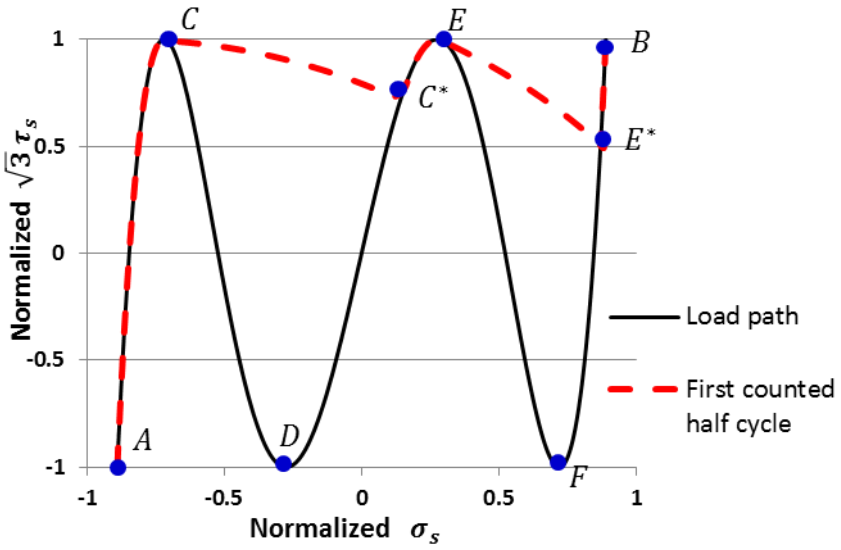

Fig. 4.8 Load path representation in normalized $\sigma_s - \sqrt{3}\tau_s$ plane and illustration of PDMR based path determination (red dashed lines) for the 1st half cycle exhibiting the maximum stress range

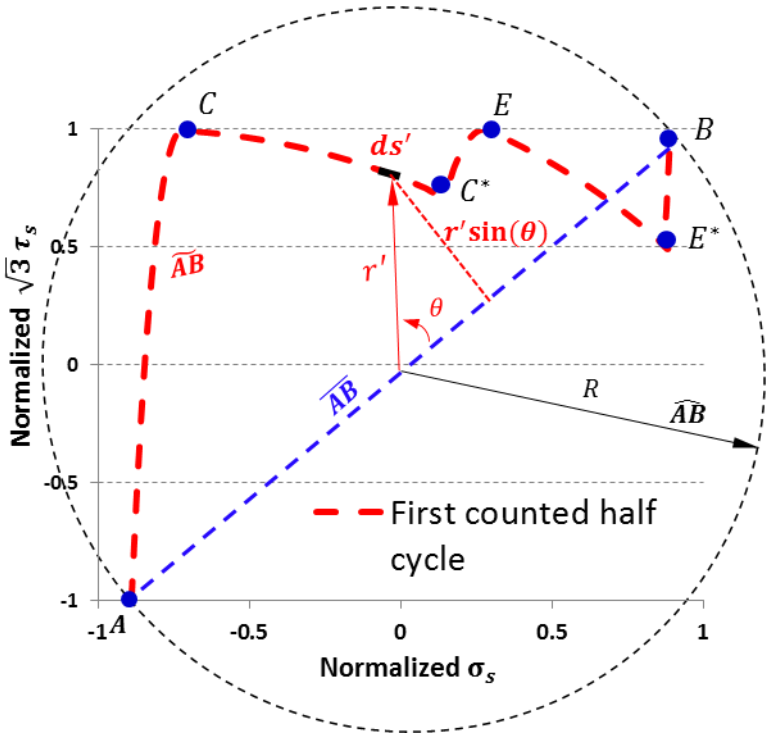

Fig. 4.9 Illustration of load path non-proportionality (g_{NP}) calculation for load path AC-CC*-C*E-EE*-E*B, determined by PMDR in Fig. 4.8

Table 4.3 PDMR counted cycles (N_i), effective stress ranges ($\Delta\sigma_{e,i}$), non-proportionality factor $g_{NP,i}$ for asynchronous loading case with frequency ratio of $f_b/f_t = 1/5$

ID (i)	Counted cycles (N_i)	Effective stress range ($\Delta\sigma_{e,i}$)		Load path	Non-proportional factor($g_{NP,i}$)
		Stress range	Range value		
1	1	AB	2.67	AC-CC*-C*E-EE*-E*B	0.66
2	1	CD	2.04	CD	0.1
3	1	EF	2.03	EF	0.1
4	1	DC*	1.8	DC*	0.09
5	1	FE*	1.45	FE*	0.08

Following the procedures illustrated with the two examples described above, g_{NP} values are calculated for all test conditions. The material sensitivity parameter (α) in Eq.

(4.21) for all structural steels involved in this study is assumed to be unity, i.e., $= 1$, with justifications being given in [18].

4.3.4 Data Correlation Using Proposed Method

Since the majority of non-proportional fatigue tests in Table 4.1 are under stress-relieved conditions, we will examine this group of test data first. By using the proposed equivalent structural stress range given in Eq. (4.21), all stress-relieved test data shown in Table 4.1 are plotted in Fig. 4.10 (a) in which test data corresponding to proportional multi-axial loading are shown as solid symbols while those corresponding to non-proportional loading are shown as empty symbols. The overall correlation gives a standard deviation of 0.33 and a correlation of coefficient (R^2) of 0.825. It should be pointed out that among the test data shown, those by Yousefi et al. [30] involving asynchronous loading paths and Siljander et al.'s [29] involving triangular load paths, require PDMR based cycle counting for breaking down complex load paths into individual fatigue cycles in the same manner as shown in Fig. 4.8 and Fig. 4.9, as summarized in Table 4.3. Then, Palmgren-Miner rule based equivalent stress range with respect to one equivalent cycle for each load block is used for plotting purpose in Fig. 4.10 (a) (see [18] for further details).

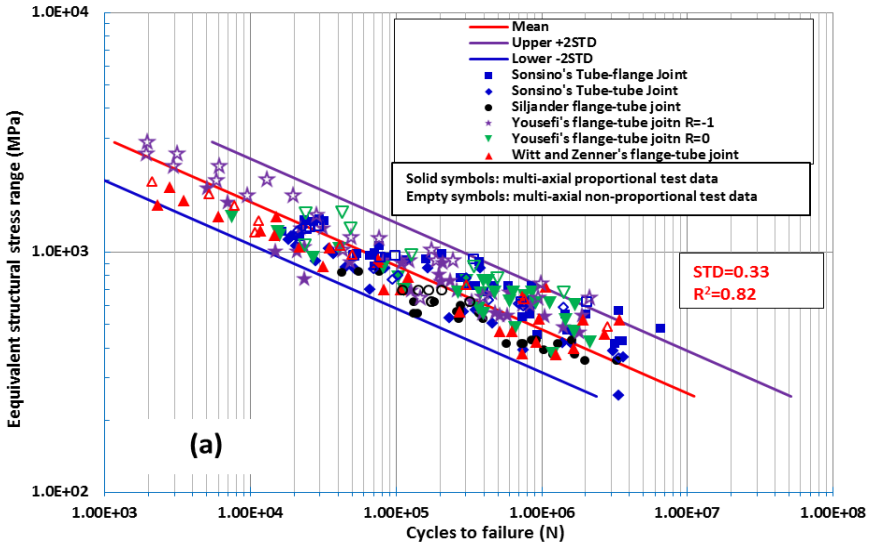
Mean
Upper +2STD
Lower -2STD
Sonsino's Tube-flange Joint
Sonsino's Tube-tube Joint
Siljander flange-tube joint
Yousefi's flange-tube joitn R=-1
Yousefi's flange-tube joitn R=0
Witt and Zenner's flange-tube joint
Solid symbols: multi-axial proportional test data
Empty symbols: multi-axial non-proportional test data
STD=0.33
R²=0.82
(a)
Eequivalent structural stress range (MPa)
Cycles to failure (N)
1.0E+04
1.0E+03
1.0E+02
1.00E+03
1.00E+04
1.00E+05
1.00E+06
1.00E+07
1.00E+08

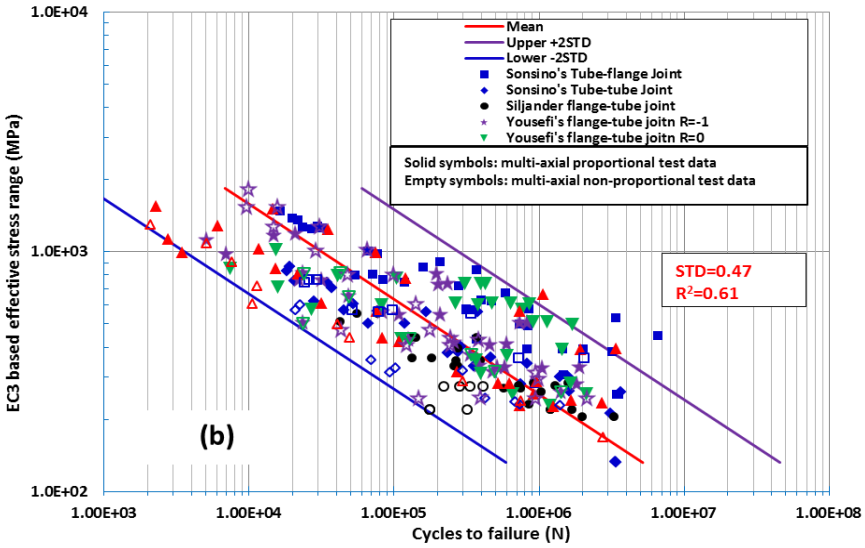
Mean
Upper +2STD
Lower -2STD
Sonsino's Tube-flange Joint
Sonsino's Tube-tube Joint
Siljander flange-tube joint
Yousefi's flange-tube joitn R=-1
Yousefi's flange-tube joitn R=0
Solid symbols: multi-axial proportional test data
Empty symbols: multi-axial non-proportional test data
STD=0.47
R²=0.61
(b)
EC3 based effective stress range (MPa)
Cycles to failure (N)
1.0E+04
1.0E+03
1.0E+02
1.00E+03
1.00E+04
1.00E+05
1.00E+06
1.00E+07
1.00E+08

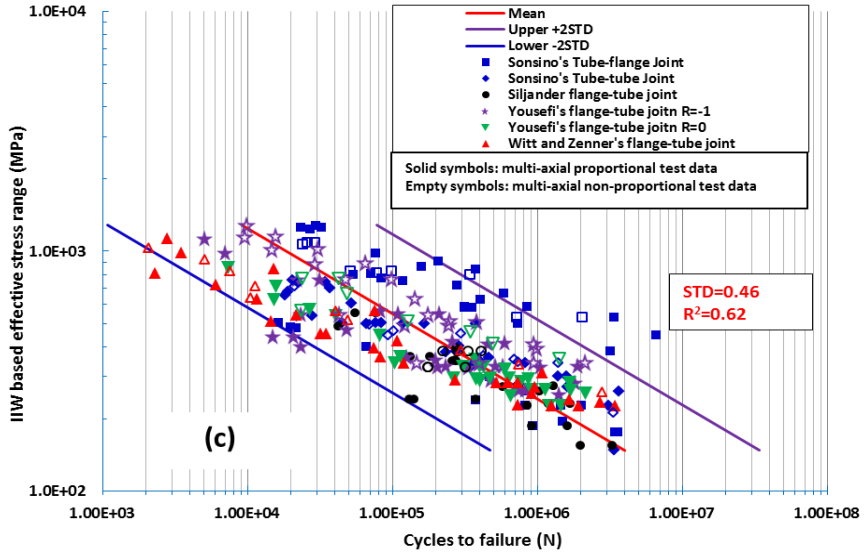
Mean
Upper +2STD
Lower -2STD
Sonsino's Tube-flange Joint
Sonsino's Tube-tube Joint
Siljander flange-tube joint
Yousefi's flange-tube joitn R=-1
Yousefi's flange-tube joitn R=0
Witt and Zenner's flange-tube joint
Solid symbols: multi-axial proportional test data
Empty symbols: multi-axial non-proportional test data
STD=0.46
R²=0.62
(c)
IIW based effective stress range (MPa)
Cycles to failure (N)
1.0E+04
1.0E+03
1.0E+02
1.00E+03
1.00E+04
1.00E+05
1.00E+06
1.00E+07
1.00E+08

Fig. 4.10 Correlation of test data among three different multi-axial fatigue methods – stress relieved conditions: (a) proposed equivalent structural stress range according to Eq. (4.21); (b) Eurocode 3 (using surface extrapolated hot spot stress definition); (c) IIW recommendation (using surface extrapolated hot spot stress definition)

In the same manner, Fig. 4.11 (a) shows the equivalent structural stress (Eq. (4.21)) based correlation of the test data under as-welded conditions, which contains fewer data points than that under stress-relieved condition. Again, the proposed equivalent structural stress parameter given in Eq. (4.21) seems to provide an effective data correlation among test data from different component geometries and loading conditions. Furthermore, the ASME master S-N curve scatter band [47] is also given in Fig. 4.11 (a) for comparison purpose, which represent large scale fatigue test data obtained mostly under as-welded and dominantly unixial fatigue loading conditions. The majority of the mulaxial test data (under either proportional or non-proportional loading conditions) analyzed here seem to fall within the ASME scatter band. This suggests that both uniaxial and multiaxial test data can be reasonablly represented by a single scatter band once Eq. (4.21) is used.

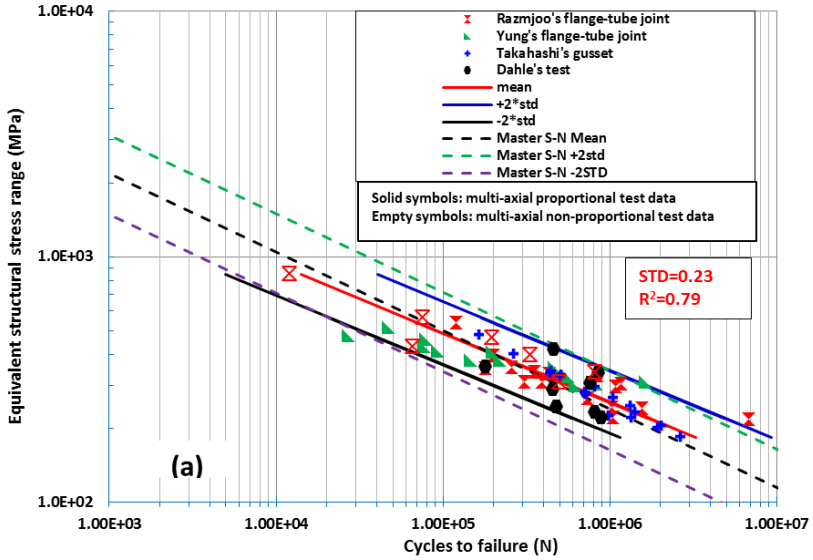
Razmjoo's flange-tube joint
Yung's flange-tube joint
Takahashi's gusset
Dahle's test
mean
+2*std
-2*std
Master S-N Mean
Master S-N +2std
Master S-N -2STD
Solid symbols: multi-axial proportional test data
Empty symbols: multi-axial non-proportional test data
STD=0.23
R²=0.79
(a)
Equivalent structural stress range (MPa)
Cycles to failure (N)
1.0E+04
1.0E+03
1.0E+02
1.00E+03
1.00E+04
1.00E+05
1.00E+06
1.00E+07

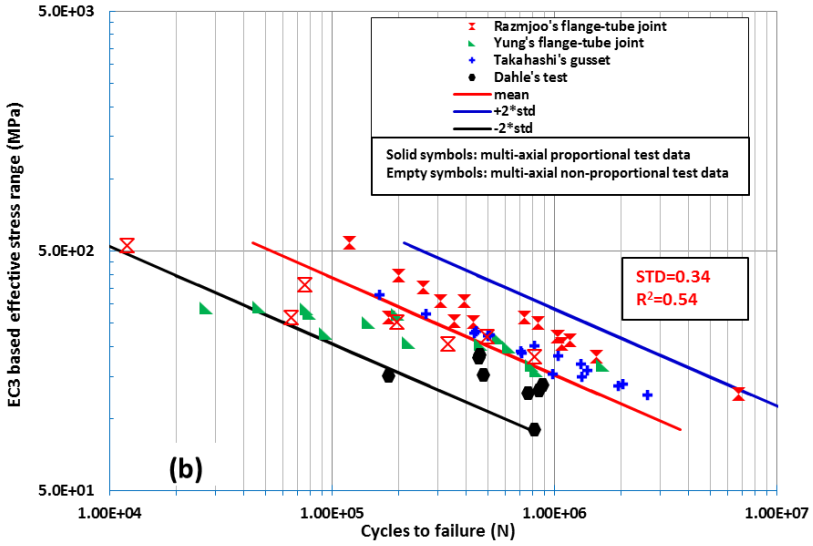
Razmjoo's flange-tube joint
Yung's flange-tube joint
Takahashi's gusset
Dahle's test
mean
+2*std
-2*std
Solid symbols: multi-axial proportional test data
Empty symbols: multi-axial non-proportional test data
STD=0.34
R²=0.54
(b)
EC3 based effective stress range (MPa)
Cycles to failure (N)
5.0E+03
5.0E+02
5.0E+01
1.00E+04
1.00E+05
1.00E+06
1.00E+07

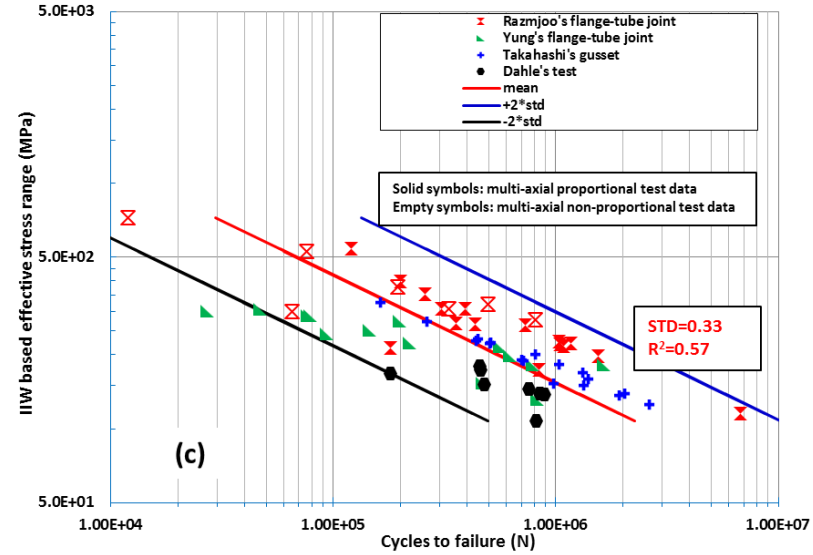
Razmjoo's flange-tube joint
Yung's flange-tube joint
Takahashi's gusset
Dahle's test
mean
+2*std
-2*std
Solid symbols: multi-axial proportional test data
Empty symbols: multi-axial non-proportional test data
STD=0.33
R²=0.57
(c)
IIW based effective stress range (MPa)
Cycles to failure (N)
5.0E+03
5.0E+02
5.0E+01
1.00E+04
1.00E+05
1.00E+06
1.00E+07

Fig. 4.11 Correlation of test data (as-welded conditions) among three different multi-axial fatigue methods: (a) proposed equivalent structural stress range according to Eq. (4.21); (b) Eurocode 3 (using surface extrapolated hot spot stress definition); (c) IIW recommendation (using surface extrapolated hot spot stress definition)

4.3.5 Data Correlation Using Eurocode 3 and IIW Methods

In dealing with both multi-axial fatigue (both for proportional and non-proportional loading), either nominal stress or hot spot stress can be used through an interaction equation between normal and shear stress components, according to Eurocode 3 [46] and IIW [41]. There are no cyclic counting procedures given when dealing with complex load paths such as asynchronous sinusoidal load paths by Youselfi et al. [30], as illustrated in Fig. 4.8. Therefore, fatigue cycle definitions by the original authors are used here for data correlation purposes in using the two methods, which can be questionable according to recent developments in multi-axial cycle counting [53-55, 18]. As suggested by one of the reviewers of this manuscript, surface extrapolation based hot spot stresses, instead of nominal stresses, are used here for examining how the same test data shown in Figs. 4.10 (a) and Fig. 4.11 (a) can be correlated using Eurocode 3 and IIW methods.

According to Eurocode 3 [46], multi-axial fatigue can be assessed using the following interaction equation:

$$\left(\frac{\Delta\sigma_h}{\Delta\sigma_f}\right)^3 + \left(\frac{\Delta\tau_h}{\Delta\tau_f}\right)^5 \leq D_{EC} \tag{4.24}$$

where $\Delta\sigma_h$ and $\Delta\tau_h$ are normal and shear hot spot stress ranges calculated based on their respective nominal stress ranges and hot spot stress SCFs listed in Table 4.2; $\Delta\sigma_f$ is referred to as fatigue strength under pure axial loading, $\Delta\tau_f$ fatigue strength under pure

shear loading, and $D_{EC} = 1$ for both proportional and non-proportional loading conditions. Note that the left side of Eq. (4.24) represents a simple linear summation of the damage caused by each of two stress components carrying a negative inverse slope of 3 and 5 in S-N curve in log-log scale, respectively. Eq. (4.24) can be rewritten in an effective stress range form for facilitating data plotting in Fig. 4.10 (b) and Fig. 4.11 (b):

$$\Delta\sigma_{EC} = \sqrt[3]{(\Delta\sigma_h)^3 + k_{EC}\,(\Delta\tau_h)^5} \tag{4.25}$$

where $k_{EC} = {\Delta\sigma_f}^3/{\Delta\tau_f}^5$.

The method recommended by IIW [41] has the following form:

$$\left(\frac{\Delta\sigma_h}{\Delta\sigma_f}\right)^2 + \left(\frac{\Delta\tau_h}{\Delta\tau_f}\right)^2 \leq D_{IIW} \tag{4.26}$$

where $k_{IIW} = {\Delta\sigma_f}^2/{\Delta\tau_f}^2$ in which $\Delta\sigma_f$ and $\Delta\tau_f$ are defined in the same way as in Eq. (4.24) and the sum of total damage D_{IIW} takes on the value of 1 for proportional loading conditions and 0.5 for non-proportional loading conditions. Again, for data plotting purpose, Eq. (4.26) can be rewritten as:

$$\Delta\sigma_{IIW} = \frac{1}{\sqrt{D_{IIW}}}\sqrt[2]{(\Delta\sigma_h)^2 + k_{IIW}(\Delta\tau_h)^2} \tag{4.27}$$

With the hot spot stress SCF values given in Table 4.2, the same test data shown in Fig. 4.10 (a) corresponding to stress-relieved conditions can be presented using Eurocode 3 (Eq. (4.25)) and IIW (Eq. (4.27)) methods, as shown in Fig. 4.10 (b) and Fig. 4.10 (c), respectively. As can be seen by comparing the standard deviations among the three methods, the newly proposed equivalent stress parameter according to Eq. (4.21) (see Fig.4.10 (a)) gives the smallest standard deviation (at 0.33) among the three methods,

whereas Eurocode 3 and IIW methods yield a standard deviation of above 0.46. Under as-welded conditions, Fig. 4.11 shows the comparison among the three methods. Again, the proposed equivalent structural stress is seen effective in collapsing as-welded test data into a narrower band (Fig. 4.11 (a)) than Eurocode 3 and IIW methods (Fig. 4.11 (b) and Fig.4.11 (c) respectively).

4.4 Design S-N Curve Representation

In addition to its ability to consistently capturing proportional and non-proportional load path effects on fatigue damage, the equivalent stress parameter in Eq. (4.21) shares a similar structure to that used in the master S-N curve method adopted by ASME Div 2 [47] and API 579 [48]. It would be useful to examine the equivalent stress parameter given by Eq. (4.21) in terms of its ability for fatigue life evaluation under more general conditions regardless of stress-relieved or as-welded conditions, uniaxial dominated or multi-axial loading conditions with a varying degree of load-path non-proportionality. For comparison purposes, both Eurocode 3 and IIW methods will also be examined in this context.

4.4.1 Equivalent Stress Parameter Incorporating Stress Ratio Effects

As noted in Sec. 3.1, there exist noticeable differences between as-welded and stress-relieved conditions in that under stress-relieved conditions, test data tends show a noticeable upward shift in S-N plots by comparing Fig. 4.10 (a) and Fig. 4.11 (a). The 2007 ASME Code [47] provides an applied stress ratio (R) correction scheme for an added conservatism, which is derived based on a two-stage crack growth model [40] under ideal stress-relieved conditions. As such, it can be shown that the equivalent structural stress parameter in Eq. (4.21) becomes:

$$\Delta S_{NP}^{R} = \frac{\Delta\sigma_{NP}}{(1-R)^{\frac{2}{m}}\, t^{*\frac{2-m}{2m}}\, I(r_e)^{\frac{1}{m}}} \tag{4.28}$$

Note that the term $(1-R)^{\frac{2}{m}}$ is valid for negative R, $(1-R)^{\frac{1}{m}}$ for positive R when dealing with stress-relieved test data, and is set as unity for applications under as-welded conditions. Applying Eq. (4.28) to the test data in both Fig. 4.10 (a) and 4.11 (a) leads to the results shown in Fig. 4.12, in which ASME design master S-N curve scatter band (i.e., mean ± 2 STD) is also shown. The result suggests a rather reasonable comparison between all multi-axial test data analyzed in this paper and those (over 1000 tests) under uniaxial loading conditions used by 2007 ASME Code. Even though a somewhat poor correlation occurs at high cycle regime, say above 10^6, the use of the ASME design S-N curve yields conservative life estimates.

Another way of assessing fatigue life predictability resulted from using the ASME design S-N curve given in Fig. 4.12 is to examine the predicted lives versus actual lives from tests for all test data considered in this paper, as shown in Fig. 4.13 containing a total of 306 multi-axial fatigue test results. Except for few data points, most of the predicted fatigue lives are within a factor of 4 of actual fatigue lives obtained from tests, demonstrating the effectiveness and robustness of the equivalent structural stress as a multi-axial fatigue damage parameter.

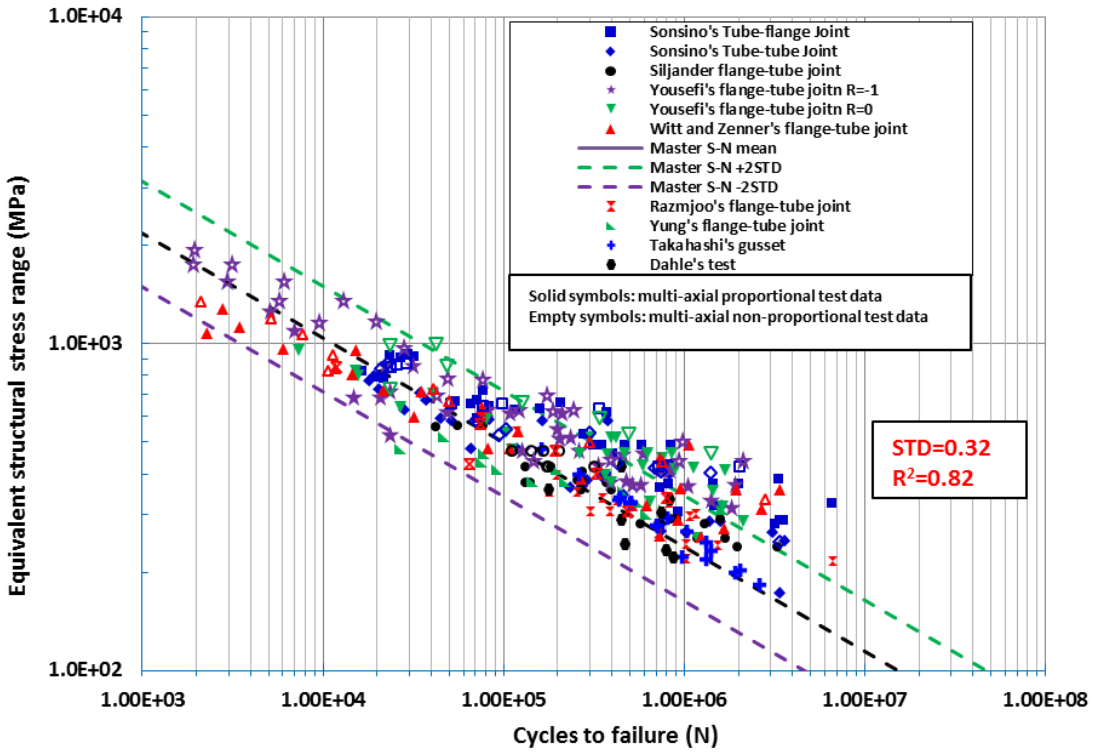

Fig. 4.12 Equivalent structural stress range based correlation of all test data including stress ratio using Eq. (4.28)

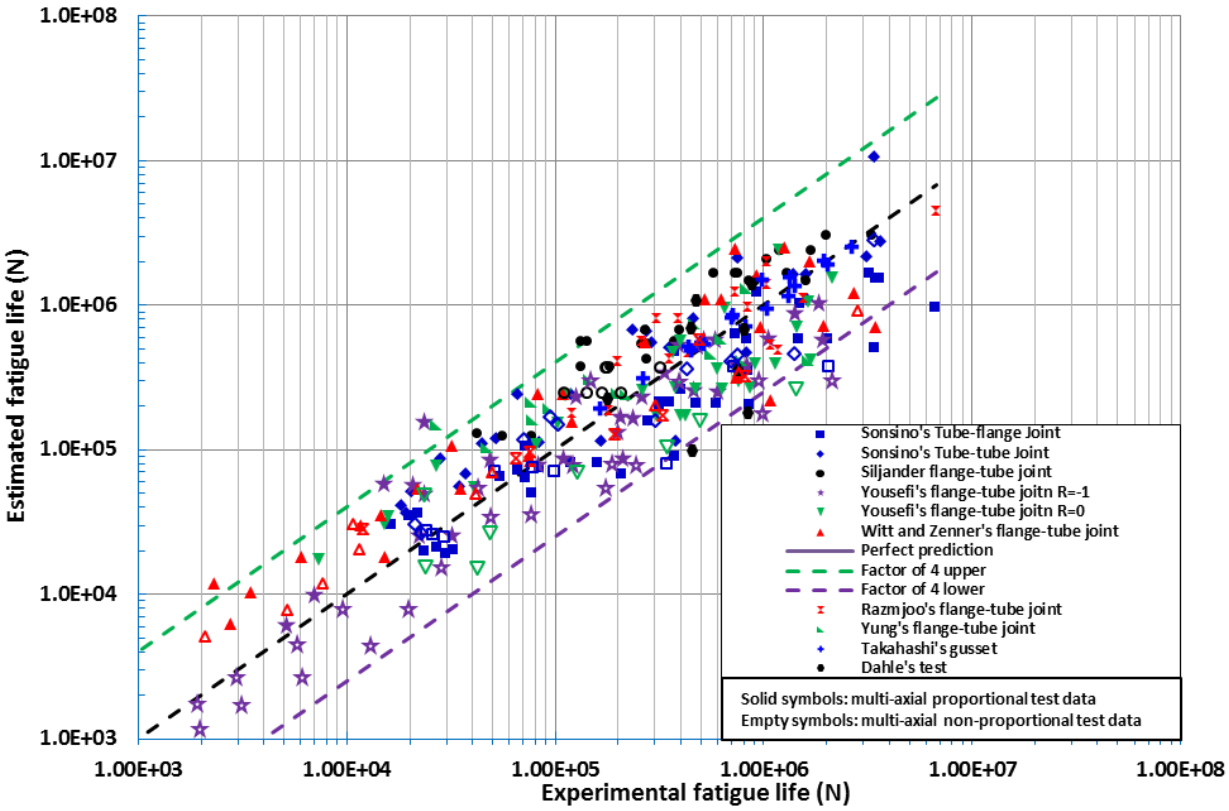

Fig. 4.13 Experimental fatigue life vs. predicted fatigue life by the proposed equivalent structural stress parameter (Eq. (4.28))

4.4.2 Eurocode 3 and IIW Methods

Built upon the results discussed in Sec. 3.5 in which as-welded and stress-relieved conditions are treated separately, both sets of the results can be combined by introducing a correction against applied stress ratio (R) for stress-relieved conditions. To do so in the context of Eurocode 3 [46] method, the hot spot stress component ranges given in Eq. (4.25) is calculated by its tension part of stress cycle plus 60% of compression part of the stress cycle. Similarly, IIW recommendations [41] is implemented by calculating its component hot spot stress range given in Eq. (4.27) and applied stress ratio is considered through a f(R) function [41] which is defined according three sets of conditions, e.g.,

stress relieved, thin structures with short cracks, and complex structures with high restraint conditions. The results are shown in Fig. 4.14 and Fig. 4.15 corresponding to Eurocode 3 and IIW methods, respectively. By comparing with Fig. 4.12, the test data correlated using both methods (Fig. 4.14 and Fig. 4.15), show a rather large scatter band in terms of either standard deviations or correlation coefficients R^2 for fatigue design and evaluation purposes, in which IIW method seems to offers somewhat improvement over Eurocode 3 method.

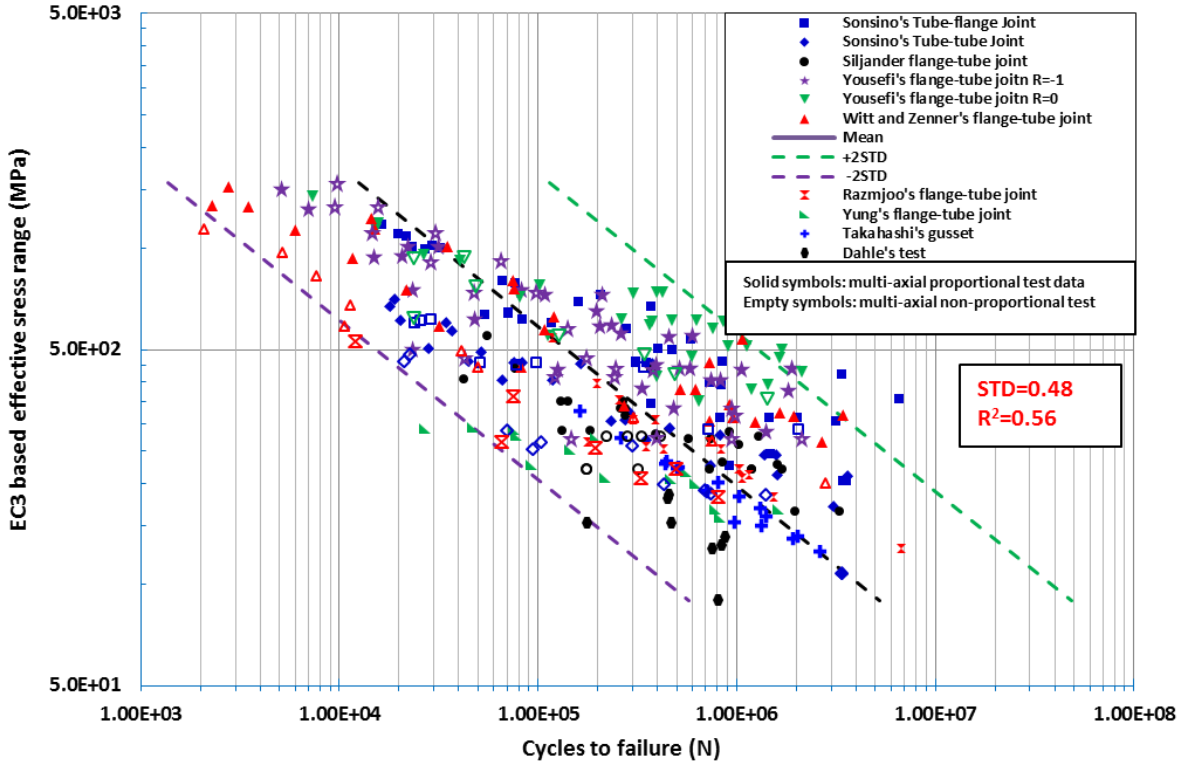

Fig. 4.14 S-N curve plot of all multi-axial test data based on Eurocode 3 in terms of hot spot stress according to Eq. (4.25)

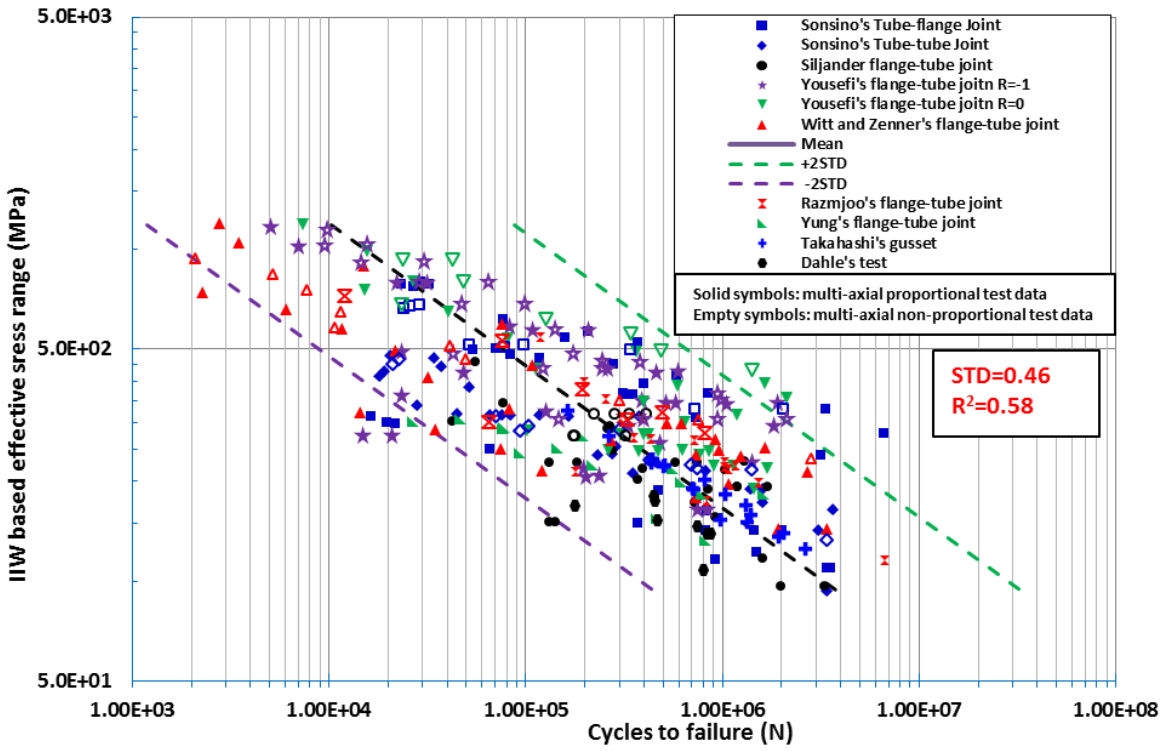

Fig. 4.15 S-N curve plot of all multi-axial test data based on IIW method in terms of hot spot stress according to Eq. (4.27)

4.5 Conclusions

This paper aims at establishing an effective stress parameter that can be used for performing fatigue evaluation of welded structures that may be subjected to a varying degree of non-proportional multi-axial fatigue loading. In doing so, effects of plate thickness (t), stress distribution gradient (r), and applied stress ratio when dealing with as-welded versus stress-relieved conditions are also considered by taking advantage of some the recent developments. The feasibility of using some of the existing methods such as those stipulated in Eurocode 3 [46] and IIW recommendations [41] is also quantitatively evaluated for comparison purposes.

As a result, the equivalent (structural) stress parameter as given in Eq. (4.28) is developed by building upon some recent developments in traction structural stress procedure, master S-N curve formulation, and MLP based non-proportional damage parameter. Its effectiveness has been demonstrated in correlating a large amount of test data under both uniaxial-dominated and non-proportional multi-axial fatigue loading conditions over various component types, joint geometries and loading conditions. Furthermore, the developments presented in this paper enables the use of the same master S-N curve method adopted by the 2007 ASME and API for applications in fatigue evaluation of non-proportional multi-axial fatigue for welded components. This is accomplished through the introduction of a MLP-based non-proportional fatigue damage parameter and applied stress ratio correction parameter for stress-relieved welded components subjected to multi-axial loading. Although ΔS_{NP}^{R} in Eq. (4.28) shows its promise in effectively correlating the test data studied in this paper (see Fig. 4.12), its generality still requires further confirmation once more non-proportional multi-axial test data become available. For fatigue design and evaluation purposes, the use of the newly proposed equivalent stress parameter without the stress ratio correction parameter ΔS_{NP} in Eq. (4.21) against the 2007 ASME structural stress based design S-N curve should result in a conservative estimate of fatigue lives for welded components in general.

Acknowledgment

The authors acknowledge the support of this work through a grant from the National Research Foundation of Korea (NRF) Grant funded by the Korea government (MEST) through GCRC-SOP at University of Michigan under Project 2-1: Reliability and Strength Assessment of Core Parts and Material System. P. Dong acknowledges the

financial support made possible by Traction Power National Key Laboratory Open Competition Grant (No. TPL 1605).

References

[1] Socie DF, Marquis G. Multiaxial fatigue. Warrendale, PA: Society of Automotive Engineers; 1999.

[2] Susmel L. Multiaxial notch fatigue. Elsevier; 2009.

[3]Kanazawa K, Miller KJ, Brown MW. Low-cycle fatigue under out-of-phase loading conditions. J Eng Mater Technol. 1977;99:222–8.

[4] Socie DF. Multiaxial fatigue damage models. J Eng Mater Technol 1987;109:293–298.

[5] Itoh T, Sakane M, Ohnami M, Socie DF. Nonproportional low cycle fatigue criterion for type 304 stainless steel. J Eng Mater Technol 1995;117:285–292.

[6] Kida S, Itoh T, Sakane M, Ohnami M, Socie DF. Dislocation structure and non-proportional hardening of Type 304 stainless steel. Fatigue Fract Eng Mater Struct 1997;20:1375–1386.

[7] Shamsaei N, Fatemi A, Socie DF. Multiaxial fatigue evaluation using discriminating strain paths. Int J Fatigue 2011;33:597–609.

[8] Itoh T, Nakata T, Sakane M, Ohnami M. Nonproportional low cycle fatigue of 6061aluminum alloy under 14 strain paths. Eur Struct Integr Soc 1999;25:41–54.

[9] Zhao T, Jiang Y. Fatigue of 7075-T651 aluminum alloy. Int J Fatigue 2008;30:834–849.

[10] Wu M, Itoh T, Shimizu Y, Nakamura H, Takanashi M. Low cycle fatigue life of Ti-6Al-4V alloy under non-proportional loading. Int J Fatigue 2012;44:14–20.

[11] Fatemi A, Shamsaei N. Multiaxial fatigue: An overview and some approximation models for life estimation. Int J Fatigue 2011;33:948–958.

[12] Nakamura H, Takanashi M, Itoh T, Wu M, Shimizu Y. Fatigue crack initiation and growth behavior of Ti–6Al–4V under non-proportional multiaxial loading. Int J Fatigue 2011;33:842–848.

[13] Itoh T, Yang T. Material dependence of multiaxial low cycle fatigue lives under non-proportional loading. Int J Fatigue 2011;33:1025–1031.

[14] Sonsino CM. Influence of material's ductility and local deformation mode on multiaxial fatigue response. Int J Fatigue 2011;33:930–947.

[15] Pejkowski Ł, Skibicki D, Sempruch J. High cycle fatigue behavior of austenitic steel and pure copper under uniaxial, proportional and non-proportional loading. Stroj Vestn. J Mech Eng 2014;60:549–560.

[16] de Freitas M, Reis L, Li B. Comparative study on biaxial low-cycle fatigue behaviour of three structural steels. Fatigue Fract Eng Mater Struct 2006;29:992–999.

[17] Shamsaei N, Gladskyi M, Panasovskyi K, Shukaev S, Fatemi A. Multiaxial fatigue of titanium including step loading and load path alteration and sequence effects. Int J Fatigue 2010;32:1862–1874.

[18] Mei J, Dong P. A new path-dependent fatigue damage model for non-proportional multi-axial loading. Int J Fatigue 2016;90:210–221.

[19] Papadopoulos IV. Critical plane approaches in high-cycle Fatigue: on the definition of the amplitude and mean value of the shear stress acting on the critical plane. Fatigue Fract Eng Mater Struct 1998;21:269–285.

[20] Li B, Reis L, de Freitas M. Comparative study of multiaxial fatigue damage models for ductile structural steels and brittle materials. Int J Fatigue 2009;31:1895–1906.

[21] Skibicki D. Phenomena and computational models of non-proportional fatigue of materials. Springer; 2014.

[22] Findley WN. A theory for the effect of mean stress on fatigue of metals under combined torsion and axial load or bending. J Eng Industry 1959;81:301–306.

[23] Brown MW, Miller KJ. A theory for fatigue failure under multiaxial stress–strain conditions. Proc Inst Mech Eng 1973;187:745–755.

[24] Fatemi A, Socie DF. Critical plane approach to multiaxial fatigue damage including out-of-phase loading. Fatigue Fract Eng Mater Struct 1988;11:149–165.

[25]Smith K, Topper TH, Watson P. Stress-Strain Function for the Fatigue of Metals. J Mater 1970;5:767–778.

[26] Bäckström M. Multiaxial fatigue life assessment of welds based on nominal and hot spot stresses. Ph.D. thesis. Laapeenranta University; 2003.

[27] Sonsino CM, Kueppers M. Multiaxial fatigue of welded joints under constant and variable amplitude loadings. Fatigue Fract Eng Mater Struct 2001;24:309–327.

[28] Sonsino CM, Łagoda T. Assessment of multiaxial fatigue behaviour of welded joints under combined bending and torsion by application of a fictitious notch radius. Int J Fatigue 2004;26:265–279.

[29] Siljander A, Kurath P, Lawrence FV. Nonproportional fatigue of welded structures. In Advances in fatigue lifetime predictive techniques. ASTM Int. 1992; 319-338

[30] Yousefi F, Witt M, Zenner H. Fatigue strength of welded joints under multiaxial loading: experiments and calculations. Fatigue Fract Eng Mater Struct 2001;24:339–355.

[31] Witt M, Zenner H. Multiaxial fatigue behaviour of welded flange-tube connections under combined loading. Experiments and lifetime prediction. 5th International conference on biaxial/multiaxial fatigue and fracture,Cracow, Poland; 1997; 421–434.

[32] Razmjoo GR. Fatigue of load-carrying fillet welded joints under multiaxial loading. Fatigue – core research from TWI. Woodhead, UK, 63-99.

[33] Yung JY, Lawrence FV. Predicting the fatigue life of welded joints under combined bending and torsion. Biaxial and multiaxial fatigue, EGF3. London, 1989; 53–69.

[34] Takahashi I, Ushijima M, Takada A, Akiyama S, Maenaka H. Fatigue behaviour of a box-welded joint under biaxial cyclic loads. Fatigue Fract Eng Mater Struct 1999;22:869–877.

[35] Takahashi I, Takada A, Ushijima M, Akiyama S. Fatigue behaviour of a box-welded joint under biaxial cyclic loading: Effects of biaxial load range ratio and cyclic compressive loads in the lateral direction. Fatigue Fract Eng Mater Struct 2003;26:439–448.

[36] Dahle T, Olsson KE, Jonsson B. High strength welded box beams subjected to torsion and bending – test results and proposed design criteria for torsion/bending interaction. First North European Engineering and Science Conference, Stockholm, Sweden; 1997; 143–161.

[37] Dong P, Hong J, A Robust Structural Stress Parameter for Evaluation of Multiaxial Fatigue of Weldments. J ASTM Int 2006;3(7):206-222.

[38] Bäckström M, Marquis G. A review of multiaxial fatigue of weldments: Experimental results, design code and critical plane approaches. Fatigue Fract Eng Mater Struct 2001;24:279–291.

[39] Pedersen MM. Multiaxial fatigue assessment of welded joints using the notch stress approach. Int J Fatigue 2016;83:269–279.

[40] Dong P, Hong JK, Osage DA, Dewees DJ, Prager M. "The Master S-N Curve Method: An Implementation in 2007 ASME Div 2 International Codes for Boilers and Pressure Vessels," Welding Research Council Bulletin, No. 523, 2010.

[41] Hobbacher AF. IIW recommendations for fatigue design of welded joints and components. Springer; 2015

[42] Barsoum Z, Jonsson B. Influence of weld quality on the fatigue strength in seam welds. Engineering Failure Analysis 2011;18(3):971-979.

[43] Barsoum Z, Jonsson B. Fatigue assessment and LEFM analysis of cruciform joints fabricated with different welding processes. Welding in the World 2008;52:93-105.

[44] Taylor D, Barrett N, Lucano G. Some new methods for predicting fatigue in welded joints. Int J Fatigue, 2002;24(5): 509-518.

[45] Lazzarin P. Lassen T. Livieri P., A notch stress intensity approach applied to fatigue life predictions of welded joints with different local toe geometry. Fatigue Fract Eng Mater Struct. 2003;26(1): 49-58.

[46] Eurocode 3, design of steel structures-Part 1–9: Fatigue, CEN;2005

[47] 2007 ASME Boiler and Pressure Vessel Code, Sec VIII,Div. 2 (ASME BPVC-VIII-2-2007), American Society of Mechanical Engineers, New York, 2007

[48] API 579 RP-1/ASME FFS-1, Fitness-For-Service, American Petroleum Institute, Houston 2007.

[49] Dong P. A structural stress definition and numerical implementation for fatigue analysis of welded joints. Int J Fatigue 2001;23:865–876.

[50] Dong, P. A robust structural stress method for fatigue analysis of offshore/marine structures

J. Offshore Mech. Arct. Eng 2005; 127(1): 68-74.

[51] Nie C, Dong P. A traction stress based shear strength definition for fillet welds. J Strain Anal Eng Des 2012;47:562–575.

[52] Mei J, Dong P. Modeling of path-dependent multi-axial fatigue damage in aluminum alloys. Int J Fatigue 2017;95:252–263.

[53] Dong P, Wei Z, Hong JK. A path-dependent cycle counting method for variable-amplitude multi-axial loading. Int J Fatigue 2010;32:720–734.

[54] Wei Z, Dong P. A generalized cycle counting criterion for arbitrary multi-axial fatigue loading conditions. J Strain Anal Eng Des 2014;49:325–341.

[55] Wei Z, Dong P. Multiaxial fatigue life assessment of welded structures. Eng Fract Mech 2010;77:3011–3021.

[56] Dong P. Stresses and stress intensities at notches: ‘anomalous crack growth’ revisited revisited. Int J Fatigue 2003;25:811–825.

[57] BS 7608: 2014 Guide To Fatigue Design And Assessment Of Steel Products, British Standards Institution; 2014

[58] Xing S, Dong P, Threstha A. Analysis of fatigue failure mode transition in load-carrying fillet-welded connections. Mar Struct 2016;46:102–126.

Chaper 5.

A Path-Dependent Mixed-Mode Crack Propagation Model for Non-Proportional Multi-Axial Fatigue Loading

ABSTRACT

It has been well established that fatigue damage process is load-path dependent under non-proportional multi-axial loading conditions. Most of studies to date have been focused on interpretation of S-N based test data by constructing a path-dependent fatigue damage model. This paper presents a two-parameter fatigue crack growth model for taking into account of crack growth dependency on load path traversed in a stress intensity factor plane ($K_I - \sqrt{\beta^K} K_{III}$ plane) and mean stress effect for mixed Mode I and Mode III loading. By taking advantage of a path-dependent maximum range (PDMR) cycle definition (Dong et al., 2010 and Wei and Dong, 2010), the two parameters are formulated by introducing a moment of load path (MLP) based equivalent stress intensity factor range (ΔK_{NP}) and a maximum effective stress intensity K_{Max}, defined with respect to K space. Crack growth rate data obtained from 304 stainless steel disk specimens under combined non-proportional modes I and III loading conditions (with circular, proportional, and inversely proportional loading paths) are then investigated for examining the validity of the proposed two-parameter non-proportional fatigue crack growth model. Furthermore, non-proportional crack growth test data on 1070 steel under

similar three load-path conditions published by Feng et al (2007) are also analyzed using the model proposed in this study. The results show that the proposed model is quite effective in correlating non-proportional mixed mode fatigue crack growth of both 304 stainless steel 1070 steel.

Keywords: Multi-axial fatigue, mixed mode crack, non-proportional loading, fatigue damage modeling

5.1 Introduction

Mixed mode fatigue crack growth phenomena have been investigated by many researchers by formulating an effective stress intensity range definition such as those proposed by Tanaka [1], Richard, et al .[2], Pook [3], Forth, et al.[4] for combined Mode I, Mode II and Mode III loadings. However, these investigations have been focused upon proportional loading conditions in which one loading mode history can be scaled by another. As discussed by Sonsino and Kueppers [5], there exist numerous applications such as stir propeller in chemical processing industry, in which mixed mode fatigue crack propagation phenomena under non-proportional loading conditions must be considered. Their test data obtained under non-proportional Mode I and Mode III sinusoidal loadings showed that out-of-phase loading with a phase shift of 90^0 resulted in significantly more fatigue damage than in-phase loading (i.e.., phase shift of 0^0). Since then, there have been a plenty of experimental evidences [5-7] showing that non-proportional mixed-mode loading can significantly accelerate fatigue crack growth rate using simple fracture mechanics specimens. For instance, Fremy et al. [6] carried out complex mixed-mode fatigue crack growth tests using pre-cracked cruciform specimens that were subjected to Mode I, Mode II and Mode III loadings by six independently controlled actuators. By

following various load paths (proportional and non-proportional load path, e.g., "cube", "star", etc.), they reported that crack growth rates measured were significantly different among different load paths.

Along this line, the authors of this paper found the mixed mode crack growth test results by Feng et al [7] particularly intriguing, who conducted mixed-mode (Modes I and III) crack growth rate tests using 1070 steel disk specimens using three rather simple load paths: proportional (0^0 phase angle), inversely proportional (180^0 phase angle), and out-of-phase (90^0 phase angle). Their test results clearly show not only that the load path with a 90^0 phase angle yields the highest crack growth rate, but also that inversely proportional load path (180^0 phase angle) produces the lowest crack growth rate. In addition, they pointed out that they were not aware of any existing mixed-mode fatigue crack growth models that could be used to correlate their test data at that time. By taking advantage of some recent developments on modeling of non-proportional multi-axial fatigue damage process, Mei et al [8] recently proposed a two-parameter mixed mode crack growth model which incorporates the effects of both load-path non-proportionality and maximum effective stress intensity factor computed in K plane (spanned by K_I and K_{III}). The two-parameter model was shown effective for correlating the test data reported by Feng et al [7]. However, the multi-axial fatigue damage parameter involved is analytically formulated in terms of a parameter $F(\delta)$, where δ is phase shift between Modes I and III loading histories (see [9]), which requires phase angle (δ) a known a priori. As a result, the model cannot be used for a general treatment of variable amplitude non-proportional mixed-mode loading conditions.

A more recent development was reported by Mei and Dong [10] who proposed a path-dependent fatigue damage model for general non-proportional multi-axial fatigue loading conditions, which was shown effective for modeling fatigue damage caused by arbitrary load-paths in either stress or strain space. In their model, fatigue damage parameter was formulated by integrating a moment of an incremental load path along a given load path forming one half fatigue cycle with respect to a reference load path defined in either stress or strain space, referred to as moment of load path (MLP) method. They showed that a large amount of available test data obtained under various non-proportional loading conditions can be effectively correlated for both structural steels and aluminum alloys [10, 11]. Its applicability for modeling non-proportional multi-axial fatigue in welded components was also demonstrated in [12].

The aim of this study is to examine the applicability of MLP based fatigue damage parameter in *K* space for modeling mixed-mode crack growth phenomena in stress intensity based *K*-space by formulating a MLP based equivalent stress intensity factor range *(*i.e., ΔK_{NP} with subscript NP representing non-proportional (NP) effect) for mixed mode non-proportional fatigue crack growth problems. Then, a two-parameter fatigue crack growth model that takes into account of both load path-dependent effects in terms of MLP based equivalent stress intensity factor range (ΔK_{NP}) and mean stress effects by a maximum effective stress intensity factor (i.e., K_{Max}) in *K*-space is proposed for modeling non-proportional mixed mode fatigue crack growth problems. The validity of this proposed mixed mode crack growth model is then demonstrated by examining crack growth rate data on stainless steel (Type 304) performed as a part of this study and on 1070 steel reported by Feng et al [7].

5.2 Path-Dependent Mixed Mode Fatigue Crack Growth Model

5.2.1 Problem Definition

Without losing generality, we consider a mixed mode (mode I and mode III) crack growth problem for which a plate of width w and thickness of B with an initial edge crack (a) is shown in Fig. 5.1. Mode I crack growth in Fig. 5.1 is operated by time-varying tension load *P(t)* which produces a far field normal traction stress (σ) and mode III crack growth is operated by time-varying out-of-plane force, Q(t) which produces a far field out-of-plane shear traction stress τ_{III}, both of which may vary independently from each other as a function of time. It should be noted that non-proportional multi-axial fatigue behaviors of welded joints subjected to such loading conditions have already been investigated by introducing an effective multi-axial fatigue damage parameter, referred to as MLP concept (see Mei and Dong [10,12]) in terms of far field stresses. In what follows, we extend will extend MLP concept to K space defined on a $K_I - \sqrt{\beta^K}\, K_{III}$ plane for modeling non-proportional crack propagation problems.

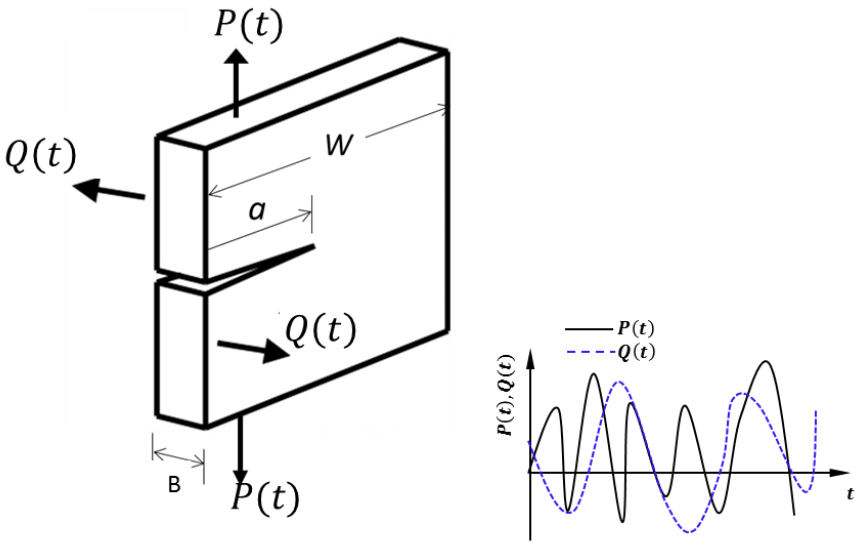

Fig. 5.1 Illustration of mixed Mode I and Mode III fatigue crack propagation problem under non-proportional loading conditions (remote tension ($P(t)$) and remote out-of-plane shear ($Q(t)$).

5.2.2 Damage Parameter Definition in K Plane

5.2.2.1 MLP based equivalent stress intensity factor range

For a mixed mode crack propagation problem shown in Fig. 5.1, the applied tensile force $P(t)$ and out of plane shear force $Q(t)$ can be directly related to their respective stress intensity factors $K_I(t)$ and $K_{III}(t)$ as:

$$K_I(t) = \frac{P(t)}{B\sqrt{\pi a}} F_I\left(\frac{a}{W}\right) \tag{5.1}$$

$$K_{III}(t) = \frac{Q(t)}{B\sqrt{\pi a}} F_{III}\left(\frac{a}{W}\right) \tag{5.2}$$

where B is plate thickness, F_I and F_{III} can be dimensionless compliance functions of relative crack size a/W corresponding to Mode I and Mode III loading conditions, respectively. For given independent variable loading histories of $P(t)$ and $Q(t)$ shown in Fig. 5.1, their corresponding stress intensity factor histories can be obtained either through existing stress intensity factor solutions or by means of finite element computation which is case here, as described in Sec. 4. In order for fatigue damage assessment under non-proportional variable amplitude loading, an appropriate multi-axial cycle counting procedure must be first carried out to break complex stress intensity factor histories ($K_I(t)$ and $K_{III}(t)$) into simple fatigue loading events. The path-dependent maximum range (PDMR) originally developed [13-15] for treating variable amplitude non-proportional multi-axial stress histories ($\sigma(t)$ and $\tau(t)$) can be adopted here for treating variable amplitude load path in $K_I - \sqrt{\beta^K} K_{III}$ plane for the case shown in Fig.

5.1. The basic idea of PDMR cycle counting procedure [13-15] is that it searches successively the maximum ranges available in a given multi-axial stress history in a stress space, e.g., $\sigma - \sqrt{\beta}\tau$ plane and counts their occurrences as half cycles. More details of PDMR cycle counting procedure can be found in [13-15].

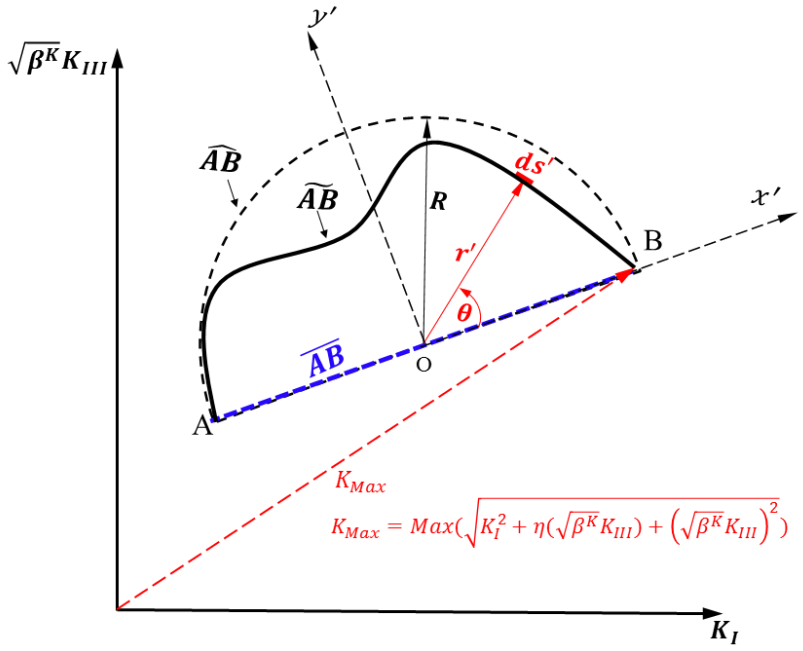

Fig. 5.2 Moment of Load Path (MLP) based damage parameter definition on $K_I - \sqrt{\beta^K}K_{III}$ plane ($\widetilde{AB}$: non-proportional load path under consideration; $\widehat{AB}$: reference circular load path; and $\overline{AB}$: reference linear path)

Now consider a mixed mode fatigue loading event at a given crack size a. the corresponding $K_I(t)$ and $K_{III}(t)$ given in Eqs. (5.1) and (5.2) form a load path from A to B ($\widetilde{AB}$) in $K_I - \sqrt{\beta^K}K_{III}$ plane (see Fig. 5.2), which can be shown to constitute one half fatigue cycle according PDMR [13-15]. By applying the Moment of Load Path (MLP) concept in K-plane in Fig. 5.2, the resulting damage factor contributing to fatigue crack growth resulted from non-proportional load path $\widetilde{AB}$ in Fig. 5.2 can assumed to be partitioned into two parts:

$$D = D_P^K + D_{NP}^K \tag{5.3}$$

in which D_P^K represents damage caused by a reference proportional loading path from A to B (i.e., $\overline{AB}$), which can be directly related to distance from A to B, or the effective stress intensity factor range ΔK_e:

$$\Delta K_e = \sqrt{\Delta {K_I}^2 + \beta^K \Delta {K_{III}}^2} \tag{5.4}$$

The second part in Eq. (5.3), i.e., D_{NP}^K represents load path non-proportionality caused damage due to any excursions of load path $\widetilde{AB}$ deviating from the reference load path ($\overline{AB}$), which can be expressed in an incremental form as:

$$dD_{NP} \propto r' \left| sin\,(\theta) \right| ds' \tag{5.5}$$

in terms of local coordinate $x' - y'$ system in Fig. 5.2. Note that Eq. (5.5) is a direct implementation of the MLP concept proposed by Mei and Dong [10] but in *K* space here. Then, the total load path non-proportionality induced fatigue damage (D_{NP}) along path $\widetilde{AB}$ can then be expressed by integrating Eq. (5.3) as:

$$D_{NP} \propto \int_{AB} r' \cdot \left| \sin(\theta) \right| ds' \tag{5.6}$$

A dimensionless form of load-path non-proportionality damage factor defined on $K_I - \sqrt{\beta^K} K_{III}$ plane for $\widetilde{AB}$ with respect to the non-proportional load path $\widehat{AB}$ which yields the maximum possible damage can then be written as:

$$g_{NP}^{K} = \frac{D_{NP}^{K}}{D_{Max}^{K}} = \frac{\int_{AB} r' |\sin(\theta)| ds'}{\int_{AB} R |\sin(\theta)| ds'} = \frac{\int_{AB} r' |\sin(\theta)| ds'}{2R^2} \tag{5.7}$$

where D_{Max}^{K} represents the maximum possible damage [10] of a non-proportional damage load path $\widehat{AB}$, which is a semi-circular path with a radius of R on the K plane.

For any arbitrary loading path $\widetilde{AB}$ on K plane, a MLP based equivalent stress intensity factor incorporating path-dependent non-proportionality effect can be expressed as:

$$\Delta K_{NP} = \Delta K_e (1 + a^K \cdot g_{NP}^{K}) \tag{5.8}$$

where a^K is a material sensitivity parameter to non-proportional loading defined in $K_I - \sqrt{\beta^K} K_{III}$ plane and g_{NP}^{K} is a normalized load path non-proportionality damage factor given by Eq. (5.7).

As reported in [10-13], when a similar form of Eq. (5.8) with respect to stress plane (i.e., $\sigma - \sqrt{\beta}\tau$ plane) or strain plane (i.e., $\varepsilon - \sqrt{\beta^{\varepsilon}}\gamma$ plane) was used, excellent correlations have been achieved in correlating a large amount of non-proportional multi-axial test data for both structural steels and aluminum alloys. It has been shown that in [19, 21], $\beta = 3$ and $a = 1$ defined on $\sigma - \sqrt{\beta}\tau$ stress plane resulted a good correlation in multi-axial fatigue test data of both welded and non-welded structural steels from various sources. Therefore, it is assumed that the same values, i.e. $\beta^K = 3$ and $a^K = 1$ are applicable for K plane based mixed mode crack growth characterization, at least as a first

approximation. Refined estimations of these parameters can be achieved through the data analysis procedures described in [11].

5.2.2.2 Maximum effective stress intensity factor

In addition to MLP-based equivalent stress intensity factor range ΔK_{NP} given in Eq. (5.8), either a mean or maximum effective stress intensity factor definition in *K* plane should be considered, as suggested by a careful examination of relevant test data reported by various authors, particularly those by Jiang et al [7]. They conducted a series of rather interesting mixed-mode crack growth tests using non-proportional load histories resulting in $K_I(t)$ and $K_{III}(t)$ histories as illustrated in Fig. 5.3 with unit amplitude of stress intensity factor and R=0, involving proportional loading (0^0 phase shift), non-proportional loading (90^0 phase shift), and inversely proportional loading (180^0 phase shift). It was found that the load case corresponding to inversely proportional loading yields the minimum crack growth rates or least damaging among all cases considered. It should be noted that under inversely proportional loading (Fig. 5.3(b)), K_I reaches its maximum when K_{III} reaches its minimal, intuitively suggesting a reduced interaction between $K_I(t)$ and $K_{III}(t)$ throughout a fatigue cycle in comparison with other two load cases. Therefore, a maximum effective stress intensity factor definition should contain a term in the form of $K_I K_{III}$, in addition to the requirements that it must remain valid when either one of the two vanishes. As a result, a maximum effective stress intensity factor can be postulated as follows:

$$K_{max} = Max(\sqrt{K_I^2 + \eta K_I\left(\sqrt{\beta^K}K_{III}\right) + \left(\sqrt{\beta^K}K_{III}\right)^2}) \qquad (5.9)$$

where β^K is an equivalency parameter between Mode I and Mode III crack growths as described previously and η can be treated as material-related parameter measuring interaction effects between Mode I and Mode III crack growths.

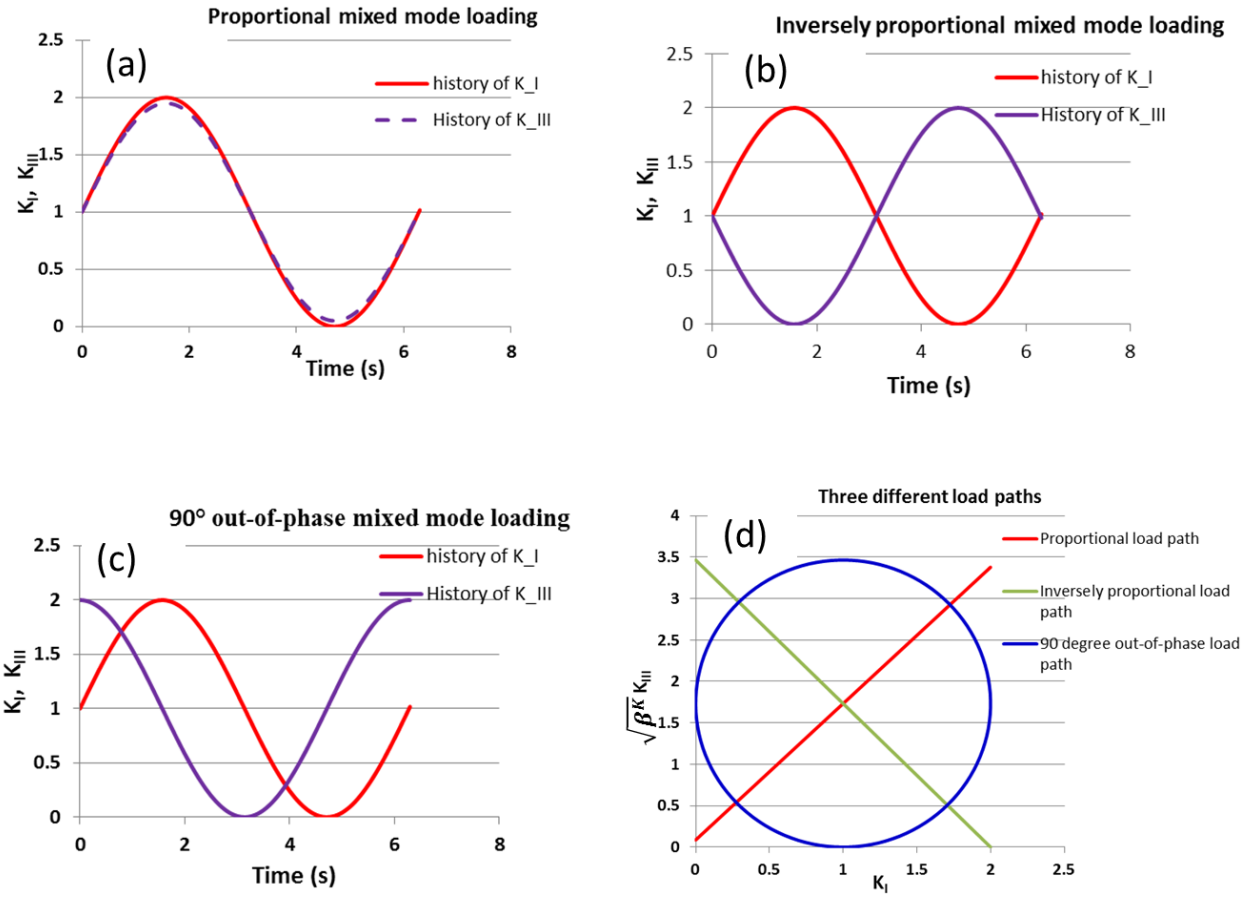

Fig. 5.3 Representative non-proportional sinusoidal loading histories (with unit amplitude of stress intensity factor and R=0) and K-plane based representations: (a) Proportional (0^0 phase shift); (b) Non-proportional (90^0 phase shift), (c) Non-proportional (180^0 phase shift); and (d) K-planed based representations

5.2.3 Two-Parameter Mixed-Mode Crack Growth Model

With the developments discussed in the previous sections (Secs. 2.2.1 and 2.2.2), a two-parameter non-proportional crack growth model is proposed as follows:

$$\frac{da}{dN} = C(K_{Max})^p(\Delta K_{NP})^q \tag{5.10}$$

which can be written in an equivalent form as:

$$\frac{da}{dN} = C(K^*)^{\lambda} \tag{5.11}$$

where

$$K^* = (K_{Max})^{1-\gamma}(\Delta K_{NP})^{\gamma} \tag{5.12}$$

In Eq. (5.12), K^* represents an equivalent stress intensity factor and the exponent γ is a curve-fitting parameter through analysis of experimental test data. A higher γ value suggests a less sensitivity of crack growth rate to maximum effective stress intensity factor K_{Max}. As suggested in [16], γ can also be related to material ductility. Note that when $\gamma = 0.5$, Eq. (5.12) is reduced to the form of Smith-Watson-Topper (SWT) fatigue damage parameter [17] but in terms of stress intensity factor parameters defined in K space. Furthermore, it has been shown [18] that when crack growth is dominated by elastic stress field, $\gamma = 0.5$ leads to rather reasonable correlations of fatigue crack growth data containing different stress ratios. For the purpose of demonstrating the general applicability of the two parameter model given in Eq. (5.12), $\gamma = 0.5$ is chosen here for performing data correlation in this study, recognizing the fact a best fit γ would certainly improve data correlation for a given set of test data. However, the focus here is to demonstrate the effectiveness of the proposed two-parameter model (see Eq. (5.12)) through its mechanics structure, without going through any best-fit based data analysis.

5.3 Non-Proportional Mixed Mode Fatigue Tests

5.3.1 Test Procedure

Two sets of non-proportional mixed mode I and mode III crack growth test data are considered here for validating the proposed two parameter crack growth model. One set is generated as a part of this study using 304 stainless steel disk plate specimens as shown in Fig. 5.4(a) subjected to three combined Mode I and Mode III loading conditions or load paths in terms of tension and torsion forces (P and T) described in Fig. 5.5(a). For each load path, two load levels were used, as shown in Fig. 5.5(a). The other data set is taken from Feng et al [7] who used 1070 steel disk plate specimens shown in Fig. 5.4(b) which were subjected to the load paths shown in Fig. 5.5(b). For 1070 specimens, fatigue crack growth rate tests were carried out at one load level. Note that both 304 steel specimens and 1070 steel specimens have the same plate thickness of 3.8mm, even though the dimensions of the 1070 specimens are about 1.5 times larger than that of 304 steel specimens.

A pre-crack was generated through pure Mode I cyclic loading before combined tension and torsion loads are applied independently in subsequent fatigue crack growth tests. To avoid potential crack surface contact during fatigue testing, which might introduce additional uncertainties in crack growth rate data, a positive R-ratio (R=0.1) for the axial load and a zero R-ratio for the torsion load were used. As will be demonstrated in a later section, mean stress effects (R-ratio effect) on crack growth rate can be taken account through K_{max} in Eq. (5.9) in the proposed two-parameter crack growth model described in Eq. (5.10). For the three load paths used for both types of steels, Load Path I yields proportional loading conditions between tension and torsion, while Path II may be

referred to as inversely proportional loading condition (see Fig. 5.3(b)), in which K_{III} decreases linearly with the increase of K_I. Path III is an out-of-phase load path with 90° out-of-phase angle between tension and torsion.

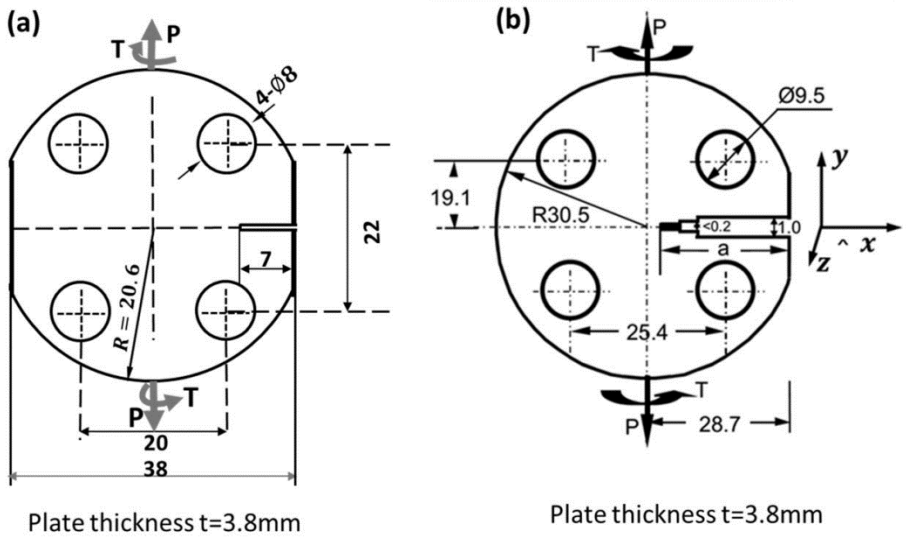

Fig. 5.4 Disk type CT crack growth test specimens: (a) 304 stainless steel and (b) 1070 steel [7]

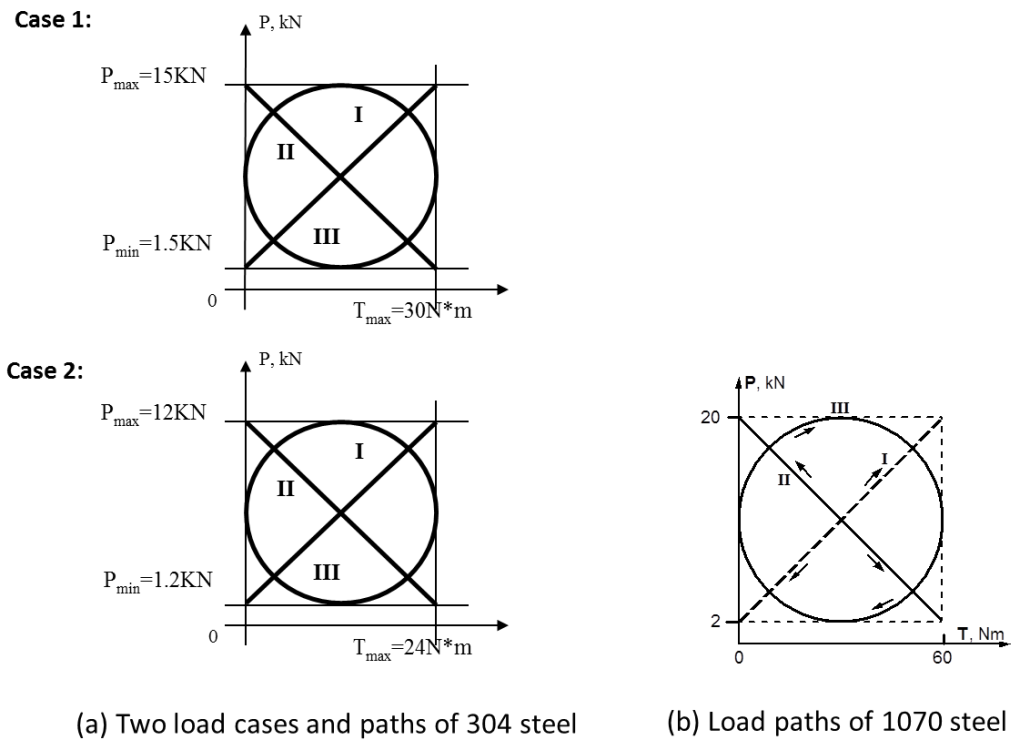

(a) Two load cases and paths of 304 steel (b) Load paths of 1070 steel

Fig. 5.5 Load paths used in fatigue crack growth testing: (a) 304 stainless steel specimens; (b) 1070 steel specimens [7]

All the above crack growth rate tests were conducted using an Instron 8870 load frame and 8800 electronics with computer control and data acquisition systems. The testing system can generate and control the axial and torsion loads independently. The loading frequencies were ranged from 2 to 5 Hz, dependent on the loading path and crack length. An optical reading micrometer with a magnification of 40 was used to measure the crack length.

5.3.2 Test Results

Similar to those observed in [7], the overall global crack growth direction is consistent with pre-crack plane, in spite of some local deviations or crack branching at a rather small length scale. The measured crack growth results as a function of load cycle

are summarized in Fig. 5.6 for 304 stainless steel specimens and in Fig. 5.7 for 1070 steel specimens. Note that the measured instantaneous crack size *a* includes the length of the machined slit before pre-cracking, as shown in Fig. 5.4 (b). The detailed measurement procedure for 304 steel specimens follows the one described in [7] in which mixed-mode crack growth behaviors were investigated under non-proportional loading conditions. As indicated in Fig. 5.6, the two sets of crack growth rate data subjected to out-of-phase loading (Path III) consistently show a more rapid crack growth than the other two load paths, i.e., Path I and Path II, while Path II (inversely proportional) results in the slowest crack growth among the three load paths.

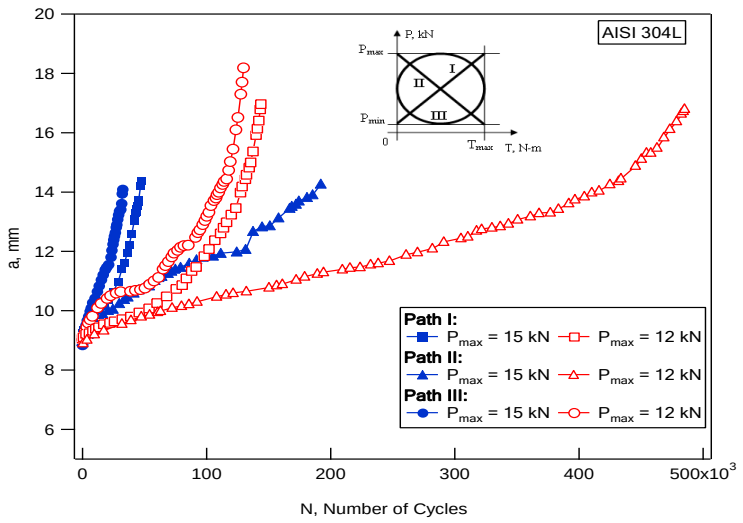

Fig. 5.6 Measured crack growth results - 304 stainless steel specimens

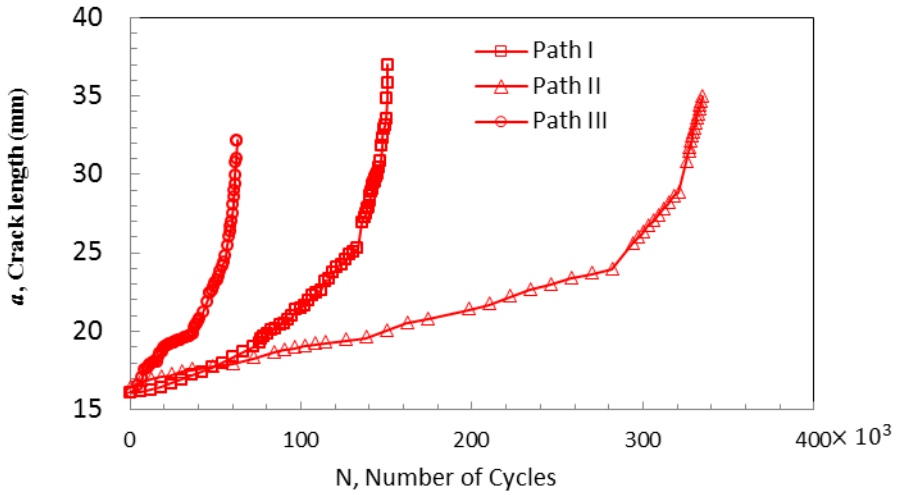

Fig. 5.7 Crack growth test results – 1070 steel (Feng et al, [7])

5.4 Analysis

5.4.1 Stress Intensity Factor Calculations

Since stress intensity factor solutions for the specimen geometries shown in Fig. 5.4 are not available from any existing sources, a finite element based energy release rate method is used to compute stress intensity factors corresponding to tension ($P(t)$) and torsion ($T(t)$) as a function of crack size, which can be implemented as a nodal force/displacement based procedure [19, 20]. The procedure used in this study is illustrated by considering a simple finite element mesh layout around crack tip in Fig. 5.8 (a) under Mode I loading conditions. Nodal forces F_1 and F_2 in y direction at crack tip are first extracted before crack propagation. Then, releasing node at the crack tip shown in Fig. 5.8 (a), results in a crack tip advance by Δa, shown in Fig. 5.8 (b). The new finite element solution corresponding to the current configuration (Fig. 5.8 (b)) yields nodal

displacements u_1 and u_2 in y direction. The work done by the nodal force (F_1 and F_2) to advance the crack length by Δa is equal to the energy released by the system, leading to:

$$\frac{1}{2}F_1 \cdot u_1 + \frac{1}{2}F_2 \cdot u_2 = G\Delta a \tag{5.13}$$

where G is energy release rate. For plane stress problems, $G = {K_I}^2/E$, where K_I is the Mode I stress intensity factor when crack size is at a. As long as Δa (i.e element size at crack tip) is reasonable small, e.g., $\Delta a = 0.2mm$ used in the current study, the resulting K_I values calculated are verified on simple edge crack specimen for which a closed-form solution is available. For Mode III loading, F_1, F_2 and u_1, u_2 in Eq. (5.13) can be simply replaced by nodal forces and nodal displacements in z direction. Eq. (5.13) offers a simple and reliable method for computing stress intensity factors for the problem definition given in Fig. 5.1. With the nodal force/displacement procedures described above, the computed dimensionless compliance function results in K_I and K_{III} expressions given in Eq. (5.1) and Eq. (5.2) for 304 stainless steel specimens (Fig. 5.4(a)) are plotted as a function of relative crack size in Fig. 5.9(a) and Fig. 5.9(b). In addition, the corresponding compliance function results for 1070 steel specimens tested by Feng et al [7] are also given in Fig. 5.9 for comparison purpose. Note that crack growth tests on 304 stainless steel specimens covered a rather small crack growth ranges comparing with tests on 1070 steel specimens.

With these computed function results obtained and applied load path in terms of applied loads (P and T) given in Fig. 5.5), the mixed mode load paths on $K_I - \sqrt{\beta^K}K_{III}$ plane can then generated by using Eq. (5.1) and Eq. (5.2) at each crack size increment on

which da/dN versus N data are available. Then, the corresponding ΔK_{NP} and K_{max} can be computed through Eq. (5.8) and Eq. (5.9).

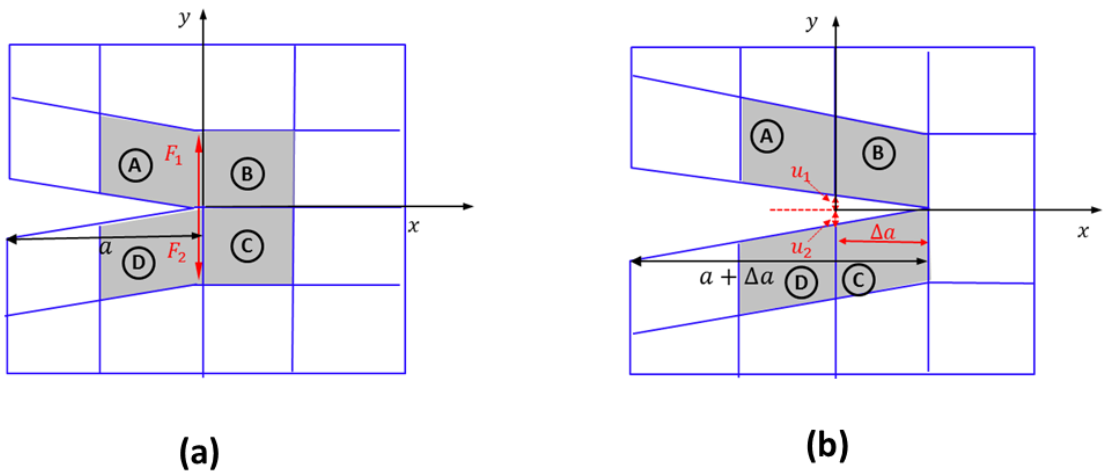

Fig. 5.8 Illustration of nodal force based energy release rate calculation method: (a) extract nodal forces at initial crack tip; (b) extract displacements at the same after node release resulting in a crack size increment by Δa

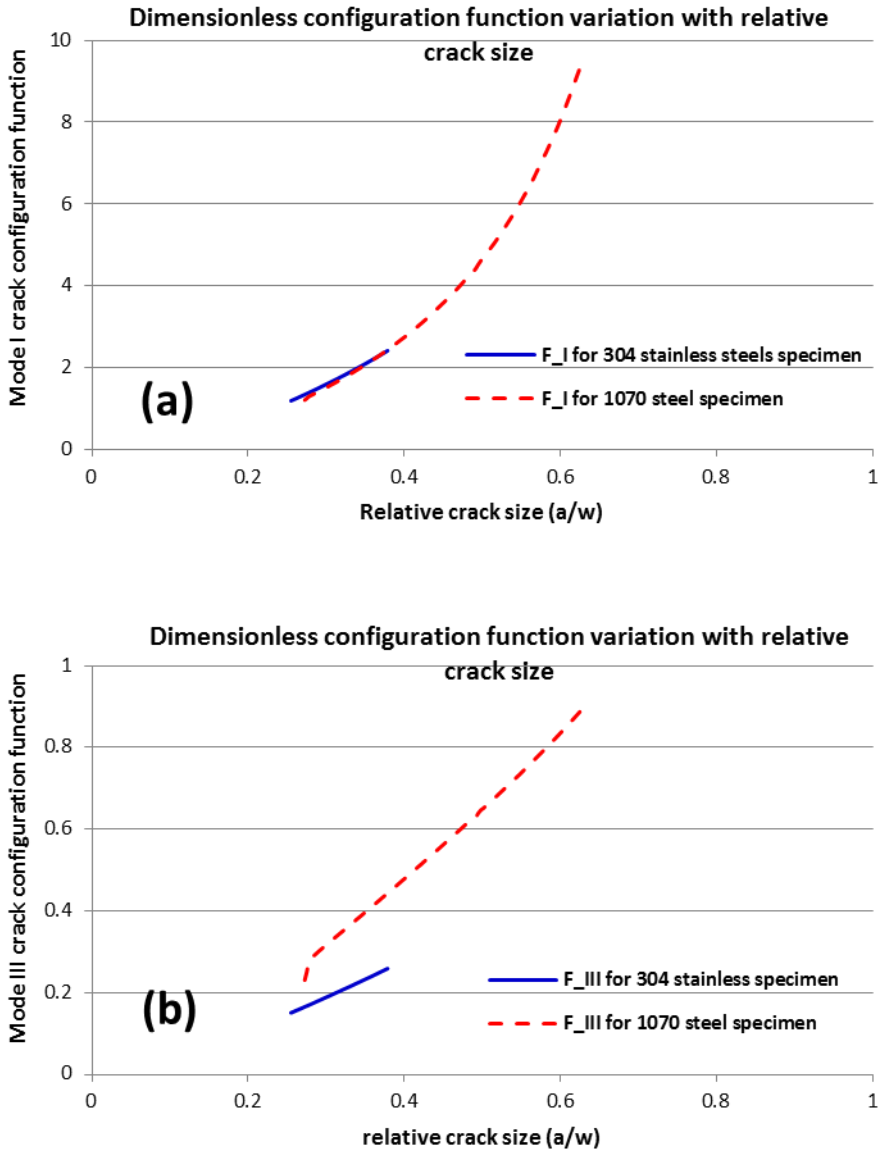

Fig. 5.9 Dimensionless compliance functions as a function of relative crack size crack size calculated for 304 stainless steel specimen and 1070 steel specimen

5.4.2 Determination of ΔK_{NP} and K_{Max}

At each given crack size, the load paths described in Fig. 5.5 in terms of applied tension (P) and torsion (Q) can now be mapped onto $K_I - \sqrt{\beta^K} K_{III}$ plane through Eqs. (5.1) and (5.2), as given in Fig. 5.10 for 1070 steel specimens with a crack size of $a = 26\text{mm}$. It should be noted that as crack size changes, the resulting load paths in

$K_I - \sqrt{\beta^K} K_{III}$ plane change as a function of crack size, as described in Eq. (5.1) and Eq. (5.2). The procedure for calculating ΔK_{NP} can be illustrated as follows. For Path I and Path II shown in Fig. 5.10, MLP based non-proportionality factor $g^K{}_{NP} = 0$ according to Eq. (5.7). As a result, straight line load paths (Path I and Path II) result in $\Delta K_{NP} = \Delta K_e$. Load Path III constitutes two half fatigue cycles represented by two semi-elliptical segments, one is the upper half ($\widetilde{ACB}$) and the other is the lower half ($\widetilde{A'C'B'}$), sharing a common linear reference load path, which is the long axis $\overline{AB}$ of the ellipse, as illustrated in Fig. 5.10. By numerically integrating Eq. (5.7) over the two semi-elliptical loading paths, the non-proportionality factor g_{NP}^K and MLP based equivalent stress intensity factor range ΔK_{NP} corresponding to one full cycle can be calculated through Eq. (5.7) and Eq. (5.8) respectively.

As discussed in Section 2.2, K_{Max} in Eq. (5.9) represents the maximum value attained through a quadratic function of K_I and K_{III} during one fatigue cycle along each of the three load paths. The resulting values (denoted by K_{Max}^I, K_{Max}^{II} and K_{Max}^{III} for load path I, II and III, respectively) at $a = 26mm$ in 1070 steel specimen are also given in Fig. 5.10. Note that $\eta = 1$ in Eq. (5.9) is assumed here for illustration purpose and that an estimation procedure for η for achieving an improved data correlation will be discussed in the next section. For comparison purpose, all relevant parameters required the two-parameter crack growth model described by Eq. (5.11) are summarized in Table 5.1 for the three load paths shown in Fig. 5.10. It is interesting to note that the relative differences in K^* among the three load paths seem to provide a consistent ranking in trend with fatigue crack growth rates observed in Fig. 5.7. For instance, the lowest K* is

calculated for load Path II which resulted in the slowest crack growth rates (see Fig. 5.7) while the highest K* for load Path III which resulted in the highest crack growth rate.

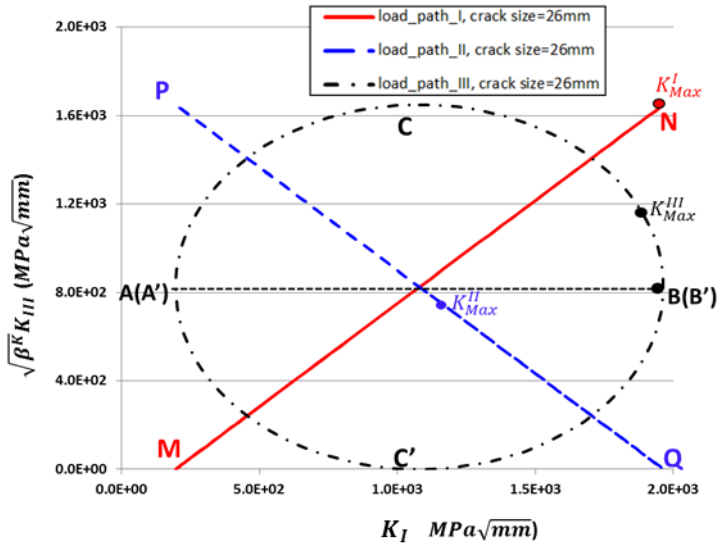

Fig. 5.10 Loading paths in $K_I - \sqrt{\beta^K}K_{III}$ for 1070 steel specimens at a =26mm

Table 5.1 Summary of parameters involved in two-parameter mixed-mode crack growth model - 1070 steel specimens at $\boldsymbol{a = 26mm}$

g^K_{NP} and K parameters of 1070 steel ($a = 26mm$)	Load path I	Load path II	Load path III
$g^K{}_{NP}$	0	0	0.91
$\Delta K_{NP}(MPa\sqrt{mm})$	2435	2430	3421
$K_{max}(MPa\sqrt{mm})$	3155	1976	2730
$K^*(MPa\sqrt{mm})$	2771	2191	3056

5.4.3 Data Correlation

Before the application of proposed two parameter fatigue crack growth model in Eq. (5.10) to all of non-proportional fatigue test data investigated in this paper, the

interaction coefficient η in Eq. (5.10)) needs to be determined first. This can be achieved by comparing fatigue test data corresponding to Path I and Path II based on Eq. (5.11). Since ΔK_{NP} values for Path I and Path II according to Eq. (5.8) are the same, any difference in measured fatigue crack growth rates between two load paths can be attributed to the difference in K_{max}. By fitting the crack growth rate data between Path I and Path II for 304 stainless steel, $\eta \approx 3$ is obtained and used throughout the rest of the paper.

For comparison purpose, conventional definition of effective stress intensity factor range ΔK_e given in Eq. (5.4) is first used in the form of Eq. (5.11) with K^* being replaced by ΔK_e for correlating the crack growth data for stainless steel and 1070 steels. As shown in Fig. 5.11, the scatter band is rather large, with a standard deviation of 0.47 for data from 304 stainless steel specimens. Once the proposed two-parameter non-proportional mixed mode growth model in the form of Eq. (5.11) in which K^* is calculated according to Eq. (5.12) is used, a significantly improved data correlation can be seen, as shown in Fig. 5.12, with a standard deviation of 0.25. The improvement can be attributed to both the use of MLP based equivalent stress intensity factor range (ΔK_{NP}) relevant to Load Path III and the maximum effective stress intensity factor K_{Max} which takes on a different value among the three loading paths involved. The results for 1070 steel crack growth data are shown in Fig. 5.13 using the conventional effective stress intensity factor range ΔK_e and in Fig. 5.14 using the two parameter fatigue crack growth model. Again, the effectiveness of the two-parameter mixed crack growth model in correlating the 1070 steel is clearly shown. It should be pointed out that throughout this paper, the same value of coefficient η is used for computing K_{max} for both 304 stainless

steel and 1070 structural steel specimens. Furthermore, both material sensitivity parameter (i.e. $\alpha^K = 1$) and fatigue equivalency parameter (i. e. $\beta^K = 3$) are assumed in this study, based on previous investigations [19-21]. The exponent in Eq. (5.11) is taken as $\gamma = 0.5$, as used in SWT model [17]. No attempts have been made in determining all these three parameters for achieving a best fit.

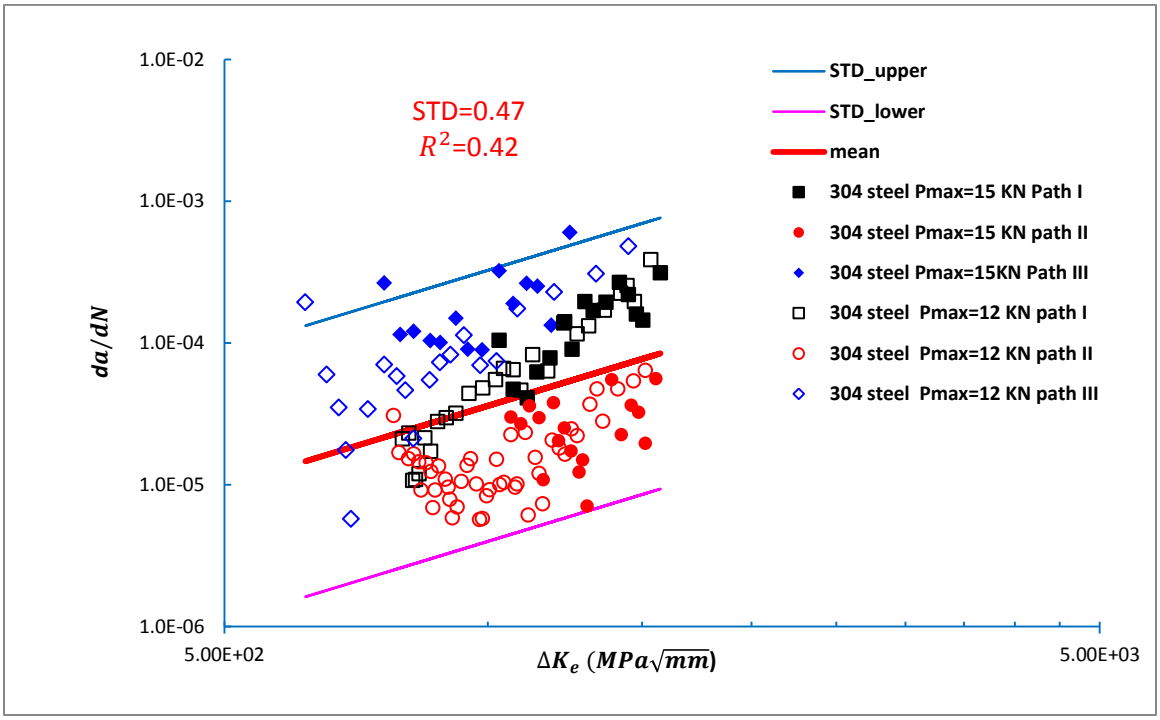

Fig. 5.11 Data correlation using conventional ΔK_e for 304 steel specimens

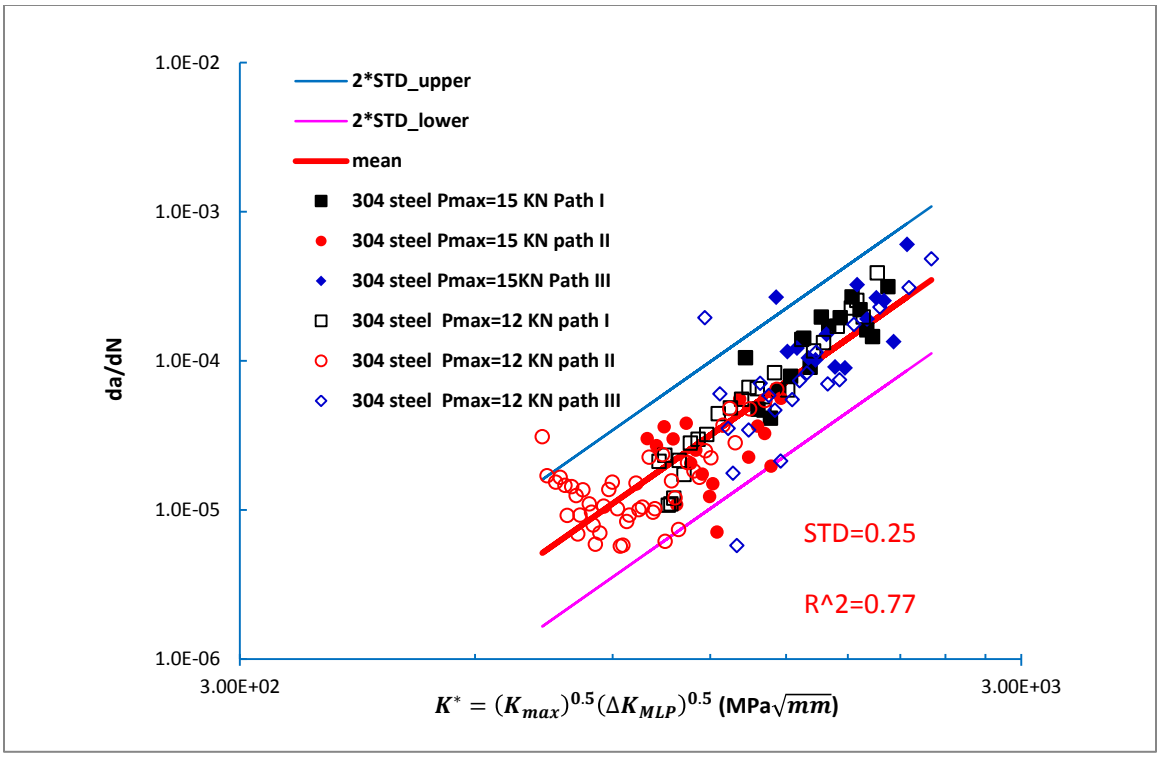

Fig. 5.12 Data correlation using MLP based two-parameter crack growth model (Eq. 5.11) – stainless steel 304 specimens

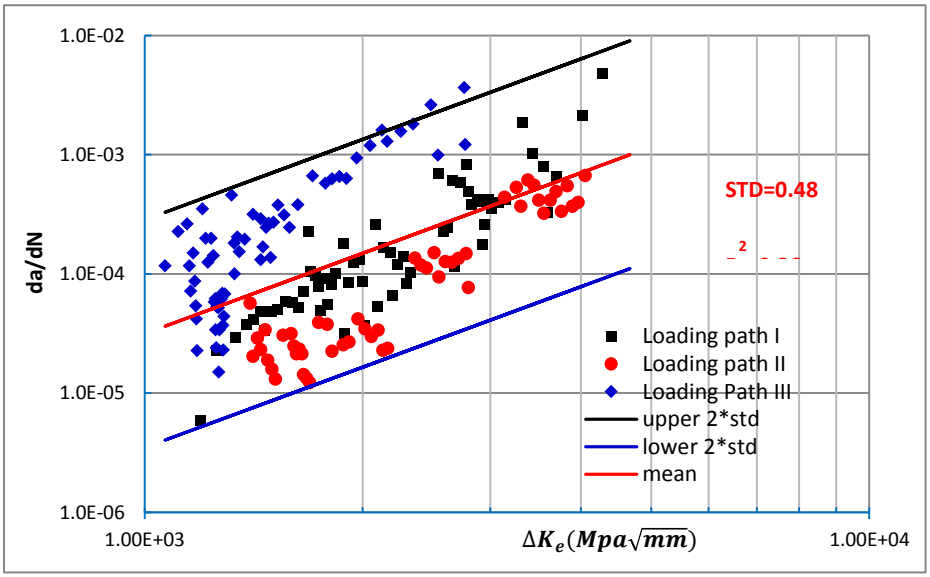

Fig. 5.13 Data correlation using conventional ΔK_e for 1070 steel specimens

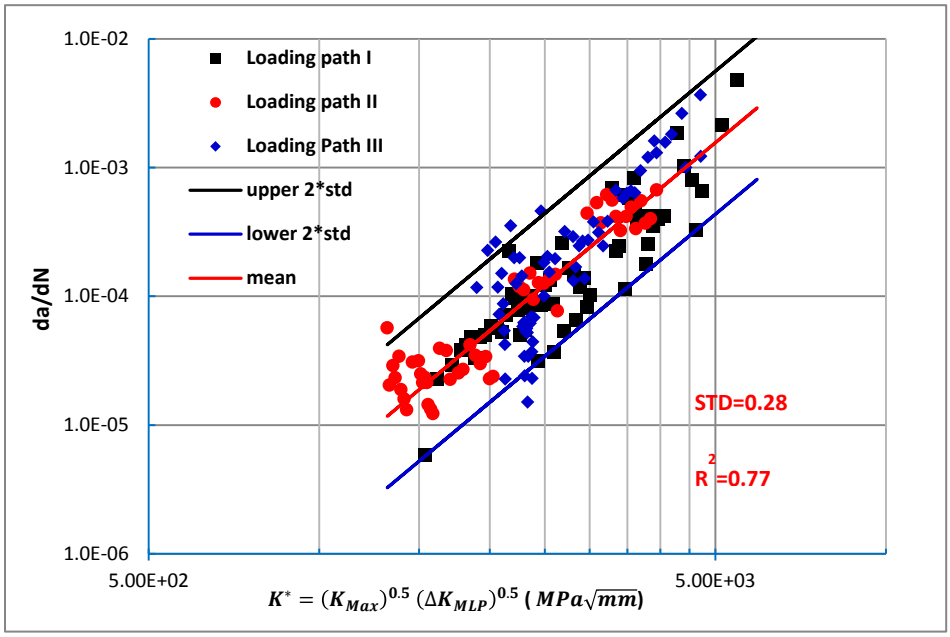

Fig. 5.14 Data correlation using MLP based two parameter crack growth model (Eq. 5.11) - 1070 steel specimens

5.5 Conclusions

A two parameter mixed mode crack growth model has been proposed for achieving an effective treatment of fatigue damage caused by both proportional and non-proportional multiaxial fatigue loading conditions. The two parameters defined with a respect to K space are: (1) Moment of Load Path (MLP) based effective stress intensity factor range which measures load path dependent fatigue damage; (2) maximum effective stress intensity factor which measures mean-stress induced fatigue damage. The effectiveness of the proposed two-parameter model has been shown in its ability to correlate crack growth rate data obtained from both 304 stainless and 1070 steel disk specimens tested under both proportional and non-proportional modes I and model III loading conditions.

Reference

[1] Tanaka K. Fatigue crack propagation from a crack inclined to the cyclic tensile axis. Eng Fract Mech 1974;6:493–507. doi:10.1016/0013-7944(74)90007-1.

[2] Richard, H. A., M. Fulland, and M. Sander. "Theoretical crack path prediction." Fatigue & fracture of engineering materials & structures 28.1-2 (2005): 3-12.

[3] Pook, L. P., "The Fatigue Crack Direction and Threshold Behaviour of Mild Steel Under Mixed Mode I and III loading," International Journal of Fatigue, Vol. 7, No. 1, 1985, pp. 21-30.

[4] Forth, S. C., Keat, W. D., and Favrow, L. H., "Experimental and Computational Investigation of Three-Dimensional Mixed-Mode Fatigue," Fatigue & Fracture of Engineering Materials & Structures, Vol. 25, No. 1, 2002, pp. 3-15.

[5] Sonsino, C. M., and Kueppers, M., "Multiaxial Fatigue of Welded Joints Under Constant and Variable Amplitude Loadings," Fatigue & Fracture of Engineering Materials & Structures, Vol. 24, No.5, 2001, 309-327.

[6] Fremy F, Pommier S, Poncelet M, Raka B, Galenne E, Courtin S, et al. Load path effect on fatigue crack propagation in I+II+III mixed mode conditions – Part 1: Experimental investigations. Int J Fatigue 2014;62:104–12. doi:10.1016/j.ijfatigue.2013.06.002.

[7] Feng, M., Ding, F., and Jiang, Y., "A Study of Loading Path Influence on Fatigue Crack Growth under Combined Loading," International Journal of Fatigue, Vol.28, No. 1, 2006, pp. 19-27.

[8] Mei, J., Dong, P., Jiang, Y., and Wei, Z., "A Path-Dependent Mixed-Mode Crack Growth Model for Non-Proportional Multi-Axial Fatigue Loading," 15th International ASTM/ESIS Sy mposium on Fatigue and Fracture Mechanics, Anaheim, CA, 2015.

[9] Dong P, Hong J, A Robust Structural Stress Parameter for Evaluation of Multiaxial Fatigue of Weldments. J ASTM Int 2006;3:100348.

[10] Mei J, Dong P. A new path-dependent fatigue damage model for non-proportional multi-axial loading. Int J Fatigue 2016;90:210–21.

[11] Mei J, Dong P. Modeling of path-dependent multi-axial fatigue damage in aluminum alloys. Int J Fatigue 2017;95:252–63.

[12] Mei J, Dong P. An equivalent stress parameter for multi-axial fatigue evaluation of welded components including non-proportional loading effects. Int J Fatigue 2017.

[13] Dong, P., Wei, Z., and Hong, J. K., "A Path-Dependent Cycle Counting Method for Variable-Amplitude Multi-Axial Loading," International Journal of Fatigue, Vol. 32, No. 4, 2010, pp. 720-734.

[14] Wei, Z. and Dong, P., "A Generalized Cycle Counting Criterion for Arbitrary Multi-Axial Fatigue Loading Conditions," The Journal of Strain Analysis for Engineering Design, Vo. 49, No. 5, 2014, pp. 325-341.

[15] Wei, Z., and Dong, P., "Multiaxial Fatigue Life Assessment of Welded Structures," Engineering Fracture Mechanics, Vol. 77, No.15, 2010, pp. 3011-3021.

[16] Dowling, N. E., "Mean Stress Effects in Stress-Life and Strain-Life Fatigue," No. 2004-01-2227, SAE Technical Paper, 2004.

[17] Dowling, N. E., Calhoun, C. A., and Arcari, A., "Mean Stress Effects in Stress-Life Fatigue and the Walker Equation," Fatigue & Fracture of Engineering Materials & Structures, Vol. 32, No. 3, 2009, pp. 163-179.

[18] Noroozi, A. H., Glinka, G., and Lambert, S., "A Two Parameter Driving Force for Fatigue Crack Growth Analysis," International Journal of Fatigue, Vol. 27, No. 10, 2005, pp. 1277-1296.

[19] de Morais, A. B., "Calculation of Stress Intensity Factors by the Force Method," Engineering Fracture Mechanics, Vol. 74, No. 5, 2007, pp. 739-750.

[20] Raju, I. S., and Newman, J. C., "Three Dimensional Finite-Element Analysis of Finite-Thickness Fracture Specimens," NASA TN D-8414 (1977).

Chaper 6.

Summary and Further Research

6.1 Summary of Proposed of MLP Based Model

The proposed non-proportional fatigue damage model, referred to as MLP based model can be defined with respect to $\sigma - \sqrt{\beta}\tau$ plane, $\varepsilon - \sqrt{\beta^{\varepsilon}}\gamma$ plane or even K plane (e.g. $K_I - \sqrt{\beta^K}K_{III}$ plane), depending on the problem to be solved. The essential elements of the proposed model, by taking its formulation in $\sigma - \sqrt{\beta}\tau$ plane as an illustration can be summarized as:

(i) For a PDMR cycle counted non-proportional load path segment defined on $\sigma - \sqrt{\beta}\tau$ plane, one can always find its proportional (reference) path which is a straight line connecting start and end point of the path segment. With reference path identified, the total fatigue damage (D) of the non-proportional path is assumed to be linearly decomposed into proportional (reference) damage part (D_P) and non-proportional damage part (D_{NP}). The proportional (reference) part can be simply represented by effective stress range (i.e. path length) of the reference path. The non-proportional part (D_{NP}) can be intuitively characterized by the extent of load path excursion away from reference path. One way of such a representation is the moment of non-proportional path with respect to its reference path.

(ii) From a mechanics perspective, the non-proportional damage part (D_{NP}) of a load path can be expressed as an integral form of strain energy density contributed by both normal and shear stresses, with each being weighted by a path dependent function. Therefore, it can be argued that non-proportional damage part is linked with the additional strain energy (in a weighted form) needed for following a non-proportional path.

(iii) A dimensionless representation of non-proportional damage part (D_{NP}) is by normalizing it with respect to a non-proportional path that has the maximum non-proportional damage effect. Based on experimental observations, circular load path is usually found to be the most damaging one among all non-proportional paths with the same reference path and is thus chosen for normalization purpose. The normalized form, termed as load path non-proportionality (g_{NP}) is load path dependent and independent of materials tested. For elliptical paths commonly employed for non-proportional fatigue test in laboratories, their analytical forms of g_{NP} are derived.

(iv) It is experimentally observed that different materials have different sensitivities to non-proportional loading in terms of their fatigue life reduction. As a result, material sensitivity parameters are needed for different alloys. With both load path non-proportionality (g_{NP}) and material sensitivity parameter (α) in place. A non-proportional fatigue damage parameter is defined in the following simple form:

$$\Delta\sigma_{NP} = \Delta\sigma_e(1 + \alpha \cdot g_{NP}) \qquad (6.1)$$

With the above MLP based equivalent stress definition, a specific procedure is provided for determining material sensitivity by examining two groups of fatigue tests results, with one group of proportional loading and another group of non-proportional loading. The first obvious advantage of MLP based equivalent stress definition is its simplicity in both its form and application, especially when compared with critical plane methods. Secondly, it characterizes non-proportionality (g_{NP}) of load path and material responses explicitly and separately.

(v) The proposed fatigue model in conjunction with PDMR cycle counting procedures constitutes an integrated approach to non-proportional multi-axial fatigue under variable amplitude loading conditions. This integrated approach is demonstrated by correlating a large amount of multi-axial fatigue test data obtained using plenty load-path patterns in either stress-plane in high cycle fatigue regime or in strain-plane in low-cycle fatigue regime.

6.2 Summary of MLP Model Applied to Aluminum Alloys

MLP based modeling of non-proportional multi-axial fatigue of aluminum alloys are carried out by examining a total amount of around 3 hundreds tests from eight independent research groups. These different types of aluminum alloys ranges from 7000 series, 6000 series, 5000 series to 2000 series. To the author's best knowledge, this is the most comprehensive analysis of non-proportional fatigue of different aluminum alloys. Different from structural steels, for which pretty good correlations are achieved by assuming a default value of material sensitivity parameter (i.e. $\alpha = \alpha^{\varepsilon} = 1$) in MLP based analysis, material sensitivity parameter is calculated for each group of aluminum test data by comparing two sets of test data (one set of proportional test data and the other

non-proportional). After that, it is then used consistently in MLP based analysis for all different load paths examined within the test group. The major findings of applying MLP model to different aluminum alloys include:

i. Compared with structural steels, all series of aluminum alloys studied show a less degree sensitivity to non-proportional cyclic loading. The material sensitivity parameters (α defined with respect to stress plane and α^{ε} to strain plane) calculated ranges from 0.35 to 0.5, much smaller than that of structural steels for which material sensitivity is generally around unity (i.e. $\alpha \approx \alpha^{\varepsilon} \approx 1$).

ii. It is found that material sensitivity parameters for same series of alloys generally remain the same regardless of the planes ($\sigma - \sqrt{\beta}\tau$ plane or $\varepsilon - \sqrt{\beta^{\varepsilon}}\gamma$ plane) with respect to which they are calculated. Also note that for different steels examined in Chapter 2, the default value of unit is used for both α defined on $\sigma - \sqrt{\beta}\tau$ plane and α^{ε} defined on $\varepsilon - \sqrt{\beta^{\varepsilon}}\gamma$ plane. It seems that α and α^{ε} can be used interchangeably at current stage.

iii. Besides demonstrating that MLP-based equivalent stress range or equivalent strain range are quite effective in correlating a large amount of non-proportional multi-axial fatigue test data, an approximately linear relationship between material sensitivity parameter and material ductility (in terms of percentage of elongation obtained from standard tests) is observed for aluminum alloys for the first time.

iv. The common belief that material sensitivity to non-proportional loading is directly related to additional hardening effect is questionable based on our research into this subject. Three arguments are given in Chapter3 and the most obvious one is

that some materials don't exhibit noticeable non-proportional hardening but still show significant non-proportional fatigue damage effect. As a result, it is recommended that the determination of material sensitivity parameter can be done by following procedures provided in this chapter or from the relationship established between material sensitivity and ductility.

6.3 Summary of MLP Model Applied to Welded Components

Based on a detailed assessment of currently available multi-axial fatigue test data in literature, the most comprehensive analysis of well-documented test data on welded steel joints are done in Chapter 4 by MLP model. These welded components are first classified as stress-relieved and as-welded components to examine if residual stress relief will have an impact on fatigue lives of examined joints. A new equivalent stress parameter is then proposed to take into account of thickness effect, stress gradient effect and non-proportional loading effect (by MLP model) based on traction structural stress definition. Furthermore, the feasibility of using current existing methods such as those stipulated in Eurocode 3 and IIW recommendations based on hot spot stress definition are also evaluated for comparison purpose. The main conclusions are:

(i) when data correlation of stress-relived and as welded test data are examined separately, by following a similar form of equivalent stress definition adopted in ASME, the following equivalent structural stress definition:

$$\Delta S_{NP} = \frac{\Delta\sigma_{NP}}{t^{*\frac{2-m}{2m}} I(r_e)^{\frac{1}{m}}} \tag{6.2}$$

further takes into account of non-proportional damage effect (by the term $\Delta\sigma_{NP}$ in Eq. 6.1) besides thickness effect and bending ratio (r_e) effect. Pretty good

collapse of test data are observed for both stress-relieved and as welded test data when compared with Eurocode 3 and IIW methods.

(ii) Residual stress relief has a beneficial effect for current examined multi-axial fatigue test data. Further consideration of stress ratio correction is done by

$$\Delta S_{NP}^{R} = \frac{\Delta\sigma_{NP}}{(1-R)^{\frac{2}{m}} t^{*\frac{2-m}{2m}} I(r_e)^{\frac{1}{m}}} \tag{6.3}$$

In this way, both stress-relived and as-welded test data can be examined as a whole. Furthermore, the new equivalent stress parameter in Eq. 6.3 enables the use of only one master S-N curve that are currently adopted by the 2007 ASME and API 579 for fatigue evaluation of non-proportional multi-axial fatigue of welded components.

(iii) Current Eurocode 3 and IIW are less reliable for non-proportional fatigue assessment of welded components for several reasons. First of all, hot spot stress calculated varies a lot even for similar types of tested welded joints when these standards are followed. Secondly, thickness and stress gradient corrections are not made for these two methods. Thirdly, non-proportional loading effects are not considered in Eurocode 3 while IIW only takes it into account in a qualitatively manner. Finally, no multi-axial cycle counting procedures are suggested in Eurocode 3 and IIW for treating non-proportional loading histories (e.g. asynchronous loading between torsion and bending). All of these above issues are resolved by our proposed equivalent stress parameter in Eq. 6.3 when integrated with PDMR cycle counting.

6.4 Summary of MLP Model Applied to Mixed Mode Fatigue Crack Growth

Mixed mode fatigue crack growth under non-proportional loading is much more challenging than cases examined in Chapter 2 and Chapter 3 for which fatigue damage is dominated by crack initiation and a proper definition of stress/strain can be used in MLP model. The difficulty of mixed mode fatigue crack growth problem, especially under non-proportional loading is twofold: determination of crack growth direction and an effective stress intensity factor applicable for both proportional and non-proportional loading. For our current examination of mixed mode I and mode III fatigue crack growth tests done by Feng et. al, it is generally observed that crack grows along initial pre-crack plane. As a result, the prediction of fatigue crack growth direction is avoided in these specific cases. Furthermore, since the mixed mode fatigue crack tests are designed with a R ratio of 0.1, crack surface interaction are avoided to make life easier. With the above considerations and simplifications, our major contributions are:

(i) MLP model is further extended to $K_I - \sqrt{\beta^K} K_{III}$ plane for constructing a MLP based equivalent stress intensity factor range parameter for non-proportional mixed mode I and mode III fatigue crack growth problem. Still, the material sensitivity parameters are also assumed to be unity as what we did in Chapter 2 and Chapter 4.

(ii) For treatment of mean stress effect, a new definition of K_{Max} defined with respect to $K_I - \sqrt{\beta^K} K_{III}$ plane is proposed. The advantage of the proposed K_{Max} in Eq. 4.9 is that it not only can be reduced to conventional definition of maximum stress intensity factor for single mode fatigue crack growth problem, but also the coupling between K_I and K_{III} is captured.

(iii) With MLP based equivalent stress intensity factor as a range parameter and K_{Max} to take into account of mean stress effect, two-parameter crack growth model in Eq. 4.10 is used for crack growth rate correlation among proportional, inversely proportional and 90° out-of-phase mixed mode fatigue crack growth test data. Its effectiveness further demonstrates that MLP based fatigue damage model can be extended to K plane as long as other factors such as crack growth direction, crack surface interaction and mean stress effect are treated in a reasonable manner.

6.5 Further Work and Recommendations

(i) The rotation of reference path.

It is important to bear in mind that non-proportional loading effect for each PDMR counted load path segment is defined with respect to its reference load path. However, for different counted load path, their respective reference paths for complex variable amplitude loading are likely to be all over the space in stress/strain planes. One such example is illustrated in Fig. 6.1. For the whole load paths A-B-C-D, PDMR cycle counting will leads to three load path segments:$\widehat{AB}$,$\widehat{CD}$ and $\widehat{BC}$. The reference path for $\widehat{AB}$ and $\widehat{CD}$ is the straight lines connecting A to B ($\overline{AB}$), C to D ($\overline{CD}$) respectively. One would notice that there is a rotation of reference path $\overline{CD}$ with respect to $\overline{AB}$. As a result of the rotation in stress plane, non-proportional fatigue loading effect is created. Our current consideration of non-proportional loading effect does not take reference path rotation into account. One extreme case done by Shamsaei et. al. [1] is shown in Fig. 6.2. Proportionally fully reversed loading with 1° of increments gradually within a circular boundary in $\varepsilon - \sqrt{\beta^{\varepsilon}}$ plane is applied until a total of 360° are swept. As described in [1], even though this strain blocks includes 360 proportional cycles based PDMR, it also

activates the rotation of principal axes and non-proportional damage is introduced as demonstrated by fatigue test results. For this special case, each proportional path (also reference path) rotates gradually and the non-proportional damaging effect is solely caused by the rotation of reference path. As a result, the rotation of reference paths can be considered in the further.

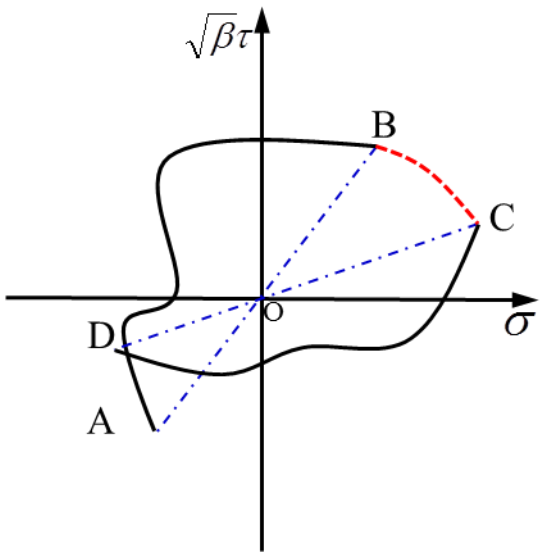

Fig. 6.1 illustration of reference path rotation between two load path segments between $\widehat{AB}$ and $\widehat{CD}$

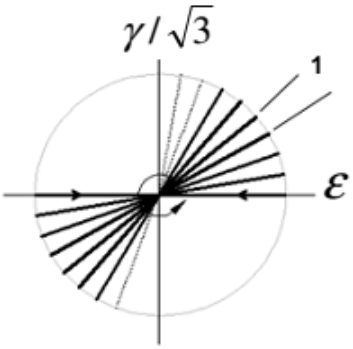

Fig. 6.2 Fully reversed with 1° increments load blocks used by Shamsaei et. al. [1]

(ii) Systematic examination of the relationship between material sensitivity and ductility

One of the most important observations throughout this dissertation is that material sensitivities for different materials tend to be related to their ductility in terms of elongations based on our examination of different types of metallic alloys. This finding is vital for non-proportional fatigue assessment of metallic alloys since once the linkage between them is established, proportional and non-proportional fatigue experiments can be avoided for material sensitivity determination. Therefore, it is necessary for researchers to further look into the connection between the two material properties by carrying out well-controlled proportional and non-proportional fatigue tests on different materials with different levels of ductility. We would suggest that materials with low ductility, medium ductility and all the way to high ductility (i.e. stainless steel) are tested. Once such a relationship is firmly established, the mechanisms leading to such a conclusion can be investigated further at a micro-scale from material's point of view.

(iii) Application of MLP model in frequency domain

This is a topic that has not been explored yet and it is of both academic and practical significance in the near future. Frequency domain (PSD) based fatigue life estimation has already been generally established and used as an important way of fatigue damage assessment. It seems that one way of characterizing load path non-proportionality may be related with covariance between different loading components. However, a probabilistic distribution of loading cycles for different stress ranges is a challenging issue to be solved. Derivation of such an analytical/empirical form of distribution would require a strong background of stochastic process.

(iv) Real and more complex variable amplitude loading history for engineering application

We have examined a large variety of non-proportional load paths including asynchronous loading paths (i.e. different loading frequency ratios between axil loading and torsion loading). These are the majority of complex non-proportional loading paths available in the literature. Unfortunately, more complex variable amplitude loading histories test data such as those non-proportional service loading histories can't be easily obtained from literature. The next leve of validation and application of MLP model can be done by examining non-proportional fatigue damage of engineering structures under real and complex non-proportional variable amplitude loading histories.

Reference

[1] Shamsaei N, Fatemi A, Socie D F. Multiaxial fatigue evaluation using discriminating strain paths. Int J Fatigue 2011;33:597–609.